UNIVERSITÀ DEGLI STUDI DI TRIESTE

XXIX CICLO DEL DOTTORATO DI RICERCA IN

INGEGNERIA E ARCHITETTURA

DETERMINISTIC SEA WAVE AND SHIP MOTION FORECASTING: FROM REMOTE WAVE SENSING TO PREDICTION ERROR ASSESSMENT

Settore scientifico-disciplinare: **ING-IND/01 ARCHITETTURA NAVALE**

DOTTORANDO
Fabio Fucile

COORDINATORE
Diego Micheli
Università degli Studi di Trieste

SUPERVISORE DI TESI
Gabriele Bulian
Università degli Studi di Trieste

CO-SUPERVISORE DI TESI
Claudio Lugni
CNR-INSEAN

ANNO ACCADEMICO 2015/2016

UNIVERSITÀ DEGLI STUDI DI TRIESTE

XXIX CICLO DEL DOTTORATO DI RICERCA IN

INGEGNERIA E ARCHITETTURA

DETERMINISTIC SEA WAVE AND SHIP MOTION FORECASTING: FROM REMOTE WAVE SENSING TO PREDICTION ERROR ASSESSMENT

Settore scientifico-disciplinare: **ING-IND/01 ARCHITETTURA NAVALE**

Ph.D. Candidate
Fabio Fucile

DOCTORATE COORDINATOR
Diego Micheli
University of Trieste

SUPERVISOR
Gabriele Bulian
University of Trieste

CO-SUPERVISOR
Claudio Lugni
CNR-INSEAN

ACADEMIC YEAR 2015/2016

ABSTRACT

Presently, the assessment of the operational safety of ships and offshore structures is typically addressed within a statistical framework, both at design stage and for the specification of operational limits. Recently, however, the availability of new remote sensing technologies is paving the way for complementary approaches based on deterministic predictions of sea waves and ship motions. In this respect, the marine wave radar is considered as the key asset for the deterministic prediction of wave elevation. Indeed, the possibility of measuring the sea surface, almost instantaneously and for large areas, can be used to forecast the wave elevation at the location of the operating units. Eventually, the coupling of deterministic wave forecast with suitable ship motion models opens the possibility for giving anticipated prediction and guidance. The application of this emerging approach can be beneficial to those short-time offshore operations requiring sea wave or ship motions to be forecast in the time horizon of tens of seconds to minutes. This envisages the possibility of development of finely tuned early warning, hazard control and support decision systems. One of the main aspects of this chain of models, which is oftentimes overlooked, is the importance of providing the forecast with a consistent assessment of the prediction error. Moreover, the additional sources of uncertainty coming from the wave measurement and from the inversion of the wave radar images are also seldom accounted for.

In this thesis, the whole chain of models, that from the wave radar measurement leads to the ship motion prediction, is investigated. The first step is the proposal of a novel technique for the inversion of wave radar images that can consistently account for those regions of the sea surface that cannot be uniformly illuminated because of the shadowing effect. The adoption of a linear least square fitting approach, provided with a regularization technique, allows the proposed inversion method the needed flexibility to address the shadowed regions as missing data. Afterwards, the assessment of the error associated with deterministic wave predictions is addressed. A novel semi-analytical procedure is proposed which allows estimating the ensemble variance of prediction error, in a simple and flexible way, naturally embedding the characteristics of the linear fitting and propagation procedures. The approach also allows the inclusion, in the estimation of prediction error, of the effect of measurement error coming from the radar inversion techniques. The same technique for the estimation of wave elevation prediction error is then extended to linear ship motions, using linear transfer functions. In fact, the developed framework can deal with any linear transformation of the wave elevation, resulting in the definition of a sound measure of the prediction error of linear responses. The method can be used to provide deterministic predictions with confidence intervals, as well as for a consistent setup of the whole forecasting chain.

The developed models are then tested for a set of application examples considering both linear and nonlinear wave fields. In this latter respect, a high order spectral method has been implemented to provide more realistic wave elevation fields. Example applications regarding linear ship motions have also been carried out. The proposed inversion procedure has shown interesting results for synthetic radar images generated from both linear and moderately nonlinear wave fields. However, further investigations are needed to reduce the high computational cost required for the inversion. The proposed approach for wave and ship motion prediction error, instead, can represent a convenient novel sound method for the consistent setup of deterministic prediction procedures, remaining, however, limited to those scenarios where nonlinearities play a minor role.

SOMMARIO

Attualmente, la valutazione della sicurezza delle navi e delle strutture offshore è affrontata dal punto di vista statistico, sia in fase di progettazione che per la specifica dei limiti operativi. Recentemente, tuttavia, la disponibilità di nuove tecnologie di *remote sensing* sta aprendo la strada ad approcci complementari, basati sulla previsione deterministica delle onde e dei moti nave. A tal proposito, il *wave radar* è considerato lo strumento chiave per la previsione deterministica d'onda. Esso, infatti, permettendo la misura delle onde, in maniera quasi istantanea e per grandi aree, può essere utilizzato per prevedere l'elevazione onda in corrispondenza delle posizioni di interesse per le unità in operazione. L'eventuale accoppiamento di tali previsioni d'onda con adeguati modelli di moti nave, può permettere, infine, di fornire previsioni dei moti e supporto operativo. In particolare, questo nuovo approccio può risultare particolarmente utile a quelle operazioni offshore, di breve durata, che richiedono la conoscenza anticipata del moto ondoso o dei moti nave, con un orizzonte temporale che va dalle decine di secondi ai minuti. Esso, inoltre, apre alla possibilità di sviluppo di sistemi integrati di allerta rapida, controllo del rischio e di supporto decisionale. Uno degli aspetti principali di questa catena di modelli, che viene spesso trascurato, è l'importanza di associare alle previsioni deterministiche una valutazione coerente dell'errore previsionale, eventualmente includendo in questa stima, anche ulteriori fonti di incertezza legate agli errori di misura delle onde e ai modelli di inversione delle immagini radar, aspetto, quest'ultimo, che è considerato ancor più di rado.

In questa tesi, si è analizzata l'intera catena di modelli che partendo dalla misurazione radar delle onde porta alla previsione dei moti nave. Il primo passo è stato sviluppare una nuova tecnica per l'inversione delle immagini radar che possa prendere in considerazione, in modo consistente, quelle regioni della superficie del mare che, a causa dell'effetto di *shadowing*, non sono illuminate. L'utilizzo di un approccio lineare ai minimi quadrati, associato ad una tecnica di regolarizzazione, fornisce al metodo proposto la flessibilità necessaria per gestire le regioni in *shadowing* come *missing data*. Successivamente si è affrontato il problema della valutazione dell'errore associato alle previsioni d'onda deterministiche. A tal proposito, si è sviluppata una nuova procedura semi-analitica, semplice e flessibile, per stimare il valore atteso della varianza dell'errore di previsione. La procedura prende in considerazione, fin da principio, le caratteristiche del *fitting* e della propagazione lineare delle onde. Questo approccio permette anche di includere agevolmente, nella stima dell'errore di previsione, l'effetto dell'errore di misura proveniente dalle tecniche di inversione delle immagini radar. La stessa tecnica per la stima di errore di previsione d'onda è stata poi estesa al calcolo dei moti nave lineari grazie all'utilizzo delle funzioni di trasferimento lineari. Infatti, il metodo sviluppato permette di considerare una qualunque trasformazione lineare dell'elevazione d'onda, associando, alle relative risposte lineari, una misura consistente dell'errore di previsione. Quindi, il metodo sviluppato, può essere utilizzato con due diverse finalità: può essere impiegato per associare alle previsioni deterministiche i relativi intervalli di confidenza , ma anche, e più in generale, per progettare, dal punto di vista quantitativo, tutta la catena di previsione deterministica.

I modelli sviluppati nell'ambito di questa tesi sono stati poi testati per una serie di applicazioni di esempio, definite in modo da considerare sia onde lineari che onde nonlineari. A tal fine, e quindi per poter generare treni d'onda più realistici, si è provveduto a sviluppare un metodo spettrale di alto ordine. A questi test si sono aggiunti anche test di esempio per i moti nave. La procedura proposta per l'inversione delle immagini radar ha permesso di ottenere risultati interessanti sia nel caso di inversione di immagini radar per onde lineari che nel caso di onde moderatamente nonlineari. Tuttavia, ulteriori approfondimenti sono necessari al fine di abbattere l'elevato costo computazionale della procedura di inversione proposta. Per quanto riguarda l'approccio proposto per la stima dell'errore associato alla previsione d'onda e dei moti nave, esso può rappresentare sicuramente un metodo innovativo e consistente per la messa a punto delle procedure di previsione. Si sottolinea, tuttavia, come il suo utilizzo sia da intendersi limitato alle situazioni in cui gli aspetti nonlineari del problema siano trascurabili.

ACKNOWLEDGEMENTS

CNR-INSEAN is gratefully acknowledged for the financial support granted for the research activities undertaken for this thesis, through the funding of Ph.D. scholarship D/4 - Cycle XXIX. This work has been carried out at University of Trieste and at CNR-INSEAN, and the author would like also to thankfully acknowledge CNR-INSEAN for the kind hospitality and personal support.

TABLE OF CONTENTS

LIST OF FIGURES

LIST OF TABLES

1 INTRODUCTION

1.1 Deterministic wave and ship motion forecasting

The assessment of the behaviour of a ship or an offshore structure, especially when facing adverse weather conditions in open sea, is a fundamental aspect in the design of ships and offshore units and in the planning and execution of offshore activities. The most important objective is to guarantee the safety of such operations, concerning both human safety and the safety and integrity of the structure. On the other hand, the possibility of extending and optimizing the performances of offshore units is economically relevant for the industry. The assessment of ship motions historically was, and still is, mainly addressed from a statistical point of view. Ship motions, considered as forced by environmental excitations and especially by the waves, can indeed be modelled relating the ship responses to the statistical properties of the sea environment. This allows tackling the problem of defining the ship safety and operability requirements in a probabilistic framework, providing for a solid ground for the design of such offshore units. Moreover, this allows to define, accounting for the sea spectrum main characteristics, the allowable limits which the operability of the ship is bound to. In the planning of medium/long term offshore activities, the forecasting of the sea state characteristics is a well-established practice. However, this usually results in a coarse grained criterion that establishes, for the given time interval of the wave forecasting, whether it is possible to operate or whether it is better to stay in a controlled and safer condition.

In this respect, the advances in the remote wave sensing technologies are giving new opportunities for the setup of complementary approaches to the classical statistical/spectral ones, and based on a real time assessment of the operational danger through deterministic ship motion forecasting. The whole idea underlying the deterministic ship motion forecasting procedure can briefly summarised in the workflow reported in Figure 1.1. First, the sea surface is assumed to be measured at a suitable distance from the ship from an appropriate sensor, typically a wave radar. Then, wave elevation measurements are used to initialize a wave prediction model that from the far field information can reconstruct the wave elevation in correspondence to the position of the structure or any other needed location. This information are eventually coupled with a ship motions model in order to forecast the behaviour of a ship in the near feature, the typical time horizon is in the order of minute. It is clear that delicate

and/or short time operations, like for example rescue missions, loading/unloading operations, airborne vehicle recovery or any operation for which a correct ship motion prediction is of crucial importance, will possibly benefit for this kind of approach. Indeed, this little glimpse of predicted future certainly will allow for a finer tuning of offshore operation, a sensible delay for warning of safety shutdown procedures, with consequent reduction of downtime, and possibly, also, for the automatization of certain operations at sea.

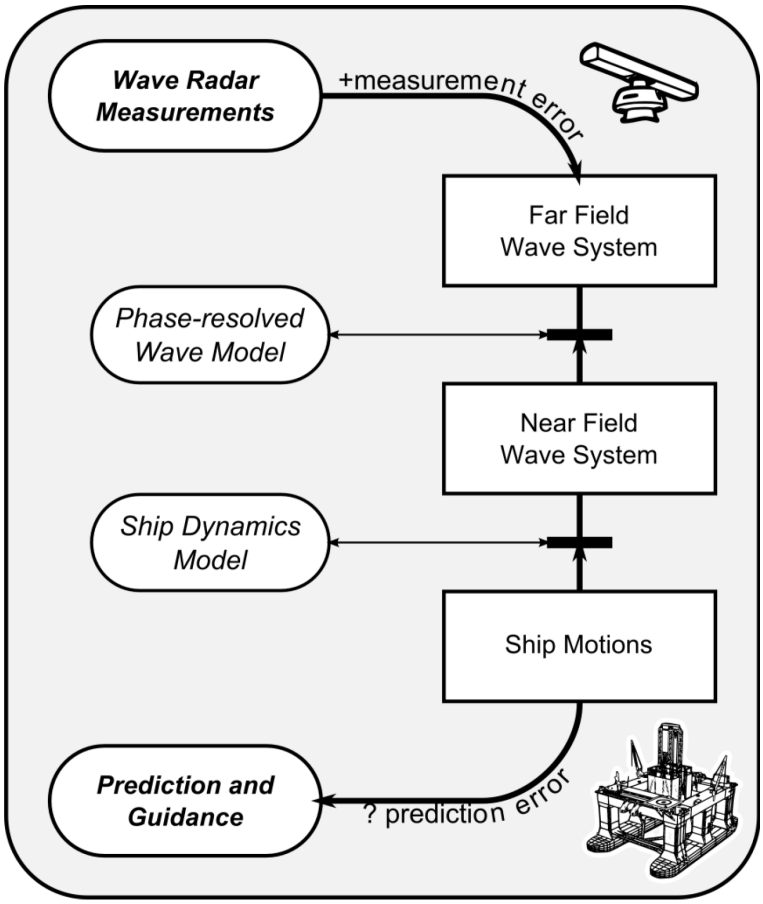

Figure 1.1: Schematic representation of the deterministic ship motion forecasting workflow.

In fact, there is an increasing interest on the topic of deterministic predictions that has led to extensive investigations on the feasibility of this technology and to a multiplication of proposals for its implementation (see for example Alford et al. [3], Clauss et al [30], Kusters et al. [75], Naaijen et al. [101]). In the majority of the studies, the wave radar has been assumed as the central asset for the measurement of the sea surface, as indicated in Figure 1.1. Indeed, marine wave radars are capable of scanning, almost instantaneously, large areas of the sea surface by a combination of a radial range of kilometres and an azimuthal sweeping period of the order of the seconds. Moreover, the installation of this technology will results particularly cost-effective in case non-coherent wave radars are concerned, since they are most of the times already present on ships for anti-collision and ranging purposes. The acquired time series of backscattered radar images must undergo an inversion process, before being actually available for the wave prediction step. This is related to how the wave radar actually works. In fact, the wave radar senses the presence of the wave field as a modulation in the received backscatter signal from the wavy sea surface. In essence, the main backscattering phenomena are the tilt modulation, that accounts for the titling of the backscattering surface facet as the longer gravity waves pass by, and the showing effect, accounting for the fact that the wave radar is prevented from uniformly illuminating the whole sea

surface, especially at low grazing angles, because of the presence of wave peaks (Nieto Borge et al. [105]). Several technique have been proposed for the deterministic reconstruction of the wave elevation field starting from radar images (Dankert and Rosenthal [35]; Naaijen and Wijaya [104]; Nieto Borge et al. [105]; Serafino et al. [129]). In this respect, it has to be noted that the majority of the proposed inversion techniques only partially account for the shadowing effect, by adopting *a-posteriori* correction procedures, simplifying or even completely neglecting the problem. Moreover, the measurement error, inevitably affecting the measurement and the inversion processes, is seldom characterized and its effect on the subsequent forecasting chain is, most of the times, disregarded.

The next step in the forecasting chain is the deterministic wave prediction through a phase-resolved approach, see Figure 1.1. The most widespread approach for this step is based on the use of linear wave propagation models. Indeed, linear models are considered accurate enough to reproduce the main features of the wave field and, due to the limited computational cost, they are particularly suitable for real time applications (Hilmer and Thornhill [68]). Different aspects of the implementation of linear wave prediction model have been investigated, for example, by Belmont et al. [9][10], Blondel-Couprie and Naaijen [17], Connell et al. [33], Naaijen and Blondel-Couprie [97]. Nonetheless, there are different proposals to account also for the nonlinear evolution of the wave field, as investigated for example by Alford et al. [3], Blondel-Couprie et al. [14][15], Wu [159], Clauss et al. [29] and Yoon et al. [166]. In any case, all the deterministic wave prediction techniques, being them only an approximation of the underlying true wave field, will inevitably be affected by a prediction error. Therefore, the need of providing, beforehand, for an assessment of the space/time region where the wave prediction can be considered as reliable, becomes a central problem in deterministic forecasting. Presently, there are two main criteria which are used to assess the quality of a determinist prediction: the Predictability Region and the Predictability Indicator (Wu [159]; Naaijen et al. [102]). Both these techniques are based on semi-empirical assumptions about the modelling of the prediction error. The main idea is that the group velocity of the measured wave components (an assumption which has been questioned by Abusedra and Belmont [1]) can be used for the identification of where the prediction is possible or not, as in the case of the Predictability Region, or what is the expected quality of the prediction, as in the case of the Predictability Indicator. However, neither of these two techniques, although widely used for the setup of forecasting procedures, can provide for a consistent statistical measure of the expected prediction error that can eventually be used to supplement the deterministically predicted wave elevation with a suitable confidence interval. More importantly, the additional source of uncertainties due to the measurement error is oftentimes overlooked and none of the presently available techniques directly accounts for it.

The prediction of the ship motions is the last step in the forecasting chain, see Figure 1.1. The most straightforward way to link the wave elevation prediction with the ship motions is by assuming the possibility of using an approach based on transfer functions, typical of the linear seakeeping framework (Naaijen and Huijsmans [99]; Naaijen et al. [101]; Kosleck [74]). In addition, also linear/nonlinear hybrid time domain models have been proposed (Alford et al. [3]; Connell et al. [33]), and some interesting results for the calculation of the low frequency second order motions have also been reported (Naaijen and Huijsmans [100]). In detail, the experimental tests, carried out by Naaijen and Huijsmans [99], are particularly interesting because they highlight how the prediction error for the linear ship motion cannot be directly linked to, and qualitatively

represented by, the wave elevation prediction error. This is mainly related to the wave-structure interaction. Nonetheless, the assumption of a perfect matching, in terms of performance, of the deterministic wave elevation prediction and of the ship motion deterministic prediction is very common. Although this could represent a reasonable working hypothesis, it may results to be too general and possibly inaccurate. In addition, presently, no clear indication about the expected magnitude of the motion prediction error can be provided, making therefore impossible the assessment of the degree of accuracy of the forecasted motion. Eventually, as for the deterministic wave prediction, the measurement error is generally not accounted for. Therefore, a systematic characterization of the impact, on the motion prediction, of the uncertainties embedded in the first step of the forecasting chain is missing in existing techniques.

1.2 Objectives and outline of the work

It is apparent that the deterministic forecasting of ship motions is a complex procedural task that requires different models to work together: the radar inversion model, the wave propagation model and the ship motion model. Each of these models uses, as input, the output coming from the previous ones. This chain of input-output relations propagates the possible sources of error across the whole forecasting chain. For this reason, a methodology for the assessment of the prediction error capable of treating different error sources in a consistent way becomes of central importance. This thesis aims in this direction, trying to investigate and develop alternative techniques to contribute to the solution of some of the identified limitations of presently available models and providing for a more general and consistent treatment of the prediction error.

The first objective has been the development of a novel radar inversion technique and the characterisation of the associated reconstruction error. The critical point, that has been spotted, concerns the treatment of the shadowing effect. The main idea to overcome this problem is to cope directly with the shadowing effect by a redefinition of the inversion problem as a missing data problem. By means of a linearized radar model, the radar images can be fitted only considering those regions that are not affected by shadowing. The resulting linear inversion problem has been setup as a least squares problem with the addition of a regularization technique. The resulting technique is referred to as Least SQuares with Regularization method (LSQR). Eventually, the reconstruction error, due to the inversion, has been investigated defining the main statistical quantities relevant to the following modelling steps.

Secondly, the lack of consistent tools for the assessment of the prediction error has led to the definition of a novel approach for the estimation of prediction error, the Linear Estimator of the Prediction Error (LEPrE) method. The deterministic prediction problem has been redefined in a probabilistic framework that allows to account directly for the expected error associated to any linear propagation procedure of the wave fields. At the same time, the developed approach allows to account for the measurement error coming from the reconstruction process. The LEPrE method has been developed as semi-analytical tool to quantify the ensemble variance of the prediction error. The new methodology not only allows to quantitatively assess the performance of a linear prediction but it can also be used to redefine the concept of predictability region on a more solid ground.

Finally, the LEPrE method has been extended to the assessment of the linear motion prediction error. The resulting method allows to consistently account for the error introduced by the wave prediction model, as well as for the error coming from the radar

inversion process. The result is a new methodology that could provide an important tool for the design of deterministic motion prediction procedures having at disposal a probabilistically consistent measure of the prediction error.

The need to benchmark the developed linear methodologies with more realistic nonlinear wave fields has required the implementation of a High-Order Spectral (HOS) method. The developed HOS has been implemented on the basis of the state-of-the-art. In order to provide information which might be useful for further studies, some special care has been dedicated to the analysis and description of initialization and stability issues for the generation of nonlinear wave fields.

This thesis is organized as follows. In chapter §2, the main aspects of the implementation of the HOS code are presented. The overall theory and the numerical implementation of the tool are reported. Some tests, considered as relevant for the verification of the software, are eventually carried out. Finally, some results about the generation of nonlinear wave fields are presented.

In chapter §3, the developed LSQR inversion technique is presented. First, the linearized model of the wave radar is derived. Then, the LSQR inversion technique is described by reporting how the model has been set-up and by providing a detailed discussion about the implementation of the regularization technique. Examples of detailed characterizations of the reconstruction error are provided, by the LSQR inversion of synthetic radar images generated for both linear and nonlinear wave fields.

In chapter §4, the LEPrE methodology is presented. The main assumptions about the definition, in a probabilistic framework, of the wave prediction problem are discussed. The LEPrE formulation for the calculation of the ensemble variance of the prediction error is derived. Eventually, some example applications are presented, considering linear long crested and short crested sea conditions. The inclusion in the model of the measurement error is also considered, by providing some example of assessment of the wave prediction error, accounting for simplified models of radar inversion error, both in case of linear long crested and short crested seas, as well as in case of nonlinear long crested sea conditions.

In chapter §5, the LEPrE methodology is extended to the estimation of the motions prediction error. The way the linear motion transfer functions are included in the method is presented, as well as the formulation of the motion prediction error taking into account the wave measurement error. Some examples of motion prediction are reported considering two different ships: a FPSO considered as stationary (zero-speed) and a Containership advancing in the seaway. A discussion is provided on how the wave-structure interaction affects the prediction error of the ship motion. In addition, some technological and practical considerations, based on the developed LEPrE for motion are drawn through some example applications.

Eventually, in chapter §6, some concluding remarks about the presented methods and some proposals for further investigations are provided.

2 WATER WAVE MODELLING

In this chapter, the water wave problem is presented in the framework of the potential flow theory with particular focus on the introduction of the High Order Spectral (HOS) method. The main analytical and numerical aspects of the method are presented and discussed. A series of specific notes are provided throughout the chapter regarding details of the implementation of the HOS method in the code developed starting from the reported theory. Some test case and the application of the HOS method to the generation of long crested nonlinear wave field are reported.

2.1 Introduction

In the framework of deterministic sea wave prediction method (DSWP) a key role is played by the water wave models. The linear wave model is still the most wide used because of the limited computational burden and capability of modelling the main wave field characteristics, especially in consideration of the limited time and space horizon required by a typical DSWP application (Hilmer and Thornhill [69]). The linearity assumption, by allowing a straightforward implementation of the Fast Fourier Transform (FFT) makes this model suitable for real time application. Besides this, the coupling of linear DSWP procedures with water wave measurement still represent the starting point for many wave forecasting techniques (Blondel-Couprie and Naaijen [17]; Naaijen and Blondel-Couprie [97]; Connell et al. [33]). Weakly nonlinear second order or adjusted second order models, the latter corrected to account for the third order dispersion relation, have also been investigated for an application to the DSWP problem (Blondel-Couprie [14]). Nonetheless, in the recent years, increasing interest is rising about employing nonlinear phase-resolved models for the DSWP application. Among others, the High-Order Spectral method (HOS) and the Dirichlet Newman Operator Methods (DNO) have been widely investigated for their direct application to the deterministic wave forecasting (Blondel-Couprie et al. [15]; Blondel-Couprie et al. [16]; Wu et al. [160]; Xiao et. al. [163]; Aragh and Nwogu [5]). These two nonlinear models are mode-coupling methods and they share interesting computational characteristics because of the adoption of a pseudo-spectral approach, the computational cost is proportional of the spatial discretization, order $O(N \log N)$. They can also conveniently deal with broad-band and multidirectional wave fields. The DNO and HOS methods have strong commonalities in how the nonlinear wave problem is solved. The main point is the definition of system of evolution equations for the wave elevation and the

free surface velocity potential based on the formalism introduced by Zakharov [169]. Then, the two methods differ in the way the associated Dirichlet boundary value problem is imposed. However, the HOS and DNO methods are in general difficult to associate with only a wave measurement because of the need of the simultaneous initialization of the nonlinear wave elevation and the velocity potential. For example, device like the wave radars, although being capable of imaging instantaneously a large areas of the sea surface, are hardly compatible with the nonlinear initialization required of the HOS method. In this respect, different techniques have been developed in order to match the initial condition for the HOS or DNO models with the wave data measurements. This implies optimization or data assimilation techniques on the initial wave elevation and free surface velocity potential (Blondel-Couprie et al. [14]; Wu [159]; Yoon et al. [166]; Hassanaliaragh [67]). Nevertheless, the HOS method is still considered an accurate tool for the simulation of the water wave fields. In particular it has been used for the investigation about the statistical quantities of nonlinear sea states and for the study of the nature of rouge waves (Ducrozet et al. [44]; Fedele et al. [46]; Tanaka [138]; Toffoli et al. [140]; Toffoli et al. [141]; Xiao, [161]; Xiao et al. [162]). Recently, HOS method has been used to determine the probability occurrence of a rogue wave within the Hurricane Joacquin and its probability of meeting with the El Faro ship during the 2015 accident which caused the ship sink and the loss of the crew (Fedele et al. [47]). In these cases, indeed, the statistical analysis is of interest and then, the exact initialization of the HOS, necessary for an accurate match of the real initial condition, is less relevant. Therefore, the model can be simply initialized through condition deriving by low order methods, typical linear and based on wave spectra data. In this respect, the adoption of the HOS method is particularly convenient for the generation of nonlinear wave fields because of its flexibility in accounting for the wave nonlinearities and the good computational performances. Because of the above considerations, the HOS method is herein studied and developed as a tool to generate nonlinear and complex sea states.

This chapter is organized to give a global description of the water wave problem; main focus is given on the numerical aspects associated with the implementation of the HOS method. First, the theory of the water wave problem is outlined, introducing the main topics relevant to the discussion. Then, the analytical bases of the HOS method are presented. The Zakharov [169] equations are introduced and the Dirichlet boundary value problem is defined following the works of Dommermuth and Yue [41] and West et al. [151]. Different approaches for the calculation of the nonlinear terms are explained along with the definition of the spectral basis. Afterwards, numerical aspects of the HOS implementation are discussed. The pseudo-spectral approach and aliasing removal techniques are presented with details about the implementation in the developed code. The time integration scheme is explained with the choice of the time step associated for the linearized problem. Then, the high frequency spurious terms which typically arise in HOS simulations are described, defining the filtering strategies to overcome the issue. Some aspects of the initialization of the HOS are presented with particular attention to the definition of the adjustment scheme for the initialization from linear wave models. The HOS is then tested following the main results available in literature. The accuracy of the method in reproducing the velocity field of Stokes wave is reported and a simulation of evolution of a Stokes wave train perturbed by side band instabilities is carried out. Finally, an application of the HOS method is presented, where a set of long crested sea states is generated with the HOS and the main emerging nonlinear features are discussed.

2.2 Water wave problem

The main aim of this section is to present the water wave problem in the framework of the potential flow theory.

Let us consider a fluid domain V, bounded by the surface $\partial V = S_{FS} \cap S_B \cap S_L$ where S_{FS} is the free surface, S_B the bottom surface and S_L the lateral surface bounding the domain, (see Figure 2.1). The spatial coordinates are defined as (x, y, z), where the vectors $(\mathbf{e}_x, \mathbf{e}_y, \mathbf{e}_z)$ define a Cartesian reference frame with the origin placed on the mean free surface, S_{FS0}.

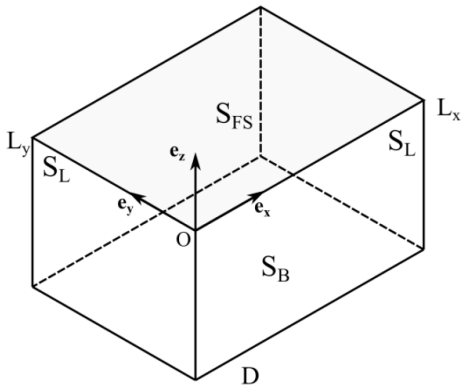

Figure 2.1: Schematic representation of the fluid domain.

The water is assumed as an incompressible and inviscid fluid in a constant gravitational field $\mathbf{F} = -\rho g \mathbf{e}_z$ (for example Johnson [70]) with density, ρ, constant in the whole domain V and g gravity acceleration. The velocity field, $\mathbf{u} = \mathbf{u}(x, y, z, t) = [u, v, w]^T$, satisfies the mass and momentum conservation equations:

$$\nabla \cdot \mathbf{u} = 0 \text{ mass conservation} \tag{2.1}$$

$$\frac{\partial \mathbf{u}}{\partial t} + (\mathbf{u} \cdot \nabla)\mathbf{u} = -\frac{1}{\rho}\nabla p - g\mathbf{e}_z \text{ momentum conservation} \tag{2.2}$$

where $p = p(x, y, z, t)$ is the pressure field.

The further assumption of irrotational flow, i.e. $\nabla \times \mathbf{u} = \mathbf{0}$, enables the definition of the velocity potential the velocity potential as $\nabla \phi = \mathbf{u}(x, y, z, t)$ on each point of the fluid domain V. Furthermore, the mass conservation equation can be rewritten in the form of the Laplace equation for the velocity potential:

$$\nabla^2 \phi = \phi_{xx} + \phi_{yy} + \phi_{zz} = 0 \tag{2.3}$$

and the momentum equation can be written in the form of the Bernoulli unsteady equation:

$$\phi_t + \frac{1}{2}|\nabla\phi|^2 + gz + \frac{p}{\rho} = C(t) \tag{2.4}$$

where $C(t)$ is the Bernoulli constant, depending only on time. Some attention has to be paid in accounting for the Bernoulli constant depending on the particular problem set-up. In general, the Bernoulli constant is either absorbed by the time derivative of the potential, e.g. by defining $\phi' = \phi + \int_0^t C(t)dt$, or by a suitable definition of a reference pressure or water level (in the case the fluid at infinity is considered at rest (Johnson, [70]). The associated boundary value problem is completed by proper conditions at the boundaries of the domain. In particular for the water wave problem, the "free surface" approximation is introduced to reproduce the dynamic evolution of the air-water interface. With free surface we mean a geometrical surface described through a continuous function $z = \eta(x, y, t)$ in space and time, over which external pressure still persists. The Bernoulli equation, calculated on the free surface, takes the following form:

$$\phi_t + \frac{1}{2}|\nabla\phi|^2 + gz = -\frac{p}{\rho} \qquad \text{on } S_{FS} \tag{2.5}$$

where the pressure $p = p(x, y, t)$ is the external pressure acting on the wave surface. In case the coupling between the external pressure and the wave dynamics can be neglected a usual assumption is to consider the pressure as constant and equal to the mean air pressure as $p = P_a = const$. Moreover if the external pressure is set to zero, $P_a = 0$, equation (2.5) is rewritten as:

$$\phi_t + \frac{1}{2}|\nabla\phi|^2 + gz = 0 \qquad \text{on } S_{FS} \tag{2.6}$$

Along the free surface the fluid is assumed to have only tangential motion, which leads to the kinematic condition:

$$\eta_t + \phi_x\eta_x + \phi_y\eta_y = \phi_z \qquad \text{on } S_{FS} \tag{2.7}$$

In the case of a flat bottom, located at $z = -D$, the no cross-flow condition is ensured by:

$$\phi_z = 0 \qquad \text{on } S_B \tag{2.8}$$

Alternatively in the case of a deep water problem, the condition (2.8) becomes:

$$\phi_z \to 0 \qquad z \to -\infty \tag{2.9}$$

Finally, the nonlinear wave field is defined in terms of the solution of Laplace problem with the associated set of boundary conditions, as:

$$\nabla^2\phi = 0, \qquad \begin{matrix} -D < z < \eta(\mathbf{x},t) \\ (-\infty < z < \eta(\mathbf{x},t)) \end{matrix} \tag{2.10}$$

$$\eta_t + \phi_x\eta_x + \phi_y\eta_y = \phi_z \qquad \text{on } z = \eta(\mathbf{x},t) \tag{2.11}$$

$$\phi_t + \frac{1}{2}\left|\nabla\phi\right|^2 + g\eta = 0 \qquad \text{on } z = \eta(\mathbf{x},t) \tag{2.12}$$

$$\phi_z = 0 \quad (\phi_z \to 0) \qquad \text{for } z = -D \ (z \to -\infty) \tag{2.13}$$

The boundary conditions at the lateral surface S_L are intentionally omitted in the definition since these conditions are often associated with the particular problem taken into account. In particular, for wave propagation problems, the boundary conditions to be applied on S_L results in the definition of a suitable radiation condition (Johnson [70]; Stoker [135]; Mei [90]). For open water wave problems, the velocity potential and the wave elevation are usually assumed to be periodic in the horizontal domain. With reference to Figure 2.1, this means:

$$\begin{aligned} \phi(x,y,z,t) &= \phi(x+L_x,y,z,t) \\ \phi(x,y,z,t) &= \phi(x,y+L_y,z,t) \\ \\ \eta(x,y,t) &= \eta(x+L_x,y,t) \\ \eta(x,y,t) &= \eta(x,y+L_y,t) \end{aligned} \tag{2.14}$$

2.3 Linear wave modelling

Assuming the wave elevation η and the potential ϕ to be small quantities of the order $\mathcal{O}(\epsilon)$ with $\epsilon \ll 1$ the water wave problem can be linearized as follows:

$$\nabla^2\phi = 0 \qquad \begin{matrix} -D < z < 0 \\ (-\infty < z < \eta(\mathbf{x},t)) \end{matrix} \tag{2.15}$$

$$\eta_t = \phi_z \qquad \text{on } z = 0 \tag{2.16}$$

$$\phi_t = -g\eta \qquad \text{on } z = 0 \tag{2.17}$$

$$\phi_z = 0 \quad (\phi_z \to 0) \qquad \text{for } z = -D \ (z \to -\infty) \tag{2.18}$$

where the free surface boundary conditions has been linearized and written with respect to the reference level $z = 0$. Only the linear terms are kept in the model, higher order terms are dropped. Assuming the periodicity in time of η and ϕ, and exploiting the

lateral boundary condition of (2.14) , a progressive wave solution of the linearized problem can be found as (Mei [90]):

$$\begin{aligned} \eta(x,t) &= A\cos\left(\kappa x-\omega t+\vartheta\right) \\ \phi(x,z,t) &= \frac{Ag}{\omega}\frac{\cosh(\kappa(z+D))}{\cosh(\kappa)}\sin\left(\kappa x-\omega t+\vartheta\right) \qquad \text{finite depth} \\ \phi(x,z,t) &= \frac{Ag}{\omega}\exp(\kappa z)\sin\left(\kappa x-\omega t+\vartheta\right) \qquad \text{deep water} \end{aligned} \tag{2.19}$$

where κ is the wave number $\kappa = 2\pi / L$, ω is the wave frequency $\omega = 2\pi / T$ and T is the wave period. The linear dispersion relation for finite depth is $\omega^2(\kappa) = g\kappa\tanh(\kappa D)$ and for deep water is $\omega^2(\kappa) = g\kappa$. A more general solution of the linear problem can be built by linear superposition of multiple monochromatic wave components defined according to (2.19) and propagating in possibly different directions. In the deep case it reads as:

$$\begin{aligned} \eta(\mathbf{x},t) &= \sum_{n=1}^{N} A_n\cos\left(\mathbf{k}_n\cdot\mathbf{x}-\omega_n t+\vartheta_n\right) \\ \phi(\mathbf{x},z,t) &= \sum_{n=1}^{N}\frac{A_n g}{\omega_n}\exp(\kappa_n)\sin\left(\mathbf{k}_n\cdot\mathbf{x}-\omega_n t+\vartheta_n\right) \end{aligned} \tag{2.20}$$

Where, now, $\mathbf{k} = [k_x, k_y]^T$ is the wave number vector with $k_x = 2\pi / L_x$ and $k_y = 2\pi / L_y$ identifying the direction of wave propagation and $\kappa = |\mathbf{k}| = \sqrt{k_x^2 + k_y^2}$ is the wave number.

2.4 High-Order Spectral method

2.4.1 Analytical model

The HOS method is based on the reformulation of the free surface boundary conditions (2.11) and (2.12) as function of the velocity potential calculated at the free surface This allows to derive a set of evolution equations of the water wave field. Following, Zakharov [169] the potential at the free surface , ϕ^s is defined as:

$$\phi^s(\mathbf{x},t) \equiv \phi\left(\mathbf{x}, z=\eta(\mathbf{x},t), t\right) \tag{2.21}$$

The time derivative and the spatial derivative of the free surface velocity potential can then be calculated by applying the chain rule as:

$$\begin{aligned} \phi_t^{\,s}(\mathbf{x},t) &= \phi_t(\mathbf{x},\eta,t) + \phi_z(\mathbf{x},\eta,t)\eta_t \\ \phi_x^{\,s}(\mathbf{x},t) &= \phi_x(\mathbf{x},\eta,t) + \phi_z(\mathbf{x},\eta,t)\eta_x \\ \phi_y^{\,s}(\mathbf{x},t) &= \phi_y(\mathbf{x},\eta,t) + \phi_z(\mathbf{x},\eta,t)\eta_y \end{aligned} \tag{2.22}$$

Finally, the dynamic and kinematic dree surface boundary conditions by substituting equation (2.22), in the boundary condition (2.11) and (2.12) become:

$$\eta_t = -\nabla_{\mathbf{x}}\eta \cdot \nabla_{\mathbf{x}}\phi^s + \left(1+\nabla_{\mathbf{x}}\eta \cdot \nabla_{\mathbf{x}}\eta\right)W \tag{2.23}$$

$$\phi_t^s = -g\eta - \frac{1}{2}\nabla_{\mathbf{x}}\phi^s \cdot \nabla_{\mathbf{x}}\phi^s + \frac{1}{2}\left(1+\nabla_{\mathbf{x}}\eta \cdot \nabla_{\mathbf{x}}\eta\right)W^2 \tag{2.24}$$

where $\nabla_{\mathbf{x}} = \left(\frac{\partial}{\partial x}, \frac{\partial}{\partial y}\right)$ is the gradient with respect to the horizontal coordinates only, $\mathbf{x} = (x, y)$, and W is the vertical velocity at the free surface defined as:

$$W = \left.\frac{\partial \phi}{\partial z}\right|_{z=\eta(\mathbf{x},t)} \tag{2.25}$$

In principle, equations (2.23) and (2.24) allow to follow the time evolution of the free surface quantities, η and ϕ^s, starting from a suitable initial condition $\phi^s(\mathbf{x}, t=0), \eta(\mathbf{x}, t=0)$, once the vertical velocity at the free surface, W, is known. Moreover, the velocity potential $\phi(\mathbf{x}, z, t)$ and, consequently, the vertical velocity on the free surface, W, has to comply with the original Laplace problem presented in equation (2.10) up to the free surface. In this respect, Dommermuth and Yue [41] and West et al. [151], developed the core procedure of the HOS method allowing to calculate the vertical velocity, W, starting form η and ϕ^s at each time instant. First, the free surface elevation, η, and velocity potential, ϕ, are considered to be of leading order $\mathcal{O}(\epsilon)$, where $\epsilon \ll 1$ is a small parameter that can be identified as the wave steepness. Then the velocity potential is expanded in a perturbation series in ϵ up to the order M as:

$$\phi(x, z, t) = \sum_{m=1}^{M} \phi^{(m)}(x, z, t) \tag{2.26}$$

where $\phi^{(m)} = \mathcal{O}\left(\epsilon^m\right)$. The free surface potential is then calculated by means of an analytical continuation of the velocity potential, ϕ, from $z = 0$ up to the free surface. The formal Taylor expansion can be then written as:

$$\phi^s(\mathbf{x}, t) = \sum_{l=0}^{\infty} \frac{\eta^l}{l!} \frac{\partial^l \phi(\mathbf{x}, 0, t)}{\partial z^l} \tag{2.27}$$

Considering now the perturbation expansion of the potential, (2.26), and consistently keeping the terms of the potential up to the given M-th order, ϕ^s is written as:

$$\phi^s(\mathbf{x}, t) = \sum_{m=1}^{M} \sum_{l=0}^{M-m} \frac{\eta^l}{l!} \frac{\partial^l \phi^{(m)}(\mathbf{x}, 0, t)}{\partial z^l} \tag{2.28}$$

Rearranging the terms, and grouping with respect to the same order of perturbation, the following system of conditions on the perturbation term of the potential can be derived:

$$\begin{aligned}
\phi^{(1)}(\mathbf{x},0,t) &= f^{(1)} = \quad \phi^{s} \\
\phi^{(2)}(\mathbf{x},0,t) &= f^{(2)} = \quad -\eta\phi_z{}^{(1)} \\
&\ldots \\
\phi^{(m)}(\mathbf{x},0,t) &= f^{(m)} = \quad -\sum_{l=1}^{m-1}\frac{\eta^l}{l!}\frac{\partial^l\phi^{(m-l)}}{\partial z^l}
\end{aligned} \tag{2.29}$$

The perturbation terms of the potential are then associated with the Laplace problem with a new Dirichlet condition on $z=0$ defined by (2.29):

$$\begin{aligned}
\nabla^2\phi^{(m)} &= 0 \qquad z<0 \\
\phi^{(m)} &= f^{(m)} \qquad z=0 \\
\phi_z{}^{(m)} &\to 0 \qquad z\to-\infty
\end{aligned} \tag{2.30}$$

The recursive solution of problem (2.30) allows then to calculate W at the free surface as function of η and ϕ^s at each time instant. A typical way for solving the recursive Dirichlet problem (2.30) is to resort to the mode-coupling technique. It consists in expressing the potential at the different orders as functions of the spatial spectral basis already solving the Laplace problem and accounting for all the boundary conditions (comprised the possible lateral boundary condition) with the exception of the condition at $z=0$. The structure of equation (2.30) is a smart way of projecting the information coming from the free surface potential on the undisturbed free surface. It allows to solve the Dirichlet problem for the different order of perturbation of the potential but now considering a simplified domain with the boundary condition applied at $z=0$. Eventually a consisted velocity field is derived allowing to calculate, by analytical continuation, the vertical velocity at the free surface.

From this point on, the methods proposed by Dommermuth and Yue [41] and West et al. [151] differs regarding the calculation of the vertical velocity at the free surface and in its inclusion in the equations (2.23) and (2.24). For Dommermuth and Yue [41] the vertical velocity is calculated simply as:

$$W=\sum_{m=1}^{M}\sum_{l=0}^{M-m}\frac{\eta^l}{l!}\frac{\partial^{l+1}\phi^{(m)}(\mathbf{x},0,t)}{\partial z^{l+1}} \tag{2.31}$$

and the evolution equations of the wave field remains the ones introduced in (2.23) and (2.24). West et al. [151], instead, proposed to expand the vertical velocity at the free surface in a perturbation expansion on the parameter ϵ as:

$$W=\sum_{m=1}^{M}W^{(m)} \tag{2.32}$$

where each perturbation term of the vertical velocity is calculated as:

$$\begin{aligned} W^{(1)} &= \phi_z^{(1)} \\ &\dots \\ W^{(m)} &= \sum_{l=0}^{m-1} \frac{\eta^l}{l!} \frac{\partial^{l+1} \phi^{(m-l)}}{\partial z^{l+1}} \end{aligned} \tag{2.33}$$

Moreover West et al. [151] introduced the following terms related to the vertical velocity that allows to consistently account for different perturbation orders:

$$\begin{aligned} W_M &= \sum_{m=1}^{M} W^{(m)} \\ \left(W^2\right)_M &= \sum_{m+n \le M} W^{(m)} W^{(n)} \end{aligned} \tag{2.34}$$

Now, in order to consistently take into account the vertical velocity contributions to equation (2.23) and (2.24) up to the M-th order of perturbation, West et al. [151] proposed the following reformulation of the terms related to the vertical velocity:

$$\begin{aligned} \left(1+\left(\nabla_{\mathbf{x}}\eta\right)^2\right) W &\to W_M + \left(\nabla_{\mathbf{x}}\eta\right)^2 W_{M-2} \\ \left(1+\left(\nabla_{\mathbf{x}}\eta\right)^2\right) W^2 &\to \left(W^2\right)_M + \left(\nabla_{\mathbf{x}}\eta\right)^2 \left(W^2\right)_{M-2} \end{aligned} \tag{2.35}$$

This second formulation more consistently accounts for the perturbation expansion terms (West et al. [151]) and it has been found to perform better in long term simulations (Clamond et al. [28]). For this reason, hereinafter, the West et al. [151] formulation will be adopted.

2.4.2 Spectral basis

The velocity potential is expanded as a spectral basis series as:

$$\phi(\mathbf{x}, z, t) = \sum_{n=1}^{\infty} \hat{\phi}_n(t) \Psi_n(\mathbf{x}, z) \qquad \text{for } z \le 0 \tag{2.36}$$

where $\hat{\phi}_n(t)$ are the spectral coefficient of the expansion depending, at most, on time.

The Ψ_n are harmonic function, satisfying the Laplace problem, and compatible with the boundary condition at the bottom and the periodic boundary condition, (2.30) and (2.14). A suitable choice of this function, for the deep water and finite depth cases, is:

$$\begin{aligned} \Psi_n(\mathbf{x}, z) &= \exp\left(\kappa_n z\right) \exp\left(i\mathbf{k}_n \cdot \mathbf{x}\right) && \text{deep water} \\ \Psi_n(\mathbf{x}, z) &= \frac{\cosh\left(\kappa_n \left(z+h\right)\right)}{\cosh\left(\kappa_n h\right)} \exp\left(i\mathbf{k}_n \cdot \mathbf{x}\right) && \text{finite depth} \end{aligned} \tag{2.37}$$

where $\mathbf{k}_n = [k_{x,n}, k_{y,n}]^T$ is the wave number vector, $\kappa_n = |\mathbf{k}|$ is the wave number and i is the imaginary unit.

The spatial partial derivatives of the velocity potential can now be calculated, by derivation of the spatial basis only, as:

$$\begin{aligned}\frac{\partial^l \phi}{\partial x^l} &= \sum_{n=1}^{\infty} \phi_n(t) \frac{\partial^l \Psi_n(\mathbf{x},z)}{\partial x^l} = \sum_{n=1}^{\infty} \hat{\phi}_n(t) \left(ik_{x,n}\right)^l \Psi_n(\mathbf{x},z) \\ \frac{\partial^l \phi}{\partial y^l} &= \sum_{n=1}^{\infty} \phi_n(t) \frac{\partial^l \Psi_n(\mathbf{x},z)}{\partial y^l} = \sum_{n=1}^{\infty} \hat{\phi}_n(t) \left(ik_{y,n}\right)^l \Psi_n(\mathbf{x},z)\end{aligned} \tag{2.38}$$

The partial derivatives in the z directions can be calculated as:

deep water:

$$\frac{\partial^l \phi}{\partial z^l} = \sum_{n=1}^{\infty} \hat{\phi}_n(t) \left(\kappa_n\right)^l \exp\left(\kappa_n z\right) \exp\left(i\mathbf{k}_n \cdot \mathbf{x}\right)$$

finite depth:

$$\frac{\partial^l \phi}{\partial z^l} = \sum_{n=1}^{\infty} \hat{\phi}_n(t) \left(\kappa_n\right)^l \frac{\cosh\left(\kappa_n\left(z+h\right)\right)}{\cosh\left(\kappa_n h\right)} \exp\left(i\mathbf{k}_n \cdot \mathbf{x}\right) \qquad \text{with } l \text{ even}$$

$$\frac{\partial^l \phi}{\partial z^l} = \sum_{n=1}^{\infty} \hat{\phi}_n(t) \left(\kappa_n\right)^l \frac{\sin\left(\kappa_n\left(z+h\right)\right)}{\cosh\left(\kappa_n h\right)} \exp\left(i\mathbf{k}_n \cdot \mathbf{x}\right) \qquad \text{with } l \text{ odd} \tag{2.39}$$

2.4.3 HOS numerical implementation

The numerical implementation of the HOS as a pseudo-spectral method comes directly from the representation of the wave elevation and velocity potential in terms of Fourier basis. The first step is to accept a truncation error allowing the representation of the quantities, η and ϕ^s , as a truncated Fourier series up to a given order N (Canuto et al. [26]). This allows collocating η and ϕ^s on a spatial grid by the Fourier interpolation technique. In this case Discrete Fourier Transform (DFT) of the two signals is considered as:

$$\begin{aligned}\eta(x_i,y_j,t) &= \sum_{n_y=-N_y/2}^{N_y/2-1} \sum_{n_x=-N_x/2}^{N_x/2-1} \hat{\eta}_{n_x,n_y}(t) \exp\left(i\frac{2\pi}{L_x} n_x \cdot x_i\right) \exp\left(i\frac{2\pi}{L_y} n_y \cdot y_j\right) \\ \phi^s(x_i,y_j,t) &= \sum_{n_y=-N_y/2}^{N_y/2-1} \sum_{n_x=-N_x/2}^{N_x/2-1} \hat{\phi}^s_{n_x,n_y}(t) \exp\left(i\frac{2\pi}{L_x} n_x \cdot x_i\right) \exp\left(i\frac{2\pi}{L_y} n_y \cdot y_j\right)\end{aligned} \tag{2.40}$$

The DFT formalism requires the wave number grid and the spatial grid to be linked. The collocation points are defined on an evenly spaced grid of $N = N_x N_y$ points with x coordinates discretized as $x_i = x_0 + idx$, with $dx = L_x / N_x$, and with y coordinates discretized as $y_j = y_0 + jdy$, with $dy = L_y / N_y$. The discretized wave number vectors are defined as $k_{x,n} = \frac{2\pi}{L_x} n_x = \frac{2\pi}{N_x dx} n_x$ with $n_x \in [-N_x/2, \ldots, N_x/2 - 1]$ and

$k_{y,m} = \frac{2\pi}{L_y} n_y = \frac{2\pi}{N_y dy} n_y$ with $n_y \in [-N_y/2, ..., N_y/2-1]$ (where N_x and N_y are herein assumed to be even numbers for simplicity). The resulting system of equations (2.23), (2.24) can then be reformulated in terms of evolution equations of the DFT coefficients as:

$$\begin{aligned} \frac{\partial \hat{\eta}_{n_x,n_y}}{\partial t} &= \mathcal{L}_1\left(\hat{\eta}, \hat{\phi}^s\right) + \mathcal{N}_1\left(\hat{\eta}, \hat{\phi}^s\right) \\ \frac{\partial \hat{\phi}^s_{n_x,n_y}}{\partial t} &= \mathcal{L}_2\left(\hat{\eta}, \hat{\phi}^s\right) + \mathcal{N}_2\left(\hat{\eta}\ , \hat{\phi}^s\right) \end{aligned} \tag{2.41}$$

where $\mathcal{L}\left(\hat{\eta}, \hat{\phi}^s\right)$ indicates the linear terms and $\mathcal{N}\left(\hat{\eta}, \hat{\phi}^s\right)$ indicates the nonlinear terms in equation (2.23) and (2.24) and can be formally defined as:

$$\begin{aligned} \mathcal{L}_1\left(\hat{\eta}, \hat{\phi}^s\right) &= \hat{W}^{(1)} \\ \mathcal{L}_2\left(\hat{\eta}, \hat{\phi}^s\right) &= -g\hat{\eta} \\ \mathcal{N}_1\left(\hat{\eta}, \hat{\phi}^s\right) &= \mathcal{FFT}\left(-W^{(1)} - \nabla_{\mathbf{x}}\eta \cdot \nabla_{\mathbf{x}}\phi^s + \left(1 + \nabla_{\mathbf{x}}\eta \cdot \nabla_{\mathbf{x}}\eta\right)W\right) \\ \mathcal{N}_2\left(\hat{\eta}, \hat{\phi}^s\right) &= \mathcal{FFT}\left(-\frac{1}{2}\nabla_{\mathbf{x}}\phi^s \cdot \nabla_{\mathbf{x}}\phi^s + \frac{1}{2}\left(1 + \nabla_{\mathbf{x}}\eta \cdot \nabla_{\mathbf{x}}\eta\right)W^2\right) \end{aligned} \tag{2.42}$$

All the spatial derivatives involved in the calculation of the right-hand side of equation (2.23), (2.24) and (2.29) are then calculated, exploiting the Fourier formulation of the velocity potential and the free surface elevation (2.40), in the domain of the discretized wave numbers. The actual implementation of the discrete spectral derivatives follows equations (2.38) and (2.39).

2.4.3.1 Nonlinear terms calculations and anti-aliasing techniques

A key aspect in the implementation of the HOS method is the Fast Fourier Transform (FFT) algorithm. From a numerical point of view, the DFT of a signal is nothing but an orthogonal transformation in the domain of the complex numbers and by the use of FFT algorithm the DFT can be evaluated with a computational scaling of the order $O(N \log N)$ (Canuto et al. [26]). This, among other benefits, allows a fast computation of the spatial derivatives. Another important application of the FFT algorithm is represented by the collocation method to calculate the nonlinear terms of PDE and named, as pseudo-spectral method, after Orszag [110]. As a matter of fact, the convolution terms generated by the products of two quantities, if calculated directly in the spectral domain, would require a computational cost of $O(N^2)$, where N is the number of spectral components considered. Nonetheless, by collocating the terms of the product on a discretized grid of N points , for example by a Fourier interpolation in the physical domain, the product between these two signals can be calculated as simple multiplication, of cost N, plus 3 FFT for the transformation between the Fourier domain and the physical domain, with cost of $O(N \log N)$. However, in calculating the product between two signals or, more generally, the M-th power of a signal, special care must be given to obtain a final nonlinear term with a spectral content consistent with the needed frequency bandwidth. In fact, depending on the relative bandwidth of the

original signals, calculating the nonlinear term can give frequency content beyond the Nyquist limit, $n_{Nyq} = N/2$, imposed by the spatial discretization. This eventually leads to a misinterpretation, aliasing, of the frequency content of the nonlinear term that results to be not consistent with the required frequency discretization (Canuto et al. [26]). There are different techniques to overcome this issue, in order to obtain "aliasing free products": the truncation technique, the padding technique and the phase shift technique (Canuto et al. [26]). The padding technique consists in collocating, by Fourier interpolation, the original signals, with, say, N Fourier frequencies, on a finer grid with, $\tilde{N} > N$, discretised points by padding the signal, in the frequency domain, with $\tilde{N} - N$ zero components. After the calculation of the nonlinear terms is carried out on the finer $\tilde{N}$ points spatial grid, the results are transformed back in the Fourier space keeping only the needed N Fourier components by truncation. It is possible to prove that, to have an effective aliasing removal for a simple product, it is sufficient to collocate the signals on a grid of $\tilde{N} = 3/2N$ points (Canuto et al. [26]). In the case a nonlinear term of order M (M products) is required, the collocation has to be performed on $\tilde{N} = (M+1)/2N$ points grid (Ducrozet [42]).

In the present implementation of the HOS code, considering a spectral representation of the wave elevation and the velocity potential on a spectral with $N = N_x N_y$ frequencies, in order to carry out a aliasing free calculation of the M order nonlinear terms, the collocation grid has to account for a number of points equal to (Ducrozet [42]; Ma [84]):

$$\tilde{N}_x = pN_x = \frac{M+1}{2}N_x;\ \tilde{N}_y = pN_y = \frac{M+1}{2}N_y \tag{2.43}$$

For an easy implementation, the padding coefficient p has been defined as $p = ceil((M+1)/2)$ resulting in the padding coefficients reported in Table 2.1.

Table 2.1: Table of padding coefficient used in the full padding technique.

p	M=2	M=3	M=4	M=5
theory $\left(\frac{M+1}{2}\right)$	*3/2*	*2*	*5/2*	*3*
present	*2*	*2*	*3*	*3*

As a final remark, the collocation procedure associated with the padding techniques requires to carry out the FFT transform on an increased spectral domain of $\tilde{N} = (M+1)/2N$ frequencies resulting in an increased computational cost that, now, is of order $O(\tilde{N}\log\tilde{N})$. This detrimental effect on the computational performances can be mitigated by decomposing the calculation of the M-th order products in series of lower order product, for example M-1 simple products, and applying for each of these products a collocation accounting only for $\tilde{N} = 3/2N$ points. This technique can be referred to as partial padding, in contrast with the full padding technique which consistently accounts for the M-th order products. Although the partial padding technique results in better computational performances, this is in general obtained at the expenses of the accuracy in the calculation of the nonlinear terms. In Decrouzet [42]

and Blondel-Couprie [14] a comparison of the two padding techniques is discussed in terms of both computational cost and accuracy. In the present HOS implementation only the full padding technique is considered.

2.4.3.2 Time integration

The time integration of the evolution equations in (2.41) is carried out by means of an explicit 4th order multistep Runge Kutta scheme (RK4). The RK4 method produces an approximation of the time derivatives to update the solution at the required time step with four function evaluations. Let us consider the system of ODE, $\dot{\mathbf{y}} = \mathbf{f}\left(\mathbf{y}(t), t\right)$ where $\mathbf{y} \in \mathbb{R}^N$, the vectorial function $\mathbf{f}$ is a general nonlinear function $\mathbf{f}\left(\mathbf{y}(t), t\right) : (\mathbb{R}^N, \mathbb{R}) \to \mathbb{R}^N$ and $\mathbf{y}_0$ is a suitable initial condition $\mathbf{y}(t = t_0) = \mathbf{y}_0$. The RK4 scheme associated with the discretization of this ODE produces the following scheme:

$$
\begin{aligned}
\mathbf{y}^{n+1} &= \mathbf{y}^n + \frac{dt}{6}\left[\mathbf{K}_1 + 2\mathbf{K}_2 + 2\mathbf{K}_3 + \mathbf{K}_4\right] \\
\mathbf{K}_1 &= \mathbf{f}(\mathbf{y}^n, t^n) \\
\mathbf{K}_2 &= \mathbf{f}\left(\mathbf{y}^n + \frac{dt}{2}\mathbf{K}_1, t^n + \frac{dt}{2}\right) \\
\mathbf{K}_3 &= \mathbf{f}\left(\mathbf{y}^n + \frac{dt}{2}\mathbf{K}_2, t^n + \frac{dt}{2}\right) \\
\mathbf{K}_4 &= \mathbf{f}\left(\mathbf{y}^n + dt\mathbf{K}_3, t^n + dt\right)
\end{aligned}
\tag{2.44}
$$

where dt is the discrete time step and the value of the solution at the nth time step is defined as $\mathbf{y}^n = \mathbf{y}(t_0 + ndt)$.

Following Colicchio and Landrini [32], a step forward in the analysis can be undertaken in recognising that the system of equation (2.41), in the simplified case of a single Fourier term, can be written in the following form as:

$$
\begin{bmatrix} \dot{\hat{\eta}}_n \\ \dot{\hat{\phi}}_n \end{bmatrix} = \begin{bmatrix} 0 & \kappa_n \\ -g & 0 \end{bmatrix} \begin{bmatrix} \hat{\eta}_n \\ \hat{\phi}_n \end{bmatrix} \to \dot{\mathbf{y}} = \mathbf{A}\mathbf{y} \tag{2.45}
$$

Now the matrix $\mathbf{A}$ has two complex eigenvalues $\lambda_{1,2} = \pm i\sqrt{g\kappa_n}$ and it can be diagonalized as $\mathbf{A} = \mathbf{P}^{-1}\mathbf{D}\mathbf{P}$ where $\mathbf{P}$ is the eigenvector matrix and $\mathbf{D} = diag(\lambda_1, \lambda_2)$ is the diagonal eigenvalues matrix. By substituting equation (2.45) in (2.44) the following is obtained:

$$
\begin{aligned}
\mathbf{K}_1 &= \mathbf{A}\mathbf{y}^n \\
\mathbf{K}_2 &= \mathbf{A}\left(\mathbf{y}^n + \frac{dt}{2}\mathbf{A}\mathbf{y}^n\right) \\
\mathbf{K}_3 &= \mathbf{A}\left(\mathbf{y}^n + \frac{dt}{2}\mathbf{A}\left(\mathbf{y}^n + \frac{dt}{2}\mathbf{A}\mathbf{y}^n\right)\right) \\
\mathbf{K}_4 &= \mathbf{A}\left(\mathbf{y}^n + dt\mathbf{A}\left(\mathbf{y}^n + \frac{dt}{2}\mathbf{A}\left(\mathbf{y}^n + \frac{dt}{2}\mathbf{A}\mathbf{y}^n\right)\right)\right)
\end{aligned}
\tag{2.46}
$$

$$
\mathbf{y}^{n+1} = \left(\mathbf{I} + \mathbf{A}dt + \frac{1}{2}\mathbf{A}^2(dt)^2 + \frac{1}{6}\mathbf{A}^3(dt)^3 + \frac{1}{24}\mathbf{A}^4(dt)^4\right)\mathbf{y}^n
$$

Noting that $\mathbf{A}^n = \left(\mathbf{P}^{-1}\mathbf{D}\mathbf{P}\right)\ldots\left(\mathbf{P}^{-1}\mathbf{D}\mathbf{P}\right) = \mathbf{P}^{-1}\mathbf{D}^n\mathbf{P}$ the final equation of (2.46) can be written in the decoupled form as:

$$
\begin{aligned}
x_i^{n+1} &= \left(1 + \lambda_i dt + \frac{1}{2}(\lambda_i dt)^2 + \frac{1}{6}(\lambda_i dt)^3 + \frac{1}{24}(\lambda_i dt)^4\right)x_i^n \\
&= \left(1 + z_i + \frac{1}{2}z_i^2 + \frac{1}{6}z_i^3 + \frac{1}{24}z_i^4\right)x_i^n = Z_i x_i^n
\end{aligned}
\tag{2.47}
$$

The absolute stability region of the RK4 method applied to the linear problem (2.45) is defined by region of the complex plane for which $|Z_i| \le 1$. In case the linearized water wave problem of equation (2.45) is considered, the largest eigenvalues have absolute value $|\lambda_{\max}| = \sqrt{g\kappa_{Nyq}}$ with $\kappa_{Nyq} = \sqrt{\left(\frac{\pi}{dx}\right)^2 + \left(\frac{\pi}{dy}\right)^2}$. The complex solution for $|Z_i| = 1$ is $|\lambda_i dt| = 2\sqrt{2}$. This result in a condition on the maximum allowable time step to have a stable RK4 scheme, that can be written as:

$$
dt^2 \le \frac{8}{g\kappa_{Nyq}} = \frac{8}{\pi g}\frac{dxdy}{\sqrt{dx^2 + dy^2}}
\tag{2.48}
$$

Equation (2.48) in the case of 1D application coincides with the well know result $(dt)^2 \le \frac{8}{g\pi}dx$ (Fornberg [51]; Dommermuth and Yue [41]). However, the value given by (2.48) has to be considered only as a starting value in the selection of the simulation time step.

In literature a rather usual approach is to integrate analytically the linear part of equation (2.41) and apply the RK4 scheme only to the remaining nonlinear terms (Tanaka [137]; West et al. [151]; Ducrozet [42]). Ducrozet, 2007 [42] and Tanaka [137] have taken advantage of this technique reporting a sensible improvement both in the size of time step required in the RK4 time stepping and in the solution accuracy. Nonetheless, in the present implementation the code, the RK4 scheme is applied to the whole equation (2.41) without separating the linear part and the nonlinear part of the equations.

2.4.3.3 Numerical instabilities and filtering

The perturbation expansion of the Dirichlet boundary value problem presented in (2.29) and (2.30) is the core of the HOS method. One of the fundamental assumptions on which this computation step is based, is the Taylor expansion of the free surface velocity potential presented in (2.27). In general, the velocity potential series expansion can be found to be slowly or even not convergent, especially for those cases where the free surface elevation presents a large spectral bandwidth and for which the short-wave/long-wave interaction is triggered (Bruckner and West [20]). Nonetheless, Bruckner and West [20] showed that, even in the case of potentially divergent series expansion of velocity potential, the formal expansion of the derived vertical velocity could still give a convergent series. This is guaranteed by a formal cancellation of the short-wave/long-wave interaction terms provided that all the terms in the series are kept. However, from a numerical point of view, it is not possible to keep all the terms of the Taylor series. From a general perspective, i.e. beyond the HOS method, Milder [92] analysed how the truncation of the series affects the mode-coupling models. The major effect consists is a spurious high-frequency content of in the solution. Dommermuth and Yue [41] observed a similar effect by using numerical considerations about the HOS method. In order to understand the nature of the instability, let us assume the true modal amplitudes $\hat{\phi}_n^{(m)}$ of the velocity potential affected by small numerical error as $\tilde{\hat{\phi}}_n^{(m)} = \hat{\phi}_n^{(m)}(1+\delta_{mn})$. Then, comparing the true and the approximate solution by equation (2.30) the following error assessments is obtained:

$$f^{(m)}(\tilde{\hat{\phi}}^{(m)}) - f^{(m)}(\hat{\phi}^{(m)}) = -\sum_{l=1}^{m-1} \frac{\eta^l}{l!} \sum_{n=1}^{N} \hat{\phi}_n^{(m-l)} \delta_{(m-l),n} \frac{\partial^l \psi_n(\mathbf{x},0)}{\partial z^l} \tag{2.49}$$

with ψ_n coming from the modal expansion of the velocity potential as in (2.36). Because the spectral derivative $\frac{\partial^l \psi_n(\mathbf{x},0)}{\partial z^l}$ is proportional to ${\kappa_n}^l$, (2.49) shows that the numerical errors are mostly amplified at high frequency. This effect leads to the unphysical growth of amplitudes at the high-wave numbers resulting in a noisy solution and, possibly, an unstable numerical integration. The solution proposed by Dommermuth and Yue [41] is the use of a low pass frequency filter able to keep only the frequency numbers that can be considered free from numerical errors. Different authors consider different implementation of the low pass filter. In general, a widespread solution is the adoption of a simple ideal low pass filter. Another filter which is often used is the five point filter (Dommermuth and Yue [41]; Bateman et al. [7]). In the present implementation of the code the following ideal low pass filter has been used:

$$G(\kappa,\nu)\begin{cases} 1 & \frac{\kappa_n}{\kappa_{max}} \le \nu \\ 0 & \frac{\kappa_n}{\kappa_{max}} > \nu \end{cases} \quad \text{with } 0 \le \nu \le 1 \tag{2.50}$$

with κ_{max} the maximum wave number considered in the simulation.

For the selection of the cut-off parameter ν, Guyenne and Nicholls [62], for instance, suggests a value of 0.8. However, the cut-off value has to be considered as dependent on the simulation characteristics, the reference steepness for example, and in general, as

long as the experience of the author is concerned, the selection of ν results to be a trade-off between accuracy and stability of the calculation.

Other works (Xiao [161]; Xiao et al. [162]; Yue [168]; Wu [160]) have proposed an alternative approach to the high wave number filtering. Starting from the argument regarding the impossibility of the HOS method alone to damp out the high frequency number that naturally will be damped by wave breaking phenomena, they introduced an artificial filter for this purpose. In other words, Xiao [161] assumed a parametrized exponential filtering function and tuned its parameters against experimental results in order to give, heuristically, the same kind of energetic damping induced by the wave breaking. Since this kind of filtering is particularly effective for complex sea state with high steepness (it is adopted also by other authors, for example Xu and Guyenne [164]) the herein developed code has been provided with this kind of filtering function, which is defined as :

$$G(\kappa,\beta_1,\beta_2)=\exp\left(-\left(\frac{\kappa}{\beta_1\kappa_0}\right)^{\beta_2}\right) \tag{2.51}$$

being κ_0 is a characteristic wave number of the spectrum, for example the peak wave number, and where following Xiao [161], the parameters β_1,β_2 takes the values in the intervals $\beta_1=7\div8$, $\beta_2=20\div35$.

In the developed code the ideal filter presented in (2.50) is always preferred. The application of this filter is done following Ducrozet [42] for which the optimal solution is to apply the filtering at each time step of the numerical integration both on the wave elevation and free surface potential, and at their time derivatives in the evolution equation.

2.4.3.4 Operation count of the Dirichlet problem

Dommermuth and Yue [41] shown that the computational cost of a HOS method, per each time step, should be $O(MN\log N)$, with N the total number of Fourier modes and M the order of perturbation. The same result is reported also by Mei et al. [91], for an equation equivalent to (2.28). Other authors, like Schäffer [122] and Ducrozet [42], agreed in finding that the main computational cost of the HOS method is associated to the Dirichlet iterative problem (2.29) and that the expected computational cost is of order $O(M^2N\log N)$. The computational burden is associated with the calculation of the nonlinear term of equation (2.29), with the FFT algorithm the most time consuming step. In the following, a schematic review of the implemented code is presented in order to count for the number of application of the FFT/IFFT algorithm. The analysed part of the code is the implementation of the Dirichlet problem in (2.29). In terms of input/output the related routine can be summarised as a single function that, starting from the Fourier components of the free surface elevation and the free surface potential, determines the velocity potential perturbation terms, $G=G\left(\hat{\eta},\hat{\phi}^s\right)\rightarrow\hat{\phi}^{(1)},...,\hat{\phi}^{(M)}$, see (2.29). The function G involves the calculation of spectral derivatives in the Fourier space and nonlinear products in the physical space, requiring several application of either the FFT or the IFFT algorithm. Table 2.2 presents an assessment of the number of FFT/IFFT applications in the calculation of function G. The total number of FFT/IFFT

operation is $\frac{1}{2}(M+1)M$, which is in line with Schäffer [122] at least for the part of the algorithm accounting for the velocity potential perturbation terms. The computational effort of $O(M^2 N \log N)$ calculated in Schäffer [122] seems to be confirmed also by this simple assessment calculation.

Table 2.2: Number of FFT and IFFT operations for the solution on the velocity potential in the Dirichlet problem. Data refer to the implementation developed by the author.

Fourier Space to Physical Space	IFFT op.
$\hat{\eta} \rightarrow \eta, \ldots, \frac{\eta^{(M-1)}}{(M-1)!}$	*1*
$\frac{\partial \phi^{(1)}}{\partial z}, \ldots, \frac{\partial^{M-1} \phi^{(1)}}{\partial z^{M-1}}$ $\frac{\partial \phi^{(2)}}{\partial z}, \ldots, \frac{\partial^{M-2} \phi^{(2)}}{\partial z^{M-2}}$ $\frac{\partial \phi^{(M-1)}}{\partial z}$	$\frac{1}{2}(M-1)M$

Physical Space to Fourier Space	FFT op.
$\phi^{(2)} \rightarrow \hat{\phi}^{(2)}, \ldots, \phi^{(M)} \rightarrow \hat{\phi}^{(M)}$	*M-1*
FFT/IFFT count	$\frac{1}{2}M(M+1)$

2.4.4 Initialization issues & strategies

For the initialization of HOS simulation two initial conditions are needed: the initial condition for the wave elevation $\hat{\eta}_0 = \hat{\eta}(t = t_0)$ and the initial condition for the free surface potential $\hat{\phi}_0^s = \hat{\phi}^s(t = t_0)$. These two quantities, at the first time step, are used to calculate the nonlinear terms of the evolution equation integrated in time to find the solution at the new time step. As a result, the initial conditions will drive the evolution of the wave field and their impact on the simulation, in general, cannot be overlooked. In the case the HOS method is used as a phase-resolved wave prediction model, the correct knowledge of the initial (measured) data is a key point for a correct forecasting of the wave field. However, from a practical point of view, the proper reconstruction of the initial condition can be challenging, especially for severe sea state. In general, indeed, the only information available are in the form of wave spectra and, even in the case wave elevation measurement are available, the free surface potential remains out of reach. For these reasons, the wave elevation and the free surface potential are usually initialized with low order nonlinear models and, most of the times, the initial condition are just generated by linear models. However, Dommermuth [40] argued that the linear initialization of nonlinear HOS simulations leads to the formation of spurious effects in the form of high-frequency standing waves. Dommermuth [40] presented a set of n HOS simulations where the spurious effects eventually lead to an incorrect evolution of the bound waves associated with carrier free-waves. The suggested strategy to overcome these initialization issues consists in a temporal ramp for the nonlinear terms

in the evolution equations. The adjustment technique proposed by Dommermuth [40] can be explained resorting to equation (2.41) and (2.42) rewritten as follows:

$$\begin{aligned}\frac{\partial \hat{\eta}_n}{\partial t} &= \mathcal{L}_1\left(\hat{\eta},\hat{\phi}^s\right) + f(t)\mathcal{N}_1\left(\hat{\eta},\hat{\phi}^s\right)\\ \frac{\partial \hat{\phi}^s_n}{\partial t} &= \mathcal{L}_2\left(\hat{\eta},\hat{\phi}^s\right) + f(t)\mathcal{N}_2\left(\hat{\eta},\hat{\phi}^s\right)\end{aligned} \tag{2.52}$$

where $f(t)$ is a monotonic function going from zero to one, $f:\mathbb{R}\to[0,1]$. Several ramping function can be envisaged, for example Wu [159] used a polynomial ramp, while Dommermuth [40] proposed an exponential ramp:

$$f(t) = \left(1-\exp\left(-\left(\frac{t}{T_a}\right)^n\right)\right) \tag{2.53}$$

For sake of reference, the adjustment procedure has been tested for the simulation of a Stokes wave initialized with linear initial condition. Further details about the simulation parameters and the Stokes reference solution can be found in Dommermuth [40]. Figure 2.2 shows the amplitude of the harmonics of the Stokes wave as function of the simulation time. The HOS simulation results are reported as thick lines and the reference solution is reported as thin lines. Figure 2.3 shows the same test of Figure 2.2 with the application of a time ramp with parameters $T_a = 8T_0$, $n=4$, where T_0 is the period. The application of the time ramp shows a visible improvement in the reproduction of the amplitudes bound waves and a closer reproduction of the reference solution.

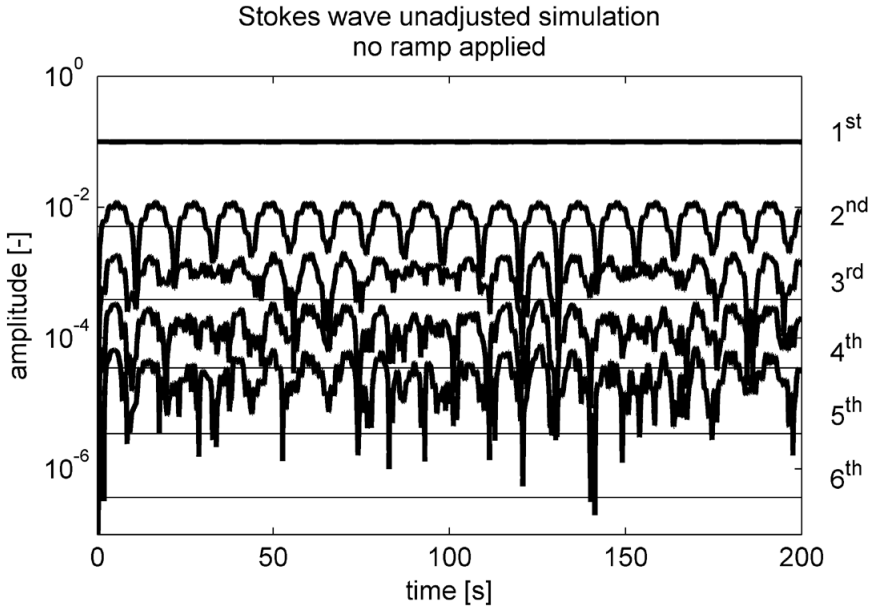

Figure 2.2: Unadjusted Stokes wave simulation, no ramp is applied. The amplitudes of the Stokes harmonics are reported as function of the simulation time: HOS results thick line; reference solution (Dommermuth [40]) thin line.

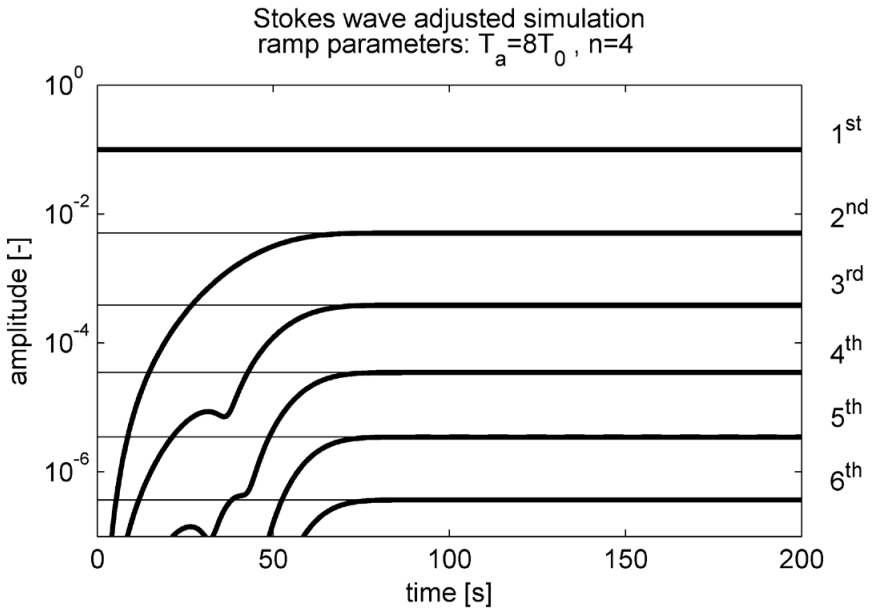

Figure 2.3: Adjusted Stokes wave simulation, the time ramp of equation (2.53) is applied with parameters $T_a = 8T_0$, $n = 4$. The amplitude of the Stokes harmonics are reported as function of the simulation time: HOS results thick line; reference solution (Dommermuth [40]) thin line.

The ramp proposed by Dommermuth [40] at the time $t = T_a$ attains the value $f(T_a) = 1 - \frac{1}{e}$ taking longer to attains a value close enough to one. In order to improve this behaviour a slightly different ramp has been defined and adopted hereinafter. In the proposed modification, the exponential ramp time parameter T_a is substituted by the value $T_a^* = T_a / log(1/\delta)^{(1/n)}$, with $\delta \ll 1$ is an arbitrary small value. This correction guarantees that at the time $t = T_a$ the ramping function is equal to $f(T_a) = (1-\delta)$. The resulting ramp function is:

$$f(t) = \left(1 - \exp\left(log(\delta)\left(\frac{t}{T_a}\right)^n\right)\right) \tag{2.54}$$

The use of the adjustment techniques depends on the purpose for which the HOS nonlinear simulations are carried out. For the generation of synthetic complex irregular sea states, initialized by state spectrum, this technique seems to be usually accepted (Decrouzet [42]; Fedele et al. [46]; Wu [159]; Xiao [161]). Decrouzet [42] tested the application of an adjustment ramp checking the typical nonlinear statistical features of a developed nonlinear wave field, obtaining results which are consistent with the theory, for a ramp of $T_a = 10T_p$ where T_p is the peak period. In all these investigations the ramp time is related to the typical wave period of the sea state, say it T_0, and the adopted duration of the ramp time is usually of the order $T_a \approx (5 \div 10) \cdot T_0$. On the other hand, when the HOS is used to reproduce a phase-resolved propagation of the wave field starting from wave measurements, the adjustment technique is no longer considered an applicable option. This is because the introduction of a ramp, in accounting for the nonlinear boundary conditions, can lead to discrepancies with respect to the measured wave data. Therefore, for this kind of simulations, a set of complex data assimilation tool is usually used for the reconstruction of the free surface potential and the nonlinear wave elevation field from the available measurement. The simulations are usually

matched with the measured data by means of different optimization tools and data assimilation techniques (Blondel-Couprie et al. [14]; Wu [159]; Yoon et al. [166]; Hassanaliaragh [67]). As a final remark, since in this work the HOS simulations are mainly used as a tool for the generation of realistic sea states, it seems to be justified to adopt the usual linear generation of free surface initial condition coupled with a suitable adjustment ramp. The ramp used in the present simulation of nonlinear wave field is the ramp reported in (2.53) with the correction of the time parameter described.

2.4.5 Convergence test for vertical velocity

In this section some results are presented about the convergence of the boundary value problem for the calculation of the vertical velocity. As reference solution a Stokes wave has been calculated with the method proposed by Rienecker and Fenton [120]. The Stokes wave has been calculated for a wave steepness of $\kappa a = 0.3$ and for a water depth of $h = 10\lambda_w$ where the $\lambda_w = 2\pi$ is the reference wave length. The stream function has been expanded keeping up to $N_{RF} = 32$ frequency component for which the Rienecker and Fenton [120] method has reached the convergence up to the machine precision. The test consists in prescribing η and ϕ_s from the Stokes solution, and then calculating the vertical velocity solving the Dirichlet problem in (2.29) and (2.33). The Dirichlet problem has been solved for a set of perturbation orders $M = [1,2,3,4,8,12,16,20]$ and for a set of spatial discretization $N = [4,8,16,32,48,64,80,128]$. Results are presented in terms of the maximum absolute relative error, calculated as:

$$err_W = \frac{\max(|W_{HOS} - W_{RF}|)}{\max(|W_{RF}|)} \tag{2.55}$$

Figure 2.4 and Figure 2.5 present the results obtained for the reconstruction of the vertical velocity. Increasing the perturbation order M and the number of discretization points N reduce the relative error until an error plateau is reached. For the higher M, i.e. M=20, the HOS solution diverges even if the number of the frequency components N is increased. This is mainly related with the numerical instabilities involving the high frequency numbers caused by the many perturbation terms required for the solution of the boundary value problem. Similar are obtained in Dommermuth and Yue [41], Bonnefoy [19], Skandrani et al. [132] where for Stokes wave with high steepness and for high values of the perturbation order the error on the vertical velocity increases. Decrouzet [42] suggested that the main sources of this kind of instability come from the spectral derivatives at high wave number and high perturbation order. In this case, the numerical errors introduced in the calculation of the nonlinear products is be amplified with $\kappa_n^{\ M}$. The proposed strategy to improve the convergence is to filter out the higher wave harmonics in the calculation of the nonlinear terms of the boundary value problem. The filtering is associated with the spectral derivative operator from which the wave components of index $n > 2N$ are removed from the full padding technique for the calculation of the nonlinear products (Decrouzet [42]). Figure 2.6 and Figure 2.7 show the results obtained from the filtering of the spectral derivative. The error behaves much better, decreasing constantly for almost all the range of tested perturbation orders. Some problem can still be noticed for the calculation with the highest tested perturbation order.

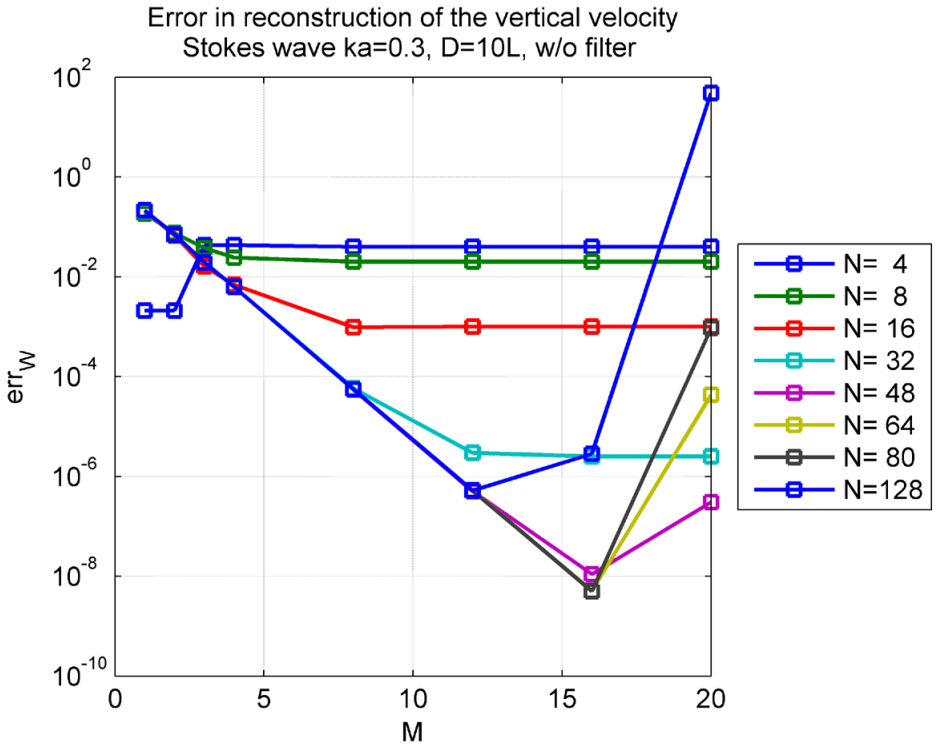

Figure 2.4: Vertical velocity calculation prescribing the free surface elevation η and the free surface potential ϕ_s from a Stokes wave solution. Results are reported as function of the perturbation order M. No filtering has been applied to the spectral derivative.

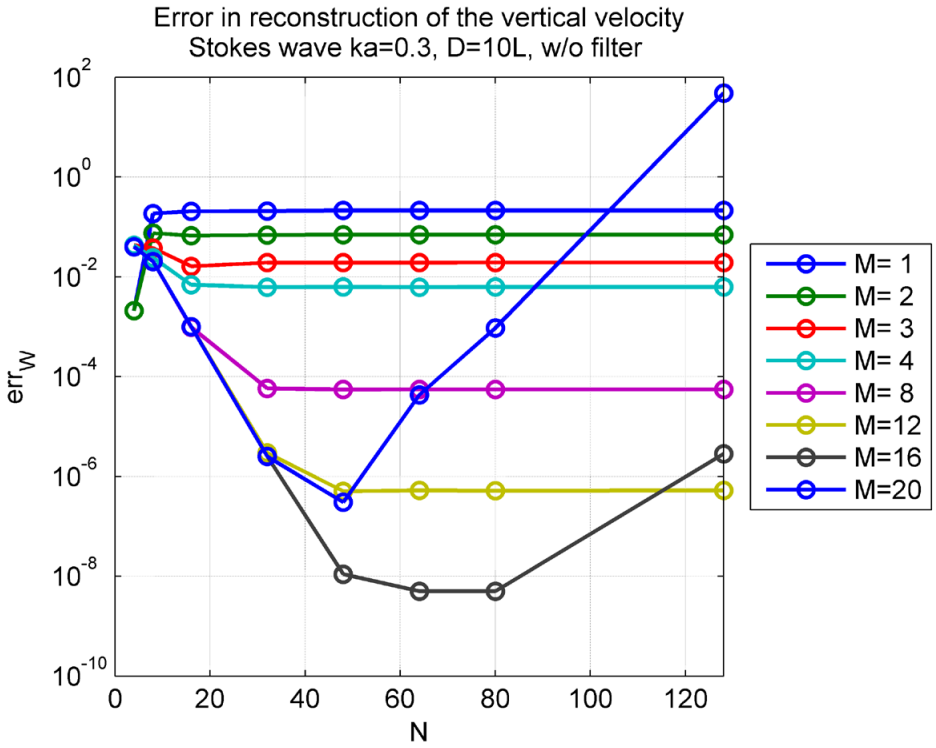

Figure 2.5: Vertical velocity calculation prescribing the free surface elevation η and the free surface potential ϕ_s from a Stokes wave solution. Results are reported as function of the number of discretization points N. No filtering has been applied in the calculation of the spectral derivative.

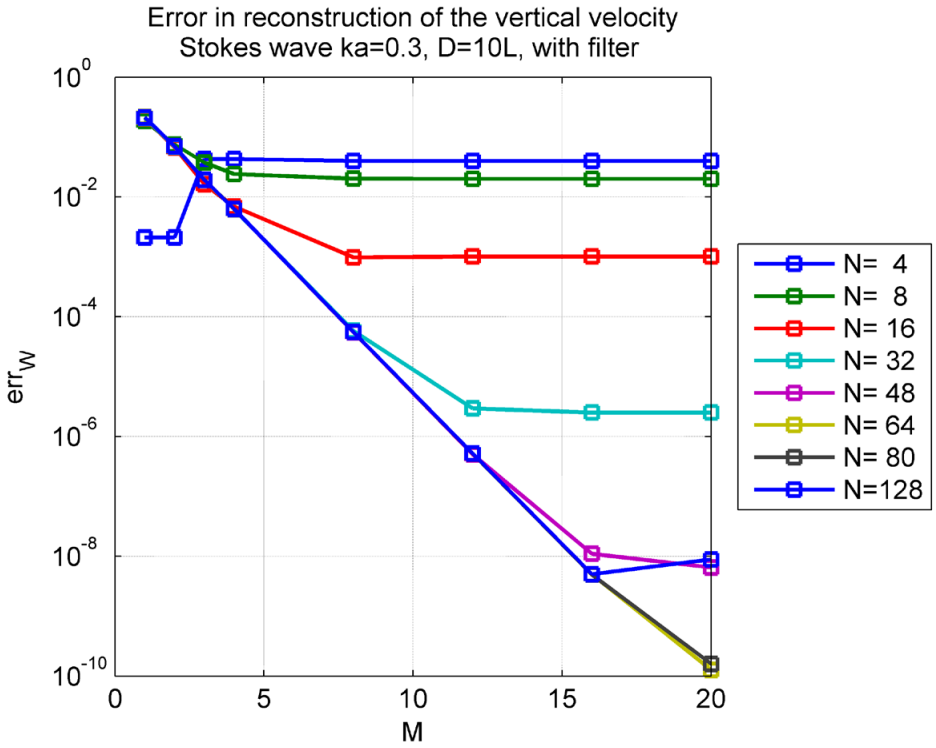

Figure 2.6: Vertical velocity calculation prescribing the free surface elevation η and the free surface potential ϕ_s from a Stokes wave solution. Results are reported as function of the perturbation order M. An ideal filter has been applied in the calculation of the spectral derivative.

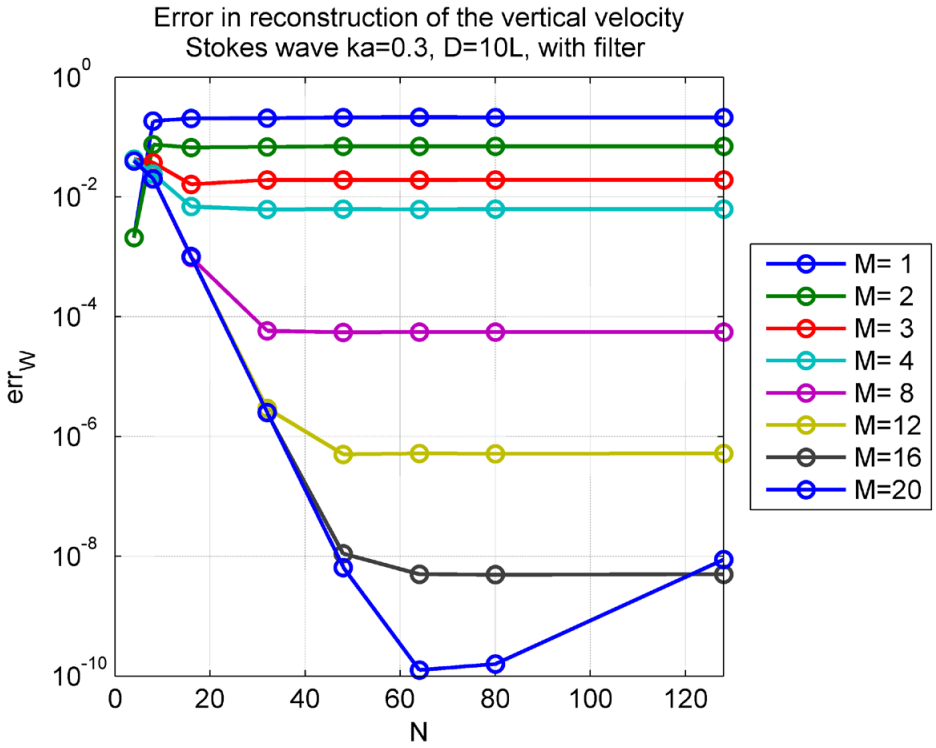

Figure 2.7: Vertical velocity calculation prescribing the free surface elevation η and the free surface potential ϕ_s from a Stokes wave solution. Results are reported as function of the number of discretization points N. An ideal filter has been applied in the calculation of the spectral derivative.

2.4.6 Nonlinear wave interaction

Following Dommermuth and Yue [41], the HOS method is tested herein for simulation of the evolution of a Stokes wave train perturbed by two side band instabilities. The main purpose is to check the performances of the HOS in accounting for the quartet wave interaction where a carrier wave with wave number κ_0 is perturbed by two collinear side band with wave numbers $\kappa = \kappa_0(1 \pm p)$ (Phillips [113]). Depending on the wave steepness of the carrier wave, this condition can trigger what is known as class I instability, also known as Benjamin-Feir instability (Benjamin, and Feir [12]; McLean [87]). According to Stiassnie and Shemer [134], for a carrier wave of steepness $\kappa a = 0.13$, the most unstable class I modes correspond to the side band parameter $p = 0.22$. In Figure 2.8 the evolution of the normalized harmonics corresponding to the carrier wave, with wave numbers, $\kappa_0 = 9$ and two side bands $\kappa_\pm = \kappa_0(1 \pm p) \sim [7,11]$ is presented. The carrier wave η_0 and $\phi_{s,0}$ have been calculated with a fifth order Stokes wave solution (Skjelbreia and Hendrickson [133]) and the side bands disturbances are defined as:

$$\begin{aligned}
\eta(x,0) &= \eta_0 + 0.1a_0 \cos\left(7x - \frac{1}{4}\pi\right) + 0.1a_0 \cos\left(9x - \frac{1}{4}\pi\right) \\
\phi_s(x,0) &= \phi_{s0} + 0.1\frac{a_0}{\sqrt{7}}\exp(7\eta)\sin\left(7x - \frac{1}{4}\pi\right) + 0.1\frac{a_0}{\sqrt{9}}\exp(9\eta)\sin\left(9x - \frac{1}{4}\pi\right)
\end{aligned} \tag{2.56}$$

The solution has been obtained with a perturbation order $M = 4$ with a space discretization of $N = 64$ points. The amplitude of the harmonics has been normalized with respect to the carrier amplitude at the first time instant. The amplitudes of the side bands start to grow, showing a recurrence period $T_0 / (\kappa a_0)^2$, which is consistent with the theory (Dommermuth and Yue [41]). After a few oscillations, the simulation starts to degrade showing noisy fluctuations of the sidebands amplitudes and a reduction of the recurrence period. This result is coherent with those presented by Dommermuth and Yue [41], Stiassnie and Shemer [134] and Skandrani et al. [132].

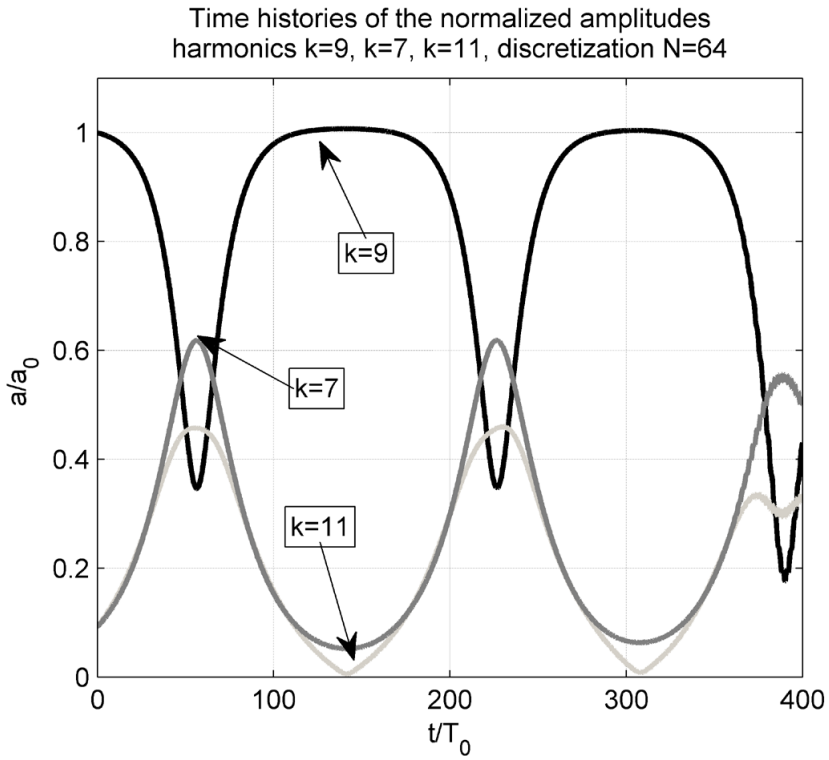

Figure 2.8: Time histories of the normalized harmonics $\kappa = 9; \kappa = 11; \kappa = 7$ for an evolving Stokes wave. The Stokes wave has steepness $\kappa a = 0.13$. The space discretization accounts for $N = 64$ points and the perturbation order is $N = 4$.

2.5 Generation of nonlinear irregular waves

In the present work the HOS method has been developed as a flexible tool for the generation of nonlinear wave fields. The capabilities of the HOS allows to simulate, with an acceptable computational cost, those nonlinear features that linear or low order wave propagation models cannot taken into account. Depending on the severity of the sea state, the time evolution of the wave field simulated by HOS accounts naturally for the high order bound waves, the energy transfer due to wave-wave interaction and also for the changes of the wave kinematics due to the nonlinear dispersion relation. This characteristic makes the HOS a valuable tool for generating "realistic" wave fields for benchmarking and testing purposes. However, the initialization of the HOS in the case of complex sea states may need special care because of the need of resorting to lower order models for the generation of the initial condition.

The strategy adopted herein is to employ a linear wave model to generate the initial condition starting from a given wave spectrum. Then, the adjustment time ramp is applied to smoothly introduce the wave nonlinearities, through the introduction of the nonlinear terms in the evolution equations (Dommermuth [40]). For the present test cases, the initial linear wave field is generated by a superposition of unidirectional wave modes with amplitudes derived from the sea spectrum as $A = \sqrt{2S(\kappa_n)d\kappa}$ and with random phases ϑ uniformly distributed in the interval $[0, 2\pi]$. In order to satisfy the periodicity of the wave field, which is required by the HOS method, the wave components must be related to the spatial domain assuming a finite set of wave numbers with discretization $d\kappa = 2\pi / L_x$.

In the following, a description of the nonlinear features characterising the generation of long crested sea spectra are reported. Figure 2.9, Figure 2.10 and Figure 2.11 present the

normalized spectrum $S(\kappa,\omega)$ calculated from the HOS simulations of the three considered unidirectional seas. The considered sea conditions are three long crested Bretschneider spectra (corresponding to JONSWAP spectra with overshoot parameter $\gamma = 1.0$) with the same peak period $T_p = 11.97s$ and with different significant wave heights $H_s = [2.5, 4.5, 6.5]m$. The total simulation time has been set to $t = 110T_p$ with a time step $dt = 0.25s$. The total length of the domain has been selected as $L_x = 3840m$ with a spatial discretization $dx = 3.25m$, corresponding to $N_x = 1024$ points. The simulations have been carried out with a perturbation order $M = 4$. An adjustments ramp with $T_a = 10T_p$, (2.54), has been applied and the terms of the evolution equation have been filtered by means of an ideal filter, (2.50),above the wave number $\kappa > 0.8\kappa_{Nyq}$, at each time step. In the numerical determination of the spectrum $S(\kappa,\omega)$ from the HOS wave elevation data, a tapering window, function of the time, has been applied before the FFT analysis, in order to reduce leakage in the wave frequency domain. The $S(\kappa,\omega)$ spectrum for each case is reported, in logarithmic scale, and normalized with respect to the maximum value. The linear dispersion relation for the free wave is reported in the figures with red line. A third order correction to the linear dispersion relation has been calculated following Madsen and Fuhrman [85] based on the nominal wave amplitudes given as initial condition to the HOS. The corrected linear dispersion relation is reported as blue line.

The first sea condition reported in Figure 2.9 is characterised by the lower significant wave height $H_s = 2.5m$. The spectrum $S(\kappa,\omega)$ highlights the onset of second order bound waves. However, the main energy is concentrated along the linear dispersions relation. The second order branch is more evident in the case of $H_s = 4.5m$, Figure 2.10, and even more in case of $H_s = 6.5m$ in Figure 2.11. In this latter case, even the third order bounds waves can be clearly noted. A change in the wave kinematics as the significant wave height, and thus the steepness, increases is highlighted by the departure of the dispersion relation of the free waves from the linear dispersion relation. This is most noticeable in Figure 2.11. The analytical third order correction calculated according to Madsen and Fuhrman [85] closely matches the spectral trace of the free waves as obtained from HOS, with a clear departure from the linear dispersion relation.

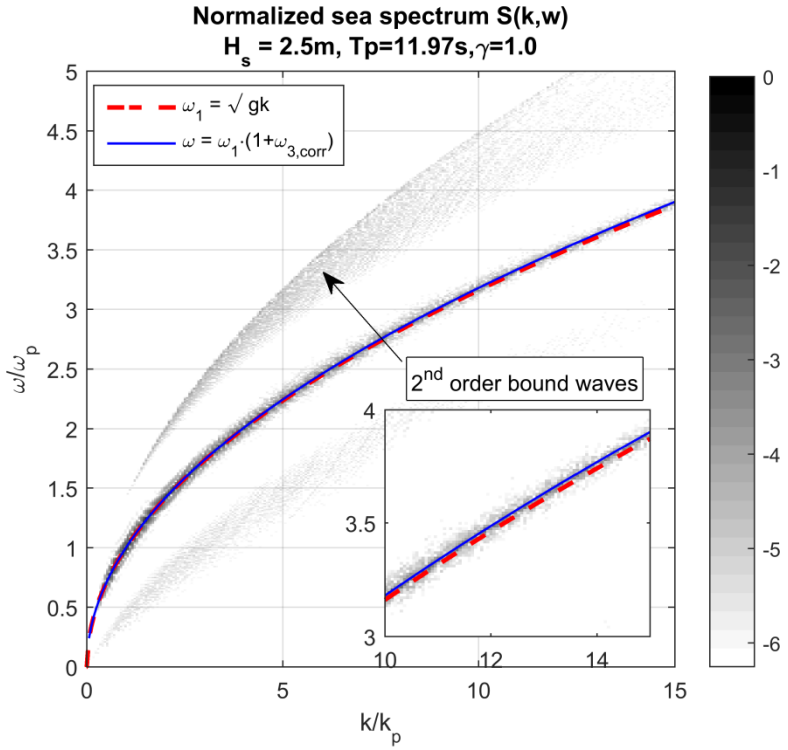

Figure 2.9: $S(\kappa,\omega)$ spectrum derived from HOS simulation. The simulation has been initialized with a Bretschneider sea spectrum with peak period $T_p = 11.97s$ and significant wave height $H_s = 2.5m$.

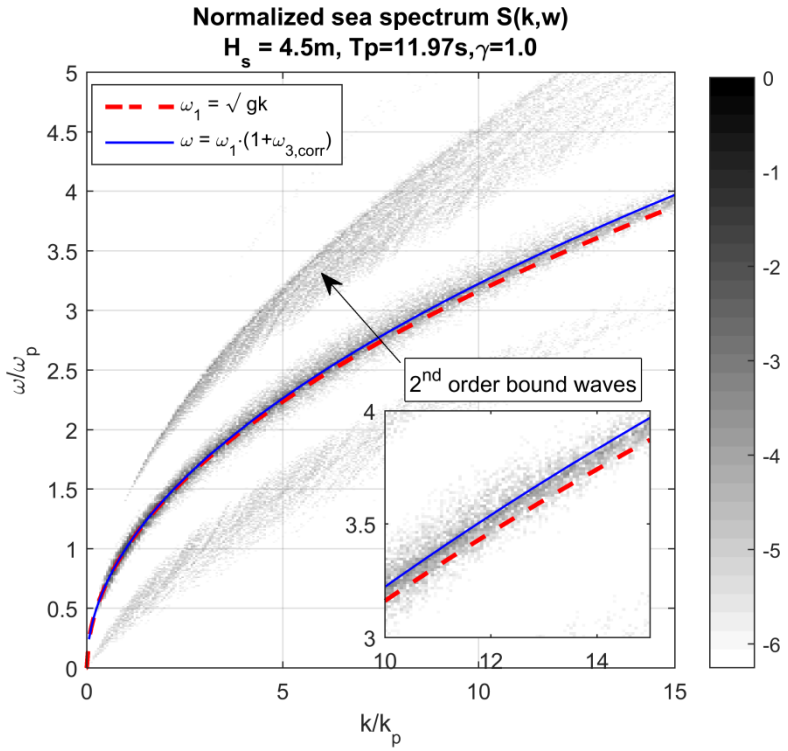

Figure 2.10: $S(\kappa,\omega)$ spectrum derived from HOS simulation. The simulation has been initialized with a Bretschneider sea spectrum with peak period $T_p = 11.97s$ and significant wave height $H_s = 4.5m$.

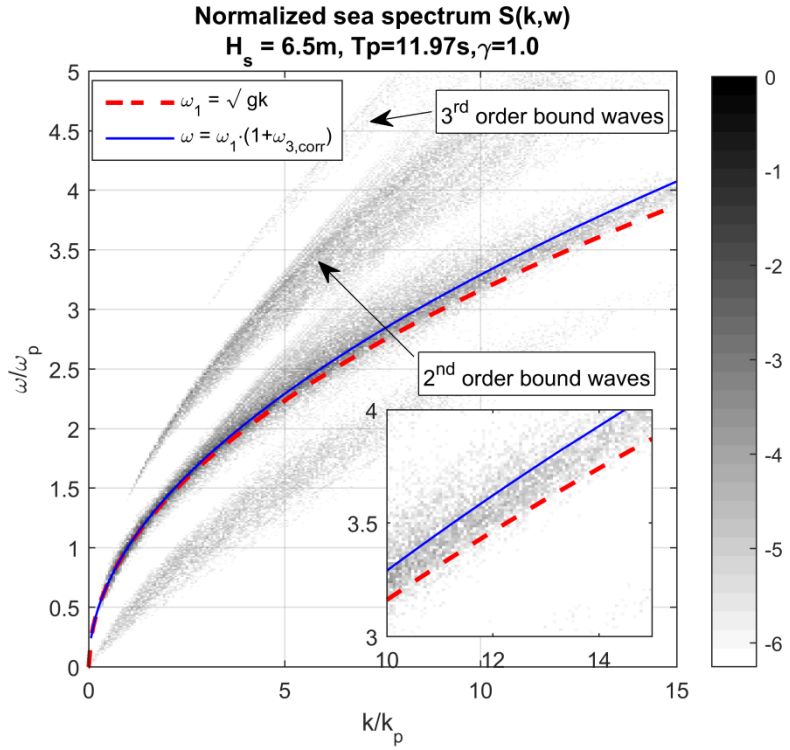

Figure 2.11: $S(\kappa,\omega)$ spectrum derived from HOS simulation. The simulation has been initialized with a Bretschneider sea spectrum with peak period $T_p = 11.97s$ and significant wave height $H_s = 6.5m$.

2.6 Concluding remarks

In this chapter, the potential water wave theory has been presented with the main purpose of explaining the main analytical steps relevant to the definition of the HOS method. The HOS method has been proven to be a valuable tool for the simulation of complex nonlinear sea states capable of reproducing the most prominent nonlinear feature of the wave field. However, there are some aspects requiring particular attention, both from the side of implementation and of the use. One of the main issues for the application of the HOS method is the initialization step. In order to avoid spurious modes in the simulation, the initial values of the free surface elevation and the velocity potential must be compliant with the nonlinear water wave boundary value problem. However, this kind of information is generally not available and can be reconstructed only from low order models. Moreover, in case the HOS solution is required to match with wave measured data, the lack of information on the free surface potential may need complex techniques of optimization or data assimilation. On the other hand, the use of the HOS as a tool for generation nonlinear sea states is less challenging. An example of the use of the HOS method in the case of unidirectional sea states has been presented, highlighting the capability of the method in modelling the main nonlinear features of a water wave field. The adopted initialization strategy is an adjustment technique that consists of initializing the HOS with a linear solution, smoothly introducing the wave nonlinearities in the evolution equation. Another potential source of difficulties turns out to be more related to numerical aspects in the implementation of the HOS. The core of the HOS method is the set-up of a Dirichlet boundary value problem in the perturbation terms of the velocity potential. The free surface potential is expanded in a Taylor series with respect to the reference water level, allowing to map the Laplace problem on a simpler fluid. Once the solution is found the same analytical continuation technique is used to derive back the vertical velocity on the free surface. The numerical implementation of this procedure, however, introduces in the problem numerical errors

that, when high order solutions are required, leads to the generation of high frequency disturbances. This phenomenon is in general responsible of an artificial energy packing at the high wave numbers and it can lead to the blow up of the solution. This kind of issue is generally solved by resorting to filtering techniques that allows to filter out the unwanted disturbances. The accuracy in reconstructing of the vertical velocity in the case of Stokes waves has been tested and it has been shown that the introduction of the filtering improves the convergence of the method. The same filtering techniques are adopted also to artificially induce a damping in the HOS model. In fact, the HOS method is incapable of dissipating energy. More generally, the simulation of highly nonlinear wave fields can results to be a challenging task especially in the cases breaking phenomena are involved. Eventually, the computational cost of the HOS method has been also addressed. The count of the operations required for a single time step has been discussed noticing how the HOS scales with the order $O(M^2 N \log(N))$, where M is the perturbation order of the solution and N is the number of frequencies used in the discretization.

3 WAVE RADAR SIGNAL INVERSION

In this chapter, the deterministic reconstruction of the sea surface from synthetically generated radar images is discussed. A brief review of the wave radar working principle is presented and the simplified radar imaging model is derived. The widespread Modulation Transfer Function (MTF) technique is described in order to highlight the main underlying semi-empirical assumptions and to stress the still challenging application of the MTF to the deterministic reconstruction of wave fields. An alternative inversion technique, based on a "Least SQuares with Regularization (LSQR)" approach is introduced. The proposed technique is based on the linearization of the radar imaging process and the linearity assumption on the wave field. A least squares problem is then derived and it is solved using a Tikhonov regularization technique. The notable characteristics of the presented LSQR approach are associated with the way the shadowing effect is taken into account and the flexibility of the approach in dealing with different sea states. Application examples are carried out for long crested linear and nonlinear sea conditions, and linear short crested sea conditions, paying particular attention to the description of the main statistical features of the reconstruction error.

3.1 Introduction

In recent years, the X-band wave radar has become a reference technology for costal monitoring and ocean surface remote sensing. The main characteristics rendering the wave radar such a key asset for monitoring activities relies in its capability of providing real time measurement and long range information about the ocean surface. Several studies have promoted the application of the wave radar for the measuring different environmental quantities, such as mean near-surface currents (Senet et al. [127]; Serafino et al. [130]; Young et. al. [167]), wind fields (Danker et al. [34]) and wave spectra and wave spectra parameters (Lund et. al. [81]; Nieto Borge et al. [105]; Nieto Borge and Soares [106]; Seeman et al. [126]), highlighting the potential multi-purpose use of these devices. Wave radar devices are also particularly interesting in the perspective of coupling them with wave and ship motion forecasting procedures intended for issuing early warnings, safety and operational indications. In this context, there is a growing interest in the detailed reconstruction of local wave elevation from

wave radar images. In fact, the real time imaging of the sea surface is a fundamental step for Deterministic Sea Wave Prediction (DSWP) procedures which aim at producing, from deterministic sea elevation measurements, corresponding deterministic wave elevation forecasting (e.g. Blondel-Couprie and Naaijen[17][18]; Fucile et al. [52][53]; Hilmer and Thornhill [68]; Naaijen and Blondel-Couprie [97]; Wu [159]). Such predictions can then be linked, in principle, also to deterministic ship motion forecasting procedures (e.g. Alford et al. [3]; Connell et al. [33]; Dannenberg et al. [36]; Naaijen and Huijsmans [99]).

Several approaches have been proposed so far for the reconstruction of the wave elevation from wave radar images and, in the majority of the cases, they find a common starting point in the simplified framework of the tilt modulation theory of the radar signal for moderate sea states proposed by Wright [158] and Alpers et al. [4]. Many of these techniques rely on the application of the Modulation Transfer Function (MTF) to the radar signal in order to extract the required features of the wave field. These techniques can be described as a linear operator acting on the wave number domain and modifying the radar signal in order to get the wave elevation, or, at least, the wave elevation spectrum. However, some technological difficulties, mainly related to the fact that the radar signals measured at long range are affected by effects that are difficult to explain in terms of tilt modulation only, require the introduction of semi-empirical formulations of the MTF function based on calibration through real and/or synthetically generated radar images (Nieto Borge et al. [105]; Ziemer and Rosenthal [171]). This type of procedure has been applied to wave elevation reconstruction by Nieto Borge et al. [105] and it is nowadays a widespread procedure (Serafino et al. [129]), thanks also to its quite satisfactory performances and computational scalability. The semi-empirical nature of the MTF formulation has encouraged some authors in proposing alternative formulations of the MTF through adaptive tuning on the particular environmental conditions considered (Chen et al. [27]; Fucile et al. [54]; Ludeno et al. [79]). Other reconstruction techniques have been proposed by Dankert and Ronsenthal [35] and by Naaijen and Wijaya [104], which differ from the semi-empirical MTF technique, since they are directly based on a linearized version of the tilt model.

An important source of the nonlinear radar signal modulation, that represents a challenge for the correct analysis of wave radar images, is the shadowing effect. The geometrical/optical interpretation of this phenomenon can be explained as the tendency of the wave peaks to hide the nearby wave field preventing, thus, the wave radar from uniformly illuminating the sea surface. From a practical point of view, the shadowing effect creates regions on the sea surface from which the wave radar antenna receives back no or too few information. As shown by Senet et al. [127], a prominent side-effect of the presence of shadowing is the creation of artefacts in the Fourier spectrum of radar signals. Due to the inherent difficulties in correctly/explicitly accounting for the shadowing effect, in many works this effect is accounted for by means of simplifying assumptions (Dankert and Rosenthal [35]; Wei et al. [150]), or *a-posteriori* cured (Naaijen and Wijaya [104]).

Another aspect of radar image analysis, which is seldom addressed with a systematic approach, is the statistical characterization of the error inherent to the inversion process. Knowing the main features of reconstruction error can indeed be beneficial for the selection among alternative inversion techniques. Furthermore, the knowledge of the statistical characteristics of the inversion error (which represent wave measurement error when using a wave radar) can be used in DSWP procedures in order to provide a

deterministic forecasting of the wave elevation associated with confidence bounds accounting for the characteristics of the inversion procedure (Fucile et al. [52]).

Considering the reported background, there seems, therefore, to be space for exploring alternative inversion approaches which are capable of coping, particularly, with the presence of shadowing, without introducing semi-empirical tuning/corrections as in the case of MTF, giving due attention to the analysis of statistical characteristics of wave reconstruction error. To this end, herein a novel inversion method is proposed, with the purpose of suggesting a possible solution to some of the issues affecting the prevailing techniques. The approach proposed herein setups the inversion process as a least squares problem based on available radar data, looking for a regularized solution of the wave elevation field in terms of wave amplitudes of a set of specified harmonic components. The core assumptions of the proposed technique, referred to as "Least SQuares with Regularization (LSQR)", are the exploitation of a linearized version of the radar tilt model and the assumption that the underlying wave field is linear. The shadowing effect is dealt with by considering the shadowed region as missing information in the wave radar images. Accordingly, the reconstruction is carried out retaining only those data, above a certain threshold of backscattered intensity, that can be considered to be unaffected by shadowing. The inversion is based on the Tikhonov regularization technique with an automatic choice of the regularization parameter through the L-Curve method (Hansen [64]; Vogel [147]), and the solution of the inversion problem is herein implemented through a SVD decomposition. The performances of the LSQR reconstruction are analysed by detailed analyses of wave reconstruction error, using synthetically generated wave radar images and Monte Carlo generation of wave fields for different sea conditions.

The chapter is organized as follows. Firstly, the optical tilt model and the shadowing effect are discussed in order to give a detailed insight of the radar imaging mechanism and to define the wave radar model used for the generation of synthetic radar images. Then, the linearization of the tilt model is presented, stressing the commonalties and differences between the derivation presented herein and the linearized model proposed by Naaijen and Wijaya [104]. Then a brief review of the MTF inversion technique is reported in order to highlights the main aspects of the method. The discussion has the aim to provide an insight on the inversion issues relevant to the proposal of an alternative inversion technique. Secondly, the core of the least squares inversion procedure is described, with particular attention to the derivation of the regularized solution. In this respect, some aspects of the Tikhonov regularization, relevant to the subsequent description of the selection approach for the regularization parameter, are examined. The overall setup of the linear inversion procedure is presented and possible alternative choices about the model setup are also discussed. Two example applications are then reported, considering long crested and short crested seas. Details are firstly given regarding the way Monte Carlo synthetic radar signals have been generated, and regarding the main statistical quantities employed in the analysis of the inversion error. In the long crested sea example application, the LSQR performances are discussed focusing, firstly, on a detailed statistical characterization of the reconstruction error for a specific sea state. Then, an extensive systematic analysis for a large set of different sea conditions is performed in order to assess the LSQR capability of dealing with radar images generated from different sea states. Moreover, for one sea condition, the LSQR has been tested in the case of nonlinear wave fields in order to assess which kind of effect the linearity condition underlying the LSQR model has on the reconstruction performances on more realistic nonlinear seas. In the second example application, LSQR reconstruction performances are analysed for a short crested sea scenario,

discussing also potential shortcoming of the LSQR technique and proposing some idea for reducing of the computational effort.

3.2 Wave radar imaging model

The modulation of the scattered radar signal received back by the radar antenna is what makes the sea surface elevation visible to the wave radar. Namely, the presence of the sea wave is sensed as a modulation of the radar cross section (RCS) (i.e. the ratio between the transmitted signal power and the received signal power). In the range from low to moderate grazing angles, the Bragg scattering phenomenon is considered to be the prominent mechanism of the radar signal backscattering from the sea surface (Plant and Keller [117]; Wetzel [154]; Wright [157]). In this range, the Bragg scattering phenomenon takes place as a resonant interaction of the electromagnetic waves caused by the presence of the small scale gravity-capillary wave ripples with wavelength satisfying the Bragg scattering condition (Wright [157]). The presence of an underlying wave field of longer waves beneath the wind ripples is sensed by the wave radar as a deviation of the mean RCS from what is expected to be the backscattered footprint of a planar rough surface. The modulation of the RCS due to longer waves is explained by means of the composite surface model or two scale model (Alpers et al. [4]; Kanevsky [72]; Valenzuela [145]; Wright [158]) where the rough facet causing Bragg scattering are considered to be tilted away by the long gravity wave passing by. This phenomenon is referred to as "Tilt Modulation". The composite surface model developed, among others, by Alpers et al. [4] and by Valeunzela [145], is considered to be an adequate model, at least in the range of moderate incident angles from 20 to 70 deg (Alpers et al. [4]), to account for the tilt modulation of the RCS, whereas, for extreme values of the grazing angle, other backscattering phenomena should be taken into account.

The model used herein for the simulation of wave radar is the geometrical model presented in Nieto Borge et al. [105] based on the work by Alpers et al. [4]. This model is considered to be a simplification of the actual wave radar physics, and, as a result, it cannot capture in details the whole complexity of the phenomenon (Lyzenga et al. [83]; Plant [114]; Voronovich [148]; Wetzel [153]). Nevertheless, the geometrical model is used as the theoretical basis for many semi-empirical techniques (Nieto Borge et al. [105]; Naaijen and Wijaya [104]; Serafino et al. [129]) to simulate the wave radar RCS modulation starting from synthetic sea elevation data. In the geometrical model, the tilt modulation of the RCS, $\tilde{\sigma}_{tilt}$, is modelled as proportional to the cosine of the local angle of incidence Θ, that is the angle between the optical ray coming from the radar antenna, the vector $\mathbf{u}$, and the local normal to the wave facet, vector $\mathbf{n}$ (see Figure 3.1). Following Nieto Borge et al. [105], hereinafter, the tilt modulation is considered to be the most prominent source of the modulation of the radar signal and it is modelled as:

$$\tilde{\sigma}_{tilt} = \cos(\Theta) = \frac{\mathbf{u} \cdot \mathbf{n}}{|\mathbf{u}| \cdot |\mathbf{n}|} \tag{3.1}$$

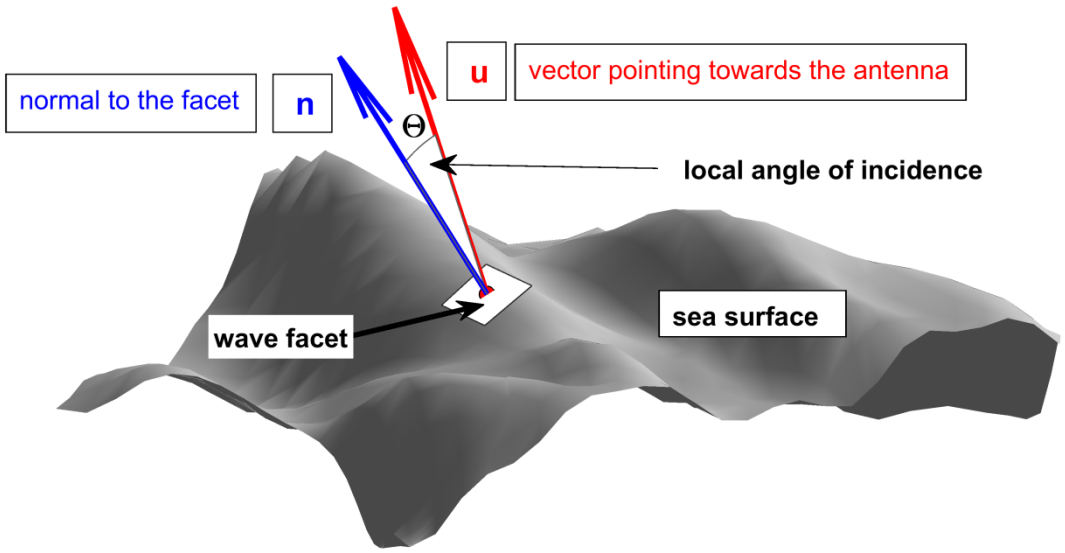

Figure 3.1: Representation of quantities involved the geometrical tilt model.

For very low grazing angles the radar backscattered signal is often interpreted by resorting, in addition, to another important modulation model: the shadowing effect (Wetzel [154]). Shadowing is intended as the phenomenon for which low or no backscattered signal is received from certain regions of the illuminated radar range. Similarly to tilt modulation, also the occurrence of shadowing phenomenon is, in reality, associated with complex electromagnetic phenomena (Barrick, 1995 [6]; Plant and Farquharson [116]; Wetzel [152][153]). Nevertheless, in the framework of the optical radar model used herein, the phenomenon is simplified using a geometrical approach. From purely geometrical consideration, the wavy surface of the sea may not be uniformly illuminated by wave radar because of the presence, especially at very low grazing angles, of wave peaks that, occasionally illuminated by the radar, prevent the nearby wave facets from being visible, see Figure 3.2 (which will be later referred to also when discussing the linearized version of the tilt model). According to Nieto Borge et al. [105], the shadowing modulation is herein modelled as a purely geometrical effect as if the radar antenna were not actually receiving any signal from the shadowed parts of sea surface. The RCS model defined by equation (3.1) is then extended with the introduction of the shadowing effect as follows:

$$\tilde{\sigma}_{tilt} = \begin{cases} \dfrac{\mathbf{u}\cdot\mathbf{n}}{|\mathbf{u}|\cdot|\mathbf{n}|} & \text{if the wave facet is illuminated} \\ 0 & \text{if the wave facet is in shadowing} \end{cases} \tag{3.2}$$

Figure 3.3 presents an example simulated (synthetic) radar image for a short-created sea based on the modelling (3.2): the shadowing is represented as missing data, with shadowed facet coloured in white. From a practical point of view, the shadowed regions in radar images could be determined as regions associated with a backscattered signal below a certain threshold level, intended to represent a background noise level.

Despite the simplification introduced by the geometrical model, from a practical point of view it provides a satisfactory description of some peculiar features of the wave radar imaging. In particular, Seemann and Ziemer [125], Seemann et al. [126] and Senet et al.

[127] have shown how the geometrical shadowing model can explain the artefacts and noise patterns observed in the spectral analysis of radar signals.

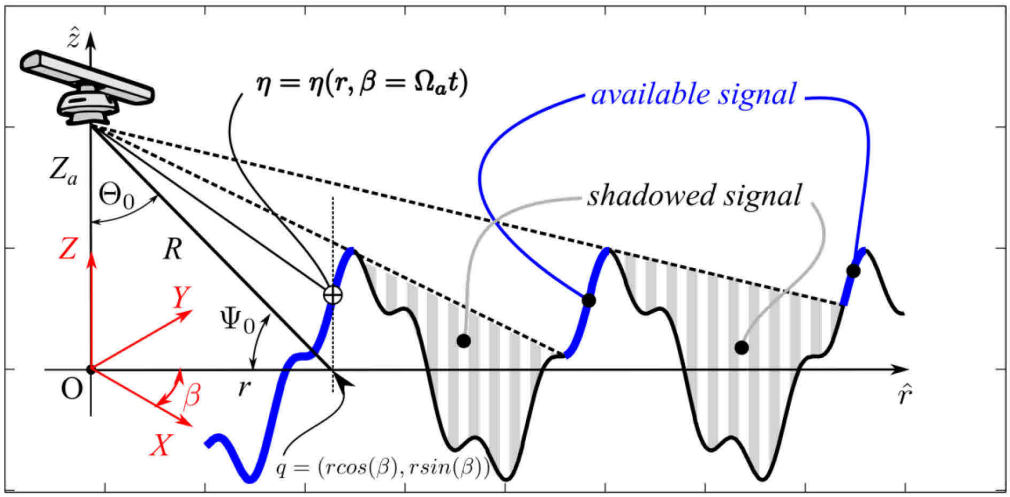

O-XYZ Cartesian reference frame

Z_a height of the antenna from the mean water level

Ψ_0 grazing angle

Θ_0 incidence angle

R distance from the antenna

β radar azimuth

r horizontal distance from the origin

Figure 3.2: Main quantities involved in the linearized tilt model, with representation of geometrical shadowing effect.

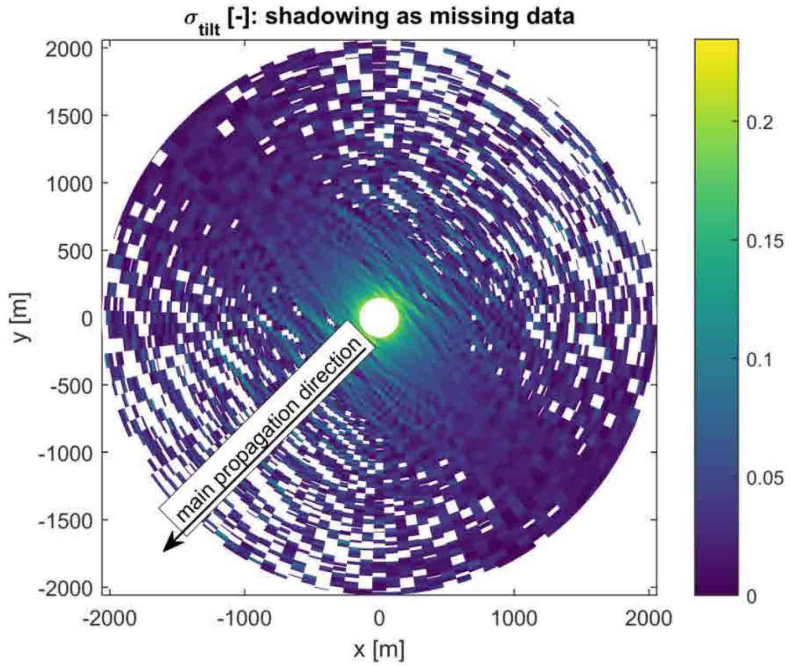

Figure 3.3: Simulated radar image: tilt modulation and shadowing mask. Shadowing is represented as missing data, with shadowed facets in white.

Due to the presence of spurious effects created by shadowing, many radar image inversion procedures introduce a band pass filter that allows isolating the energy contribution associated with gravity waves from other sources of noise and artefact. The band pass filters are usually centred along the linear wave dispersion relation linking wave frequency and wave number, and although the actual formulation of the filter may

vary from work to work, its application is a widespread procedure (Dankert and Rosenthal [35]; Nieto Borge et al. [105]; Nieto Borge and Soares [106]; Seemann et al. [126]; Serafino et al. [129]). Due to the inherent difficulties in the inversion of the radar images by explicitly accounting for the nonlinear effects of shadowing, in many works these effects are either neglected (Dankert and Rosenthal [35]), simplified (Wei et al. [150]), mitigated by data assimilation procedures (Wijaya et al. [156]), or just averaged (Naaijen and Wijaya [104]). In all mentioned techniques, however, data affected by shadowing are retained in the sample of radar data which undergo further processing.

Herein, instead, an alternative approach which is meant to explicitly deal, in the inversion process, with shadowing effects, is proposed. The main assumption is that the wave radar is able to give enough information to identify the shadowed regions in each available wave radar image. From a practical point of view, this could be carried out by setting a certain threshold to the minimum allowable RCS, see equation (3.2). The shadowed regions are treated as missing data and then excluded from the radar imaging inversion technique. In other words, the inversion step is carried out only on the illuminated portion of the radar imaging. Despite data from regions in shadowing are not used in the inversion process, the information retrieved from the inversion process can be used to reconstruct the wave field on the whole region of interest, comprising the regions originally in shadowing.

Finally, it is worth of noticing that, in general, the radar signal is available as a normalized measure (Nieto Borge et al. [105]). Therefore, a rescaling of the radar signal is eventually needed to retrieve the correct sea surface reconstruction. This kind of radar signal calibration (or, simply, radar calibration) can be described by means of a proportional scaling and an additional bias (Nieto Borge et al. [108]). These rescaling constants can be calculated, for instance, on the basis of the Signal to Noise Ratio (SNR) technique introduced by Nieto Borge et al. [108]. Although the radar calibration can represent a problem by itself (Naaijen and Wijaya [104]; Nieto Borge et al. [105]; Nieto Borge et al. [108]), in what follows, it is assumed that the radar signal is properly rescaled, i.e. the radar is properly calibrated.

3.3 MTF inversion technique

The MTF inversion technique is the reference procedure for the inversion of the wave radar signal. For this reason, hereinafter, a brief review of the procedure is reported as reference for the subsequent discussion. The MTF inversion technique is based on a model of the modulation of the radar signal RCS in presence of sea waves, as proposed by Alpers et al. [4] (see also Nieto Borge et al. [105] and Ziemer and Rosenthal [171]):

$$\sigma(x,y,t) = \sigma_0 + \delta\sigma = \sigma_0 \left(1 + \int M(\mathbf{k}) e^{j(\mathbf{k}\cdot\mathbf{x}-\omega(\mathbf{k})t)} \hat{\zeta}(\mathbf{k}) d\mathbf{k}\right) \tag{3.3}$$

where σ_0 is the mean RCS, $\delta\sigma$ is its modulation, $\mathbf{k} = (k_x, k_y)^T$ is the wave number vector, and $\hat{\zeta}(\mathbf{k})$ is the complex Fourier amplitude of the wave elevation. $M(\mathbf{k})$ is, in general, a complex transfer function that acts as a filter on the spectral components of the wave elevation field. The main idea behind the MTF techniques is to invert the modulation operator presented in (3.3) to get the reconstructed wave field from the radar signal. The approach is usually carried out in the wave numbers domain and $M(\mathbf{k})$ has to account for a correction of the amplitudes and phases of the radar signal. According to Nieto Borge [107] $M(\mathbf{k})$ is given, formally, by the sum of different contributions, the

tilt modulation, the shadowing modulation and the hydrodynamic modulation. In general, however, deriving closed formula for $M(\mathbf{k})$ is a challenging task. In the case of shipborne wave radar, this is particularly true because of the shadowing effect. In fact, the shadowing effect as presented in (3.2) represents a masking function dependent on the wave elevation. Making reference just to the optical model of shadowing, as depicted in Figure 3.2, it possible to note how the RCS received back from certain sea surface patches may depend on the presence of localized wave peaks preventing the illumination of the nearby regions. This effect is also associated with the generation, in the frequency domain, of a series of spurious replicas of the radar signal (Seemann and Ziemer [125]; Senet et al. [127]). The difficulties in modelling the modulation term $M(\mathbf{k})$ accounting for all the modulation sources, especially in the case of the shadowing effect, explain why the inversion problem is usually addressed as a semi-empirical and procedural task. The MTF techniques usually involves filtering techniques to get rid of the undesired spurious effects induced by shadowing and then the application of an empirical formula to account for the $M(\mathbf{k})$ term, as proposed by Nieto Borge et al. [105]. Actually, in the work by Nieto Borge et al. [105], the assessment of the term $M(\mathbf{k})$ is based on the fitting of a set of wave buoy measurements and synthetic wave data generated for different sea states. The final formulation proposed by Nieto Borge et al. [105] is a function of the wave number defined as:

$$\left|M(\kappa)\right|^2 = \alpha(H_s)\kappa^{\beta} \tag{3.4}$$

where α is a scaling coefficient depending on the significant wave height H_s and $\beta \approx 1.2$ is derived from the fitting of data. The question then arises if the reconstruction of the sea surface can be improved by associating specifically tuned MTF functions to different sea states. In fact, some author proposed modification of the $M(\kappa)$ terms based on the need to better account for different ranges of wave numbers (Chen et al., [27]) or to better adapt the procedure to the environmental condition they were considering (Ludeno et al. [79]). Moreover, to complete the inversion procedure and get a reconstruction of the surface elevation in the physical domain, a suitable correction of the phase is also needed. For the phase correction, different approaches can be found, such as, for instance: set it to zero and constant for all the wave components, as in the work of Nieto Borge et al. [105], consider it as a constant value of $\pi/4$ as done by Ziemer and Rosenthal [171], or the result of a fitting procedure as in Paulsen [112].

The MTF technique is usually organized as a procedural technique involving a set of different filtering steps in frequency domain. An example of a possible procedure for the derivation of tuned MTF and its application to the reconstruction of the wave fields can be found in Fucile et al. [54]. For sake of reference, an example wave frequency/wave number analysis of synthetic radar signals, derived by the application of models (3.1) and (3.2) to linear a long crested sea state in deep water, is presented in Figure 3.4. The replicas of the spectrum (Senet et al. [127]), induced by the shadowing, are clearly visible above the dispersion relation. The application of a band bass filter (BP) centred around the linear dispersion relation is, in general, one of the most crucial steps in the application of the MTF techniques that allows isolating the energy content of the radar signal relevant for the application of the empirical MTF correction. In addition, a high pass (HP) filter is usually applied to remove the low wave number modulations due to the range dependency of the radar backscattered signal (Nieto Borge et al. [105]; Serafino et al. [129]; Fucile et al. [54]). The cut-off wave number of the HP

filter and the band of the BP filter depend on the particular signal characteristics and are often chosen on the basis of heuristic considerations (Fucile et al. [54]). In Figure 3.4 a qualitative representation of the areas of application of the HP and BP filter is presented.

In general, the signal processing procedure underlying the MTF approach inevitably leads to the introduction of harmonic components which do not strictly fulfil the dispersion relation, and this represents, therefore, a theoretical drawback of the approach. However Serafino et al. [129] showed that its application can still allow achieving satisfying results in the reconstruction.

Looking, therefore, for a more physically consistent wave radar inversion technique, the LSQR procedure for the inversion of the radar signals has been developed, as described in the following. This alternative technique allows to deal in a straightforward way with the shadowing effect and to avoid the application of empirical corrections and filtering procedures as the ones used in the MTF technique.

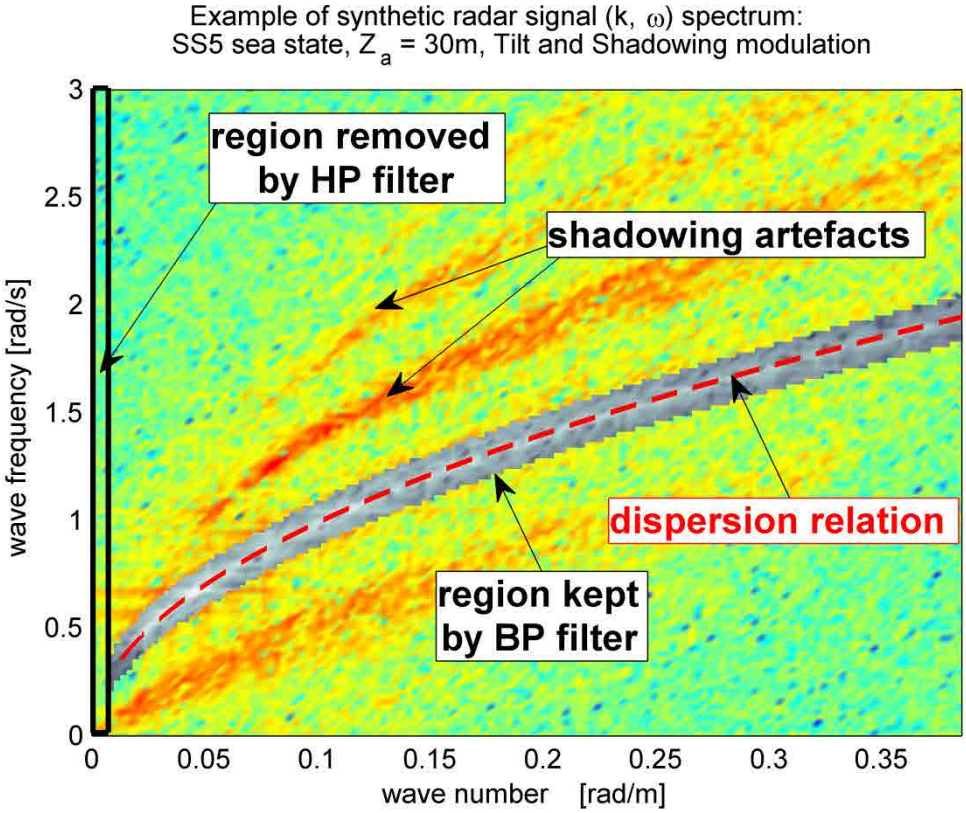

Figure 3.4: Example of synthetic radar signal analysed in the wave frequency/wave number domain in order to highlight the replicas induced by the shadowing effect. A qualitative indication of the application areas of the band pass filter (BP) and high pass filter (HP) is given in the figure.

3.4 Linearized imaging model

The inversion process described, hereinafter, is based on the linearization of the optical tilt model, presented in equation. The derived results are in line with those already provided by Naaijen and Wijaya [104]. However, since some differences are introduced with respect to Naaijen and Wijaya [104], and also for sake of reference, the full derivation is reported.

Figure 3.2 depicts a radial scan of the sea surface taken by a rotating wave radar antenna. The antenna is supposed to rotate with velocity $\Omega_a[rad/s]$ so that the current azimuth is $\beta(t)=\beta_0+\Omega_a t$, with β_0 an arbitrary reference azimuth. A Cartesian reference frame O-XYZ is defined with the origin O on the mean sea level under the vertical of the radar antenna. The Z-axis is defined as normal to the mean surface level, the X-axis is parallel to an arbitrary reference scanning direction, and the Y-axis is defined in such way to have a right-handed reference frame (see Figure 3.2). The position vector of the wave radar antenna is, then, $\mathbf{X}_a=[0,0,Z_a]^T$. The free surface is defined in polar coordinates as a function of the azimuth β and of the radial position r as $\eta=\eta(r,\beta)$. For a generic point on the free surface (illuminated by the wave radar) the normal vector to the free surface in Cartesian coordinates is:

$$\mathbf{n}=[-\eta_r\cos(\beta)+\frac{1}{r}\eta_\beta\sin(\beta),-\eta_r\sin(\beta)-\frac{1}{r}\eta_\beta\cos(\beta),1]^T \tag{3.5}$$

and the ray vector pointing to the antenna is

$$\mathbf{u}=[-r\cos(\beta),-r\sin(\beta),Z_a-\eta]^T \tag{3.6}$$

With the above definitions, equation (3.1) can then be written as:

$$\tilde{\sigma}_{tilt}=\frac{\mathbf{u}\cdot\mathbf{n}}{|\mathbf{u}|\cdot|\mathbf{n}|}=\frac{(Z_a-\eta)+r\eta_r}{\sqrt{r^2+(Z_a-\eta)^2}\sqrt{\eta_r{}^2+\frac{1}{r^2}\eta_\beta{}^2+1}} \tag{3.7}$$

Equation (3.7) highlights a nonlinear relation $\tilde{\sigma}_{tilt}(\eta,\eta_r,\eta_\beta)$ between the tilt modulation, $\tilde{\sigma}_{tilt}$, and the surface elevation (η) and its derivatives (η_r,η_β). Now, under the working hypothesis that, for each point on the free surface, $\eta,\eta_r,\eta_\beta<<1$, it is possible to approximate equation (3.7) with its linearized version as:

$$\tilde{\sigma}_{tilt,L}=\tilde{\sigma}_{tilt,0}+\nabla\tilde{\sigma}_{tilt}\big|_{\eta,\eta_r,\eta_\beta=0}[\eta,\eta_r,\eta_\beta]^T=\frac{Z_a}{R}+\frac{r}{R}\eta_r-\frac{r^2}{R^3}\eta \tag{3.8}$$

where $\tilde{\sigma}_{tilt,L}$ is the linearized version of the tilt model, $\tilde{\sigma}_{tilt,0}=\tilde{\sigma}_{tilt}(\eta=0,\eta_r=0,\eta_\beta=0)$, and R is the distance of the generic point q from the radar antenna:

$$R=\sqrt{r^2+Z_a^2} \tag{3.9}$$

Furthermore, making reference to Figure 3.2, it is possible to rewrite $\tilde{\sigma}_{tilt,L}$ in (3.8) in terms of the angle of incidence, Θ_0, as:

$$\tilde{\sigma}_{tilt,L}=\cos(\Theta_0)+\sin(\Theta_0)\eta_r-\frac{\sin(\Theta_0)^2}{R}\eta \tag{3.10}$$

Equation (3.10) is consistent with the one reported by Naaijen and Wijaya [104] except for the additional term $\frac{\sin(\Theta_0)^2}{R}\eta$ which appears in (3.10), but not in the model by Naaijen and Wijaya [104]. This additional term comes from the fact that the linearization has herein been carried out considering explicitly the surface elevation contribution. Instead, Naaijen and Wijaya [104] explicitly linearized the model only with respect to the sea surface derivatives, and the term depending on η was simplified afterwards by assuming that the surface elevation η is small enough compared to the height Z_a of the radar antenna, to be neglected. From a practical point of view, the additional term $\frac{\sin(\Theta_0)^2}{R}\eta$ is typically negligible, especially far enough from the radar antenna. Nevertheless, for consistency, herein the complete model (3.8)/ (3.10) is used as basis for the proposed inversion process described in the following section.

3.5 An alternative inversion technique: Least Squares with Regularization (LSQR)

3.5.1 Set-up of least squares problem with missing data based on linearized tilt model

The optical model for the tilt and shadowing modulation, although being a simplified version of the real radar imaging process, is often assumed as a reference model for the generation of realistic radar signal. Indeed, it is often adopted as reference model to calibrate inversion techniques to be used in real applications (Nieto Borge et al. [105]; Serafino et al. [129]). For this reason, this work focuses on the inversion of synthetic the radar images generated by the optical model (3.2). The optical model, even being a simplification of the complex actual radar imaging process, still shows a nonlinear dependence of the tilt modulation from the sea surface wave elevation and its derivatives, both due to the tilt modulation itself, as well as due to, particularly, the shadowing effects. Exactly retrieving the sea surface elevation assuming the model (3.2) to hold, would require a difficult nonlinear inversion process. As a result, the inversion task has been usually tackled following two main methodologies. One methodology is to derive semi-empirical MTF inversion techniques (Fucile et al. [54]; Nieto Borge et al. [105]). The other methodology, is to derive the inversion technique by resorting to a linearized version of the problem (Dankert and Rosenthal [35]; Naaijen and Wijaya [104]). This latter is the approach followed in this chapter. In particular, the linearized model defined by equations (3.8)/ (3.10) will be the starting point to set up a Least Squares with Regularization (LSQR) inversion technique. The technique will hereinafter be used for the inversion of synthetically generated radar images.

The key assumption in the presented LSQR approach is to assume a first-order linear model for the wave elevation field. This is a rather strong assumption about the wave elevation model and implies that the solution of the reconstruction problem is sought only among those satisfying the linear dispersion relation. The assumption of first-order linear wave field is, however, appropriate when dealing with those (low to moderate) sea states for which wave nonlinearities have negligible impact on the wave field propagation and interaction. From a computational perspective, the assumption of linearity of the wave field has the benefit of leading to a straightforward definition of the inversion process as a least squares linear inversion problem. It is also important to

mention that, despite the known limitations inherent in the linear wave assumption, the linearity of the wave field is the typical assumption in wave radar inversion techniques. In fact, the adoption of the already mentioned band-pass filters based on the linear dispersion relation, which are used to filter out the unwanted radar artefacts (a key step of many inversion techniques), can be considered to correspond, from a practical point of view, to imposing, *a-priori*, the wave field to be linear or to filter out nonlinear wave components.

Therefore, under the hypothesis of linearity of the wave field, the wave elevation and its derivatives are written as a sum of harmonic components satisfying the linear dispersion relation:

$$\begin{cases} \eta(r,\beta,t) = \sum_{n=1}^{N_h} \begin{matrix} a_n \cos\left(\kappa_n \cos(\theta_n-\beta) r - \omega_n t\right)\right) \\ +b_n \sin\left(\kappa_n \cos(\theta_n-\beta) r - \omega_n t\right) \end{matrix} \\ \eta_r(r,\beta,t) = \sum_{n=1}^{N_h} \begin{matrix} -a_n \kappa_n \cos(\theta_n-\beta) \sin\left(\kappa_n \cos(\theta_n-\beta) r - \omega_n t\right) \\ +b_n \kappa_n \cos(\theta_n-\beta) \cos\left(\kappa_n \cos(\theta_n-\beta) r - \omega_n t\right) \end{matrix} \\ \eta_\beta(r,\beta,t) = \sum_{n=1}^{N_h} \begin{matrix} -a_n \kappa_n r \sin(\theta_n-\beta) \sin\left(\kappa_n \cos(\theta_n-\beta) r - \omega_n t\right) \\ +b_n \kappa_n r \sin(\theta_n-\beta) \cos\left(\kappa_n \cos(\theta_n-\beta) r - \omega_n t\right) \end{matrix} \end{cases} \tag{3.11}$$

where N_h is the number of the wave component considered in the model, κ is the wave number, θ is the wave propagation direction, and $\omega = \omega(\kappa)$ is the wave frequency satisfying the linear dispersion relation. In case of fixed radar antenna, it is $\omega(\kappa) = \sqrt{g\kappa \tanh(\kappa D)}$ where D is the water depth and g is the gravitational acceleration. In case the radar antenna is supposed to be moving, an appropriate change of reference system should be taken into account. If the radar antenna moves with constant speed, this change of reference system leads to the classical Doppler correction which modifies the wave frequency ω to the corresponding encounter frequency. Herein, however, the radar antenna will always be considered as fixed.

The linear inversion problem can be defined, by combining equations (3.8) and (3.11), as a linear system with $2N_h$ unknowns and with M known data as:

$$\underbrace{\begin{bmatrix} & \overbrace{\quad}^{\text{n}^{\text{th}}\text{ wave number}} & & \\ \cdots & \cdots & \cdots & \cdots \\ \cdots & A_{m,2n-1} & A_{m,2n} & \cdots \\ \cdots & \cdots & \cdots & \cdots \\ & \underbrace{\quad}_{\text{cosine column}} & \underbrace{\quad}_{\text{sine column}} & \end{bmatrix}}_{\mathbf{A}\in\mathbb{R}^{M,2N_h}} \underbrace{\begin{bmatrix} \cdots \\ a_n \\ b_n \\ \cdots \end{bmatrix}}_{\mathbf{x}\in\mathbb{R}^{2N_h}} = \underbrace{\begin{bmatrix} \cdots \\ \tilde{\sigma}_{tilt,m} R_m - Z_a \\ \cdots \end{bmatrix}}_{\mathbf{b}\in\mathbb{R}^{M}} \quad \rightarrow \quad \mathbf{Ax} = \mathbf{b} \tag{3.12}$$

The unknowns in the problem are the N_h pairs of a_n, b_n coefficients (amplitudes), describing the wave elevation:

$$\begin{cases} \mathbf{x} \in \mathbb{R}^{2N_h} \\ x_{2n-1} = a_n \\ x_{2n} = b_n \\ \text{with } n = 1,...,N_h \end{cases} \tag{3.13}$$

The known term $\mathbf{b}$ of the system is obtained starting from the wave radar signal $\tilde{\sigma}_{tilt,m}$, which is assumed to be sampled on a set of, in principle arbitrary, M points $q_m(r_m, \beta_m, t_m) \quad m = 1,...,M$ in time and space:

$$\begin{cases} \mathbf{b} \in \mathbb{R}^{M} \\ \mathrm{b}_m = \tilde{\sigma}_{tilt,m} R_m - Z_a \\ \text{with } m = 1,...,M \end{cases} \tag{3.14}$$

The entries of the matrix $\mathbf{A}$ are derived by combining (3.11) with the linearized model (3.8) as:

$$\begin{cases} \mathbf{A} \in \mathbb{R}^{M,2N_h} & & \\ \mathrm{a}_n \text{ terms:} & \mathrm{A}_{m,2n-1} = -r_m \kappa_n \cos(\theta_n - \beta_m) \sin\left(\chi_{m,n}\right) - \dfrac{r_m^{\,2}}{R^2_{\,m}} \cos(\chi_{m,n}) & \\ \mathrm{b}_n \text{ terms:} & \mathrm{A}_{m,2n} = +r_m \kappa_n \cos(\theta_n - \beta_m) \cos\left(\chi_{m,n}\right) - \dfrac{r_m^{\,2}}{R^2_{\,m}} \sin(\chi_{m,n}) & \\ \text{phase function:} & \chi_{m,n} = \kappa_n \cos(\theta_n - \beta_m) r_m - \omega_n t_m & \\ \text{with } n = 1,...,N_h & & \end{cases} \tag{3.15}$$

The inversion problem as stated in equation (3.12) is in a rather general form. However, there is some constraint inherent in wave radar technology, which reflects on the actually available radar samples, which has to be highlighted. First of all, the radar signal is supposed to be potentially available only on a set of discrete values of time/azimuth and radial distance from the antenna, due to the wave radar resolution in time/azimuth and space. However, this set of potentially available sample points is, in reality, not fully available, due to the masking associated with shadowing effect that prevents the wave radar from uniformly scanning the entire wave field (see Figure 3.2). Due to the combination of the rotation of the antenna and the propagation of the wave field, the set of the actually available (i.e. not masked by shadowing) sampling points along the radial direction, for a given azimuth, changes with time. Shadowing therefore affects the radar imaging as a loss of information and as a change in the pattern of the available data at every antenna rotation. Eventually, radar data cannot be considered to be available on a uniform grid in time/azimuth and radial direction, and the global effect of shadowing is to reduce the number of actually available sampling points.

A direct way to overcome this problem is to allow the sampled data vector, $\mathbf{b}$, to be populated by radial scans taken at different time instants i.e. accounting for more than a single antenna rotation. In line with this idea, three different strategies are considered herein for the selection of the wave radar data in time, to be used for the population of $\mathbf{b}$:

$$\begin{cases} \text{Backward time window:} & t_m \in \left[t_0 - N_\tau \tau_a \, , \, t_0 \right] \\ \text{Centred time window:} & t_m \in \left[t_0 - \dfrac{N_\tau}{2} \tau_a \, , \, t_0 + \dfrac{N_\tau}{2} \tau_a \right] \\ \text{Forward time window:} & t_m \in \left[t_0 \, , \, t_0 + N_\tau \tau_a \right] \end{cases} \tag{3.16}$$

where t_0 is the time instant at which the reconstruction is carried out, $\tau_a = 2\pi / \Omega_a$ is the antenna rotation period and N_τ the number of rotations to be accounted for in the reconstruction (N_τ does not necessarily need to be integer). A graphical representation of the three considered strategies is depicted in Figure 3.5.

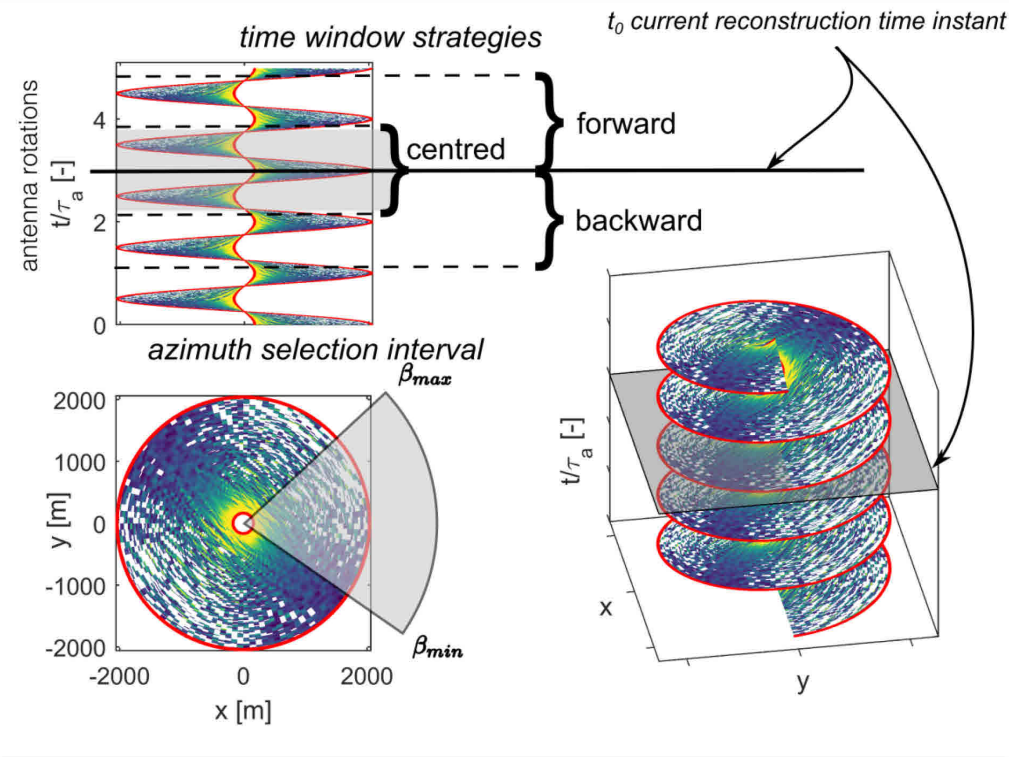

Figure 3.5: Radar imaging in time and space. Graphical representation of time window strategies and azimuth interval selection for the population of the matrices of the linear inversion problem.

At a first sight, some similarity could be found between the presented approach and the work of Naaijen and Wijaya [104]. However, this is not really the case. In fact, Naaijen and Wijaya [104] considered shadowed points as sampled points with zero radar signal, and a sort of averaging in time of the reconstructed amplitude spectra of the signal was applied to cure the shadowing effect. Instead, in the framework of the LSQR technique presented herein, the definition of the time interval that is considered for the reconstruction represents an *a-priori* assumption of the reconstruction strategy (which does not use sampled points in the shadowed regions) and not an *a-posteriori* correction of the effect of the shadowing.

It should be expected, that, although the three time window strategies can be considered to be equally valid, they will show different performance in the reconstruction of the sea surface. Moreover, it is reasonable to consider the backward time window strategy to be the most natural choice when a real-time reconstruction of the wave field is needed.

By including more than a single time instant in the reconstruction process it can be expected the reconstruction of the sea surface to be more effective. In fact, first, the inversion problem is provided with enough radar data to pursue the reconstruction, compensating for the loss of information due to shadowing. Secondly, and more importantly, the inclusion of data from different time instants allows the fitting model to better match, on average, the time-space evolution of the wave field, while being constrained by the assumed dispersion relation. These arguments have proven to be particularly important for the reconstruction of the wave elevation resulting in better performances of the approach as the number of time instant included in the reconstruction is increased, i.e. as the time window for the collection of data is widened.

Finally, in general, for a given selection of the wave model, i.e. a combination of wave numbers and wave propagation directions, the system of equations in (3.12) is set up, in practice, as an overdetermined system of equations, i.e. a system with $M > 2N_h$.

3.5.2 Tikhonov regularization

The LSQR approach, presented so far, is a typical application of a linear discrete inversion problem (Vogel [147]), where the solution is sought, in principle, among the ones minimizing the least square of the residual, i.e.:

$$\mathbf{x}_{LS} = \min_{\mathbf{x}\in\mathbb{R}^N}(\left\|\mathbf{A}\mathbf{x}-\mathbf{b}\right\|_2) \tag{3.17}$$

where $\mathbf{x}_{LS}$ is the solution of the least squares problem and $\left\|.\right\|_2$ is the Euclidean norm, and from now on the index $2N_h$ is replaced simply by $N = 2N_h$. However, looking for a direct least squares solution of the problem (3.12) according to (3.17) could lead to solution problems due to ill-conditioning of the matrix $\mathbf{A}$, a situation which very often occurs in practice.

Therefore, a regularized solution to the inversions problem (3.12) has been sought instead, by using Tikhonov regularization (Vogel [147]). This leads to a changing of the nature of the problem to be solved, from the original (3.17) to the following one:

$$\mathbf{x}_{\lambda} = \min_{\mathbf{x}\in\mathbb{R}^N}(\left\|\mathbf{A}\mathbf{x}-\mathbf{b}\right\|_2 + \lambda^2\left\|\mathbf{x}\right\|_2) \tag{3.18}$$

where, now, the solution $\mathbf{x}_{\lambda}$ is the minimizer of the quadratic functional which also depends on the value of the regularization parameter λ. It is worth to note that the problem (3.18), as defined by the equations from (3.12) to (3.15), is dimensionally consistent, the whole problem is in length units, and the regularization parameter turn out to be dimensionless.

For the solution of the inversions problem (3.12), robustness and straightforward implementation has been preferred over performances. Therefore, among the various numerical direct techniques to solve the problem in (3.18) (Golub and Von Matt [59]), in this work a technique based on the SVD decomposition has been preferred (Hansen [64]). In fact, although being a computationally expensive technique, the SVD decomposition shows a robust behaviour for rank-deficient problems and can be provided with straightforward regularization procedures in the case of ill-conditioned matrices (Golub and Van Loan [58]; Hansen [64]; Trefethen and Bau [142]). For sake

of reference, the main steps to construct the regularized solution and the selection of the regularization parameter are presented in the following (Hansen [64]).

In general a full rank matrix $\mathbf{A} \in \mathbb{R}^{M,N}$ can be factorized via SVD as follows:

$$\mathbf{A} = \mathbf{U}\boldsymbol{\Sigma}\mathbf{V}^T = \sum_{j=1}^{N} \mathbf{u}_j \sigma_j \mathbf{v}_j^T \tag{3.19}$$

where $\mathbf{U} = [\mathbf{u}_1 | ... | \mathbf{u}_N] \in \mathbb{R}^{M,N}$ is the left singular vectors matrix, $\mathbf{V} = [\mathbf{v}_1 | ... | \mathbf{v}_N] \in \mathbb{R}^{N,N}$ is the right singular vectors matrix and $\boldsymbol{\Sigma} \in \mathbb{R}^{N,N} = diag(\sigma_1, ..., \sigma_N)$ is a diagonal matrix with diagonal elements σ_j called singular values. The last term in equation (3.19) is to be intended as an outer product (Hansen [64]). The regularized solution to the problem in (3.18) can now be written as:

$$\mathbf{x}_\lambda = \mathbf{V}\boldsymbol{\Theta}(\lambda)\boldsymbol{\Sigma}^\dagger \mathbf{U}^T \mathbf{b} = \sum_{j=1}^{N} f_j(\lambda) \frac{\beta_j}{\sigma_j} \mathbf{v}_j \tag{3.20}$$

where $\beta_j = \mathbf{u}_j^T \mathbf{b}$, $\boldsymbol{\Sigma}^\dagger$ is a diagonal matrix defined as $\boldsymbol{\Sigma}^\dagger = diag(1/\sigma_1, ..., 1/\sigma_N)$, $\boldsymbol{\Theta}(\lambda)$ is the diagonal filter matrix defined as $\boldsymbol{\Theta}(\lambda) = diag(f_1(\lambda), ..., f_N(\lambda))$ with $f_j(\lambda) = \dfrac{\sigma_j^2}{\sigma_j^2 + \lambda^2}$ filter factors characterised by $0 \le f_j \le 1$ (Hansen [64]). It is noted here that it is necessary only one SVD decomposition of the matrix $\mathbf{A}$ to obtain $\mathbf{x}_\lambda$ for any value of the regularization parameter λ, and this is a very useful feature, from a computational point of view, when λ is not *a-priori* set, which, as shown later on, is the present case. It is clear that for $\lambda = 0$ the classical least squares solution of problem (3.17) is retrieved as $\mathbf{x}_{LS} = \sum_{j=1}^{N} \frac{\beta_j}{\sigma_j} \mathbf{v}_j$. The residual can be defined as:

$$\mathbf{r}_\lambda = \mathbf{b} - \mathbf{A}\mathbf{x}_\lambda = \sum_{j=1}^{N} (1 - f_j) \beta_j \mathbf{u}_j + \mathbf{r}_\perp \tag{3.21}$$

where $\mathbf{r}_\perp = \mathbf{b} - \sum_{j=1}^{N} \beta_j \mathbf{u}_j$ is the component of the residuals orthogonal to the left singular vectors matrix.

From a practical point of view, the filter factors smooth out the smallest singular values contribution of the solution ($\sigma_j << \lambda \Rightarrow f_j \approx \sigma_j^2 / \lambda^2 \to 0$) while leaving unchanged the contribution of the larger singular values ($\sigma_j >> \lambda \Rightarrow f_j \approx 1$). The regularisation parameter λ can be chosen via several techniques (Vogel [147]). Herein, the L-curve method, described in §3.5.3, is used

3.5.3 Selection of regularization parameter: L-curve method

Herein the L-curve approach has been selected (Hansen [64]). Although the L-curve approach can suffer from some issues which can lead to a non-optimal selection of the

regularisation parameter (Vogel [147]; Hansen [64]), it has herein been chosen for its robustness and straightforward implementation (Hansen [65]; Hansen and O'Leary [66]). According to the L-curve approach, the selection of the regularization parameter λ represents a trade-off choice between minimizing the norm of the residual $\left\|\mathbf{A}\mathbf{x}_\lambda - \mathbf{b}\right\|_2$ and the norm of the solution $\left\|\mathbf{x}_\lambda\right\|_2$. From (3.19)-(3.21) the following quantities can be defined:

$$\begin{aligned}\eta^2(\lambda) &= \left\|\mathbf{x}_\lambda\right\|_2^2 = \sum_{j=1}^{N}\left(f_j\frac{\beta_j}{\sigma_j}\right)^2 \\ \rho^2(\lambda) &= \left\|\mathbf{r}_\lambda\right\|_2^2 = \sum_{j=1}^{N}\left((1-f_j)\beta_j\right)^2 + \left\|\mathbf{r}_\perp\right\|_2^2\end{aligned} \tag{3.22}$$

Hansen and O'Leary [66] have shown that, under suitable hypotheses, the parametric log/log curve defined as $\gamma = (\hat{\eta}(\lambda), \hat{\rho}(\lambda))$, where $\hat{\eta}(\lambda) = \log(\eta), \hat{\rho}(\lambda) = \log(\rho)$, is concave and shows an L-shaped "corner" dividing the curve in two branches: for large values of λ the solution is dominated by the regularization error, i.e. the regularized solution may tend to be over-smoothed, while for small values of λ the solution is driven by stability issues. The optimal regularization parameter can be chosen by finding the value of the regularization parameter λ corresponding to this L-shaped "corner". This can be done by finding the value of λ maximizing the curvature of the L-curve, $\gamma = (\hat{\eta}(\lambda), \hat{\rho}(\lambda))$. Following Hansen and O'Leary [66], the curvature is defined as :

$$\kappa(\lambda) = \frac{\hat{\rho}'\hat{\eta}'' - \hat{\rho}''\hat{\eta}'}{\left(\hat{\rho}'^2 + \hat{\eta}'^2\right)^{3/2}} \tag{3.23}$$

where the prime symbol denotes the differentiation with respect to λ. The calculation of $\kappa(\lambda)$ can make effective use of the analytical expressions for the first and second derivatives of $\hat{\rho}(\lambda)$ and $\hat{\eta}(\lambda)$ as reported by Hansen [65]. Then a simple maximization algorithm can be used to find the suitable value of λ. An example of L-curve and corresponding optimal selection of the regularization parameter is presented in Figure 3.6 for a synthetic radar signal generated from Bretschneider spectrum with significant wave height $H_s = 2.5m$ and peak period $T_p = 11.97s$. A very convenient guide to the implementation of the L-curve technique has been provided by Hansen [65].

The main steps for the inversion based on the regularized problem (3.18), leading to the sea surface reconstruction for a single time instant, can therefore be summarised as follows:

- Model setup and population of the matrix $\mathbf{A}$ and of the vector $\mathbf{b}$ on the basis of the selected reconstruction strategy (see (3.12), (3.14) and (3.15));
- Calculation of the SVD decomposition of the matrix $\mathbf{A}$ (see (3.19));
- Automatic selection of the regularisation parameter by means of the L-curve approach, via minimization of (3.23) through a suitable algorithm, and definition of the filter matrix $\mathbf{\Theta}(\lambda)$;
- Solution of the regularized problem (see (3.20));
- Reconstruction of the sea surface (see (3.11)).

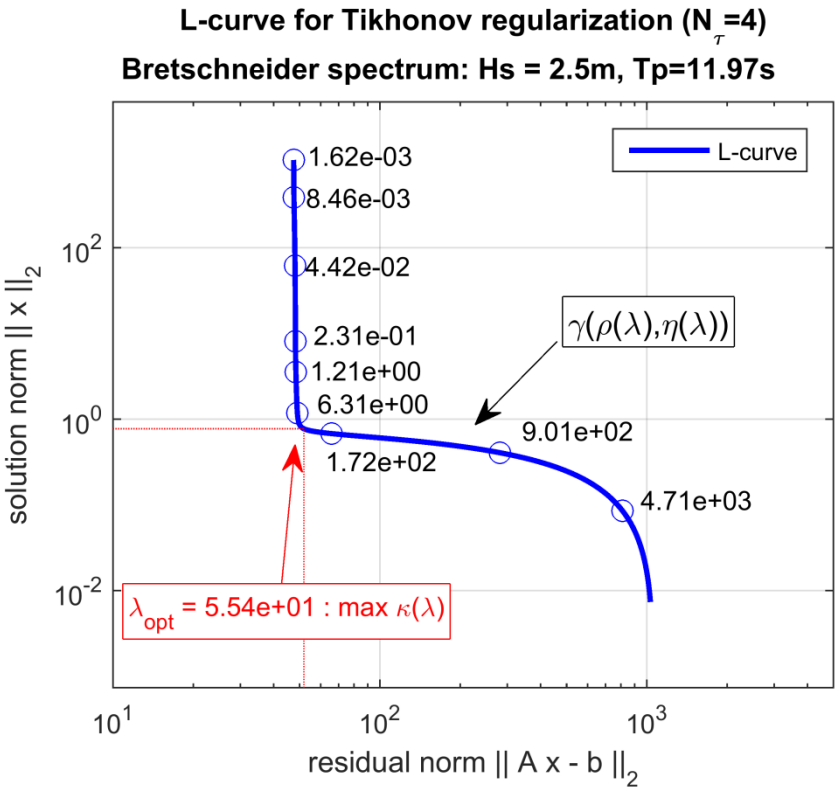

Figure 3.6: L-curve and point of maximum curvature for the choice of the L-curve optimal regularization parameter. The L-curve plot is obtained by the inversion of a synthetic radar signal generated from a Bretschneider spectrum with $H_s = 2.5m$ and $T_p = 11.97s$. $N_\tau = 4$ radar images have been considered in the set-up of the inversion problem.

The most computationally expensive step of this workflow is associated with the SVD decomposition. In fact, following Golub and Van Loan [58], the expected amount of computations associated with the calculation of the SVD on M fitting points and N_h selected frequencies is $11N^3 + 2MN^2$ ($N = 2N_h$). It should be noted that, in principle, it is possible to manage the computational effort by a different setup of the linear problem, for instance, reducing the number of the requested wave components (thus reducing N) and/or by changing the fitting strategy (thus reducing M). However, when large full matrices are involved, the proposed method would likely turn out to be computationally prohibitive, especially if the target are real-time inversion applications. As a result, in such cases, the proposed approach would be of better use as an off-line reconstruction tool. Since the described procedure has been devised with straightforward implementation and robustness as main objectives, rather than targeting at this stage its computational effectiveness, further steps should be undertaken for a reduction of the computational effort. This problem will be further addressed in the example application in §3.6.

Once the problem (3.20) is solved, and the regularized solution is obtained, $\mathbf{x}_\lambda = [..., a_n(\lambda), b_n(\lambda), ...]^T$, the sea surface can be reconstructed using equation (3.11) as:

$$\eta_\lambda(r,\beta,t) = \sum_{n=1}^{N_h} \begin{array}{l} a_n(\lambda)\cos\left(\kappa_n \cos(\theta_n - \beta)r - \omega_n t\right) \\ +b_n(\lambda)\sin\left(\kappa_n \cos(\theta_n - \beta)r - \omega_n t\right) \end{array} \tag{3.24}$$

It is worth to note that the assessment of the spectral amplitude coefficients of the free surface (a_n , b_n) represents, in general, the starting step for most of the Deterministic Sea Wave Prediction (DSWP) procedures using the DFT (see among others Naaijen and Blondel-Couprie [97]). However, in this work, the attention has been focused more on the instantaneous reconstruction of the sea surface as a function space, rather than on the correct derivation of its spectral amplitudes in the Fourier space. The present approach is therefore to be intended as a sort of physics-supported surface fitting. It should therefore be expected that the solution obtained from the proposed inversion approach may need further treatments before being consistently used in a DSWP procedure.

3.5.4 Some notes on alternative setups of the inversion problem

In general, it is possible to envisage also different arrangements of equations (3.12) to (3.15). For instance, the inversion problem could have been setup by using the wave steepness as unknowns instead of the wave amplitudes, considering, then $\mathbf{x} = [..., \kappa_n a_n, \kappa_n b_n, ...]^T$ in (3.12) and modifying $\mathbf{A}$ and $\mathbf{b}$ accordingly. However, in general, the regularized solutions of the two least squares problems, would not produce the same solution in terms of the final reconstructed sea surface. In fact, focusing on the second term of equation (3.18), it is possible to see that the penalization (regularization) term, $\lambda \|\mathbf{x}\|_2$ will tend to give more weight to the high frequency waves components over the low frequency ones when the wave steepnesses are used as unknowns. This is associated with the fact that, for realistic sea states, low frequencies, i.e. long waves, have in general negligible wave steepness even with relatively large wave amplitudes. At the same time, since the very low frequency components give very little contributions to the residual term in (3.18) when using wave steepness as unknowns, this can ultimately lead to solution with unrealistically large low frequency spurious terms. Some tests have been carried out comparing the performances of the main approach described before, i.e. the alternative approaches using wave steepnesses as unknown, and the model based on the wave amplitudes has proven to be more consistent in the reconstruction of the free surface, showing less unwanted very low frequency artefacts. Nevertheless, also for the proposed LSQR approach based on the determination of wave amplitudes, it has been noted that very large wave lengths (say $\lambda_{w,n} > 1000m$ for realistic wave radar characteristics) should not be included in the wave model considered for the inversion problem, especially in case of short crested sea states.

3.6 Application examples of LSQR technique

A set of application examples has been conceived in order to analyse the performances of the proposed LSQR approach, considering different inversion strategies, by providing statistical estimators for the expected reconstruction error. The tests are based on the idea of generating synthetic radar images from simulated wave elevation fields, apply to these images the proposed inversion approach, and, finally, compare the reconstructed wave elevation with the, known, original sea surface.

To this end, a series of Monte Carlo simulations of different sea conditions have been generated for both long crested and short crested seas. In general, for short crested seas, the wave field, η_{gen}, is generated on a polar grid according to a linear model of the same type of the one used for the inversion (see (3.11)). Starting from a given directional

wave elevation spectrum $S(\kappa,\theta)$, amplitudes $a_{n,gen}, b_{n,gen}$ used for the wave simulation are generated as couples of independent Gaussian random variables with zero mean and standard deviation $\sigma_{n,gen} = \sqrt{S(\kappa_{n,gen},\theta_{n,gen})dkd\theta}$. The directional wave spectrum $S(\kappa,\theta)$ is defined by using a multiplicative cosine squared spreading function $D(\theta)$ as follows:

$$\begin{cases} S(\kappa,\theta) = S(\kappa)D(\theta) \\ \mathrm{D}(\theta) = \dfrac{2}{\theta_{spread}}\cos\left(\pi\dfrac{\theta-\theta_{mean}}{\theta_{spread}}\right)^2 \\ \theta \in \left[\theta_{mean} - \dfrac{\theta_{spread}}{2}, \theta_{mean} + \dfrac{\theta_{spread}}{2}\right] \end{cases} \tag{3.25}$$

where θ_{mean} is the main propagation direction and θ_{spread} is the spreading angle. In case of long crested seas, amplitudes $a_{n,gen}, b_{n,gen}$ are generated as two independent random Gaussian variables with zero mean and standard deviation $\sigma_{n,gen} = \sqrt{S(\kappa_{n,gen})d\kappa}$. The number of harmonic components used in the generation was chosen to be sufficiently large to provide a good approximation of the continuous case, while still retaining an acceptable computational effort. For all simulations, about $\sim 3\cdot 10^4$ harmonics have been used for the generation of long crested waves, and 10^6 harmonics have been used for the generation of short crested waves. The regions of frequencies, and directions in case of short crested waves, used for the Monte Carlo generations guarantee that the actual significant wave height, intended as four times the ensemble standard deviation of the generated process, is 98.5% and 99.2% of the nominal significant wave height, for short crested and long crested seas, respectively.

A series of irregular sea conditions, characterised by Bretschneider sea spectra have been selected for the tests, as reported in Table 3.1. The zero-crossing period T_z was varied from 4.5s to 12.5s, corresponding to peak (modal) periods T_p from 6.33s to 17.60s. A nominal range of significant wave heights from 0.5m up to a maximum of 7.5m, with steps of 1.0m, was selected for the tests. However, the actual maximum significant wave height for each for each period was limited in such a way that the nominal wave steepness, defined as $s_s = \dfrac{2\pi H_s}{gT_p^2}$ (McTaggart and de Kat [89]), does not exceed 1/50=0.02.

Table 3.1: Sea conditions used in the analysis. Spectrum shape: Bretschneider.

Sea Condition	$T_z[s]$	$T_p[s]$	$H_s[m]$	$\frac{1}{s_s}[-]$	Sea Condition	$T_z[s]$	$T_p[s]$	$H_s[m]$	$\frac{1}{s_s}[-]$
SC01	4.5	6.33	0.5	125	SC14	10.5	14.78	3.5	97
SC02	5.5	7.74	0.5	187	SC15	10.5	14.78	4.5	76
SC03	5.5	7.74	1.5	62	SC16	10.5	14.78	5.5	62
SC04	6.5	9.15	0.5	261	SC17	10.5	14.78	6.5	52
SC05	6.5	9.15	1.5	87	SC18	12.5	17.60	0.5	967
SC06	6.5	9.15	2.5	52	SC19	12.5	17.60	1.5	322
SC07	8.5	11.97	0.5	447	SC20	12.5	17.60	2.5	193
SC08	8.5	11.97	1.5	149	SC21	12.5	17.60	3.5	138
SC09	8.5	11.97	2.5	89	SC22	12.5	17.60	4.5	107
SC10	8.5	11.97	3.5	64	SC23	12.5	17.60	5.5	88
SC11	10.5	14.78	0.5	682	SC24	12.5	17.60	6.5	74
SC12	10.5	14.78	1.5	227	SC25	12.5	17.60	7.5	64
SC13	10.5	14.78	2.5	136					

For each generated wave field, the tilt model and the optical shadowing model (see (3.2)), have been used in order to generate a corresponding synthetic wave radar signal, $\tilde{\sigma}_{tilt}$. In the case of long crested waves the, tilt model should be intended as restricted only to quantities in the plane of incidence.

The wave radar device considered in the set of simulations has been selected to have characteristics similar to those adopted by Dankert and Rosenthal [35]. In particular, the wave radar is assumed to have a radial resolution $dr = 7.5m$ and an azimuthal resolution of $d\beta = 3\deg$. It is assumed to rotate at $\Omega_{a,rpm} = 40\ rpm$, corresponding to a complete rotation of the antenna in $\tau_a = 1.5s$. According to these characteristics, the radar will take a radial scan of the sea surface every $dt_a = 0.0125s$ at the discrete azimuth values $\beta(t_m) = \beta_0 + \Omega_a m dt_a$. The radar antenna is assumed to be positioned at an elevation above the calm water level $Z_a = 30m$. The radar data of the free surface can then be organized in time/azimuth sequences of radial scans as depicted in Figure 3.5. The inversion approach based on (3.12) allows the selection of any arbitrary subsets of the radar scan data set. In this work, the radar data are selected by defining an antenna azimuth range, $\beta_{min} \le \beta_m \le \beta_{max}$, and a time interval $t_{min} \le t_m \le t_{max}$. In particular, the selection of time instants used for the reconstruction is linked to the windowing strategy adopted in the definition of the problem (3.12) as discussed in §3.5.1.

The performances of the proposed inversion approach have been analysed by deriving statistical indicators of the quality of the reconstruction. The derivation of ensemble domain statistics allows analysing the global features of the inversion process, providing a statistical characterization of the reconstruction error. Furthermore, this information can eventually be fed to models for the estimation of the wave prediction error in DSWP procedures, as the one derived by Fucile et al. [52][53]. The main quantity which has been analysed is the reconstruction error, defined as:

$$\varepsilon_j(r,\beta,t) = \eta_{\lambda,j}(r,\beta,t) - \eta_{gen,j}(r,\beta,t) \tag{3.26}$$

where $\eta_{gen,j}$ is the j-th realization of the sea elevation surface, i.e. the "true" wave elevation in the present context, and $\eta_{\lambda,j}$ is the corresponding regularized solution of the inversion problem. The main statistical quantities used herein for the

characterisation of the inversion error process are the sample mean (μ_ε), the sample standard deviation (σ_ε) and the covariance (COV), for which corresponding estimators are defined as:

$$\begin{aligned}
\hat{\mu}_\varepsilon(r,\beta,t) &= \frac{1}{N_{real}}\sum_{j=1}^{N_{real}}\varepsilon_j(r,\beta,t) \\
\hat{\sigma}_\varepsilon(r,\beta,t) &= \sqrt{\frac{1}{N_{real}-1}\sum_{j=1}^{N_{real}}\left(\varepsilon_j(r,\beta,t)-\hat{\mu}_\varepsilon\right)^2} \\
\widehat{COV}(\varepsilon(r_n,\beta_n,t_n),\varepsilon(r_m,\beta_m,t_m)) &= \frac{1}{N_{real}-1}\sum_{j=1}^{N_{real}}\left(\varepsilon_j(r_n,\beta_n,t_n)-\hat{\mu}_{\varepsilon,n}\right)\left(\varepsilon_j(r_m,\beta_m,t_m)-\hat{\mu}_{\varepsilon,m}\right)
\end{aligned} \tag{3.27}$$

where N_{real} is the number of available realizations. In addition, also the Pearson's correlation coefficient between the true wave elevation and the reconstructed wave elevation, herein indicated as c_r, has been analysed, which is defined as:

$$c_r(r,\beta,t) = \frac{\sum_{j=1}^{N_{real}}\left(\eta_{\lambda,j}(r,\beta,t)-\hat{\mu}_{\eta_\lambda}(r,\beta,t)\right)\left(\eta_{gen,j}(r,\beta,t)-\hat{\mu}_{\eta_{gen}}(r,\beta,t)\right)}{\left(N_{real}-1\right)\hat{\sigma}_{\eta_\lambda}(r,\beta,t)\hat{\sigma}_{\eta_{gen}}(r,\beta,t)} \tag{3.28}$$

where $\hat{\mu}_{\eta_\lambda}(r,\beta,t)$ and $\hat{\mu}_{\eta_{gen}}(r,\beta,t)$ are the estimators of the ensemble mean, while $\hat{\sigma}_{\eta_\lambda}(r,\beta,t)$ and $\hat{\sigma}_{\eta_{gen}}(r,\beta,t)$ are the estimators of the ensemble standard deviation, for $\eta_\lambda(r,\beta,t)$ and $\eta_{gen}(r,\beta,t)$, respectively, and they are calculated similarly to (3.27).

3.6.1 Long crested sea states

3.6.1.1 Reconstruction error statistics

In this section a systematic investigation of the performances of the LSQR method is presented in the case of long crested sea states. In the first part, the reconstruction error, considered as a stochastic process, is investigated in detail in the case of the reference sea condition SC09 (see Table 3.1). In the second part, the overall performances of the LSQR approach are tested for the whole set of sea conditions defined in Table 3.1. The shared strategy to set up the Monte Carlo simulations starts with the generation of a set of random wave elevation realizations. The wave elevation realizations are then processed, by applying the model in (3.2), in order to retrieve the corresponding synthetic wave radar image to be inverted. The radial derivative of the wave elevation, to be used in (3.2), is obtained in this case by a central difference scheme. The radar is assumed to be looking in the propagation direction of the long crested waves, therefore the derivative in the azimuth direction is zero. The spatial domain considered for the application of the inversion model in (3.12) is discretized into $N_r = 320$ grid points within the radial interval $r = 150m$ to $r = 2542.5m$. Each radar image is considered to be acquired every antenna rotation, corresponding to a time lag $\tau_a = 1.5s$. The wave numbers used for the inversion are taken as $\kappa_n = \frac{2\pi}{N_r dr}n$ with $n = 1,...,N_r/2-1$, corresponding wave length are within the range $\lambda_{w,\max} = 2400m \le \lambda_w \le \lambda_{w,min} \approx 15.1m$ .The wave frequencies are calculated as $\omega_n = \sqrt{g\kappa_n}$ (deep water assumption).

In the following, the main statistical characteristics of the reconstruction error, as defined in (3.26), are estimated and discussed. Particular attention is given to an example analysis of the error process covariance, since this is a characteristic which is typically not fully addressed. However, some fundamental consideration can already be done in advance about the expected behaviour of the main statistical features of the error process. Once the reconstruction strategies are defined, by selecting the frequency model and the strategies for the population of the problem in (3.12), it should be expected the error process to be independent of the particular time instant considered for the reconstruction. In other words, since the original wave elevation process, at least as considered in the simulations herein, is a stationary process, the same can be expected for the reconstructed sea elevation process and, consequently, for the reconstruction error process. Therefore, it is expected that the stationarity property of the reconstruction error process is reflected in the data obtained from the analysis.

Figure 3.7 presents the estimators of mean and of standard deviation of the error (see (3.27)), normalised by using the significant wave height, as calculated in the ensemble domain from a total of 500 Monte Carlo simulations. The synthetic radar images have been generated for 600 antenna revolutions, corresponding to 900s. Results from the three different time window strategies discussed in §3.5.1 are compared with different colours. The plot presents the estimators of μ_ε and σ_ε as functions of the distance from the antenna (which is positioned at $r = 0m$). The estimators obtained at different time instants are plotted as superimposed curves. It is possible to note that both statistical parameters can be considered to be stationary, since, for different time instants, the reconstruction error statistics are visibly clustered around a common trend, with a variability which can be associated with sampling uncertainty. On the other hand, the estimators of mean and standard deviation do not show uniformity over the space, since they vary with the distance from the antenna. In detail, the mean value shows a low frequency dependence on the distance from the antenna. Moreover, the shape of the mean values appears to be different for different time window strategies. Regarding the standard deviation of the reconstruction error, it presents different quantitative behaviours among the three considered time window strategies but a qualitatively common behaviour in the central region of the reconstruction space interval. In fact, a central plateau of minimal standard deviation of the error is present (this is highlighted, in the figure, by adding a notional reference level $\sigma_\epsilon / H_s = 0.05$), with an increasing reconstruction error standard deviation towards the edges of the reconstruction space interval. The difference among the three time window strategies is only appreciable at the boundaries of the space interval, where the curves appear to be shifted. This behaviour is likely linked to the different window strategies that have been selected combined with the selected wave propagation direction. In fact, if the backward window strategy is selected, it should be expect to have more problems in coping with the information carried by the wave incoming in the space interval selected for the reconstruction. Conversely, if the forward window strategy is selected, the opposite should be expected, with difficulties in retrieving the wave elevation of outgoing waves. The standard deviation of the reconstruction error shows a systematic increasing trend away for the radar antenna, which is common to the different time widow strategies, together with a marked increase close to the antenna.

Figure 3.8 presents the effect of long wave modes in the reconstruction error statistics. The mean and the standard deviation of the reconstruction error, calculated in the ensemble domain, are reported in the case of different wave models associated with different maximum reconstruction wave lengths. The results are reported, as in Figure 3.7, as functions of the distance from the radar antenna but, for this analysis, only for a

single instant of time. The different reconstruction wave models are defined by including the Fourier modes as previously described, except that in this case the minimum wave number, $\kappa_{\min} = \frac{2\pi}{N_r dr} n_{\min}$, has been varied with $n_{\min} = 1,2,3,4$. This corresponds to excluding the wave modes with length respectively longer than $\lambda_w \le \lambda_{w,\max} = [2400, 1200, 800, 600]m$. It is worth noting that, for the sea spectrum considered in this application, the wave energy contribution coming from the waves longer than $\lambda_{w,\max} = 600m$ is, from a practical point of view, negligible (<0.1%). Introducing long wave modes in the reconstruction model leads to spurious dependencies of the mean of the reconstruction error on the position. Conversely, excluding the longer wave modes from the reconstruction model makes the mean value to be more uniformly close to zero. A less prominent, but still present effect affect the standard deviation of the reconstruction error especially near the edges of the considered spatial domain. As mentioned before in §3.5.4 the LSQR method has proven to be less accurate in reconstructing the longer wave modes with a tendency to assigning, during the inversion process, incorrect and overestimated wave amplitudes to the longer wave components.

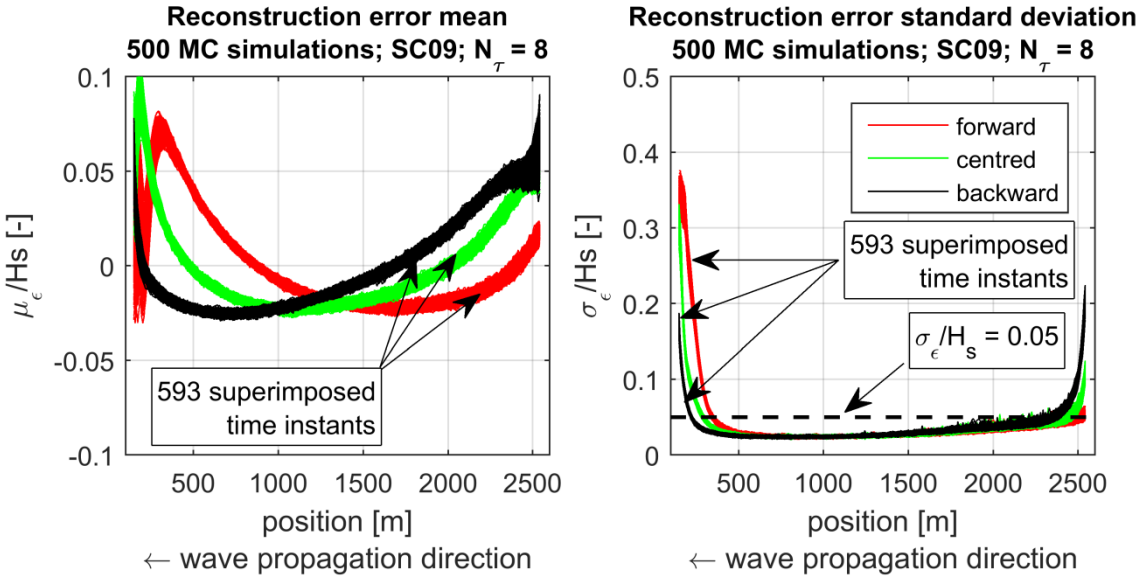

Figure 3.7: Normalized mean and normalized standard deviation of the reconstruction error as functions of the distance from the antenna (position=0m). Sea condition SC09 (see Table 3.1). Comparison among three different time window strategies: forward, backward, centred. Superimposed lines correspond to 593 different time instants at which the reconstruction of the wave elevation has been calculated. Results are based on a total of 500 Monte Carlo simulations.

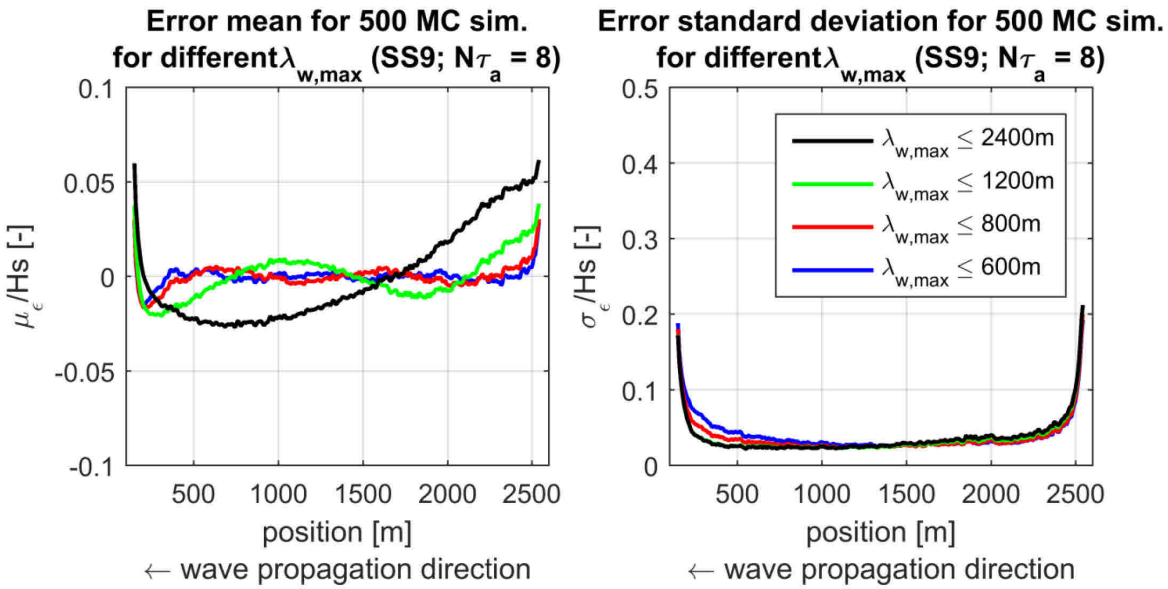

Figure 3.8: Normalized mean and normalized standard deviation of the reconstruction error as functions of the distance from the antenna (position=0m). Sea condition SC09 (see Table 3.1). Comparison among performance of four different reconstruction wave models considering associated with different maximum reconstruction wave lengths. Results are based on a total of 500 Monte Carlo simulations and are presented for a single time instant.

Another statistical quantity which is useful for the statistical characterization of the reconstruction error process is the covariance matrix. The covariance matrix plays a key role in describing the measurement error process in the framework of the procedure proposed by Fucile et al. [52] for the assessment of the statistical characteristics of the wave elevation prediction error. An example of calculated estimator of the covariance matrix, based on 500 Monte Carlo simulations, is presented in Figure 3.9. The covariance has been estimated according to (3.27) for a set of N_r discretized space points and for $N_t = 4$ time instants (the number of time instants has been limited for graphical purposes), using, for each reconstruction, a backward time window strategy based on data from the previous $N_\tau = 8$ antenna revolutions. The entries of the covariance matrix reported in Figure 3.9 are defined according to the following ordering of indices:

$$\begin{cases} \mathbf{C}_{m,n} = \widehat{COV}\left(\varepsilon\left(r_{j_r}, t_{k_t}\right), \varepsilon\left(r_{i_r}, t_{h_t}\right)\right) \\ m = m\left(j_r, k_t\right) = j_r + (k_t - 1)N_r \\ n = n\left(i_r, h_t\right) = i_r + (h_t - 1)N_r \\ \\ i_r = 1, \ldots, N_r = 320 \quad ; \quad h_t = 1, \ldots, N_t = 4 \\ j_r = 1, \ldots, N_r = 320 \quad ; \quad k_t = 1, \ldots, N_t = 4 \end{cases} \tag{3.29}$$

Figure 3.9 presents a visible sub-block pattern due to the organization of the error vector entries. Within each sub-block, the covariance depends only the space coordinates. From sub-block to sub-block the time instants are varied. The sub-blocks in diagonal descending direction (from upper left to lower right) represent the covariance, depending on space coordinate, taken at constant time lags $\tau = t_{h_t} - t_{k_t}$. In general, the covariance matrix in Figure 3.9 shows the expected symmetry coming from the fact that

$\mathbf{C}_{m,n} = \mathbf{C}_{n,m}$. From the assumption about the stationarity of the reconstruction error, it is expected the covariance matrix to depend only on the time lag between different reconstruction times instants. This is verified in Figure 3.9, where it is possible to see that, apart from random sampling uncertainty, the covariance matrix depends only on the time lag considered and not on the specific reconstruction time. On the other hand, the covariance presents variations within each of the sub-blocks, implying the non-uniformity in space of the error process.

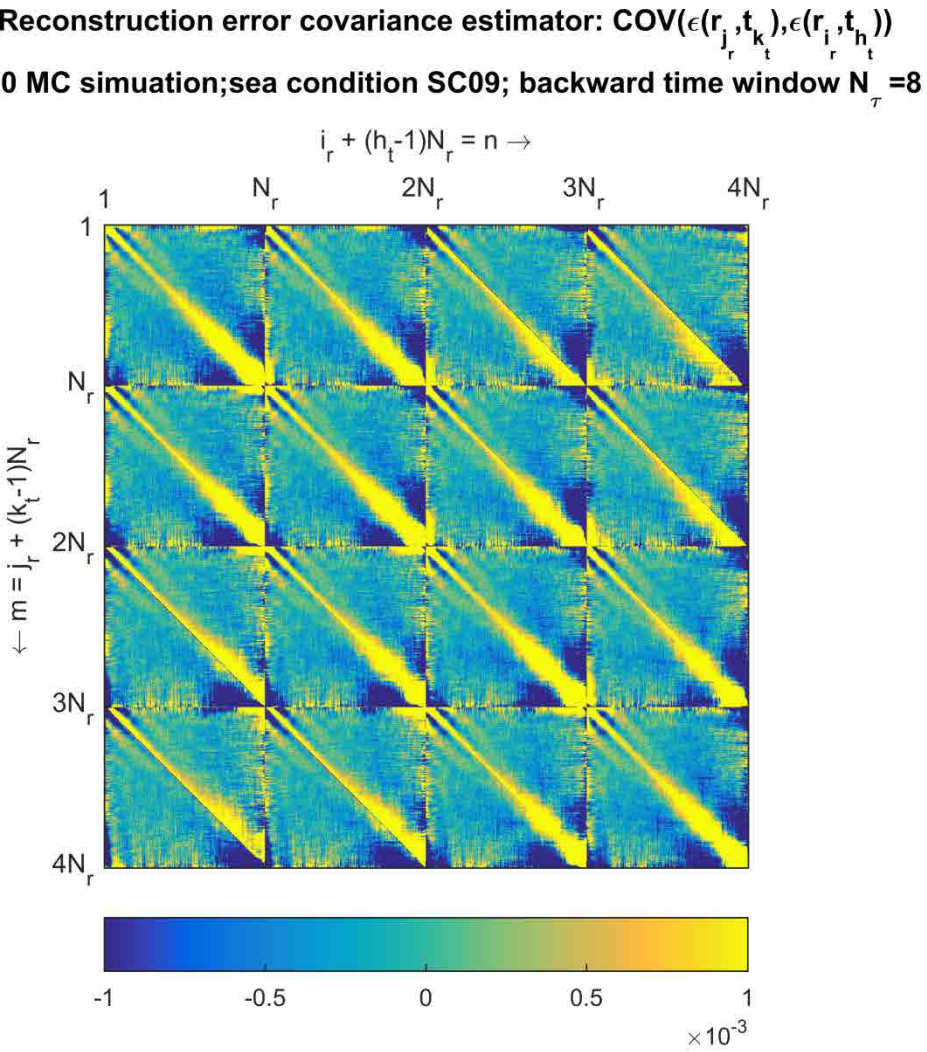

Figure 3.9: Error covariance estimator calculated for 4 time instants using 500 Monte Carlo simulations in case of sea condition SC09 (see Table 3.1). Position of the antenna: $r = 0m$. Height of the antenna above mean water level: $Z_a = 30m$. The selected radar images account for $N_\tau = 8$ time instants with a backward time window strategy. The colour scale is limited for presentation purposes.

The stationarity of the process allows to average over the time lags in order to get a more compact formulation of the estimator of the error covariance matrix as depicted in Figure 3.10. The results obtained for the covariance of the reconstruction error, even in the simplified case of long crested sea states, highlight its non-uniformity in space in addition to the variability for different time lags. Despite the emerging complexity of the inversion error characterizing the LSQR approach, a complete characterization of the covariance matrix could be potentially exploited as input for the methodology developed by Fucile et al. [52], to represent the wave radar "measurement" error characteristics.

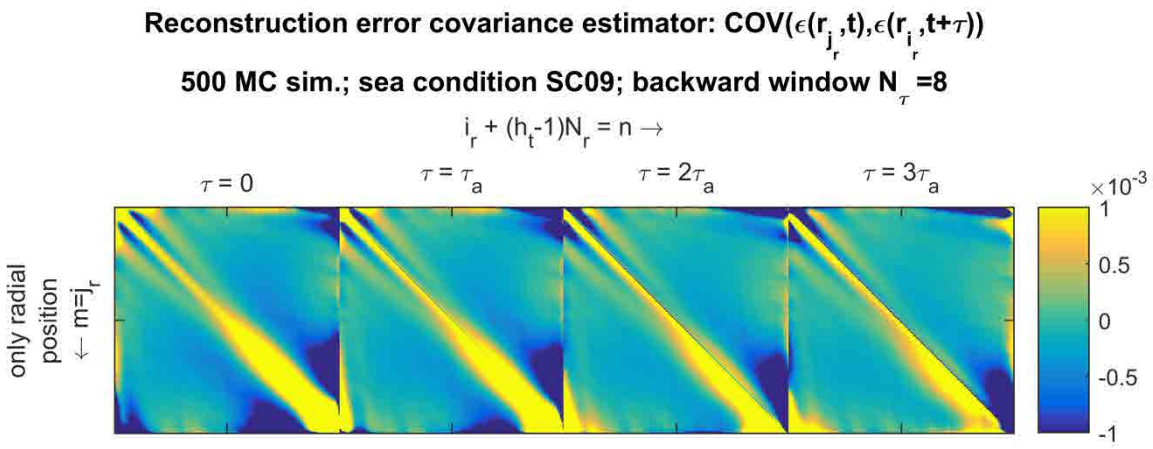

Figure 3.10: Error covariance estimator calculated for 4 time lags using 500 Monte Carlo simulations in the case of sea condition SC09 (see Table 3.1). Position of the antenna: $r = 0m$. Height of the antenna above mean water level: $Z_a = 30m$. Results have been obtained through averaging over time, taking advantage of the stationarity of the process. The selected radar images account for $N_\tau = 8$ time instants with a backward time window strategy. The colour scale is limited for presentation purposes.

After the detailed analysis for the sea condition SC09 reported so far, a systematic series of tests has been carried out in order to assess the reconstruction performances of the LSQR approach for a set of long crested sea states characterized by different peak period and significant wave height, according to Table 3.1. For each considered condition, a set of 100 Monte Carlo synthetic radar images has been generated, for a total simulation time of 180s. The estimated normalized standard deviation of the reconstruction error, σ_ϵ / H_S, and the Pearson's correlation coefficient, c_r, derived from the Monte Carlo simulations in the considered conditions are reported, as functions of the distance from the antenna, in Figure 3.11 and Figure 3.12, respectively. Considering the stationarity of the process, only the time averages are reported in the figures. Results have been organized by grouping, in the same plot, all sea conditions with the same peak period and reporting one curve for each different significant wave height. Four reconstruction strategies have been compared, one in each row of each figure, accounting for a different number of radar images used for the reconstruction. In particular, the inversion problem has been populated with $N_\tau = 4, 8, 16, 24$ radar images which are assumed to have been recorded before the actual reconstruction time instant, implementing, therefore, a backward time window strategy.

From results in Figure 3.11 a common trend can be identified for all sea conditions, with high levels of σ_ϵ / H_S at boundaries of the spatial domain and low values of σ_ϵ / H_S characterizing a central, almost flat, region. Results appear to be strongly dependent on the significant wave height H_S, with worse reconstruction performance, for a given peak period, as H_S increases. A somewhat parallel behaviour can be noted for the Pearson's correlation coefficient, c_r, in Figure 3.12. In all case c_r reduces at the edges of the domain. In addition, c_r tend to show a systematic decreasing trend moving away from the radar antenna, and the magnitude of this trend strongly depends on the significant wave height. In particular, larger values of H_S, for a given period, tend to lead to stronger trends and overall lower c_r. The observed behaviours in Figure 3.11 and Figure 3.12 can be associated with the fact that higher values significant wave

height, H_s, for a given period, lead to a stronger shadowing effect of the radar signal. This causes an increasing amount of information to be lost in the inversion process at detriment of the reconstruction performance. Each plot in Figure 3.11 and Figure 3.12 reports the ratio between the length of the time window included for a single reconstruction ($\Delta_\tau = N_\tau \tau_a$) and the peak period ($T_p$), with this ratio increasing from top to bottom. Increasing the length of the time window and the corresponding number of time instants which are taken into account for a single reconstruction improves the performance of the reconstruction for all the considered conditions. However, for large values of Δ_τ / T_p a sort of saturation of the reconstruction performance is reached. Using a time window in the range $\Delta_\tau / T_p = 1 \div 2$ seems to be, for the considered cases, a good balance between accuracy and computational effort. This means that, for the considered conditions, in order to have good reconstruction performance, radar images recorded for at least one to two peak periods should be accounted for in the LSQR inversion process. Besides, the reported results indicate that including more time radar data in the inversion process can (partially) overcome the issues in the reconstruction of signals highly affected by the shadowing effect. In order to better highlight this effect, Figure 3.13, Figure 3.14 and Figure 3.15 show examples of reconstructed wave elevation, as calculated at single time instant, for different sea conditions. For each figure, the shadowed region of the radar signal, at the time instant selected for the reconstruction, is indicated with grey bands. The shadowed region is reported for presentation purposes in order to give a qualitative indication of the extension and pattern of the shadowing. Particularly interesting is the case in Figure 3.15, where an example of reconstruction for the condition SC017 is presented. This case appears to be characterized by some systematic issue in the reconstruction, as also indicated by the corresponding data reported in Figure 3.15. In fact, for the case $N_\tau = 4$, Figure 3.11 highlights a systematic large error in the reconstruction of the wave elevation far from the radar antenna. The proposed procedure struggles in reconstructing the wave elevation, especially in correspondence to the shadowed regions of the synthetic radar images, as reported Figure 3.15. It eventually fails in the reconstruction of the wave elevation for few time instants and for a single realization of the SC17 test. In this case, the wave elevation is characterized by unphysical spikes dramatically departing from the true wave elevation, which explain the reported time averaged reconstruction error standard deviation in Figure 3.11. In fact, considering this particular time instants as outliers, and excluding them from the averaging, a more suitable behaviour is retrieved, as reported in dashed line in Figure 3.11. This phenomenon has to be ascribed to the failure of the L-curve method in finding the optimal regularization parameter for the particular case considered. Further investigation has been undertaken to deal directly with such drawbacks in the regularization procedure. Indeed, looking at Figure 3.15, it is possible to appreciate, firstly, how importantly the reported condition is affected by the shadowing effect, and, secondly, it can be noted how including more time instant in the reconstruction can improve the reconstruction by (partially) compensating for data loss due to shadowing.

Further looking at Figure 3.11, the minimum value of σ_ϵ / H_S appears to be related to the peak period of the considered sea state. Better performance are achieved for large peak periods, at least up to the ones considered in these tests: compare, for instance, the reconstruction results with peak period $T_p = 7.74s$ with the ones at $T_p = 17.60s$ in Figure 3.11. This is related to an insufficient time/space discretization of the assumed radar images in case of sea states with small periods, that causes the higher frequency tails of the spectrum to be poorly taken into account in the reconstruction. This aliasing

effect implies a misfit of the dispersion relation for the wave components with high wave number leading to a net loss of energy of the reconstructed wave elevation, an issue which is well represented in Figure 3.13.

The reported systematic analysis gives an overall satisfactory picture of the performances of the LSQR approach, both in terms of standard deviation of reconstruction error and of correlation coefficient, at least for the investigated sea conditions. It is to be underlined that the good performances could also be a partially biased result due to the fact that the underlying "true" wave have been generated with a first-order linear model, i.e. the same type of model which is used in the inversion process. Although the linear model is justifiable for sufficiently low significant wave steepness, the presence of nonlinearities, typically at large steepness, could partially modify the outcome. For this reason, in the next section, the LSQR method is applied to the reconstruction of nonlinear wave fields.

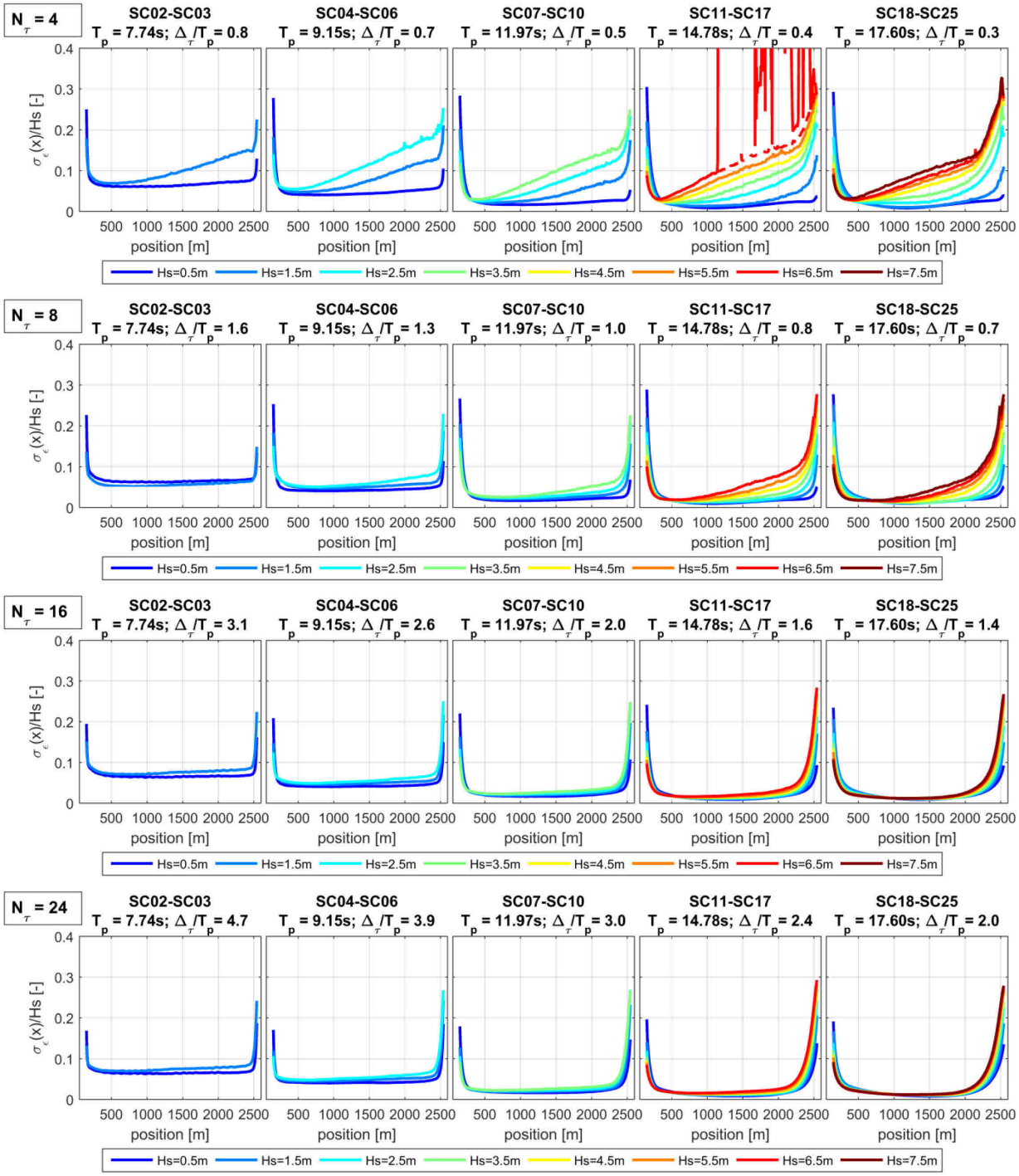

Figure 3.11: Normalized standard deviation of the reconstruction error estimated for sea conditions according to Table 3.1. 100 Monte Carlo simulations for each condition. The estimated variance of inversion error is averaged over time, and the corresponding normalised standard deviation is reported as a function of the position. Position of the antenna: $r = 0m$. Height of the antenna above mean water level: $Z_a = 30m$. Waves propagate from right to left ($\leftarrow$).

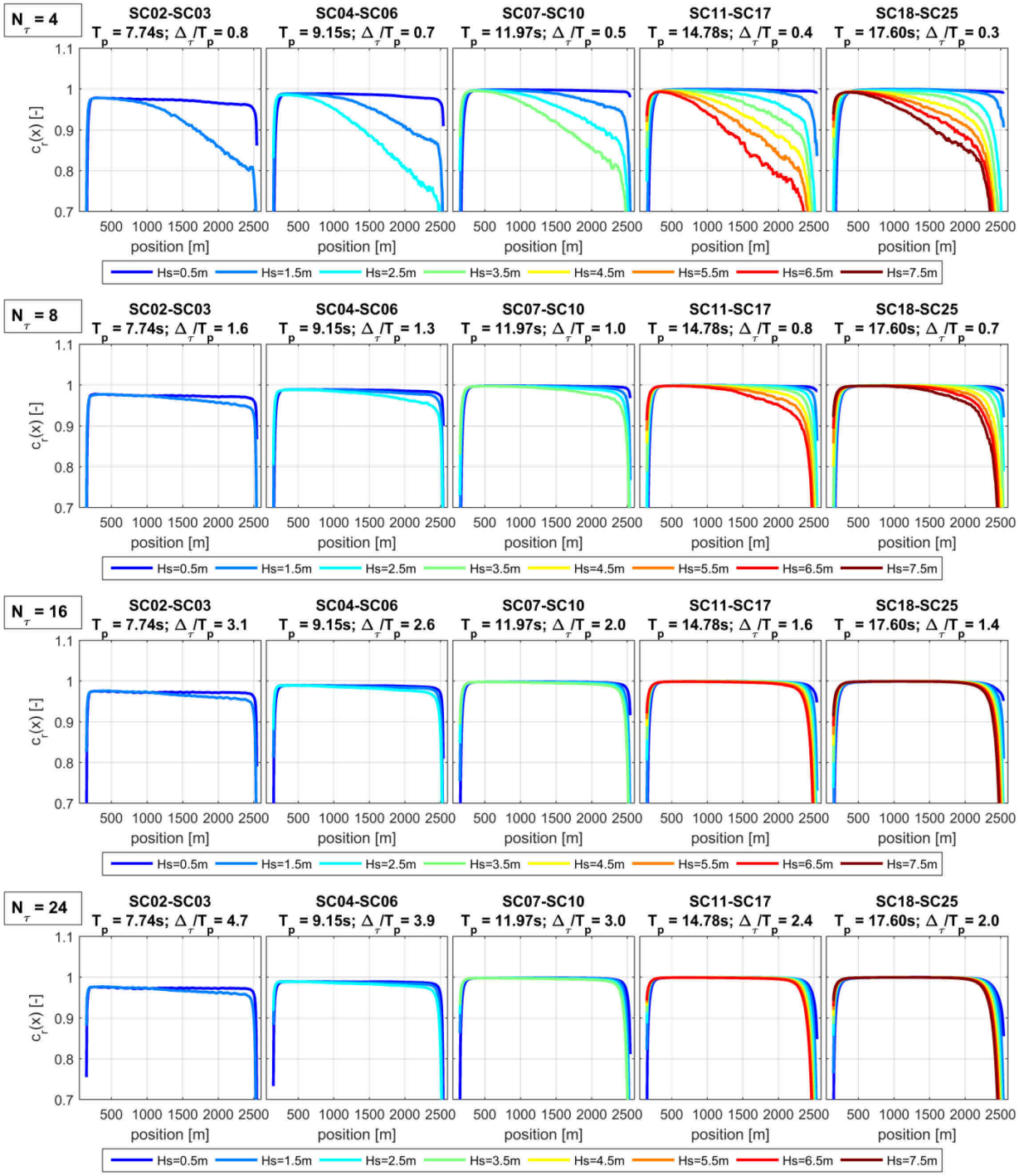

Figure 3.12: Pearson's correlation coefficient between the true wave elevation and the reconstructed wave elevation for sea conditions according to Table 3.1. 100 Monte Carlo simulations for each condition. The Pearson's correlation coefficient is averaged over time and reported as a function of the position. Position of the antenna: $r = 0m$. Height of the antenna above mean water level:. $Z_a = 30m$. Waves propagate from right to left ($\leftarrow$).

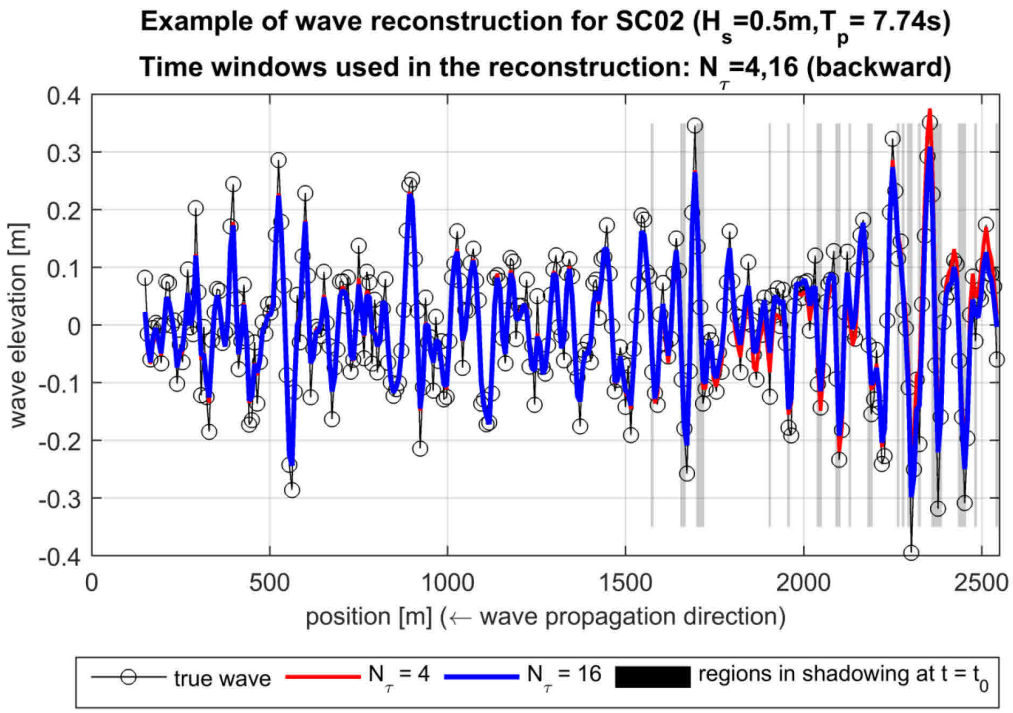

Figure 3.13: Example of instantaneous wave reconstruction from synthetic radar images using the LSQR inversion method in the case of long crested sea condition SC02 (see Table 3.1). The reconstruction is based on the backward time window strategy, considering two different time intervals for the collection of radar data $N_\tau = 4,16$. Position of the antenna: $r = 0m$. Height of the antenna above mean water level: $Z_a = 30m$.

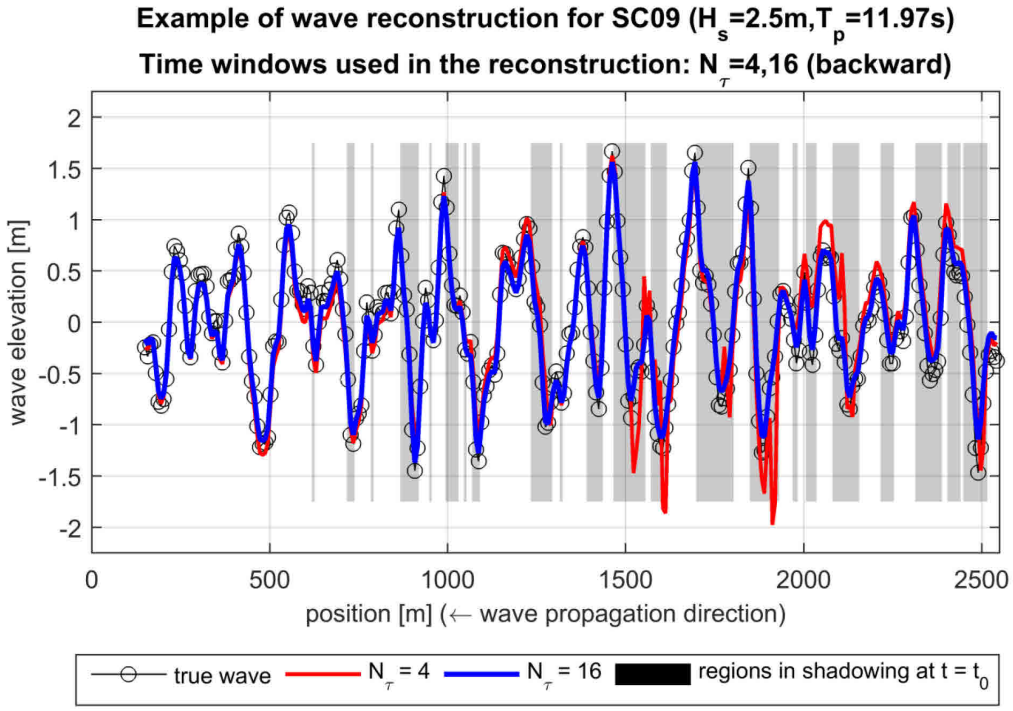

Figure 3.14: Example of instantaneous wave reconstruction from synthetic radar images using the LSQR inversion method in the case of long crested sea condition SC09 (see Table 3.1). The reconstruction is based on the backward time window strategy, considering two different time intervals for the collection of radar data $N_\tau = 4,16$. Position of the antenna: $r = 0m$. Height of the antenna above mean water level: $Z_a = 30m$.

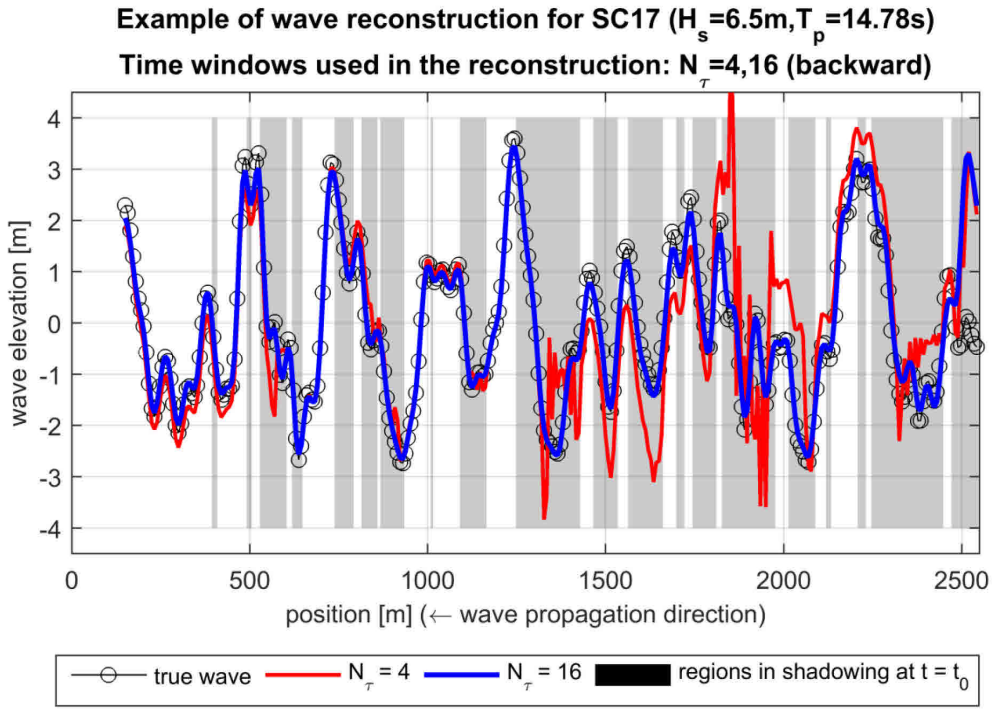

Figure 3.15: Example of instantaneous wave reconstruction from synthetic radar images using the LSQR inversion method in the case of long crested sea condition SC17 (see Table 3.1). The reconstruction is based on the backward time window strategy, considering two different time intervals for the collection of radar data $N_\tau = 4,16$. Position of the antenna: $r = 0m$. Height of the antenna above mean water level: $Z_a = 30m$.

3.6.2 Long crested sea states: LSQR applied to nonlinear wave fields

In this section the LSQR method is applied to a set of synthetic radar images generated from nonlinear wave fields. The nonlinear wave fields have been generated by means of the HOS tool described in §2 corresponding to the sea condition already presented in the section §2.5. The results are then compared with the ones derived for a corresponding set of wave fields generated by a linear model. The considered sea conditions account for a peak period $T_p = 11.97s$ and for a set of different wave heights $H_s = 2.5, 4.5, 6.4, 8.5m$. The workflow for the generation of the synthetic radar signal is the same presented in section §3.6.1. The radar has been positioned at $r = 0m$ and $Z_a = 30m$. The population of the least squares problem has been setup to account for $N_\tau = 8$ radar images and the backward window strategy has been selected. In this case, however, a reduced set of 50 Monte Carlo water wave realizations has been considered.

Since the wave elevation is generated by means of different tools, as a first step, the energy content of the different realization is compared. Figure 3.16 present the estimator of the standard deviation of the wave elevation $\hat{\sigma}_\eta$ normalized with respect to the corresponding nominal value $H_s / 4$. All the results have been calculated in the domain of the realization, as defined in (3.27), and then averaged along the space coordinates. The value of $\hat{\sigma}_\eta / (H_s / 4)$, for the nonlinear waves, show a tendency to decrease with the time. This is mainly due to the application of a low pass filter in the nonlinear simulation to improve the stability of the calculations. This implies that some energy is lost due to the filtering. However, being the values of $\hat{\sigma}_\eta / (H_s / 4)$ comprised in an

interval less than ± 0.025 the simulation has been considered as adequate for the comparisons in the following.

Figure 3.17 present the result for the standard deviation of the reconstruction error, $\hat{\sigma}_\epsilon / H_s$, as obtained in case of linear and nonlinear waves. The results have been averaged over time and presented as function of the distance from the antenna. Nonlinear results are presented in grey lines whereas linear results are presented in black lines. The lines corresponding to the same nominal H_s have been grouped. As H_s increases, both the linear and nonlinear simulation show a degradation in the reconstruction performance which is manly related to the shadowing effect. In case of the higher H_s, the reconstruction of the nonlinear wave elevation presents a significant gap with respect to the result obtained with the linear wave elevation. In addition, the gap in the reconstruction error increases has the significant wave height increases, while it is small for the smaller tested significant wave heights. This suggests that the nonlinearities of the wave fields play an important role in the reconstruction error at large significant wave heights. Indeed, the underlying linearity assumption about the wave field on which the LSQR is based on does not hold any more when nonlinear characteristics of the wave field become more important, and such effect increases with the H_s. On the other hand, at low significant wave heights, where the linearity assumption is more appropriate, results obtained using the linear and the nonlinear wave fields are very close each other.

Figure 3.18 presents the Pearson's correlation coefficient, c_r, between the true wave elevation and the reconstructed wave elevation. For both the linear and nonlinear wave cases, due to the shadowing, c_r decreases with the distance from the antenna with the increase of H_s. In addition to that, the nonlinear wave cases tend to show lower correlation coefficients with respect to the linear cases and this discrepancies increase with the nonlinearity of the wave field.

Finally, the LSQR performances for the linear and nonlinear wave fields seem to be comparable only for the lower H_s. This confirms that the LSQR technique is more suitable only for those sea states for which the linearity hypothesis is more appropriate. However, although larger differences can be noted in case of higher H_s, from a practical point of view, these cases can be considered of minor interest because of the difficulties in the radar imaging due to the large shadowing effects.

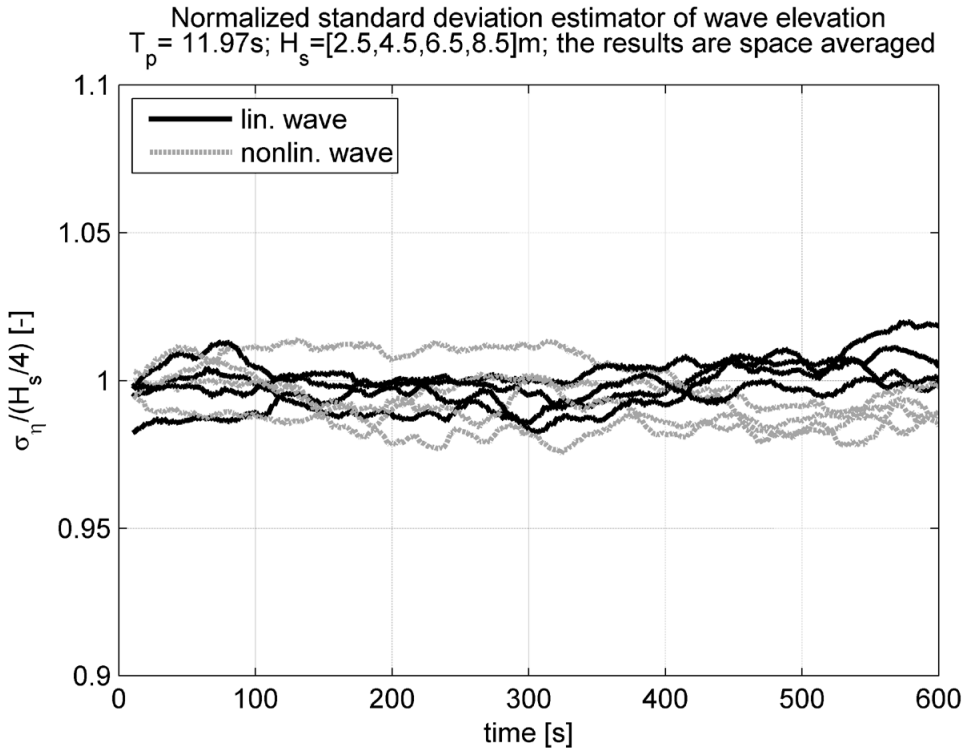

Figure 3.16: Normalized standard deviation estimator for the linear and the nonlinear wave elevations. The standard deviation estimator is averaged in the space coordinates and reported with respect to the simulation time. The normalization constant is $H_s / 4$.

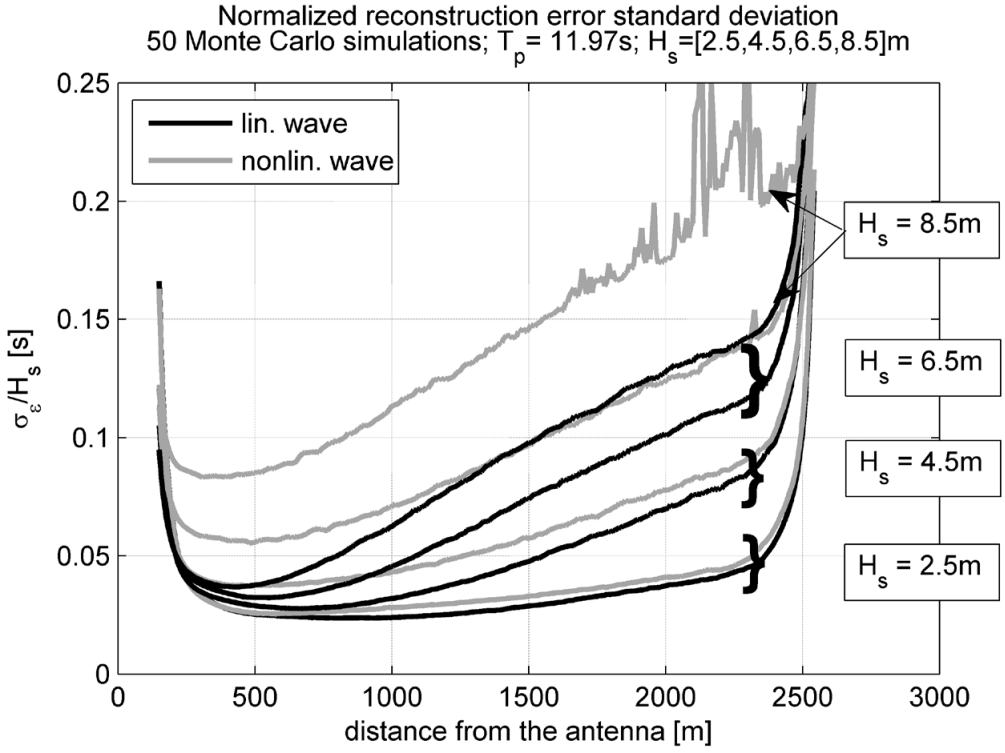

Figure 3.17: Normalized reconstruction error standard deviation as function of the distance from the antenna. Comparison of results obtained for the reconstruction of linear and nonlinear wave fields.

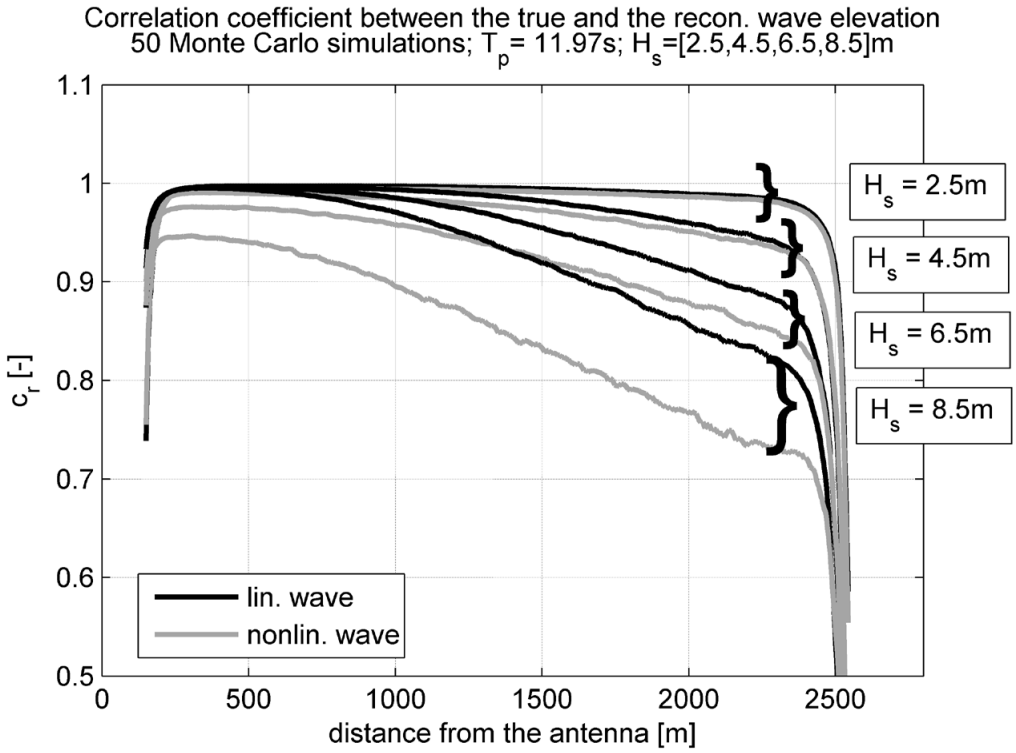

Figure 3.18: Pearson's correlation coefficient between the true wave elevation and the reconstructed wave elevation as function of the distance from the antenna. Comparison of results obtained for the reconstruction of linear and nonlinear wave fields.

3.6.3 Short crested sea states

3.6.3.1 Reconstruction error statistics

In this section a realistic application of the LSQR approach to the inversion of wave radar images from short crested linear waves is presented. A short crested sea spectrum is defined according to (3.25). The spectrum $S(k)$ corresponds to the sea condition SC09 in Table 3.1, and the main propagation direction and the spreading angle are $\theta_{mean} = 45\,\text{deg}$ and $\theta_{spread} = 60\,\text{deg}$, respectively. The synthetic radar images have been generated simulating the wave radar imaging the sea surface every $dt = 0.0125s$, during which the antenna rotates of an angle of $d\beta = 3\,\text{deg}$, see Figure 3.5. The radar images are sampled in the radial direction with resolution $dr = 7.5m$ in the range from $r = 150m$ to $r = 2062.5m$, accounting for $N_r = 256$ samples. Compared to the example case of linear long crested waves, in this case the spatial range of the radar has been reduced, for reasons associated with computational effort. The backward time window strategy has been selected for the reconstruction. Therefore, a snapshot of the complete wave elevation field is reconstructed with all the data from $t = t_0 - \Delta_\tau$ to $t = t_0$, where Δ_τ is the considered time window for the radar data collection. The radar images considered for the reconstruction of the wave elevation are those within $N_\tau = 8$ antenna rotations, corresponding to a time interval $\Delta_\tau = 12s \approx T_p$. The synthetic radar images have been generated by applying the model (3.7) to the sea elevation time histories, where the radial and azimuth derivatives of the sea elevation have been calculated by means of the analytical expressions in (3.8).

The range of wave components used for the reconstruction has been restricted in the range $20m = \lambda_{w,min} \le \lambda_{w,n} \le 500m = \lambda_{w,max}$. For the case of short crested sea reconstruction reported herein, this limitation has proved to be particularly useful in avoiding low frequency spurious effects, particularly when using reconstruction wave models characterised by a coarse discretization in the wave number domain. In order to check the performance of the LSQR approach for different choices of the reconstruction model, different discretization in the domain of wave numbers and wave directions have been considered. Wave numbers and wave directions used in the reconstruction have been defined with reference to evenly discretized grids of $N_\kappa = 81,161,241$ points in the interval $\kappa_{min} \le \kappa_n \le \kappa_{max}$, and $N_\theta = 31,61,91$ points in the interval $0 \le \theta_n \le 90\,\text{deg}$. In fact, in order to limit the number of wave directions in the wave model, the mean direction and the spreading of the wave spectrum is assumed to be known. Thus, the wave directions accounted for in the wave model cover the whole range of the wave component generated in accordance with the spreading of the wave spectrum, $\theta_{spread} = 60\,\text{deg}$, around the mean wave direction $\theta_{mean} = 45\,\text{deg}$. In total six different combinations of discretization for the reconstruction wave numbers and wave directions have been considered, out of the nine possible. For each selected combination, the number of harmonic components in the reconstruction model is $N_h = N_\kappa N_\theta$. A set of 50 Monte Carlo simulations have been generated in order to assess the performance of the different reconstruction strategies. To this end, similarly to the case of long crested waves, the normalized mean and standard deviation of the reconstruction error, as well as the Pearson's correlation coefficient between the true and the reconstructed wave elevation, have been estimated from the synthetic data. For this application example, the reconstruction of the wave elevation has been calculated only at one time instants for each Monte Carlo sample.

Figure 3.19 reports the normalized standard deviation of the reconstruction error, $\hat{\sigma}_\epsilon / H_s$, for the considered six different wave model discretization strategies. Moving from left to right of Figure 3.19, it is possible to appreciate the influence of the wave number discretization on the reconstruction error. As the discretization in the wave numbers gets finer, the inversion of the wave radar signal exhibits better reconstruction performance. On the other hand, refining the reconstruction model accounting for more wave directions (from top to bottom in Figure 3.19) does not provide significant benefits, particularly for small values of N_κ, i.e. for reconstruction models characterised by a more limited number of wave lengths. However, in all the cases, at the boundary of the reconstruction domain, $\hat{\sigma}_\epsilon / H_s$ shows larger values, especially in correspondence of a direction normal the main propagation direction of incoming waves. This appears to be a feature common to all considered wave reconstruction models, and it is in part related to the fact that the sea waves imaged at an azimuth normal to the main propagation direction of the incoming waves contribute less to the radar signal tilt modulation. The general outcome from the analysis of the reconstruction error standard deviation is confirmed, from a qualitative point of view, by Figure 3.20, where the Pearson's correlation coefficient, c_r, between the true wave elevation and the reconstructed wave elevation is reported. In fact, the maps of c_r show larger correlation values when the discretization of the reconstruction wave numbers gets finer, while negligible benefits are observed from a better discretization of the wave components directions. The edge effects are clearly visible at the boundary of the reconstruction domain where the correlation coefficient visibly drops. For sake of completeness, the normalized mean of the reconstruction error, $\hat{\mu}_\epsilon / H_s$, is reported in

Figure 3.21. In contrast to what is done for the 1D cases, for the 2D cases the wave numbers adopted for the reconstruction have been limited to those corresponding to the wave length comprised between $20m = \lambda_{w,min} \le \lambda_{w,n} \le 500m = \lambda_{w,max}$ This results in filtering out the low frequency contribution to $\hat{\mu}_\epsilon / H_s$. The effect can be noted comparing Figure 3.21, 2D short crested sea case, with Figure 3.7, 1D long crested sea case. Three instructive example reconstructions are reported in Figure 3.22, Figure 3.23 and Figure 3.24. Each figure is associated with a different azimuth angle, namely: $\beta = 45\,\mathrm{deg}$ (collinear with the main propagation direction of incoming waves - Figure 3.22), $\beta = 90\,\mathrm{deg}$ (at 45deg from the main propagation direction of incoming waves - Figure 3.23), and $\beta = 135\,\mathrm{deg}$ (orthogonal to the main propagation direction of incoming waves - Figure 3.24). For each figure, reconstructions from two different discretization in wave number and direction domains are reported, namely: $\left(N_\kappa = 81, N_\theta = 31 \Rightarrow N_h = 2511\right)$ and $\left(N_\kappa = 161, N_\theta = 61 \Rightarrow N_h = 9821\right)$. In addition, the "true" wave elevation is reported as reference target. It can be seen that the reconstruction is better for $\beta = 45\,\mathrm{deg}$ and $\beta = 90\,\mathrm{deg}$, for which an increased discretization for the reconstruction model leads to a visible improvement of the reconstruction. Instead, the reconstruction for $\beta = 135\,\mathrm{deg}$ is very poor and the increase in the discretization of the reconstruction model leads to very minor improvements.

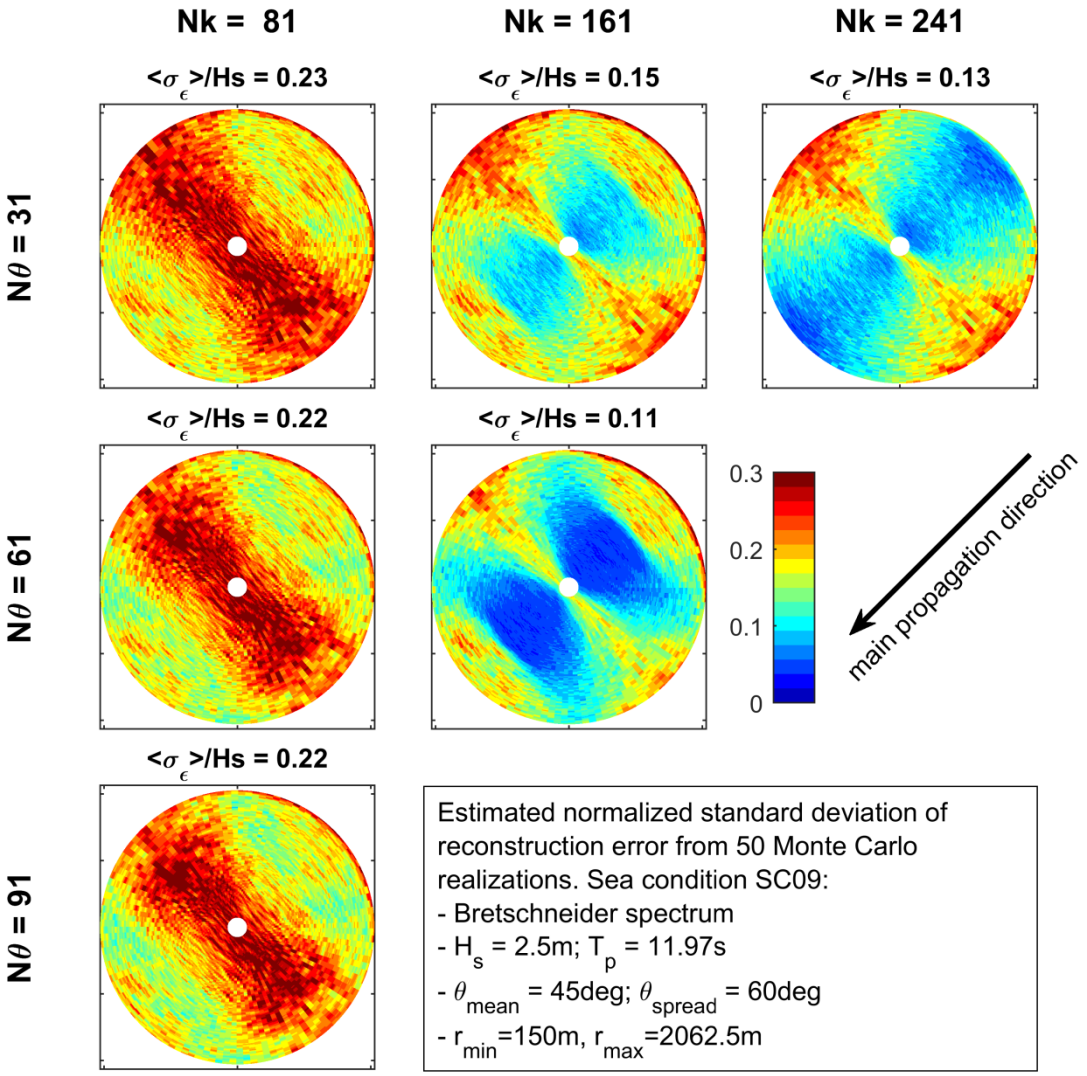

Figure 3.19: Normalized standard deviation of the reconstruction error, as estimated from 50 Monte Carlo simulations. Different reconstruction wave models are organized in a grid. The discretization in wave numbers increases from left to right, while the discretization in wave directions increases from top to bottom. The space averaged value is reported above each plot. Sea condition SC09 (see Table 3.1). Antenna at $r = 0m$ and $Z_a = 30m$. Reconstruction strategy: backward time window with length $\Delta_\tau = 12s\,(N_\tau = 8)$.

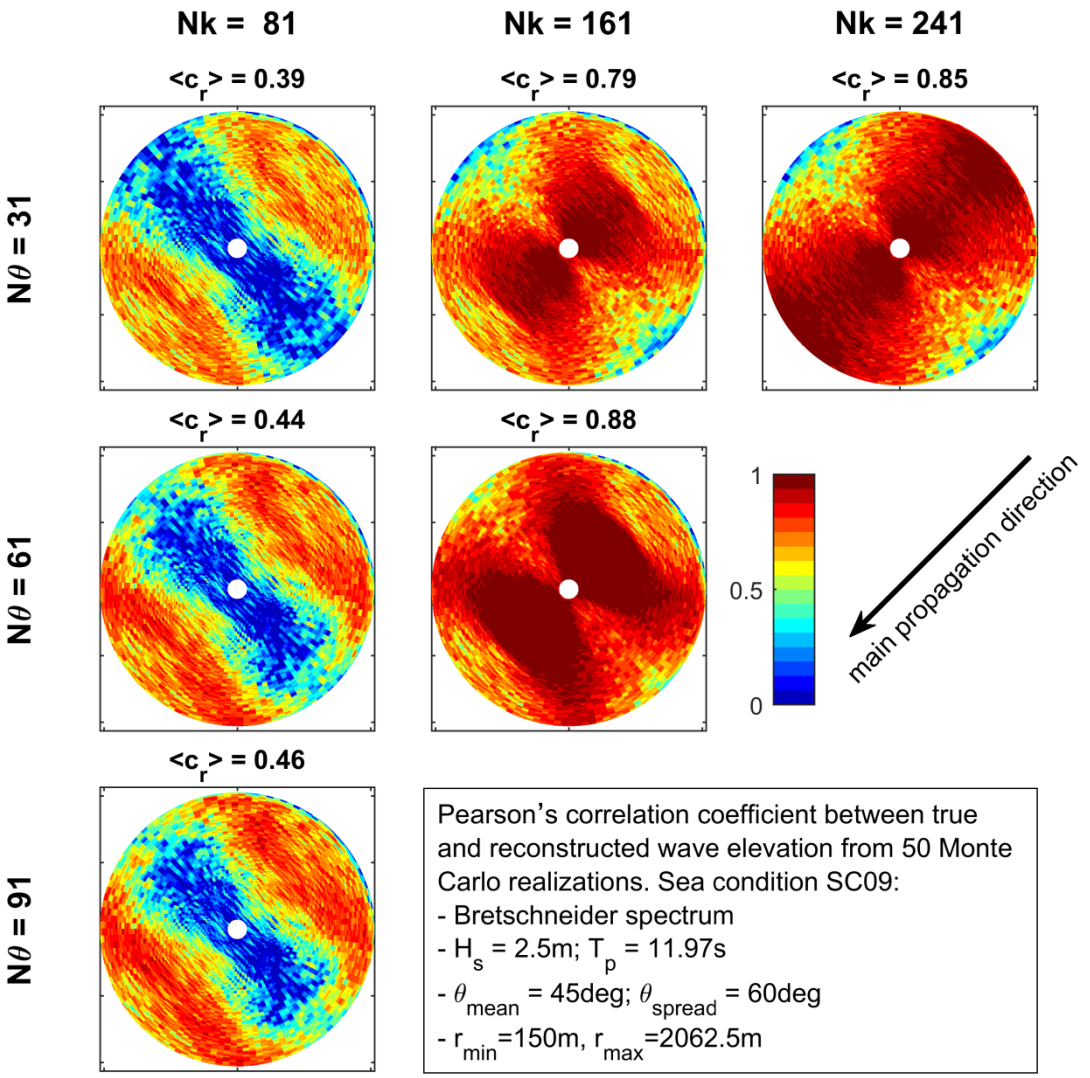

Figure 3.20: Pearson's correlation coefficient between true and reconstructed wave elevation, as estimated from 50 Monte Carlo simulations. Different reconstruction wave models are organized in a grid. The discretization in wave numbers increases from left to right, while the discretization in wave directions increases from top to bottom. The space averaged value is reported above each plot. Sea condition SC09 (see Table 3.1). Antenna at $r = 0m$ and $Z_a = 30m$. Reconstruction strategy: backward time window with length $\Delta_\tau = 12s\,(N_\tau = 8)$.

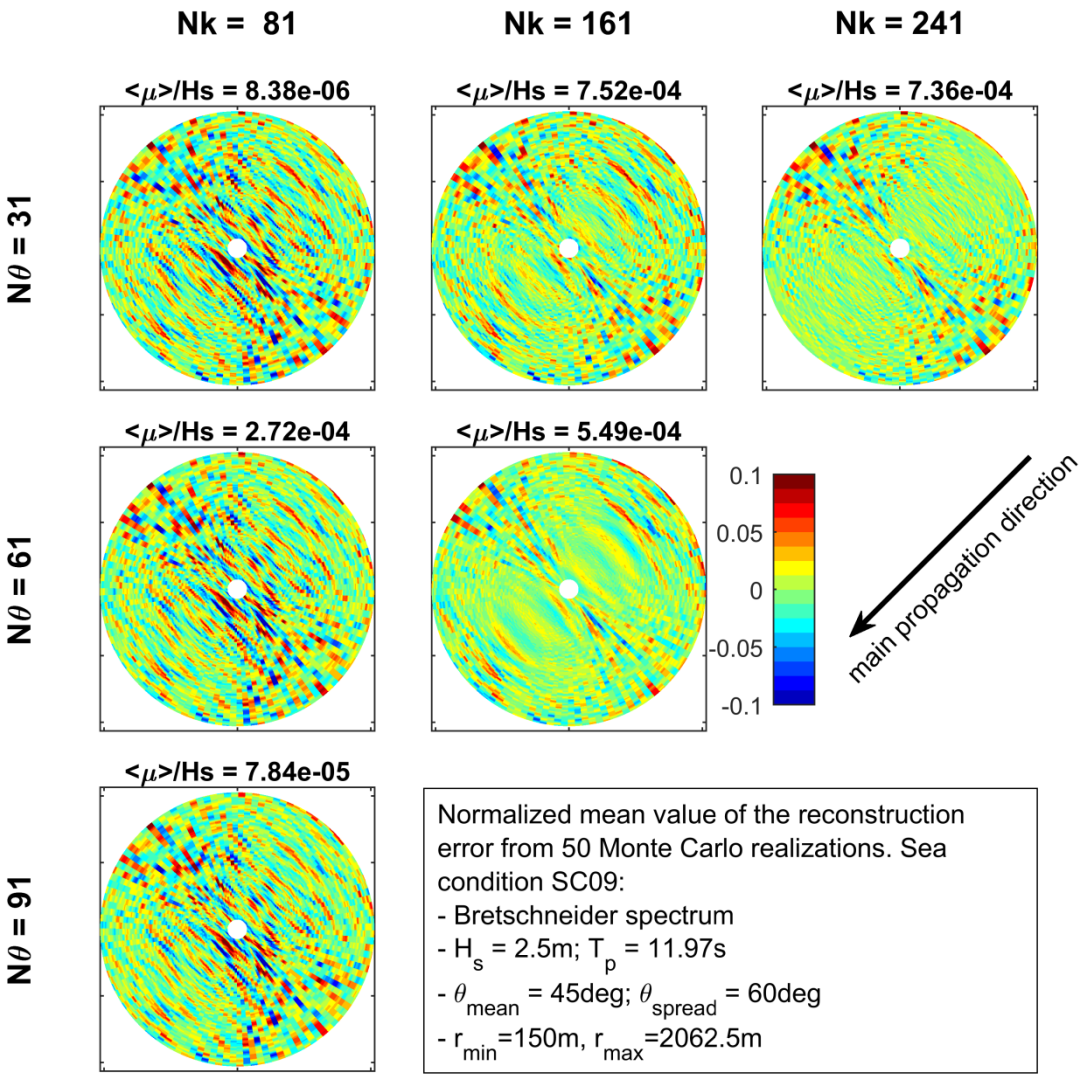

Figure 3.21: Normalized mean value of the reconstruction error, as estimated from 50 Monte Carlo simulations. Different reconstruction wave models are organized in a grid. The discretization in wave numbers increases from left to right, while the discretization in wave directions increases from top to bottom. The space averaged value is reported above each plot. Sea condition SC09 (see Table 3.1). Antenna at $r = 0m$ and $Z_a = 30m$. Reconstruction strategy: backward time window with length $\Delta_\tau = 12s\,(N_\tau = 8)$.

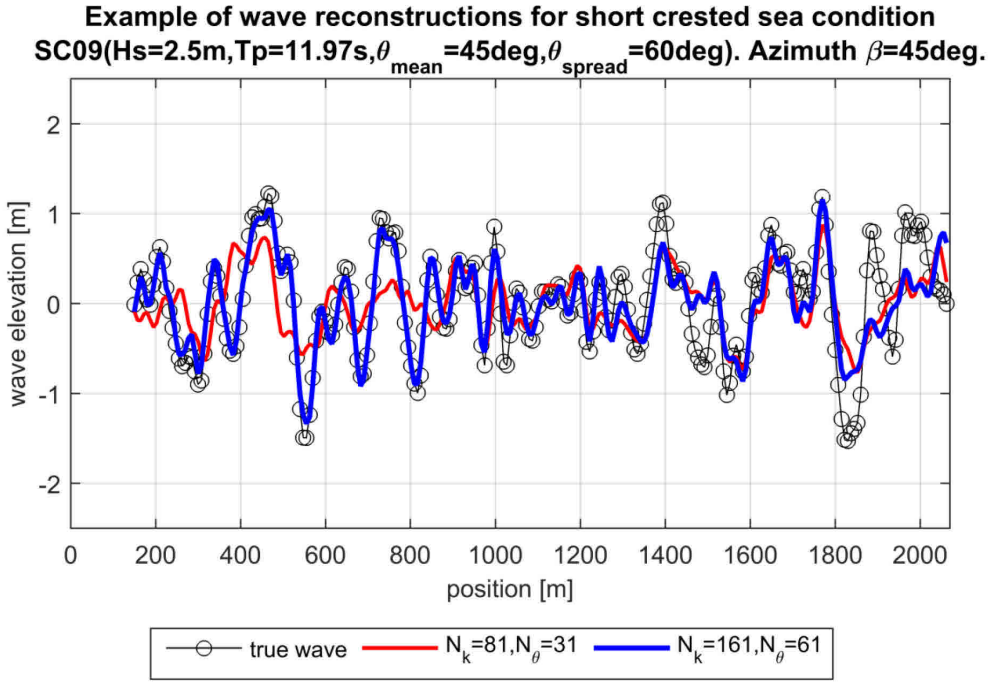

Figure 3.22: Example of wave reconstruction from synthetic radar images using the LSQR inversion method in case of short crested sea condition SC09 (see Table 3.1), with mean propagation direction $\theta_{mean} = 45\,\text{deg}$ and spreading angle $\theta_{spread} = 60\,\text{deg}$ The reconstruction is performed at the azimuth $\beta = 45\,\text{deg}$, considering two different wave models: $(N_\kappa = 81, N_\theta = 31)$ and $(N_\kappa = 161, N_\theta = 61)$. Reconstruction strategy: backward time window with length $\Delta_\tau = 12s\,(N_\tau = 8)$.

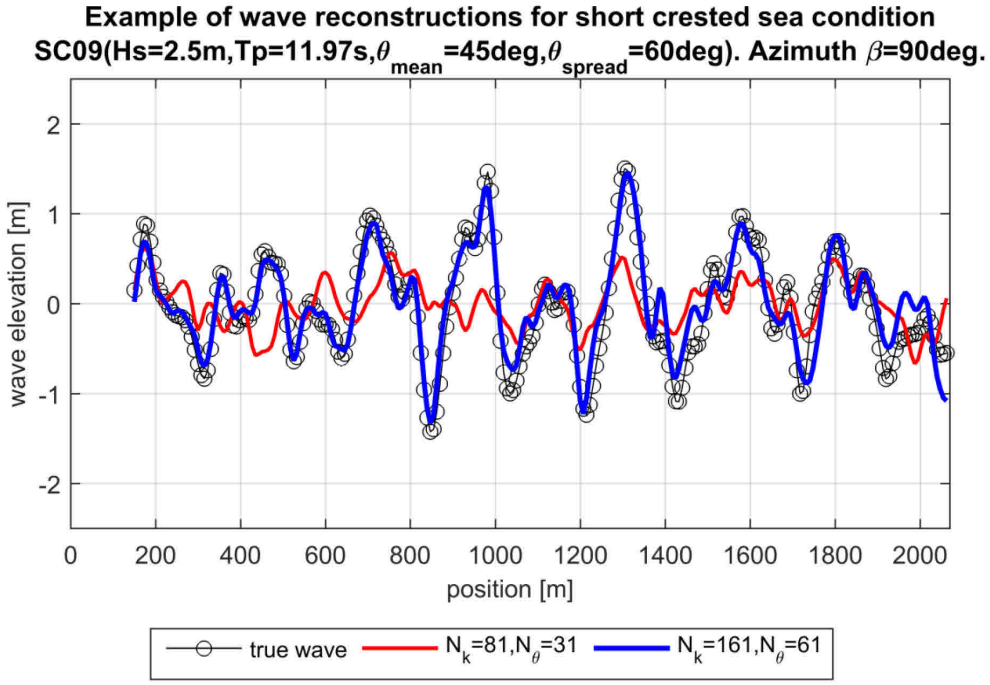

Figure 3.23: Example of wave reconstruction from synthetic radar images using the LSQR inversion method in case of short crested sea condition SC09 (see Table 3.1), with mean propagation direction $\theta_{mean} = 45\,\text{deg}$ and spreading angle $\theta_{spread} = 60\,\text{deg}$ The reconstruction is performed at the azimuth $\beta = 90\,\text{deg}$, considering two different wave models: $(N_\kappa = 81, N_\theta = 31)$ and $(N_\kappa = 161, N_\theta = 61)$. Reconstruction strategy: backward time window with length $\Delta_\tau = 12s\,(N_\tau = 8)$.

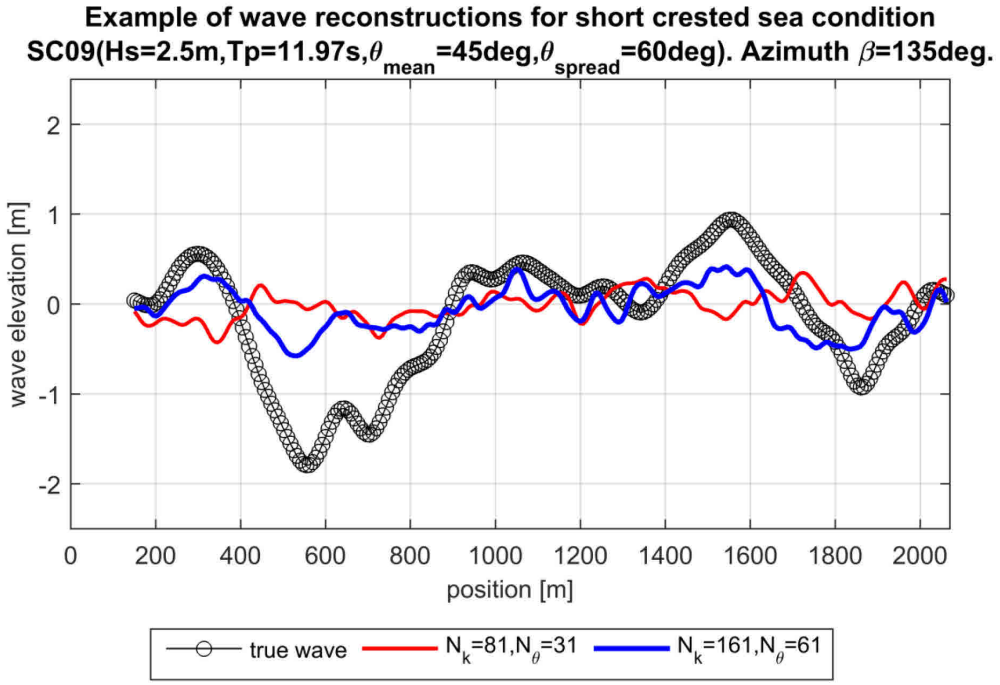

Figure 3.24: Example of wave reconstruction from synthetic radar images using the LSQR inversion method in case of short crested sea condition SC09 (see Table 3.1), with mean propagation direction $\theta_{mean} = 45\,\text{deg}$ and spreading angle $\theta_{spread} = 60\,\text{deg}$ The reconstruction is performed at the azimuth $\beta = 135\,\text{deg}$, considering two different wave models: $(N_\kappa = 81, N_\theta = 31)$ and $(N_\kappa = 161, N_\theta = 61)$. Reconstruction strategy: backward time window with length $\Delta_\tau = 12s\,(N_\tau = 8)$.

Results presented in Figure 3.19, Figure 3.20 and Figure 3.21, clearly indicate that the quality of the reconstruction depends on the considered underlying reconstruction wave model. In particular, the more the number N_h of wave components used in the reconstruction wave model is increased (particularly in terms of wave numbers), the better are the reconstruction performance. However, increasing the number of wave component considered for in the reconstruction model significantly increases the computational time. A possible solution to overcome this bottleneck is to reduce the number of radar images taken into account, for example, limiting the reconstruction region to a particular a sector of the wave field. In fact, it can be expected that less wave components can be required to guarantee the LSQR surface fitting the sufficient flexibility to adapt to real data, if the reconstruction domain is reduced. Moreover, because of the way the reconstruction strategies is defined, the number of radar data M taken into account is always much larger than the reconstruction frequencies adopted in the model. This makes the matrix $\mathbf{A}$ a thin matrix for which $N << M$. Since the computational cost of the SVD is $11N^3 + 2MN^2$ (according to Golub and Van Loan [58]) reducing the number of radar data used in the reconstruction, keeping N fixed, linearly reduces the computational effort.

Starting from the above considerations, a possible strategy to reduce the computational bottleneck due to the SVD decomposition in the LSQR approach, could then be to reduce the number of harmonic components in the reconstruction model and, at the same time, to reduce also the region from which wave radar data are retrieved and for which the wave reconstruction is carried out. The sub-region of the radar domain can be identified, for instance, as a sector $\beta_{min} \le \beta \le \beta_{max}$ (see Figure 3.5). In the previously presented results, the full radar domain was selected ($\beta_{min} = 0\,\text{deg} \le \beta \le \beta_{max} = 360\,\text{deg}$). As an alternative, the limitation of the reconstruction to, and the retrieval of the data from, the range $\beta_{min} = 0\,\text{deg} \le \beta \le \beta_{max} = 90\,\text{deg}$ is now considered.

Figure 3.22 and Figure 3.23 present $\hat{\sigma}_\epsilon / H_s$ and c_r calculated accounting only for the radar images in the interval $0\,\text{deg} \le \beta \le 90\,\text{deg}$. The rest of the inversion strategy is the same as for the case using data from $0\,\text{deg} \le \beta \le 360\,\text{deg}$. Results are compared with the previous application of the LSQR, already presented in Figure 3.19 and Figure 3.20, in terms of $\hat{\sigma}_\epsilon / H_s$ and c_r, respectively. The comparison is carried out only for the azimuth angles $0 \le \beta \le 90\,\text{deg}$, where the reconstruction of the reduced model is expected to be applicable. It can be noted that, for a fixed discretization of the reconstruction wave model, much better reconstruction performances are obtained from the reconstruction based on the reduced region of azimuth angles, both for the standard deviation of the reconstruction error (Figure 3.25) and for the Pearson's correlation coefficient (Figure 3.26). The suggested adaptation/reduction of the LSQR approach achieves much better reconstruction performances also in terms of computational time. This, however, comes at the cost of a contraction of the reconstruction domain.

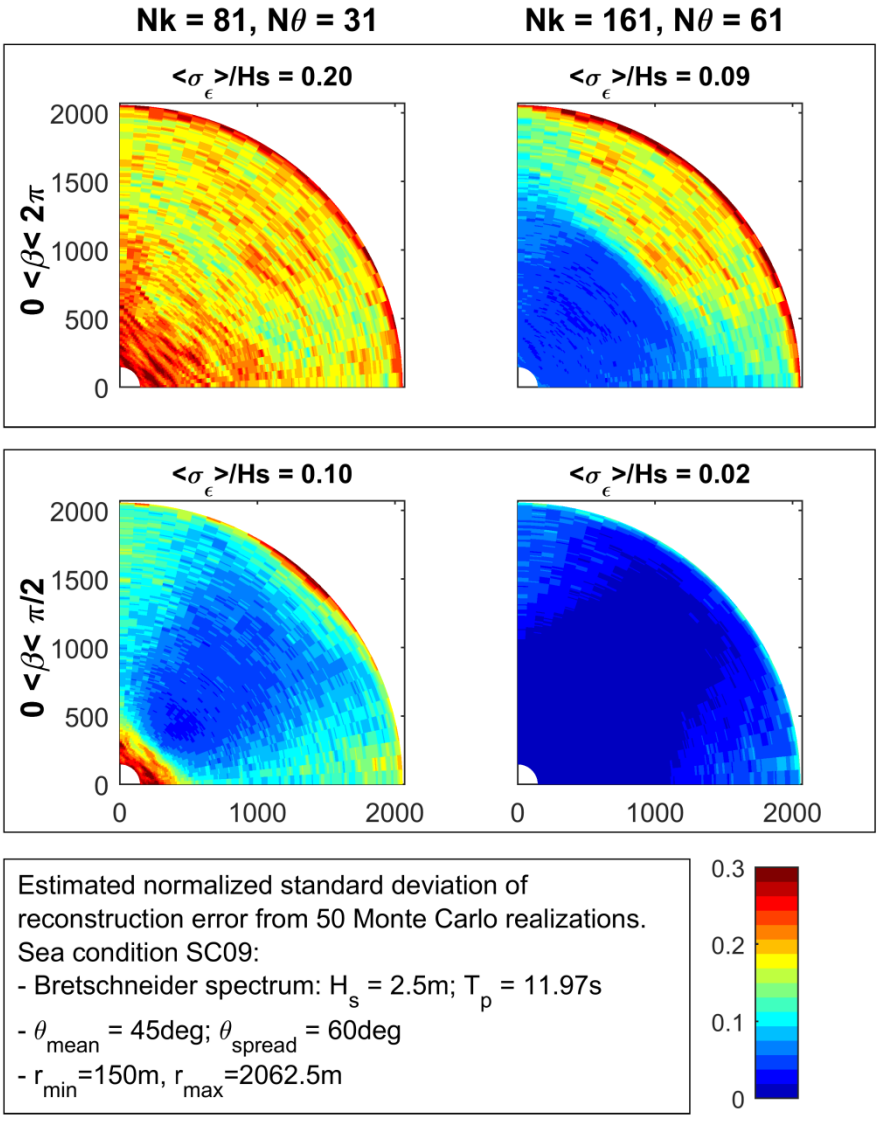

Figure 3.25: Normalized standard deviation of the reconstruction error, as estimated from 50 Monte Carlo simulations. Reconstruction strategies using data from different azimuth regions: $0\,\text{deg} \le \beta \le 360\,\text{deg}$ (top) and $0\,\text{deg} \le \beta \le 90\,\text{deg}$ (bottom). Two different wave model discretization are reported, one for each column: coarse model (left) and fine model (right). The space averaged value is reported above each plot. Sea condition SC09 (see Table 3.1). Antenna at $r = 0m$ and $Z_a = 30m$. Reconstruction strategy: backward time window with length $\Delta_\tau = 12s\,(N_\tau = 8)$.

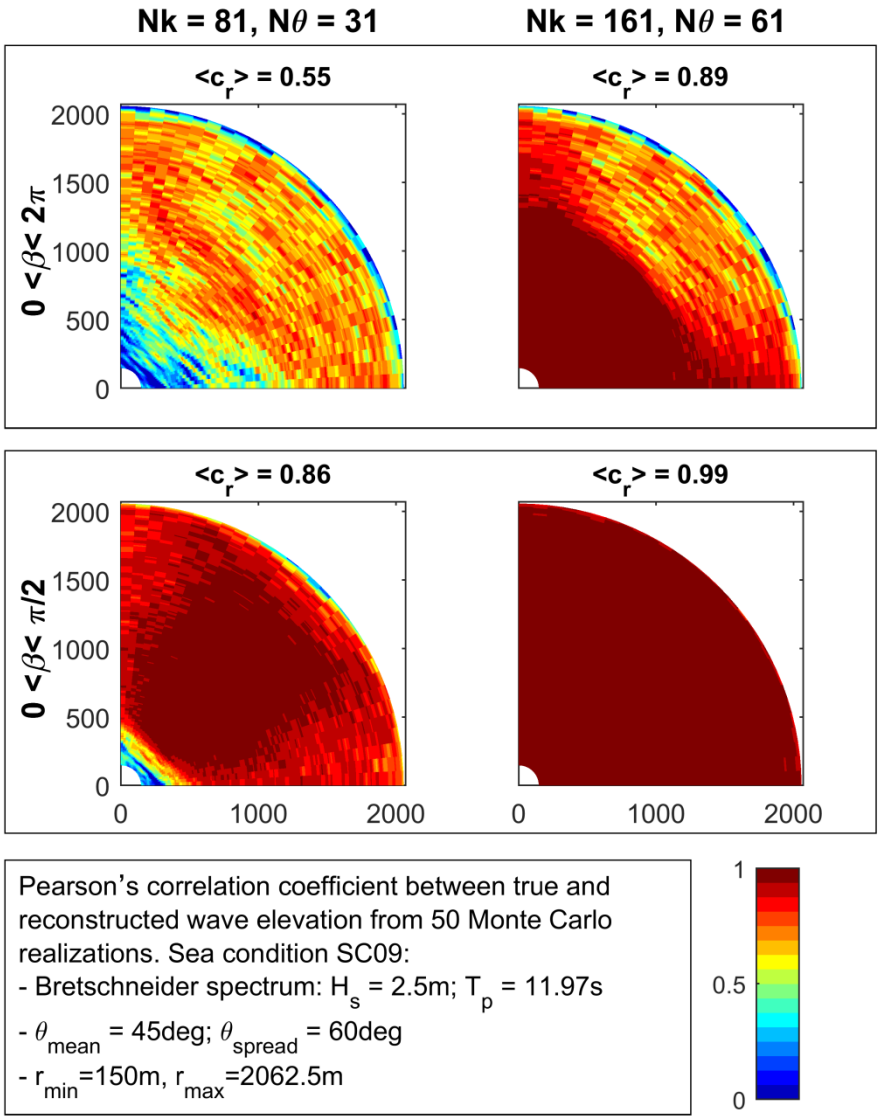

Figure 3.26: Pearson's correlation coefficient between true and reconstructed wave elevation, as estimated from 50 Monte Carlo simulations. Reconstruction strategies using data from different azimuth regions: $0\,\mathrm{deg} \le \beta \le 360\,\mathrm{deg}$ (top) and $0\,\mathrm{deg} \le \beta \le 90\,\mathrm{deg}$ (bottom). Two different wave model discretization are reported, one for each column: coarse model (left) and fine model (right). The space averaged value is reported above each plot. Sea condition SC09 (see Table 3.1). Antenna at $r = 0m$ and $Z_a = 30m$. Reconstruction strategy: backward time window with length $\Delta_\tau = 12s\,(N_\tau = 8)$.

3.7 Concluding remarks

In this chapter an approach for the inversion of wave radar images has been proposed. The method presents element of novelties with respect to prevailing techniques, in the way the inversion process is setup and regarding the way the shadowing effect is addressed. The core of the proposed procedure is based on the setup of a linear least squares inversion problem which is based on the linearization of the optical/geometrical model of the wave radar mechanism, combined with the assumption of linear (first-order) underlying wave field. The proposed approach, referred to as Least SQuares with Regularization (LSQR), is aimed at providing the reconstruction of the wave elevation starting from wave radar signals, considering the shadowing effect as a loss of information, and therefore disregarding shadowed region in azimuth/time and radial direction. This is an alternative way of dealing with the shadowing phenomenon compared to existing techniques, such as, e.g., the most common MTF approach, where

shadowed regions of the field are kept in the processing. In order to provide the proposed inversion method with a self-tuning capability, the solution of the inversion problem is sought by means of a Tikhonov regularization procedure, where the regularization parameter is automatically determined by means of the L-Curve approach. In this phase of the development, straightforward implementation and robustness of the algorithm have been preferred over computational performances. As a result, the presented implementation was based on the adoption a well-established, although computationally expensive, SVD decomposition.

The theoretical background of the methodology has been described in details, both regarding the employed model of wave radar, as well as the inversion procedure. The LSQR reconstruction performances have then been tested through the inversion of synthetically generated radar images, considering both the cases of long crested and short crested seas. The reconstruction error has been analysed as a stochastic process. Attention has been given, in the analysis, to its mean, standard deviation and covariance, which have been estimated from Monte Carlo simulations. In case of long crested seas, an extensive analysis has been carried out on a series of different sea conditions, indicating that the performances of the LSQR technique strongly depend on selected inversion strategy. In general the LSQR was capable of reconstructing the sea surface elevation with small, and in some cases very small, standard deviations of the reconstruction error in the central region of the reconstruction radar domain. However, edge effects have been observed, with the performances deteriorating at boundaries of the reconstruction domain. Nonetheless, the way the LSQR approach deals with the shadowing effect seems to allow acceptable reconstruction performance also in case of synthetic radar data deeply affected by shadowing. This is likely a consequence of the fact that, with respect to the presently available inversion techniques, whereby the shadowing effect are often disregarded or cured with *a-posteriori* corrections, the LSQR approach naturally overcomes the shadowing effect by compensating for the lack of spatial data with additional samples taken in time/azimuth domain. This compensation is possible thanks to the flexibility of the problem setup. The detailed analysis of the reconstruction error process has shown, in general, that while the process is stationary as a consequence of the assumed stationarity of the underlying wave field, there is a spatial non-uniformity of all the analysed statistical quantities. The spatial non-uniformity was more visible in cases with poor reconstruction performances and in the tested short crested sea case. The systematic characterization of the reconstruction error is a seldom addressed matter and this chapter has therefore tried to provide the LSQR regularization method with detailed information in this respect. In fact, the knowledge of the statistical characteristics of the inversion error process can potentially be fed to deterministic sea wave prediction (DSWP) methodologies, when these latter are able to provide the prediction along with an associated confidence bound accounting also for wave measurement error. In case of wave radars, in fact, the “measurement error” is represented by the reconstruction error. Finally, the reconstruction of radar images generated from nonlinear wave fields has been tested and though the inherent linearity assumption of the LSQR results in worst performance compared to the case of linear wave fields, the differences are limited to the higher significant wave height sea conditions. This confirms that the linearity assumption of the LSQR model are adequate in dealing with most of the sea condition, or at least with the ones that are of practical interest in the case of shipborne wave radars.

The main drawback of the proposed LSQR method is, however, its large computational cost, especially when finely resolved reconstruction models are necessary, as it is the case for realistic short crested seas. In this respect, the presented implementation has

shown its limitations, preventing the method to be adopted for realistic real time applications. Still, the LSQR method can be used as an off-line reconstruction procedure, for testing or analysis purposes. However, further analysis of the inversion problem and of the regularization step, for example resorting to more efficient regularized least squares techniques, could possibly open the door to improvements in the computational performances. Another limitation of the LSQR method, which is however in practice shared with other prevailing inversion techniques, is the assumption of linearity for the underlying wave field. In this respect, it is conceivable an extension of the LSQR method to the reconstruction of nonlinear wave fields, at least for the retrieval of some prominent nonlinear features. In fact, a step forward in this direction could be undertaken by dropping the linearity assumption about the reconstruction wave field assuming, for example, a weakly nonlinear wave model for the definition of the inversion problem. However, this would imply a change of paradigm in the inversion procedure, abandoning the direct linear least squares inversion techniques used herein, for different, more suited and likely more complex algorithms. Nonetheless, a technique capable to consistently retrieve wave nonlinear features from radar measurements could indeed be considered as a substantial step forward in the framework of deterministic wave elevation reconstruction from wave radar images, and it is worth being pursued in further researches. Finally, is must be underlined that tests carried out herein have all been based on synthetically generate wave radar images. Although this approach can provide relevant indications at a proof of concept stage, testing on real wave radar images is necessary in order to fully understand the potentiality of the proposed approach.

4 DETERMINISTIC SEA WAVE FORECASTING AND PREDICTION ERROR ASSESSMENT

In this chapter a semi-analytical methodology for the determination of prediction error statistics associated with a class of Deterministic Sea Wave Prediction (DSWP) methods is presented. The wave elevation is modelled as a Gaussian stochastic process and the fitting/propagation model is assumed to be a linear. The possible additional sources of error linked, for instance, to the measurement uncertainties, are explicitly taken into account in the formulation. The resulting approach provides a Linear Estimator of Prediction Error (LEPrE), which associate an assessment of the standard deviation of the prediction error to the fitting procedure assumed for the DSWP, taking into account the actual sea spectrum characteristics. The presented approach is able to complement the phase-resolved deterministic predictions methods with a sound prediction error measure, and redefines the concept of "Predictability Region" in a consistent probabilistic framework. Example applications are reported, both for long crested and short crested waves, with verification through Monte Carlo simulations. Single point wave gauge/wave buoy measurements as well as spatial extent wave radar measurements have been considered. The developed methodology is also compared with existing approaches highlighting and discussing both the differences and the interesting qualitative commonalities. Then, the performances of the LEPrE method are assessed in the case of the prediction of linear and nonlinear long crested waves. In addition, an application of the model, accounting also for the reconstruction error induced by the wave radar inversion process, is tested. Eventually, a case of linear short crested sea is reported.

4.1 Introduction

The nowadays interest about deterministic wave propagation models is justified in light of the developing capabilities of the marine wave radar technology in providing for deterministic reconstruction of the sea surface. Indeed, wave radar and phase-resolved wave models, considered as a whole, could possibly have a beneficial impact for the safety and operability at sea. For short-term wave forecasting technology (with temporal horizon of the order of minutes, and spatial horizon of the order of hundreds meters) it is of crucial importance to be in the position of relying on large scale and instantaneous sea surface measurements. Although, LIDAR technology seems to have the requested accuracy in time and space (Belmont et al. [11]; Nouguier et al. [109]) it results to be inadequate because of the too narrow imaging capability. Marine wave radars represents a more suitable device, since they are capable of scanning large areas (in the order of kilometres) with a satisfactory temporal resolution (of the order of the second) (Dankert and Rosenthal [35]; Nieto Borge et al. [105]; Serafino et al. [128]; Naaijen and Wijaya [104]).

Phase-resolved wave propagation procedures are typically based on two main steps: a *fitting step (FS)*, in which the phase-resolved sea surface measurements are fitted to a wave model, and a *propagation step (PS)*, in which the wave model, initialized by the fitting, propagates the information to the required region of space and time. The key aspects for the wave forecasting procedures to be successfully applied to real time application are the computational performances, in dealing with the *FS/PS* steps, and the accuracy in modelling the wave field evolution. In general, linear deterministic wave propagation models are preferred because of the performances of the *FS/PS* procedures and the satisfactory accuracy in modelling the most relevant wave field features in the typical time and spaces horizon of a DSWP application (Hilmer and Thornhill [68]). Different aspects of their implementation have been investigated in the past (Belmont et al. [9][10]; Blondel-Couprie and Naaijen [17]; Connell et al. [33]; Naaijen and Blondel-Couprie[97]; Naaijen et al. [102]; Naaijen and Huijsmans [99]). Usually, in the case of linear models, the *FS* of the wave elevation data is carried out in the measurement domain (time and/or space) by means of Fourier decomposition techniques, either based on the DFT(FFT) (Morris et al. [96]; Naaijen and Blondel-Couprie [97]) or on a least-squares approach (Connell et al. [33]; Naaijen et al. [103]; Vettor [146]). Afterwards, for the *PS*, linear wave models are used. Also in this case, the adoption of FFT techniques is very convenient from a computational cost point of view. An extensive discussion about the adaptation of the FFT techniques to short crested sea applications is presented in Blondel-Couprie and Naaijen [17] and Naaijen and Blondel-Couprie [97]. Different implementations of linear fitting and propagation procedures have also been proposed by, e.g., Abusedra and Belmont [1] and Belmont et al. [10].

In the framework of DSWP applications, the possible use of nonlinear wave propagation models is justified in the light of a more accurate modelling of the water wave field and the possibility to better account for its dynamics. Although steps in this direction have been proposed by several authors (e.g. Blondel-Couprie et al. [15]; Wu [159]; Yoon et al. [166]), still the inherent complexity of the *FS* from measured data represents a serious bottleneck for the application of nonlinear wave models. For example, the wave elevation data provided by wave radar devices, due to the typical assumption in the radar inversion techniques (see §3), generally lacks of those nonlinear information which are needed for a correct initialization of a nonlinear propagation models. So, usually, the measured wave elevation data have to be pre-processed before being actually ready for the nonlinear propagation step. The complexity of the pre-processing step depends mainly on the nature of the available measurements and on the

considered nonlinear model. However, the general tendency is to resort to iterative procedures on the measured data or data assimilation procedures (e.g. Wu [159]; Blondel et al. [15]; Yoon et al. [166]; Aaragh and Nwogu [5]; Hassanaliaragh, 2009 [67]). A quite complete analysis on these data assimilation procedures can be found in the work of Blondel-Couprie [14].

Whether the DSWP is based on linear or nonlinear models, a common issue to all DSWP methods is related to the need of providing an estimation of the region where the deterministic prediction can be considered as reliable. In fact, any DSWP procedure is inevitably affected by prediction errors with respect to the true wave elevation. The limits of the DSWP procedures depend directly from the adopted propagation model but also on the way the fitting/propagation steps are carried out. In fact, both the inherent limitation of the propagation model and its matching with the measured data contribute to determine the final quality of the prediction. In addition to that, in real applications, the wave measurements are usually affected by measurement errors, which bring into the problem an additional source of uncertainty, an aspect which is often overlooked. This means that a key aspect of DSWP should be the capability of providing not only an estimation of the predicted wave elevation, but also some information regarding the prediction error. However, although the assessment of the prediction error is crucial for a consistent deterministic wave prediction, the problem is rarely addressed specifically. In this context, also the way this assessment is derived is of particular importance because inevitably subject to the same requirement, of readiness and accuracy, for suitable real time DSWP application. In fact, the option of resorting to brute force approaches, such as the massive use of Monte Carlo simulations, to estimate the expected prediction errors statistics is, in general, practically unfeasible. Therefore methods of faster and more direct application are required.

The most widespread concept related to the performances assessment of a DSWP application is the so-called “Predictability Region”. The Predictability Region is considered to be the region of space and time where it is considered “possible” to predict the wave elevation, ideally without errors. It is therefore, originally, a binary concept, which splits the time/space domain in a region where the prediction “is possible”, and a region where the prediction “is not possible”. In the past, a matter of discussion has been whether to use the group velocity or the phase velocity of the waves for the identification of the Predictability Region (e.g. Abusedra and Belmont [1]; Edgar et al. [45]; Morris et al. [96]; Naaijen et al. [102]; Wu [159]). According to Wu [159] (see also Naaijen et al. [102]), the Predictability Region is defined using the group velocity of the fastest and slowest wave components of the considered sea spectrum. This concept has been further developed by Wu [159] and Naaijen et al. [102] with the introduction of the “Predictability Indicator”: a continuous measure (defined in the interval [0,1]) of the prediction capability at a generic point in time and space, which is related to the assumed/measured sea spectrum. The Predictability Indicator takes into account the distribution of the wave energy content based on the shape of the wave spectrum, representing an advance with respect to the standard Predictability Region. Naaijen et al. [102] have also verified the Predictability Indicator method with respect to Monte Carlo simulations of different wave fitting and propagation applications, showing a qualitatively consistent matching. The encouraging results showed by Naaijen et al. [102] and the simple formulation of the method makes the Predictability Indicator an interesting tool for a more advanced, and potentially more precise, definition of Predictability Region compared to the original concept. However, the Predictability Indicator still lacks a consistent statistical background theory able to provide a clear probabilistic interpretation of the obtained quantitative values.

It is then useful to make a step forward in the definition of the concept of Predictability Region, with a view to more soundly account for the prediction error from a probabilistic perspective. To this end, a theoretical approach for providing a consistent probabilistic measure of prediction error for deterministic phase-resolved linear wave prediction models, is herein presented. The approach is based on the description of the sea as a Gaussian stationary stochastic process. The features of the fitting procedure and of the prediction model are naturally embedded in the formulation. Furthermore, the formulation takes into account, in an analytic way, the actual shape of the spectrum for long crested and short crested waves. On top of this, the proposed framework also allows taking consistently into account the possible presence of additional measurement noise.

The chapter is structured as follows. First, a brief review of the definition of the Predictability Region and Predictability Indicator is reported. Then, the theoretical background of the developed alternative methodology is presented, starting from the definition of the fitting model and then providing the definition of the prediction error as a stochastic process. The assessment of the ensemble variance of the error process leads to the natural definition of a Linear Estimator of Prediction Error (LEPrE), which accounts also for the possible contribution of measurement noise. Five different test cases are then developed, considering long crested and short crested sea states, to show how the LEPrE can be used in identifying the level of prediction error. Reported results are verified along with corresponding sets of Monte Carlo simulations. Eventually, some comparison with the classical (binary) Predictability Region and the Predictability Indicator by Wu [159] and Naaijen et al. [102] are also provided, in order to show how the presented LEPrE compares with existing approaches. The first application shows details of a comparison between LEPrE approach, Monte Carlo simulations, (binary) Predictability Region and Prediction Error Indicator for a simplified bimodal spectrum made of two separated band limited white noise regions. The second application is conceived to presents an ideal, though realistic, laboratory experiment where the measurement device, used for the propagation step, is affected by measurement noise. Other two long crested wave examples have been conceived to show how the LEPrE performs in predicting nonlinear wave fields and how to possibly include in the LEPrE formulation the additional error source induced by the wave radar inversion techniques. In the last application, the LEPrE methodology is applied to a more realistic scenario where an offshore structure is considered and the wave elevation, used for the propagation model, is assumed to be measured by means of a wave radar device.

4.2 Predictability Region and Predictability Error Indicator

In this section the Predictability Region and Predictability Indicator are presented recasting their definitions (already reported in Wu [159], Naaijen et al. [102]) in the case of a wave radar like application for long crested seas.

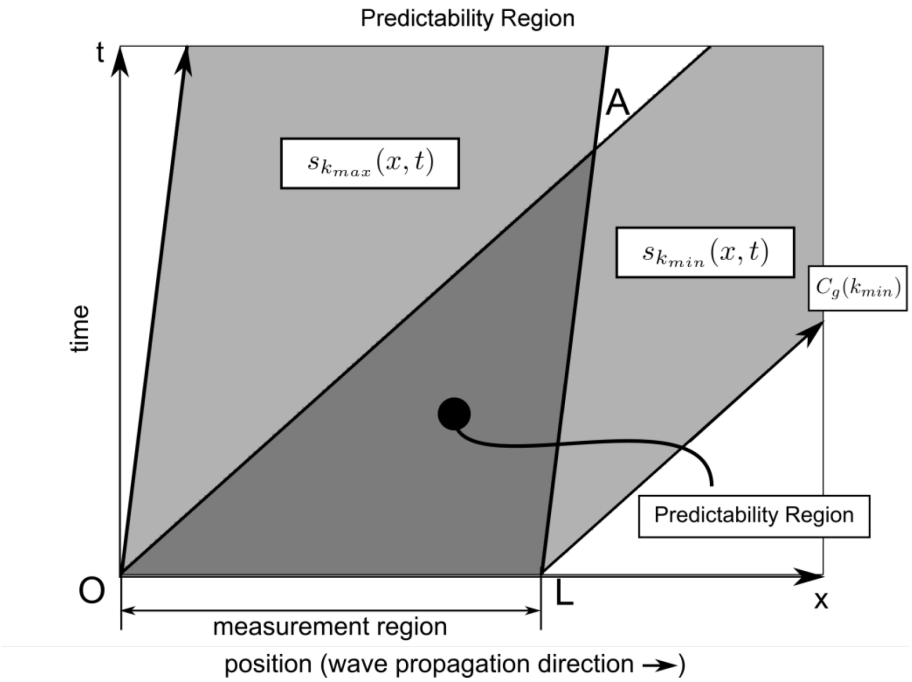

Figure 4.1:Scheme for the definition of the Predictability Region.

With reference to Figure 4.1, the wave radar is considered to image the sea surface at a time $t_0 = 0$ and on a space region defined by the interval OL as $x \in [x_O, x_L]$. Assuming two wave numbers k_{min} and k_{max} and their corresponding group speeds, the Predictability Region is defined as the space/time region for which:

$$x,t \geq 0 : \begin{cases} t \leq \dfrac{(x - x_O)}{C_g(k_{\min})} \\ t \geq \dfrac{(x - x_S)}{C_g(k_{max})} \end{cases} \tag{4.1}$$

The (x,t) region for which (5.1) holds is schematically presented in Figure 4.1, as a dark grey area identified by the triangle OLA.

An equivalent definition of the Predictability Region can now be introduced, which is relevant to the following discussion. The OLA region can be constructed as the intersection of two the plane strips $s_{k_i}(x,t)$ depending on the wave number, as defined as:

$$s_{k_i}(x,t) = \left\{ x,t : \left(t \leq \frac{(x - x_O)}{C_g(k_i)} \right) \wedge \left(t \geq \frac{(x - x_S)}{C_g(k_i)} \right) \right\} \tag{4.2}$$

The plane strips are reported as light grey areas Figure 4.1. Their intersection is actually the region $OLA = \left\{ x,t : s_{k_{min}} \cap s_{k_{max}} \right\}$, representing an equivalent definition of the Predictability Region. The Predictability Region is considered as the (x,t) region where it is possible to predict, ideally without errors, the wave elevation on the basis of the measurement taken in the measurement region OL. In fact, following the arguments proposed by Wu [159], if the energy content of the wave elevation field is considered

to be comprised within the wave number interval $k_{min} \le k \le k_{max}$ then the region where these two wave component can be propagated on the basis of the group speed completely identifies the region where the full information acquired in the measurement region OL can be used for carrying out the prediction. However, in the definition of the Predictability Region, there is no information about the relative importance of the energy associated to each wave components within k_{min} and k_{max}, with respect to the whole energy distribution.

A different and more advanced approach, that however shares many commonalities with the Predictability Region, is the Predictability Indicator, herein presented following Naaijen et al. [102].

The Predictability Indicator is a measure of the expected prediction performance based on the shape of the true wave elevation spectrum and it is defined as:

$$P(x,t) = \frac{\int_{k_{min}(x,t)}^{k_{max}(x,t)} S_\eta(k)dk}{\int_0^\infty S_\eta(k)dk} \tag{4.3}$$

where S_η is the wave elevation spectrum, the total energy is $E = \int_0^\infty S_\eta(k)dk$, and $k_{min} = k_{min}(x,t)$ and $k_{max} = k_{max}(x,t)$ are the integration limits of the numerator of (4.3) which depend on the point (x,t) considered. The interval over which the integral at the numerator of (4.3) is calculated depends on which of the wave components of the wave spectrum propagating from OL, and moving with the corresponding group velocity, can be considered to have actually reached the point (x,t). A simpler formulation of (4.3) can be obtained by assuming to discretize the wave spectrum energy as $E_j = S_\eta(k_j)\Delta k$ and introducing a discretized energy ratio for each wave number k_j as $e_j = E_j / E$. Then, by means of the definition of the plane strips (4.2), the following step valued function χ_s can be defined:

$$\chi_{s_j}(x,t \mid k_j) = \begin{cases} e_j \text{ if } (x,t) \in s_{k_j} \\ 0 \text{ otherwise} \end{cases} \tag{4.4}$$

In this way the Predictability Indicator can be defined, for every point (x,t), simply as the sum of χ_{s_j} over the wave numbers as:

$$P(x,t) = \sum_j \chi_{s_j}(x,t \mid k_j) \tag{4.5}$$

Equivalently to (4.3), equation (4.5) calculates the Predictability Indicator for each point (x,t) as the amount of wave energy of the spectrum over the total energy that actually "reaches" (at least from the point of view of information for the prediction) the prediction point (x,t). In the limit $\Delta k \to 0$, the two formulations (4.3) and (4.5) become equivalent.

The Prediction Error Indicator proposed originally by Wu [159] can be defined as a function of $P(x,t)$ as:

$$P_\epsilon(x,t) = \sqrt{1 - P(x,t)} \tag{4.6}$$

whereas Naaijen et al. [102] used in their work the value $P_\epsilon^2(x,t) = 1 - P(x,t)$. An example of calculation of the Prediction Error Indicator as presented in (4.6) is reported in Figure 4.2.

Following Wu [159], the idea underlying the Predictability Error Indicator is that for the points (x,t) for which $P_\epsilon(x,t) = 0$ the wave elevation should be perfectly predicted. Conversely, for the points (x,t) for which $P_\epsilon(x,t) = 1$, the wave elevation cannot be predicted on the basis of the measurement on OL. However, the intermediate values of $P_\epsilon(x,t)$, $0 < P_\epsilon(x,t) < 1$, are not provided with a clear interpretation that allows to use $P_\epsilon(x,t)$ as a quantitative indicator of the prediction error. Nonetheless, in this respect, Naaijen et al. [102] have shown the indicator $P_\epsilon^2(x,t)$ to be related, at least from practical point of view, to the variance of the prediction error calculated in the ensemble domain of Monte Carlo realizations, as $\dfrac{\mathrm{var}\left((\eta - \zeta)^2\right)}{2\sigma_\eta^{\,2}}$ where $\eta(x,t)$ is the true wave elevation and $\zeta(x,t)$ is the predicted wave elevation on the basis of the measurement data.

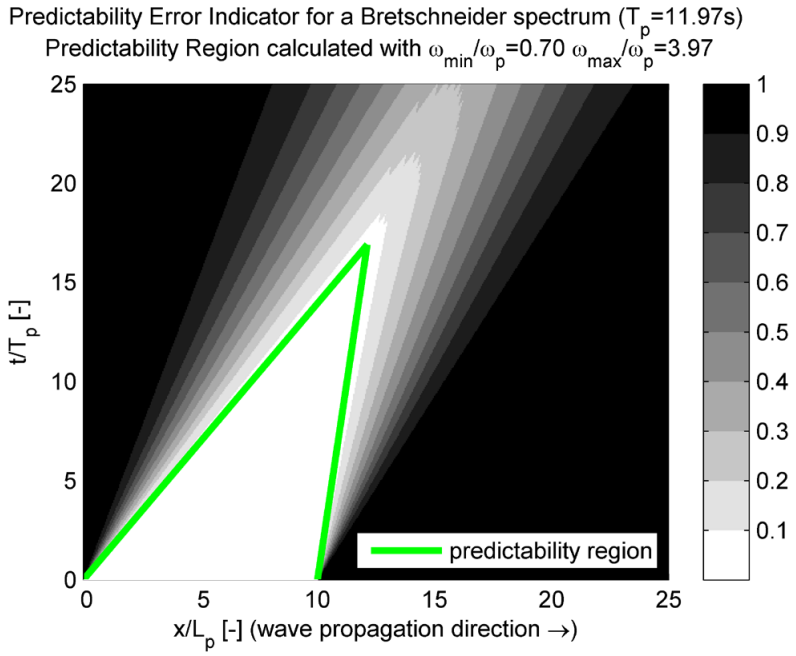

Figure 4.2: Prediction Error Indicator calculated for a Bretschneider sea spectrum ($T_p = 11.97s$). The Predictability Region is calculated based on the group velocity associated to the wave frequencies $\omega_{min} / \omega_p = 0.70$ and $\omega_{\max} / \omega_p = 3.97$.

The question arises, then, if a more formal indicator to assess the performance of a predictive model can be derived. In addition, it would be useful to have an indicator which avoids the debated a-priori assumption about the group velocity, as already discussed by Abusedra and Belmont [1]. In fact, although, in the case of an initial value problem on the wave elevation, the wave energy content of a wave packet can be seen

as propagating along the characteristic curves $\frac{x}{t} = C_g(\kappa)$ and the wave energy between any two of such lines remains constant (Witham [155]), it remains disputable if such energy arguments can be straightforwardly applied to fitting and propagation procedures typical of a DSWP applications, which are dealing with a stationary sea state. It seems to be more relevant, for the assessment of the prediction error, to account for the characteristics of the fitting of the wave elevation signal $\eta(x,t)$ through the propagation model, $\zeta(x,t)$. This is an aspect which often represents the core point of the DSWP application, but which not directly addressed by the Prediction Region and Predictability Indicator. To this end, in the next section, an alternative prediction error model is presented.

4.3 Linear Estimator of Prediction Error (LEPrE)

In order to face the gap identified in the assessment of a sound measure of the prediction error, a more consistent probabilistic approach has been developed. The *FS/PS* steps of a linear DSWP application has been redefined in a probabilistic framework. The main assumption is the description of the sea as a Gaussian stationary stochastic process. On this basis, the fitting and propagation procedures, herein assumed as linear, represent a linear transformation of Gaussian random variables. Consequently, the derived formulation embeds naturally the fitting and propagation models adopted for the DSWP, eventually accounting, in a consistent way, also for the actual shape of the wave spectrum. The result is a semi-analytical methodology for the estimation of the prediction error that is valid for generic linear fitting procedures. The developed framework is general and applicable to both long crested and short crested waves, with and without presence of measurement noise. More specific applications are reported in the application section. Preliminary results by the application of the proposed methodology for the long crested (1D) case in absence of measurement noise and using a Fourier fitting have been reported by Fucile et al. [53].

4.3.1 Theoretical Background

It is firstly assumed that the true wave elevation field $\eta(\underline{x},t)$ is a stationary Gaussian process for which a single generic realization can be represented as follows:

$$\begin{cases} \eta(\underline{x},t) = \sum_{i=1}^{N_\eta} a_i \cos(\underline{k}_i \cdot \underline{x} - \omega_i t) + b_i \sin(\underline{k}_i \cdot \underline{x} - \omega_i t) = \underline{p}_\eta(\underline{x},t)\underline{\alpha} \\ \underline{p}_\eta(\underline{x},t) = \left(\cos(\underline{k}_1 \cdot \underline{x} - \omega_1 t), \sin(\underline{k}_1 \cdot \underline{x} - \omega_1 t), ..., \cos\left(\underline{k}_{N_\eta} \cdot \underline{x} - \omega_{N_\eta} t\right), \sin\left(\underline{k}_{N_\eta} \cdot \underline{x} - \omega_{N_\eta} t\right)\right) \\ \underline{\alpha} = \left(a_1, b_1, ..., a_{N_\eta}, b_{N_\eta}\right)^T \\ \underline{p}_\eta(\underline{x},t) \in \mathbb{R}^{1,2N_\eta}; \underline{\alpha} \in \mathbb{R}^{2N_\eta,1} \end{cases} \tag{4.7}$$

In the expression for the wave elevation $\eta(\underline{x},t)$, $\underline{k}_i = \left(k_x, k_y\right)^T$ is the wave number vector for the i-th harmonic component, which is linked to the wave frequency ω_i by a suitable dispersion relation. In the case of linear waves and infinite water depth $\omega_i = \sqrt{g\|\underline{k}_i\|}$. The space and time dependent vector $\underline{p}_\eta(\underline{x},t)$ can be referred as the

"propagator vector" for η (see also Connell et al. [33]) since it propagates the wave elevation field in time and space if the coefficients vector $\underline{\alpha}$ is known. In (4.7) a finite, but sufficiently large, number of harmonic components, N_η, is considered, while the actual stochastic process is in principle recovered in the limit $N_\eta \to \infty$. It is also assumed that $\eta\left(\underline{x},t\right)$ can be measured at certain points in space ($\underline{x} \in \mathbb{R}^{2,1}$) and/or time ($t \in \mathbb{R}$), and that the measured wave elevation $\eta_M\left(\underline{x},t\right)$ is associated with a certain measurement error δ_η, i.e.:

$$\eta_M\left(\underline{x},t\right) = \eta\left(\underline{x},t\right) + \delta_\eta\left(\underline{x},t\right) \tag{4.8}$$

The case of measurements without error represents a special case of (4.8) where $\delta_\eta\left(\underline{x},t\right) = 0$ for all positions and time instants. Herein the wording "measured" is used for sake of simplicity, although, in general, the wave elevation can be either measured (e.g. at a wave gauge or wave buoy) or reconstructed (e.g. from the inversion of wave radar images, Connell et al. [33]; Dankert and Rosenthal [35]; Fucile et al. [54]; Nieto Borge et al. [105]; Wijaya et al. [156]). It is now assumed that the true wave elevation is fitted through a phase-resolved wave model $\zeta\left(\underline{x},t\right)$ having the following expression, similar to that of $\eta\left(\underline{x},t\right)$:

$$\begin{cases} \zeta\left(\underline{x},t\right) = \sum_{h=1}^{N_\zeta} \tilde{a}_h \cos\left(\tilde{\underline{k}}_h \cdot \underline{x} - \tilde{\omega}_h t\right) + \tilde{b}_h \sin\left(\tilde{\underline{k}}_h \cdot \underline{x} - \tilde{\omega}_h t\right) = \underline{p}_\zeta\left(\underline{x},t\right)\underline{\beta} \\ \underline{p}_\zeta\left(\underline{x},t\right) = \left(\cos\left(\tilde{\underline{k}}_1 \cdot \underline{x} - \tilde{\omega}_1 t\right), \sin\left(\tilde{\underline{k}}_1 \cdot \underline{x} - \tilde{\omega}_1 t\right), ..., \cos\left(\tilde{\underline{k}}_{N_\zeta} \cdot \underline{x} - \tilde{\omega}_{N_\zeta} t\right), \sin\left(\underline{k}_{N_\zeta} \cdot \underline{x} - \omega_{N_\zeta} t\right)\right) \\ \underline{\beta} = \left(\tilde{a}_1, \tilde{b}_1, ..., \tilde{a}_{N_\zeta}, \tilde{b}_{N_\zeta}\right)^T \\ \underline{p}_\zeta\left(\underline{x},t\right) \in \mathbb{R}^{1,2N_\zeta}; \underline{\beta} \in \mathbb{R}^{2N_\zeta,1} \end{cases} \tag{4.9}$$

where, in general, the harmonic components of $\zeta\left(\underline{x},t\right)$ differ from those of $\eta\left(\underline{x},t\right)$ and, in addition, typically $N_\zeta << N_\eta$. The next assumption is that, given a set of N_M measurements $\eta_M\left(\underline{x}_j, t_j\right)$ $j = 1, ..., N_M$ at different points in space and/or time, the coefficients vector $\underline{\beta}$ can be determined by a linear transformation of the available measurements through an appropriate matrix $\underline{\underline{T}}_M$, i.e.:

$$\begin{cases} \underline{\beta} = \underline{\underline{T}}_M \underline{\eta}_M \\ \underline{\underline{T}}_M \in \mathbb{R}^{2N_\zeta, N_M} \\ \underline{\eta}_M = \left(\eta_M\left(\underline{x}_1, t_1\right), ..., \eta_M\left(\underline{x}_{N_M}, t_{N_M}\right)\right)^T \in \mathbb{R}^{N_M,1} \end{cases} \tag{4.10}$$

Such an assumption covers at least three important cases. The first case is the classical Fourier analysis on rectangular grids, in which case $\underline{\underline{T}}_M$ is the DFT matrix (Golub and Van Loan [58]). The second one is associated with a direct least-squares fitting process (see Connell et al. [33]; Vettor [146]). In such case the fitting is firstly setup as follows:

$$\begin{cases} \underline{\underline{P}}_{\zeta,M}\,\underline{\beta} = \underline{\eta}_M \\ \text{with } \underline{\underline{P}}_{\zeta,M} = \begin{bmatrix} \underline{p}_\zeta\left(\underline{x}_1, t_1\right) \\ \vdots \\ \underline{p}_\zeta\left(\underline{x}_{N_M}, t_{N_M}\right) \end{bmatrix} \in \mathbb{R}^{N_M, 2N_\zeta} \\ N_M \geq 2N_\zeta \end{cases} \tag{4.11}$$

where $\underline{\underline{P}}_{\zeta,M}$ can be referred to as the propagator matrix (Connell et al. [33]) at the measurement points in time and space, and $\underline{\underline{T}}_M$ is the Moore-Penrose pseudoinverse of $\underline{\underline{P}}_{\zeta,M}$, i.e.

$$\underline{\underline{T}}_M = \underline{\underline{P}}^{+}_{\zeta,M} = \left(\underline{\underline{P}}^T_{\zeta,M}\,\underline{\underline{P}}_{\zeta,M}\right)^{-1}\underline{\underline{P}}^T_{\zeta,M} \tag{4.12}$$

assuming that the matrix $\underline{\underline{P}}_{\zeta,M}$ is a full rank matrix and, therefore, that the matrix product $\underline{\underline{P}}^T_{\zeta,M}\,\underline{\underline{P}}_{\zeta,M}$ is actually an invertible matrix.

The third case covered by the assumption (4.10) is the regularised least-square fitting using Tikhonov regularisation (Hansen [64]; Vogel [147]), where a solution $\underline{\beta}$ is sought such to minimize the following objective function:

$$\left\| \underline{\underline{P}}_{\zeta,M}\,\underline{\beta} - \underline{\eta}_M \right\|^2 + \left\| \underline{\underline{\Lambda}}\,\underline{\beta} \right\|^2 \tag{4.13}$$

In (4.13), $\underline{\underline{\Lambda}}$ is an $2N_\zeta \times 2N_\zeta$ regularisation matrix, which is often chosen as $\underline{\underline{\Lambda}} = \lambda \underline{\underline{I}}_{2N_\zeta, 2N_\zeta}$, being $\underline{\underline{I}}_{2N_\zeta, 2N_\zeta}$ the $2N_\zeta \times 2N_\zeta$ identity matrix and λ the regularisation parameter. In such case the matrix $\underline{\underline{T}}_M$ becomes:

$$\underline{\underline{T}}_M = \left(\underline{\underline{P}}^T_{\zeta,M}\,\underline{\underline{P}}_{\zeta,M} + \underline{\underline{\Lambda}}^T\,\underline{\underline{\Lambda}}\right)^{-1}\underline{\underline{P}}^T_{\zeta,M} \tag{4.14}$$

It is worth noticing that the classical least-squares case is a special case of the Tikhonov regularisation, while the classical Fourier case can also be seen as a special case of both the other two.

Using the model (4.9) and the assumption (4.10), the fitted model can be evaluated at any point in space and time as follows:

$$\zeta_{F,\delta}\left(\underline{x}, t\right) = \underline{p}_\zeta\left(\underline{x}, t\right)\underline{\beta} = \underline{p}_\zeta\left(\underline{x}, t\right)\underline{\underline{T}}_M\,\underline{\eta}_M \tag{4.15}$$

The subscript "F, δ" indicates that the model is using coefficients which have been determined through fitting taking into account the presence of measurement error δ_η. It is now possible to determine the error between the fitted model and the true wave elevation $\eta\left(\underline{x}, t\right)$ as follows:

$$\varepsilon_\delta\left(\underline{x},t\right)=\zeta_{F,\delta}\left(\underline{x},t\right)-\eta\left(\underline{x},t\right)=\underline{p}_\zeta\left(\underline{x},t\right)\underline{\underline{T}}_M\underline{\eta}_M-\underline{p}_\eta\left(\underline{x},t\right)\underline{\alpha} \tag{4.16}$$

Furthermore, using (4.7) and (4.8), the vector of measured wave elevation can be written as:

$$\begin{cases}\underline{\eta}_M=\underline{\eta}+\underline{\delta}_{\eta,M}=\underline{\underline{P}}_{\eta,M}\underline{\alpha}+\underline{\delta}_{\eta,M}\\ \underline{\underline{P}}_{\eta,M}=\begin{bmatrix}\underline{p}_\eta\left(\underline{x}_1,t_1\right)\\ \vdots\\ \underline{p}_\eta\left(\underline{x}_{N_M},t_{N_M}\right)\end{bmatrix}\in\mathbb{R}^{N_M,2N_\eta}\\ \underline{\delta}_{\eta,M}=\left(\delta_\eta\left(\underline{x}_1,t_1\right),\ldots,\delta_\eta\left(\underline{x}_{N_M},t_{N_M}\right)\right)^T\in\mathbb{R}^{N_M,1}\end{cases} \tag{4.17}$$

Combining (4.16) and (4.17), the error $\varepsilon_\delta\left(\underline{x},t\right)$ can therefore be written as:

$$\begin{cases}\varepsilon_\delta\left(\underline{x},t\right)=\underline{q}\left(\underline{x},t\right)\underline{\alpha}+\underline{n}\left(\underline{x},t\right)\underline{\delta}_{\eta,M}\\ \text{with}\\ \underline{q}\left(\underline{x},t\right)=\underline{p}_\zeta\left(\underline{x},t\right)\underline{\underline{T}}_M\underline{\underline{P}}_{\eta,M}-\underline{p}_\eta\left(\underline{x},t\right)\\ \underline{n}\left(\underline{x},t\right)=\underline{p}_\zeta\left(\underline{x},t\right)\underline{\underline{T}}_M\\ \underline{q}\left(\underline{x},t\right)\in\mathbb{R}^{1,2N_\eta}\ ;\ \underline{n}\left(\underline{x},t\right)\in\mathbb{R}^{1,N_M}\end{cases} \tag{4.18}$$

From the first equation in (4.18), it can be seen that the error $\varepsilon_\delta\left(\underline{x},t\right)$ is due to two sources. The first term, $\underline{q}\left(\underline{x},t\right)\underline{\alpha}$, represents the error due to the fact that the fitted model, in general, differs from the actual process. The second term, $\underline{n}\left(\underline{x},t\right)\underline{\delta}_{\eta,M}$, represents the propagation of the measurement error through the fitted model. Both error sources also embed the effect of the fitting procedure.

It is now worth noticing that the error $\varepsilon_\delta\left(\underline{x},t\right)$ as obtained in (4.18) is a linear function of the amplitudes of the harmonic components of the true wave elevation $\eta\left(\underline{x},t\right)$. Furthermore, taking into account the fact that $\eta\left(\underline{x},t\right)$ is, actually, a stochastic process and the fact that $\underline{\delta}_{\eta,M}$ is a random vector, the error $\varepsilon_\delta\left(\underline{x},t\right)$ can be interpreted as a stochastic process. In all the following considerations, the set of N_M measurement points is assumed to be deterministically fixed in the ensemble domain, i.e., across multiple realisations. Furthermore, it is assumed that other possible fitting parameters (e.g. the regularization matrix $\underline{\underline{\Lambda}}$ in (4.14)) are also deterministically fixed. These two latter assumption allow to consider $q\left(\underline{x},t\right)$ and $\underline{n}\left(\underline{x},t\right)$ in (4.18) as deterministic functions of space and time.

By using the assumption that $\eta\left(\underline{x},t\right)$ is a (discretised) linear Gaussian process, similarly to the one dimensional case (Tucker et al. [144]), the amplitudes a_i and b_i of the

harmonic components are considered as zero mean independent Gaussian variables. They are linked to the (single side) directional wave energy spectrum $S_\eta\left(\underline{k}_i\right)$ as follows:

$$\begin{cases} a_i \sim N\left(0,\sigma_i^2\right) \;;\; b_i \sim N\left(0,\sigma_i^2\right) \;;\; \sigma_i^2 = S_\eta\left(\underline{k}_i\right)\Delta k_{x,i}\Delta k_{y,i} \\ COV\left\{a_i,a_j\right\} = \begin{cases} 0 & i \neq j \\ \sigma_i^2 & i = j \end{cases} \;;\; COV\left\{b_i,b_j\right\} = \begin{cases} 0 & i \neq j \\ \sigma_i^2 & i = j \end{cases} \\ COV\left\{a_i,b_j\right\} = 0 \;\; \forall i,j \end{cases} \tag{4.19}$$

where $N\left(0,\sigma_i^2\right)$ indicates a normal distribution with zero mean and variance σ_i^2, $\Delta k_{x,i}$ and $\Delta k_{y,i}$ are wave number intervals associated with the assumed discretization of the spectrum $S_\eta\left(\underline{k}_i\right)$ in N_η wave components, and $COV\{.,.\}$ indicates the covariance operator. According to (4.19) the wave amplitudes vector $\underline{\alpha}$ is a zero mean Gaussian random vector with diagonal covariance matrix, that is:

$$\begin{cases} \underline{\mu}_{\underline{\alpha}} = E\left\{\underline{\alpha}\right\} = \underline{0} \\ \underline{\underline{C}}_{\underline{\alpha},\underline{\alpha}} = E\left\{\left(\underline{\alpha}-\underline{\mu}_{\underline{\alpha}}\right)\left(\underline{\alpha}-\underline{\mu}_{\underline{\alpha}}\right)^T\right\} = \begin{bmatrix} \sigma_1^2 & 0 & \cdots & 0 & 0 \\ 0 & \sigma_1^2 & \cdots & 0 & 0 \\ \vdots & \vdots & \ddots & \vdots & \vdots \\ 0 & 0 & \cdots & \sigma_{N_\eta}^2 & 0 \\ 0 & 0 & \cdots & 0 & \sigma_{N_\eta}^2 \end{bmatrix} = \\ = diag\left(\sigma_1^2,\sigma_1^2,...,\sigma_{N_\eta}^2,\sigma_{N_\eta}^2\right) \end{cases} \tag{4.20}$$

where $E\{.\}$ is the expected value operator. In addition, it is assumed that the measurement error $\delta_\eta\left(\underline{x},t\right)$ is a zero mean Gaussian process and that it is independent of η. As a consequence, given the specific set of N_M measurement points in space and time, the vector $\underline{\delta}_{\eta,M}$ is a zero mean Gaussian vector with a given covariance matrix depending on the assumed measurement error characteristics, i.e.:

$$\begin{cases} \underline{\mu}_{\underline{\delta}_{\eta,M}} = E\left\{\underline{\delta}_{\eta,M}\right\} = \underline{0} \\ \underline{\underline{C}}_{\underline{\delta}_{\eta,M},\underline{\delta}_{\eta,M}} = E\left\{\left(\underline{\delta}_{\eta,M}-\underline{\mu}_{\underline{\delta}_{\eta,M}}\right)\left(\underline{\delta}_{\eta,M}-\underline{\mu}_{\underline{\delta}_{\eta,M}}\right)^T\right\} \end{cases} \tag{4.21}$$

If it is assumed that the measurement errors δ_η at two different points in time and space are independent, then the covariance matrix $\underline{\underline{C}}_{\underline{\delta}_{\eta,M},\underline{\delta}_{\eta,M}}$ becomes diagonal:

$$\underline{\underline{C}}_{\underline{\delta}_{\eta,M},\underline{\delta}_{\eta,M}} = \begin{bmatrix} \sigma^2_{\delta_\eta}\left(\underline{x}_1,t_1\right) & 0 & \cdots & 0 \\ 0 & \sigma^2_{\delta_\eta}\left(\underline{x}_2,t_2\right) & \cdots & 0 \\ \vdots & \vdots & \ddots & \vdots \\ 0 & 0 & \cdots & \sigma^2_{\delta_\eta}\left(\underline{x}_{N_M},t_{N_M}\right) \end{bmatrix} \tag{4.22}$$

The generic term $\sigma^2_{\delta_\eta}\left(\underline{x}_j,t_j\right)$, with $j=1,...,N_M$, represents the measurement error variance at point $\underline{x}_j$ in space and at time t_j. If, in addition, it is assumed that the measurement error is a uniform noise with variance σ^2_δ, then the covariance matrix $\underline{\underline{C}}_{\underline{\delta}_{\eta,M},\underline{\delta}_{\eta,M}}$ simplifies to:

$$\underline{\underline{C}}_{\underline{\delta}_{\eta,M},\underline{\delta}_{\eta,M}} = \sigma^2_{\delta_\eta}\underline{\underline{I}}_{N_M,N_M} \tag{4.23}$$

The assumption presented so far are proposed as possible formal simplifications of the error process which, before being actually implemented within this methodology, has to be carefully characterised. Indeed, from a practical point of view, in case the error $\underline{\delta}_{\eta,M}$ is correlated in time and space, the full definition of covariance matrix in (4.21) has to be used. This has proven to be the case of the error induced by the LSQR inversion technique introduced in section §3.6.2. In addition, another important underlying hypothesis is to be stressed, i.e. the implicit assumption that $\underline{\delta}_{\eta,M}$ is independent of η, i.e. the fact that $\underline{\delta}_{\eta,M}$ is an additive error. Although for certain source of error this assumption can easily be justified, in other cases this assumption needs some special care. Notwithstanding this difficulty, in the present formulation, this assumption is necessary for the further development of the methodology.

Then, by using (4.18), (4.20) and (4.21), the assumption that $\delta_\eta\left(\underline{x},t\right)$ is independent of η, and recalling that, from the considered assumptions, $\underline{q}\left(\underline{x},t\right)$ and $\underline{n}\left(\underline{x},t\right)$ are deterministic vector functions, it is now possible to provide a full probabilistic characterisation of the prediction error $\varepsilon_\delta\left(\underline{x},t\right)$. Indeed, from (4.18), it follows that $\varepsilon_\delta\left(\underline{x},t\right)$ is a Gaussian process, since it is a linear combination of random Gaussian vectors. Furthermore, the mean and the variance of $\varepsilon_\delta\left(\underline{x},t\right)$ can be determined as follows:

$$\begin{cases} E\left\{\varepsilon_\delta\left(\underline{x},t\right)\right\} = 0 \\ Var\left\{\varepsilon_\delta\left(\underline{x},t\right)\right\} = \sigma^2_{\varepsilon_\delta}\left(\underline{x},t\right) = \underline{q}\left(\underline{x},t\right)\underline{\underline{C}}_{\underline{\alpha},\underline{\alpha}}\underline{q}^T\left(\underline{x},t\right) + \underline{n}\left(\underline{x},t\right)\underline{\underline{C}}_{\underline{\delta}_{\eta,M},\underline{\delta}_{\eta,M}}\underline{n}^T\left(\underline{x},t\right) \end{cases} \tag{4.24}$$

where $E\{.\}$ is the expected value operator, $Var\{.\}$ is the variance operator, and $\sigma^2_{\varepsilon_\delta}\left(\underline{x},t\right)$ is the variance of the prediction error at $\left(\underline{x},t\right)$. From the considered assumptions, it follows that the prediction error has zero mean. In addition, similarly to what was noticed when commenting (4.18), it can be noticed that also in (4.24) the variance of the prediction error is composed of two terms: the first term is associated with the inherent difference between the fitted model and the true process, while the second term represents the effect of the measurement error.

If use is made of the assumption that the covariance matrices $\underline{\underline{C}}_{\underline{\alpha},\underline{\alpha}}$ and $\underline{\underline{C}}_{\underline{\delta}_{\eta,M},\underline{\delta}_{\eta,M}}$ are diagonal, and by using (4.19), the expression for the variance of the prediction error can be simplified to:

$$\begin{aligned}\sigma^2_{\varepsilon_\delta}\left(\underline{x},t\right) &= \sum_{i=1}^{N_\eta}\left(q^2_{2i-1}\left(\underline{x},t\right)+q^2_{2i}\left(\underline{x},t\right)\right)\sigma_i^2 + \sum_{j=1}^{N_M} n_j^2\left(\underline{x},t\right)\sigma^2_{\delta_\eta}\left(\underline{x}_j,t_j\right) = \\ &= \sum_{i=1}^{N_\eta}\left(q^2_{2i-1}\left(\underline{x},t\right)+q^2_{2i}\left(\underline{x},t\right)\right)S_\eta\left(\underline{k}_i\right)\Delta k_{x,i}\Delta k_{y,i} + \sum_{j=1}^{N_M} n_j^2\left(\underline{x},t\right)\sigma^2_{\delta_\eta}\left(\underline{x}_j,t_j\right)\end{aligned} \tag{4.25}$$

Each term in the first summation in (4.25) represents the contribution to the prediction error variance at $\left(\underline{x},t\right)$ coming from the spectral energy around the wave number vector $\underline{k}_i$. Each term in the second summation in (4.25) represents, instead, the contribution to the prediction error variance at $\left(\underline{x},t\right)$ coming from the measurement error at the measurement point $\left(\underline{x}_j,t_j\right)$. In the limit the number of harmonics assumed in the model of $\eta\left(\underline{x},t\right)$ increases towards infinity ($N_\eta \to \infty$), the first term in (4.25) tends to an integral involving the spectrum of η, and the variance of the prediction error can be rewritten as:

$$\sigma^2_{\varepsilon_\delta}\left(\underline{x},t\right) = \iint\left(f_1^2\left(\underline{k},\underline{x},t\right)+f_2^2\left(\underline{k},\underline{x},t\right)\right)S_\eta\left(\underline{k}\right)dk_x dk_y + \sum_{j=1}^{N_M} n_j^2\left(\underline{x},t\right)\sigma^2_{\delta_\eta}\left(\underline{x}_j,t_j\right) \tag{4.26}$$

where $f_1^2\left(\underline{k},\underline{x},t\right)$ and $f_2^2\left(\underline{k},\underline{x},t\right)$ are functions depending on the fitting procedure. It is important, at this point, to underline that the single side energy spectrum $S_\eta\left(\underline{k}\right)$ appearing in (4.25) and (4.26) is the spectrum of the true wave elevation η and it must not be confused with the spectrum, assuming it could be consistently defined, of the measured wave elevation. In fact, the measured wave elevation is contaminated, in general, by the effect of the measurement error process.

A closed form analytical formulation for the functions $f_1^2\left(\underline{k},\underline{x},t\right)$ and $f_2^2\left(\underline{k},\underline{x},t\right)$ is difficult to derive in the general case, for it depends on the fitting model as it has to embed the solution step in (4.10). However, some specific consideration can be given to the case where the fitting model is derived from a Discrete Fourier Transform (DFT) approach. In fact, choosing a suitable orthogonal basis in the sense of DFT, possibly accounting only for a subset of allowed Fourier frequencies, the calculation of the $\underline{\underline{T}}_M$ matrix and of the product $\underline{\underline{T}}_M\underline{\underline{P}}_{\eta,M}$ can be carried out analytically, leading, eventually, to analytical expressions for the resulting functions $f_1^2\left(\underline{k},\underline{x},t\right)$ and $f_2^2\left(\underline{k},\underline{x},t\right)$. Further details about the calculation of the functions $f_1^2\left(\underline{k},\underline{x},t\right)$ and $f_2^2\left(\underline{k},\underline{x},t\right)$ in such special case are provided in §4.3.3.

Moreover, it is worth to mention, that, once specified, the fitting model completely defines the matrix $\underline{\underline{T}}_M$ that, consequently, will remain a constant quantity of the problem. The majority of the computational burden is then limited to the calculation of

the matrix $\underline{\underline{T}}_M$ at the beginning of the procedure, while other quantities can then be easily calculated afterwards.

The Linear Estimator of Prediction Error (LEPrE) in (4.25) (or its continuous version (4.26)) can now be used for providing a sound definition of Predictability Region. In fact, being $\varepsilon_\delta(\underline{x},t)$ a zero mean Gaussian process (in space and time), it is completely characterised, for each single point $(\underline{x},t)$, by its variance. The Predictability Region can therefore be defined as that region Π, in time and space, where the variance of the prediction error is sufficiently small. Given a threshold τ_ε for the standard deviation of the prediction error, the predictability region can then be defined as:

$$\Pi(\tau_\varepsilon) = \left\{(\underline{x},t) : \sigma^2_{\varepsilon_\delta}(\underline{x},t) \le \tau_\varepsilon^2\right\} \tag{4.27}$$

It can be noticed that, in the probabilistic framework developed herein, there is no single Predictability Region, and the Predictability Region depends on which level of prediction error is considered to be acceptable through the specification of the threshold τ_ε.

4.3.1 Embedding the effect of linear transformations of measured wave elevation signal

It is worth presenting how the LEPrE methodology can be extended to include, in its general definition, any linear transformation applied to the measured signal of the wave elevation. In this respect, the need for applying an additional linear transformation to the measured signal can be justified in the light of an improvement of certain characteristics of the original signal. For example, the application of a windowing function to the sampled signal, formally equivalent to a multiplication with a weighting matrix, is a quite common practice when there is a need for reducing, for example, the leakage effects on the Fourier coefficients, as explained in Prabu [118]. Moreover, the original signal may require a filtering step before being implemented in the LEPrE calculation, in order, for example, to filter out unwanted or spurious frequency components from the measured wave elevation. Also this case, if a linear filter is applied, as for example described in Kaiser and Reed [71] in the case of a low pass filter, a linear transformation will be involved.

Now, assuming for simplicity an arbitrary weighting matrix $\underline{\underline{W}} \in \mathbb{R}^{N_M, N_M}$, the transformed (filtered) measured wave elevation, $\underline{\eta}^*_M(\underline{x},t)$, can be redefined as:

$$\underline{\eta}^*_M(\underline{x},t) = \underline{\underline{W}}\,\underline{\eta}_M(\underline{x},t) = \underline{\underline{W}}\,\underline{\eta}(\underline{x},t) + \underline{\underline{W}}\,\underline{\delta}_\eta(\underline{x},t) \tag{4.28}$$

The coefficient of the equation (4.10) can then be simply rewritten as:

$$\begin{cases} \underline{\beta}^* = \underline{\underline{T}}_M\,\underline{\eta}^*_M = \underline{\underline{T}}^*_M\,\underline{\eta}_M \\ \underline{\underline{T}}^*_M = \underline{\underline{T}}_M\,\underline{\underline{W}} \end{cases} \tag{4.29}$$

where now the updated matrix, $\underline{\underline{T}}_M^* = \underline{\underline{T}}_M \underline{\underline{W}}$, has been introduced. This new matrix embeds also the transformation/filtering procedure applied to the measured signal.

The definition of the additional matrix $\underline{\underline{T}}_M^*$ allows keeping the previously introduced derivation of the prediction error formally unchanged. In fact, the derivation of the prediction error can just be obtained by adopting the matrix $\underline{\underline{T}}_M^*$ as (see (4.18)):

$$\begin{cases} \varepsilon_\delta^*(\underline{x},t) = \underline{q}^*(\underline{x},t)\underline{\alpha} + \underline{n}^*(\underline{x},t)\underline{\delta}_{\eta,M} \\ \text{with} \\ \underline{q}^*(\underline{x},t) = \underline{p}_\zeta(\underline{x},t)\underline{\underline{T}}_M{}^*\underline{\underline{P}}_{\eta,M} - \underline{p}_\eta(\underline{x},t) = \underline{p}_\zeta(\underline{x},t)\underline{\underline{T}}_M\underline{\underline{W}}\,\underline{\underline{P}}_{\eta,M} - \underline{p}_\eta(\underline{x},t) \\ \underline{n}^*(\underline{x},t) = \underline{p}_\zeta(\underline{x},t)\underline{\underline{T}}_M{}^* = \underline{p}_\zeta(\underline{x},t)\underline{\underline{T}}_M\underline{\underline{W}} \end{cases} \tag{4.30}$$

Moreover, the considerations already drawn about the statistical characteristics of the prediction error will still be valid and unaffected by the additional linear transformation. This leads to the definition of the following mean and variance of the prediction error, similarly to (4.24), as:

$$\begin{cases} E\left\{\varepsilon_\delta^*(\underline{x},t)\right\} = 0 \\ Var\left\{\varepsilon_\delta^*(\underline{x},t)\right\} = \sigma_{\varepsilon_\delta^*}^2(\underline{x},t) = \underline{q}^*(\underline{x},t)\underline{\underline{C}}_{\underline{\alpha},\underline{\alpha}}\underline{q}^{*T}(\underline{x},t) + \underline{n}^*(\underline{x},t)\underline{\underline{C}}_{\underline{\delta}_{\eta,M},\underline{\delta}_{\eta,M}}\underline{n}^{*T}(\underline{x},t) \end{cases} \tag{4.31}$$

The main statistically relevant quantities, the covariance matrix $\underline{\underline{C}}_{\underline{\alpha},\underline{\alpha}}$ and $\underline{\underline{C}}_{\underline{\delta}_{\eta,M},\underline{\delta}_{\eta,M}}$, are not affected by the linear transformation and they keep exactly the same statistical meaning as discussed before. The only terms affected by the linear transformation of the sea wave elevation are the $\underline{q}$ and $\underline{n}$ terms.

The definition of the LEPrE can then be obtained exactly as done already in §4.3.1, but using the newly defined terms $\underline{q}^*$ and $\underline{n}^*$.

4.3.2 Implementation and usage

Expression (4.25)/(4.26) can be used in deterministic phase-resolved wave predictions to supplement the prediction of wave elevation along with an estimation of the prediction error associated with the specific fitting and prediction procedure.

To this end, in general, a fitting model (4.19) is firstly chosen, and this corresponds to the definition of a certain set of wave number vectors $\tilde{\underline{k}}_h \quad h = 1,\ldots,N_\zeta$. Then, it is necessary to define the set of N_M points, in time and/or space, which are used for the fitting of the propagation model according to the decided fitting procedure. To further proceed it is necessary to know, or at least to have an as good as possible estimation, of the sea elevation spectrum $S_\eta(\underline{k})$. In some applications, such as laboratory experiments or numerical simulations, the spectrum $S_\eta(\underline{k})$ is known with sufficient accuracy.

However, in applications at sea, the estimation of $S_\eta(\underline{k})$ can be a critical issue; depending on the specific application, methods based on wave radar processing (Nieto Borge et al. [105]), wave buoys, or ship-as-a-wave-buoys (e.g. Tannuri et al. [139]), can be exploited to estimate $S_\eta(\underline{k})$. It is however crucial that the estimator of the true wave elevation spectrum $S_\eta(\underline{k})$ is depurated, as much as possible, from the effects of measurement noise. In this respect, if the measurement noise is assumed to have a flat spectrum S_{δ_η} additive to $S_\eta(\underline{k})$, it follows that the spectrum of the measured wave elevation becomes $S_{\delta_\eta} + S_\eta(\underline{k})$. In such case, the analysis of very low and very high wave number regions could be used to estimate the contamination S_{δ_η} which should then be removed from the spectrum of the measured wave elevation, to get, eventually, the (depurated) estimation of $S_\eta(\underline{k})$. Another step for the application of the proposed methodology is the definition of a modelling for the covariance matrix of the error in the measurement of the wave elevation (see (4.21)). In case a flat spectral noise level S_{δ_η} is determined, the variance of the measurement error can be obtained from the integration of S_{δ_η} over the region of $\underline{k}$ up to Nyquist limits from the Fourier analysis. Alternatively, the measurement error can be defined, for instance, from the knowledge of the measurement system, being it, e.g. a wave gauge, a wave buoy, or a wave radar, as appropriate. Other application-specific methods can, of course, also be used.

From the description above, almost all the major information would be available at this stage. However, in order to determine (an estimator of) $\sigma^2_{\varepsilon_\delta}(\underline{x},t)$ it is necessary to make some additional assumption regarding the process $\eta(\underline{x},t)$. If the fitting procedure is such that analytical expressions for the functions $f_1^2(\underline{k},\underline{x},t)$ and $f_2^2(\underline{k},\underline{x},t)$ can be determined, then expression (4.26) can be directly used, combined with a suitable numerical integration procedure. Alternatively the discrete formulation (4.25) can be directly used in the general case. However, when using (4.25), it is necessary to specify a certain number of harmonic components N_η which are assumed to represent the underlying (unknown) stochastic process $\eta(\underline{x},t)$. In order for $\eta(\underline{x},t)$ to be a sufficiently good approximation of the true underlying sea elevation Gaussian process, N_η should be sufficiently large. From application tests, it has been noticed that, when the number of components N_η is sufficiently large, and in particular sufficiently larger than the number of components N_ζ used for the fitted model, the behaviour of $\sigma^2_{\varepsilon_\delta}(\underline{x},t)$ converges, sufficiently for practical purposes, to the value which is obtained with much larger N_η (ideally with $N_\eta \to \infty$). This is expectable, since (part of) $\sigma^2_{\varepsilon_\delta}(\underline{x},t)$ represents the prediction error for $\zeta(\underline{x},t)$ which, loosely speaking, is associated with an insufficient frequency resolution in $\zeta(\underline{x},t)$ to resolve "all" the components of $\eta(\underline{x},t)$. The wording "all" is in quotation marks since, in reality, $\eta(\underline{x},t)$, as a stochastic process, has infinite harmonic components of infinitesimal amplitude. This convergence can also be understood from a numerical perspective when (4.25) is considered as a discretised version of the integral in (4.26). The drawback of using the discrete formulation (4.25) is that an increase of N_η tends to increase the dimensions of some of the matrices involved in the calculations, with a consequent increase of

memory consumption and computational time. In order for the procedure to be practically viable with present resources, it is necessary to find a trade-off for N_η such that it has a sufficiently large value to have a sufficiently good/converged estimation of $\sigma^2_{\varepsilon_\delta}(\underline{x},t)$, but without exceeding the available computational time and resources.

With all data available, $\sigma^2_{\varepsilon_\delta}(\underline{x},t)$ can therefore be estimated in a suitable range of space and/or time. This allows, first, to supplement the prediction $\zeta(\underline{x},t)$ with an associated Gaussian confidence interval based on $\sigma_{\varepsilon_\delta}(\underline{x},t)$. Furthermore, given a limit threshold level τ_ε, the predictability region $\Pi(\tau_\varepsilon)$ can be eventually determined in accordance with (4.27). It is also to be noted that the possibility of estimating $\sigma^2_{\varepsilon_\delta}(\underline{x},t)$ allows, in addition, to devise "optimum" prediction strategies and/or fitting and prediction setups in order to provide wave elevation predictions with minimum/smaller confidence bounds.

4.3.3 Analytical formulation of LEPrE in case of DFT fitting and long crested(1D) and short crested (2D) waves

This section presents the derivation of functions $f_1^2(k,x,t)$ and $f_2^2(k,x,t)$, in equation (4.26), in the special case when a DFT fitting approach is applied. Both the long crested (1D) and short crested (2D) cases are considered.

The derivation starts from the case of long crested (1D) sea states, where waves propagate in the same direction. In this case the generic wave number vector $\underline{k}$ can be replaced by its corresponding scalar magnitude k and the generic position vector $\underline{x}$ can be replaced by a scalar coordinate x.

The possible presence of measurement error does not affect the definition of $f_1^2(k,x,t)$ and $f_2^2(k,x,t)$ in (4.26), since the contribution to the prediction error standard deviation due to the presence of measurement error represents an additive term. Therefore, for the purpose of this appendix, the prediction error can be defined by combining equations (4.16) and (4.18) as follows, without considering measurement error:

$$\varepsilon(x,t)=\zeta_F(x,t)-\eta(x,t)=\left[\underline{p}_\zeta(x,t)\underline{\underline{T}}_M\underline{\underline{P}}_{\eta,M}-\underline{p}_\eta(x,t)\right]\underline{\alpha}=\underline{q}(x,t)\underline{\alpha} \qquad (4.32)$$

The measurement of the wave elevation is assumed to be carried out on an evenly spaced 1D grid of M points, with sampling resolution Δx so that the sampled position is $x_m=x_0+m\Delta x$ with $m=\{0,...,M-1\}$ and x_0 is a given bias position. The corresponding Fourier wave numbers are defined as $\tilde{k}_s=2\pi s/M\Delta x$, with the index s taking the values on a convenient subset of the set $\{0,1,...,M/2\}$. The fitting model is then assumed to be based on a set of N_ζ wave numbers, $\tilde{k}_i\in\{\tilde{k}_1,...,\tilde{k}_{N\zeta}\}$, chosen among the previously defined Fourier ones. For sake of simplicity, the analytical solution will not account for the zero wave number, $\tilde{k}=0$, and for the possible Nyquist wave number $\tilde{k}=\pi/\Delta x$. Exploiting the properties of the DFT matrix, it is

straightforward to prove that the matrix $\underline{\underline{T}}_M$ appearing in (4.10) can be actually written as:

$$\underline{\underline{T}}_M = \frac{2}{M} P_{\zeta,M}^T \tag{4.33}$$

The matrix product $\underline{\underline{T}}_M \underline{\underline{P}}_{\eta,M}$ can now be rewritten in the following block matrix form:

$$\underline{\underline{F}}_M = \begin{bmatrix} \underline{\underline{f}}_{1,1} & \cdots & \underline{\underline{f}}_{1,N_\eta} \\ \cdots & \underline{\underline{f}}_{i,j} & \cdots \\ \underline{\underline{f}}_{N_\zeta,1} & \cdots & \underline{\underline{f}}_{N_\zeta,N_\eta} \end{bmatrix} \text{ where } \underline{\underline{f}}_{i,j} = \begin{bmatrix} f_{cc}(\tilde{k}_i, k_j) & f_{cs}(\tilde{k}_i, k_i) \\ f_{sc}(\tilde{k}_i, k_j) & f_{ss}(\tilde{k}_i, k_j) \end{bmatrix} \tag{4.34}$$

The determination of the elements of $\underline{\underline{f}}_{i,j}$ can be carried out analytically, leading to the following results:

$$\begin{aligned} f_{cc}(\tilde{k}_i, k_j) &= \frac{2}{M} \sum_{m=0}^{M-1} \cos(\tilde{k}_i x_m) \cos(k_j x_m) = \\ &= \cos\left(\pi(\mu_i + \nu_j) \cdot \Theta\right) D(\mu_i + \nu_j, M) + \cos\left(\pi(\mu_i - \nu_j) \cdot \Theta\right) D(\mu_i - \nu_j, M) \end{aligned} \tag{4.35}$$

$$\begin{aligned} f_{ss}(\tilde{k}_i, k_j) &= \frac{2}{M} \sum_{m=0}^{M-1} \sin(\tilde{k}_i x_m) \sin(k_j x_m) = \\ &= -\cos\left(\pi(\mu_i + \nu_j)\Theta\right) D\left(\mu_i + \nu_j, M\right) + \cos\left((\pi(\mu_i - \nu_j)\Theta\right) D\left(\mu_i - \nu_j, M\right) \end{aligned} \tag{4.36}$$

$$\begin{aligned} f_{cs}(\tilde{k}_i, k_j) &= \frac{2}{M} \sum_{m=0}^{M-1} \cos(\tilde{k}_i x_m) \sin(k_j x_m) = \\ &= \sin\left(\pi(\mu_i + \nu_j)\Theta\right) D(\mu_i + \nu_j, M) - \sin\left(\pi(\mu_i - \nu_j)\Theta\right) D(\mu_i - \nu_j, M) \end{aligned} \tag{4.37}$$

$$\begin{aligned} f_{sc}(\tilde{k}_i, k_j) &= \frac{2}{M} \sum_{m=0}^{M-1} \sin(\tilde{k}_i x_m) \cos(k_j x_m) = \\ &= \sin\left(\pi(\mu_i + \nu_j)\Theta\right) D(\mu_i + \nu_j, M) + \sin\left(\pi(\mu_i - \nu_j)\Theta\right) D(\mu_i - \nu_j, M) \end{aligned} \tag{4.38}$$

where $\Theta = \left(\frac{(M-1)}{M} + \alpha\right)$ with $\alpha = 2x_0 / (M\Delta x)$. μ_i is a natural number defined as $\mu_i = \frac{\tilde{k}_i}{2\pi} M\Delta x \in \mathbb{N}$ and ν_j is in general a real number defined as $\nu_j = \frac{k_j}{2\pi} M\Delta x \in \mathbb{R}$. The function $D(p, M)$ appearing in the previous expressions is defined as:

$$D(p, M) = \frac{\sin(\pi p)}{M \sin(\pi p / M)} \quad \text{with p} \in \mathbb{R} \tag{4.39}$$

The wave numbers $\tilde{k}_i$ and k_j are, respectively, the Fourier wave number of the fitting model and the assumed wave number of the underlying model. This latter, in general, can be arbitrary, and not necessarily linked to the sampling grid.

The results reported so far are provided assuming that the measurement and fitting is carried out in the space domain. However, the obtained results can be recast in a form suitable for the dual situation where the measurement and fitting procedure is carried out in time domain. In such case, it is necessary to interchange space and time, as well as wave numbers and wave frequencies. In a time domain fitting it shall also be assumed that the fitting frequencies correspond to an orthogonal basis with respect to the measurement domain, and that the wave numbers corresponding to the fitting frequencies are determined from the dispersion relation.

It is worth noticing at this point that, in phase-resolved propagation methods, it is good practice to define the sampling grid in such a way to avoid, as much as possible, aliasing problems. However, in general, the sampling grid is defined by the sampling resolution of the measuring device and some aliasing is unavoidable. In this case the whole fitting and propagation procedure will be affected by aliasing. The LEPrE methodology naturally embeds the fitting model characteristics in its definition and consequently it will provide a prediction error that consistently takes into account the presence of aliasing.

The elements of the vector $\underline{q}(x,t)$ in (4.32) can now be rewritten as:

$$\begin{aligned} &q_{2j-1}(x,t)= \\ &= \sum_{i=1}^{N_\zeta}\left[f_{cc}(\tilde{k}_i,k_j)\cos\left(\tilde{k}_i x-\omega(\tilde{k}_i)t\right)+f_{sc}(\tilde{k}_i,k_j)\sin\left(\tilde{k}_i x-\omega(\tilde{k}_i)t\right)\right]-\cos\left(k_j x-\omega(k_j)t\right) \\ &q_{2j}(x,t)= \\ &= \sum_{i=1}^{N_\zeta}\left[f_{sc}(\tilde{k}_i,k_j)\cos\left(\tilde{k}_i x-\omega(\tilde{k}_i)t\right)+f_{ss}(\tilde{k}_i,,k_j)\sin\left(\tilde{k}_i x-\omega(\tilde{k}_i)t\right)\right]-\sin\left(k_j x-\omega(k_j)t\right) \end{aligned} \tag{4.40}$$

However, the terms $q_{2j-1}(x,t)$ and $q_{2j}(x,t)$ are now in a closed form with respect to the generic (arbitrary) wave number k_j. As a result, the subscript j can be dropped and the final formulation of the functions $f_1^2(k,x,t)$ and $f_2^2(k,x,t)$ can be written as:

$$\begin{aligned} &f_1^2(k,x,t)= \\ &= \left[\sum_{i=1}^{N_\zeta}\left[f_{cc}(\tilde{k}_i,k)\cos\left(\tilde{k}_i x-\omega(\tilde{k}_i)t\right)+f_{cs}(\tilde{k}_i,k)\sin\left(\tilde{k}_i x-\omega(\tilde{k}_i)t\right)\right]-\cos\left(kx-\omega(k)t\right)\right]^2 \\ &f_2^2(k,x,t)= \\ &= \left[\sum_{i=1}^{N_\zeta}\left[f_{sc}(\tilde{k}_i,k)\cos\left(\tilde{k}_i x-\omega(\tilde{k}_i)t\right)+f_{ss}(\tilde{k}_i,k)\sin\left(\tilde{k}_i x-\omega(\tilde{k}_i)t\right)\right]-\sin\left(kx-\omega(k)t\right)\right]^2 \end{aligned} \tag{4.41}$$

The formulation developed so far can be easily extended to the short crested (2D) case within the hypothesis the fitting procedure is carried out using an orthogonal Fourier basis. The measurement of the wave elevation is assumed to be carried out on an evenly spaced 2D grid of MN points, with sampling resolution Δx along the x direction and

Δy along the y direction. The grid points $\underline{x}_{m,n} = \left(x_m, y_n\right)^T$ are defined as $x_m = x_0 + m\Delta x$ with $m = \{0,...,M-1\}$ and $y_n = y_0 + n\Delta y$ with $n = \{0,...,N-1\}$, with x_0 and y_0 given bias position. The corresponding Fourier wave numbers, considered in their vector form $\underline{\tilde{k}} = \left(\tilde{k}_x, \tilde{k}_y\right)^T$, are defined as $\tilde{k}_{x,r} = 2\pi r / \left(M\Delta x\right)$ with the index r taking the values on a convenient subset of the set $\{0,1,...,M/2\}$ and $\tilde{k}_{y,s} = 2\pi s / \left(N\Delta y\right)$ with the index s taking the values on $\{0,1,...,N/2\}$. The fitting model is then assumed to be based on a set of N_ζ wave numbers, $\underline{\tilde{k}}_i = \left(\tilde{k}_{x,i}, \tilde{k}_{y,i}\right)^T \in \{\underline{\tilde{k}}_1,...,\underline{\tilde{k}}_{N\zeta}\}$, chosen among the previously defined Fourier ones, excluding the zero and the Nyquist wave numbers.

In this case the functions $f_{cc}, f_{cs}, f_{sc}, f_{ss}$ presented from equation (4.35) to (4.38), can be exploited to calculate a set of corresponding functions associated with the 2D case as:

$$g_{cc}(\underline{\tilde{k}}_i, \underline{k}_j) = \frac{2}{MN}\sum_{n=0}^{N-1}\sum_{m=0}^{M-1}\cos(\tilde{k}_{x,i}x_m + \tilde{k}_{y,i}y_n)\cos(k_{x,j}x_m + k_{y,j}y_n) = \\ = \frac{1}{2}\begin{bmatrix} f_{cc}(\tilde{k}_{x,i}, k_{x,j})f_{cc}(\tilde{k}_{y,i}, k_{y,j}) - f_{cs}(\tilde{k}_{x,i}, k_{x,j})f_{cs}(\tilde{k}_{y,i}, k_{y,j})... \\ -f_{sc}(\tilde{k}_{x,j}, k_{x,j})f_{sc}(\tilde{k}_{y,i}, k_{y,j}) + f_{ss}(\tilde{k}_{x,i}, k_{x,j})f_{ss}(\tilde{k}_{y,i}, k_{y,j}) \end{bmatrix} \tag{4.42}$$

$$g_{ss}(\underline{\tilde{k}}_i, \underline{k}_j) = \frac{2}{MN}\sum_{n=0}^{N-1}\sum_{m=0}^{M-1}\sin(\tilde{k}_{x,i}x_m + \tilde{k}_{y,i}y_n)\sin(k_{x,j}x_m + k_{y,j}y_n) = \\ = \frac{1}{2}\begin{bmatrix} f_{ss}(\tilde{k}_{x,i}, k_{x,j})f_{cc}(\tilde{k}_{y,i}, k_{y,j}) + f_{sc}(\tilde{k}_{x,i}, k_{x,j})f_{cs}(\tilde{k}_{y,i}, k_{y,j})... \\ +f_{cs}(\tilde{k}_{x,i}, k_{x,j})f_{sc}(\tilde{k}_{y,i}, k_{y,j}) + f_{cc}(\tilde{k}_{x,i}, k_{x,j})f_{ss}(\tilde{k}_{y,i}, k_{y,j}) \end{bmatrix} \tag{4.43}$$

$$g_{cs}(\underline{\tilde{k}}_i, \underline{k}_j) = \frac{2}{MN}\sum_{n=0}^{N-1}\sum_{m=0}^{M-1}\cos(\tilde{k}_{x,i}x_m + \tilde{k}_{y,i}y_n)\sin(k_{x,j}x_m + k_{y,j}y_n) = \\ = \frac{1}{2}\begin{bmatrix} f_{cs}(\tilde{k}_{x,i}, k_{x,j})f_{cc}(\tilde{k}_{y,i}, k_{y,j}) + f_{cc}(\tilde{k}_{x,i}, k_{x,j})f_{cs}(\tilde{k}_{y,i}, k_{y,j})... \\ -f_{ss}(\tilde{k}_{x,i}, k_{x,j})f_{sc}(\tilde{k}_{y,i}, k_{y,j}) - f_{sc}(\tilde{k}_{x,i}, k_{x,j})f_{ss}(\tilde{k}_{y,i}, k_{y,j}) \end{bmatrix} \tag{4.44}$$

$$g_{sc}(\tilde{k}_i, k_j) = \frac{2}{MN}\sum_{n=0}^{N-1}\sum_{m=0}^{M-1}\sin(\tilde{k}_{x,i}x_m + \tilde{k}_{y,i}y_n)\cos(k_{x,j}x_m + k_{y,j}y_n) = \\ = \frac{1}{2}\begin{bmatrix} f_{sc}(\tilde{k}_{x,i}, k_{x,j})f_{cc}(\tilde{k}_{y,i}, k_{y,j}) - f_{ss}(\tilde{k}_{x,i}, k_{x,j})f_{cs}(\tilde{k}_{y,i}, k_{y,j})... \\ +f_{cc}(\tilde{k}_{x,i}, k_{x,j})f_{sc}(\tilde{k}_{y,j}, k_{y,j}) - f_{cs}(\tilde{k}_{x,i}, k_{x,j})f_{ss}(\tilde{k}_{y,i}, k_{y,j}) \end{bmatrix} \tag{4.45}$$

Similarly to (4.41), the index j associated to the frequency in the underlying assumed wave elevation model η can now be dropped, so that the functions $f_1^2\left(\underline{k}, \underline{x}, t\right)$ and $f_2^2\left(\underline{k}, \underline{x}, t\right)$ for the general short crested (2D) case can finally be written as:

$$
\begin{aligned}
& f_1^2\left(\underline{k},\underline{x},t\right) = \\
& = \left[\sum_{i=1}^{N_\zeta}\left[g_{cc}(\tilde{\underline{k}}_i,\underline{k})\cos\left(\tilde{\underline{k}}_i\underline{x}-\tilde{\omega}_i t\right)+g_{cs}(\tilde{\underline{k}}_i,\underline{k})\sin\left(\tilde{\underline{k}}_i\underline{x}-\tilde{\omega}_i t\right)\right]-\cos\left(\underline{k}\underline{x}-\omega t\right)\right]^2 \\
& f_2^2\left(\underline{k},\underline{x},t\right) = \\
& = \left[\sum_{i=1}^{N_\zeta}\left[g_{sc}(\tilde{\underline{k}}_i,\underline{k})\cos\left(\tilde{\underline{k}}_i\underline{x}-\tilde{\omega}_i t\right)+g_{ss}(\tilde{\underline{k}}_i,\underline{k})\sin\left(\tilde{\underline{k}}_i\underline{x}-\tilde{\omega}_i t\right)\right]-\sin\left(\underline{k}\underline{x}-\omega t\right)\right]^2
\end{aligned}
\tag{4.46}
$$

4.4 Application examples

Some applications examples exploiting the described LEPrE methodology are reported in this section. The first two applications are simplified long crested sea cases, used to show and discuss the main characteristics and capabilities of the LEPrE methodology. In the third application a more realistic scenario, dealing with the prediction of water wave elevation for nonlinear long crested sea, is investigated. In the fourth application, the measurement noise, as derived in §3 is accounted for in the case of linear long crested sea. Eventually, the predictive performances of the LEPrE have been tested in the case of linear short crested sea.

The first application, reported in §4.4.1, has been conceived to show how the LEPrE methodology compares with respect to the Predictability Region (Wu [159]) and Predictability Indicator (Wu [159]; Naaijen et al. [102]) techniques in the case of a simplified archetypal strongly bimodal spectrum. The considered simplified spectrum is used for comparison and description purposes, in order to emphasize the effects which might appear, although less evidently, in a smoother realistic wind waves plus swell bimodal case.

The second application, reported in §4.4.2, presents a simulated laboratory experiment where the wave elevation is assumed to be produced by a wave maker. The purpose of this application is to set up a controlled and yet realistic environment where to test the LEPrE methodology dealing also with the effects of measurement error (noise). The main results are then verified with respect to a set of Monte Carlo simulations and the effect of the measurement noise is discussed.

The third example, reported in §4.4.3, shows some result about the application of the LEPrE methodology to nonlinear wave fields. In the case of moderate sea states the LEPrE method represents an adequate indicator for the prediction error level. However, for steeper sea states characterised by stronger nonlinearities, the linear assumptions underlying the LEPrE approach will show their limits.

In the fourth example, reported in §4.4.4, the LEPrE methodology has been provided with an estimation of the additional noise source coming from wave measurements. The results obtained for the LSQR inversion model (see chapter §3) have been exploited and integrated in the LEPrE approach. Despite the implemented partial characterisation of the measurement error and its simple implementation in the LEPrE approach the results show a satisfactory agreement with the reference Monte Carlo simulations.

In the last application, reported in §4.4.5, the LEPrE methodology is applied to a more realistic scenario where an offshore structure is considered and the wave elevation, used for the propagation model, is assumed to be measured by means of a wave radar device.

For this short crested application the wave elevation field is assumed as linear. By keeping the fitting model as fixed, the effect of spreading of spectral energy angles is then discussed. The results are then verified against a corresponding set of Monte Carlo simulations.

4.4.1 Verification and Monte Carlo Simulations

This example considers the application of LEPrE methodology in the case of a simplified, idealised, bimodal spectrum. The main aim is to establish a simple archetypal scenario able to highlight the common behaviours and the main differences between the LEPrE methodology, the Predictability Region and the Predictability Indicator techniques, as already described in section §4.2. In this example case, results from the LEPrE methodology are compared with the Predictability Error indicator defined in (4.6). For verification purposes, all results are also compared against a set of 500 Monte Carlo realizations.

The two bimodal spectra used for this application are reported in Figure 4.3. Each spectrum is designed as the sum of two simple band limited flat spectra with a narrow bandwidth $b_w = 0.1k_0$ and with symmetric peaks separated by $\Delta k = \{0.25 \cdot k_0, 0.75 \cdot k_0\}$ from the central reference wave number $k_0 = 2\pi / \lambda_0 [1/m]$. The corresponding reference period is $T_0 = 2\pi / \omega_0$ and the reference wave frequency in deep water is $\omega_0 = \sqrt{k_0 \cdot g}$ with g the acceleration of gravity. These spectra represent an interesting benchmark for a comparison with the Predictability Region and Predictability Indicator. Indeed, the Predictability Region approach only takes into account the fastest and lowest component of the spectrum, without accounting for the actual spectral shape, basing the identification of the predictability region on the assumption of using the group velocity as reference speed. On the other hand, the Predictability Error Indicator approach, although still using the group velocity as reference speed for the computations, is able to take into account the actual spectral shape. Finally, the LEPrE approach accounts, in an analytic way, for all the features of the fitting procedure and for the exact spectral shape of the underlying wave elevation process, without any addition semi-empirical assumption.

The fitting is carried out in the space domain on a measurement region of length $L_M = 13\lambda_0$ with sampling interval $\Delta x = \lambda_0 / 15$. The measurement interval is $0 \le x / \lambda_0 \le 13$. The fitting/propagation model is defined on the basis of DFT analysis. The Fourier wave numbers selected for the fitting model are $\tilde{k}_j = j2\pi / (N_M \Delta x)$ with $j = 1, ..., N_M / 2 - 1$, with $N_M = 196$, thus, zero and Nyquist wave frequencies are not taken into account in the calculations. For the propagation model the infinite depth dispersion relation $\tilde{\omega}_j = \sqrt{g\tilde{k}_j}$ has been used.

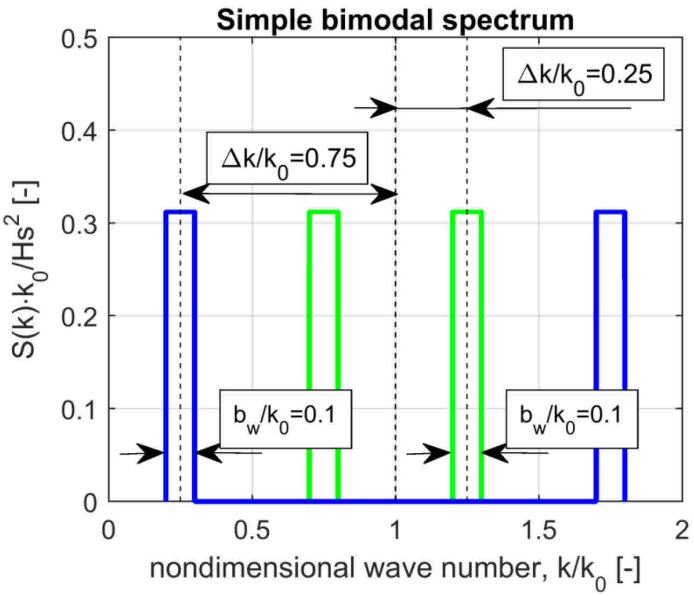

Figure 4.3: Simple bimodal spectra. Band shift parameter: $\Delta k = 0.25 \cdot k_0$ (green line) and $\Delta k = 0.75 \cdot k_0$ (blue line).

Results from the application of the different methodologies are reported in Figure 4.4, where surfaces of $\sigma_\varepsilon(x,t) \Big/ \left(H_s / 2\sqrt{2}\right)$ are shown. Since in this case no measurement error is considered, the standard deviation of prediction error is indicated as σ_ε instead of $\sigma_{\varepsilon_\delta}$. It can be noticed that there is an overall qualitative consistency among the different methodologies. The region where the LEPrE approach shows small values of prediction error standard deviation are in line with the identified Predictability Region according to Wu [159], and are also in line with the regions where the Prediction Error Indicator, according to Naaijen et al. [102], is small. Furthermore, the outcomes from the LEPrE methodology are fully verified by the comparison with Monte Carlo simulations, as the two methods show almost undistinguishable prediction error maps. It can be noticed that all methods agree in identifying a reduction of the minimum error region when the bimodal spectrum is characterised by a wider separation between the two bands, which corresponds to the presence of wave components with very different group speeds. The presence of traces in the time/space map associated with the different speeds of the components belonging to the two bands is quite evident, particularly in case of $\Delta k = 0.75 \cdot k_0$.

However, a closer look to results shows how the LEPrE method provides much more information on the prediction error in terms of error pattern, thanks to its capability of implicitly embedding the exact characteristics of the fitting model as well as the exact spectral characteristics of the underlying wave elevation process. Moreover, from the reported comparison, the high level of qualitative agreement between the Prediction Error Indicator and the LEPrE methodology is evident, which suggests the possibility of identifying some underlying relation, and provides a sort of justification to the assumptions used in the determination of the Prediction Error Indicator, at least for the considered fitting procedure set up and for the selected spectral shape.

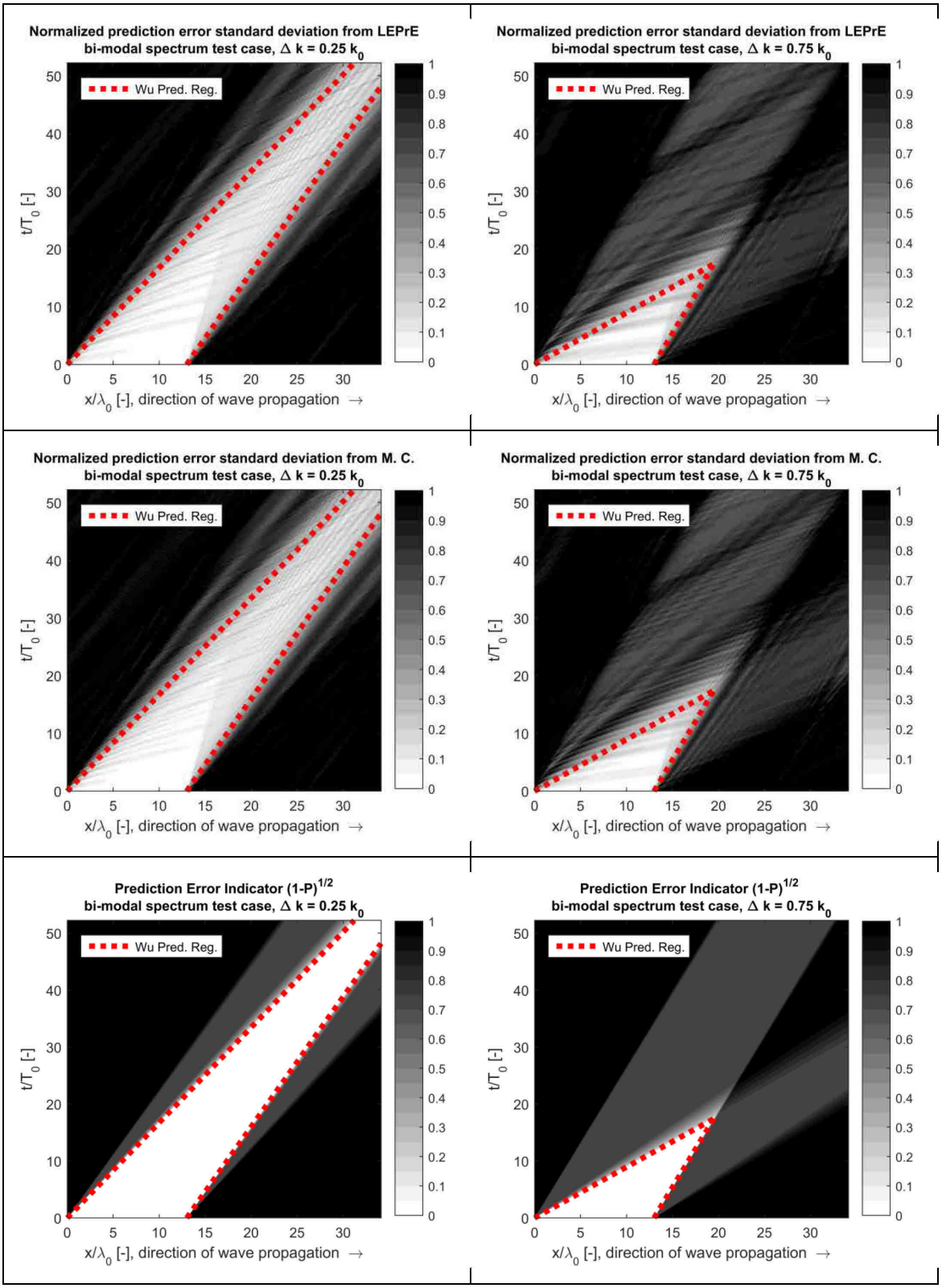

Figure 4.4: Prediction performance map according to different approaches for two bimodal spectra with band shift parameter $\Delta k = 0.25 \cdot k_0$ (left) and $\Delta k = 0.75 \cdot k_0$ (right). The limits of the Predictability Region (see §4.2) are reported as red dashed lines in all plots. Normalized prediction error standard deviation, with normalization coefficient $H_s / 2\sqrt{2}$, according to LEPrE (top) and as estimated by means of 500 Monte Carlo realizations (centre). Bottom: Prediction Error Indicator according to (4.6).

4.4.2 Prediction error and measurement error

Seakeeping experiments may require measuring the wave elevation at particular locations along the wave tank or at the tested model surroundings. In some cases, an instrumental measurement may be prevented by the presence of obstacles, like the tested model itself, or the setup of the wave probes can turn out to be particularly inconvenient. A possible solution is to measure the wave elevation at suitable distance upstream from the points of interest and then derive an indirect measure of the (undisturbed) wave elevation where this information is needed. This kind of reconstruction process will eventually be affected by errors and therefore it must be supplemented with a sound error analysis. The LEPrE methodology can be applied to this scenario in its complete definition (4.25) or (4.26), which allows dealing with deterministic predictions in presence of measurement noise.

For this example application a wave probe is assumed to be placed in the middle of a wave tank with water depth $D_T = 3.8m$, see Figure 4.5. The indirect predicted wave elevation is required at two downstream probing points at distance $d_1 = 3.0m$ and $d_2 = 6.0m$ from the measuring wave probe. According to (4.25)/(4.26), the LEPrE methodology requires the knowledge of the wave spectrum S_η. In general, the "true" wave spectrum is unknown and it has to be assessed from the wave measurement. However, for sake of simplicity, in this case the nominal spectrum is assumed to be known, since it is a typical input for the experimental wave generation. In particular, the spectrum considered in this example is a JONSWAP spectrum with significant height $H_s = 5m$, peak period $T_p = 9.30s$ and peak enhancement factor $\gamma = 3.3$. It is assumed that this spectrum is realized in the experimental laboratory at a model scale $\lambda = 50$. The wave probe measurements are considered to be affected by Gaussian random noise with a standard deviation proportional to H_s. Two different levels of noise are considered, namely $\sigma_n = 0.02H_s$ and $\sigma_n = 0.10H_s$.

The characteristics of the fitting model are defined by the recording time window, assumed to be $T_M = 10 \cdot T_p$, and the wave probe sampling frequency, assumed to be 50Hz, corresponding to $\Delta t = 0.02s$. The measurement is defined to start at $t = 0s$ and to finish at $t = 13.14s$. The fitting/propagation model is based on DFT analysis. The selected Fourier frequencies used for fitting model are $\tilde{\omega}_j = j2\pi / (N_M \Delta t)$ with $j = 1,..., N_M / 2 - 1$ where $N_M = 658$, thus, zero and Nyquist wave frequencies are not taken into account in the calculations. For the propagation model the finite depth dispersion relation $\tilde{\omega}_j = \sqrt{g\tilde{k}_j \tanh(\tilde{k}_j D_T)}$ has been used.

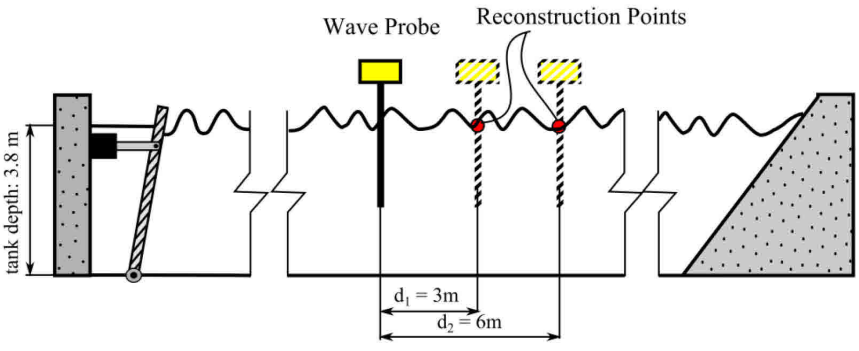

Figure 4.5: Scheme of the wave tank and of the considered laboratory experimental setup.

Results from the LEPrE methodology are verified against a set of 500 Monte Carlo realizations and a 95% confidence interval is provided to account for sampling uncertainty of Monte Carlo simulations. The prediction error standard deviation $\sigma_{\varepsilon_\delta}$ is presented in non-dimensional form, i.e. by normalization with respect to H_s.

First, Figure 4.6 reports the reconstruction of the wave elevation for four different random realizations of the considered sea state at the probe location $d_1 = 3m$ and with the measurement noise level of $\sigma_n = 0.02H_s$. The true wave elevation is also reported. The LEPrE methodology is used to provide the reconstructed wave elevation with an error bound $\pm 2\sigma_{\varepsilon_\delta}$ corresponding, approximately, to the 95% confidence interval (the exact 95% confidence interval would correspond to $\pm 1.96\sigma_{\varepsilon_\delta}$). It is possible to note that there is a time interval where the reconstructed wave elevation matches particularly well the true wave elevation and this time window is independent on the realization. Assuming a conventional threshold level $\sigma_{\varepsilon_\delta} < 0.05H_s$, a predictability time window can therefore be defined on the basis of the LEPrE prediction error standard deviation. Such time window is indicated in Figure 4.6 by two vertical dashed lines. It can be noticed that, consistently for all the reported realizations, within the defined predictability time window, the reconstructed wave elevation well reproduces the true wave elevation, whereas, outside, the prediction tends to deviate more significantly from the true wave elevation.

Figure 4.7 and Figure 4.8 show the time history of the prediction error standard deviation as calculated at the two probe locations for the two considered levels of noise. Furthermore, the "optimal time delay" δt_{opt} is also identified and highlighted; this is the time delay from the beginning of the measurement window at which the standard deviation of prediction error, σ_ε, shows its minimum for the considered probe location. This information could be useful in devising optimum reconstruction strategies, based on the minimization of the prediction error. LEPrE results in Figure 4.7 and Figure 4.8 are almost indistinguishable from Monte Carlo simulations and clearly within the confidence interval, indicating that the LEPrE methodology has been properly implemented. Looking at Figure 4.7 and Figure 4.8 it can be seen how the distance from the measurement wave probe changes the behaviour of $\sigma_{\varepsilon_\delta}$, with the region of minimum error shifting forward in time and higher in value as the reconstruction point is farther from the measurement probe in the direction of wave propagation. A comparison between results of Figure 4.7 and Figure 4.8 indicates that, as the noise level increases, the prediction error standard deviation tends to saturate, flattening the region of minimum error. However, at least for the two tested cases characterised by small and moderate noise levels, the optimal prediction delay δt_{opt} is independent of the noise level and it only depends on the probe location.

Figure 4.9 and Figure 4.10 provide a wider picture, by showing the space/time error maps for both the noise levels using the LEPrE methodology. In the figures, the locations of the probe are highlighted with vertical red lines and the points of minimum prediction error standard deviation are indicated by a circular yellow symbol. The comparison of the two maps shows that the LEPrE methodology consistently accounts for the presence of higher measurement noise: the increase of the noise level causes an increase of the values of $\sigma_{\varepsilon_\delta}$ in the whole space/time domain.

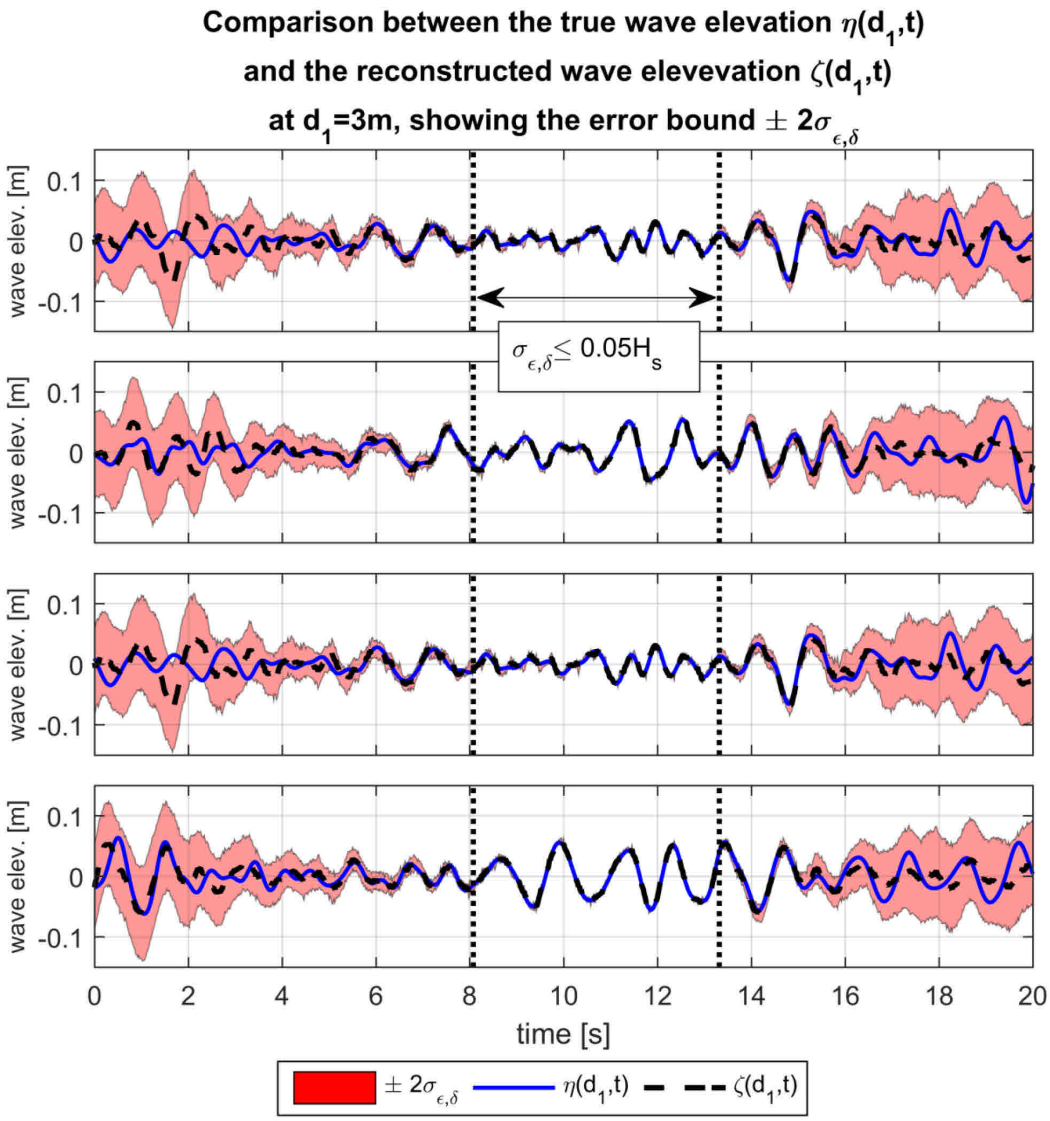

Figure 4.6: Comparison between the true wave elevation, $\eta(d_1,t)$, and the reconstructed wave elevation, $\zeta(d_1,t)$ at the first probing point $d_1 = 3m$. Time histories for four different realizations of the same sea state. Measurement noise level: $\sigma_n = 0.02H_s$. The error bound $\pm 2\sigma_{\varepsilon_\delta}$ is reported as a red band. The two vertical dotted black lines indicate the limit of the time window where the prediction error standard deviation from LEPrE is smaller than the considered threshold value, i.e. $\sigma_{\varepsilon_\delta} < \tau_\varepsilon = 0.05H_s$.

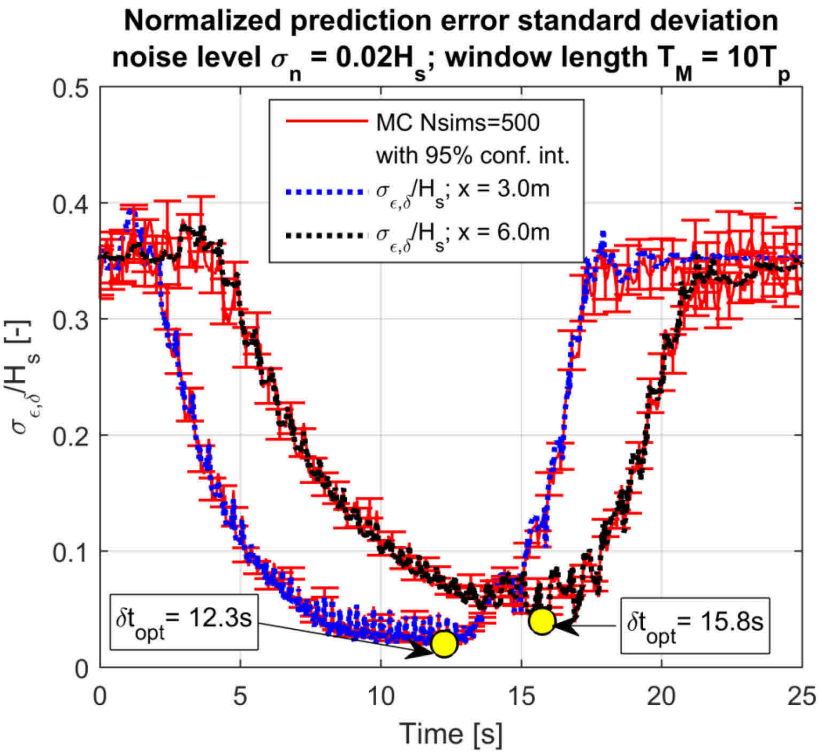

Figure 4.7: Normalized prediction error standard deviation as a function of time for two different probe locations. Measurement noise level: $\sigma_n = 0.02H_s$.

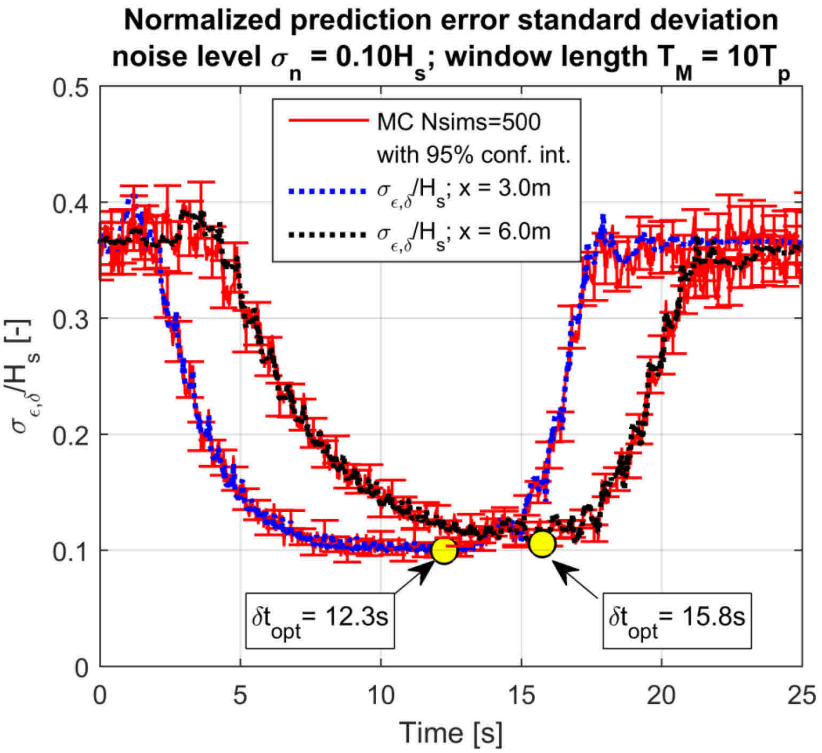

Figure 4.8: Normalized prediction error standard deviation as a function of time for two different probe locations. Measurement noise level: $\sigma_n = 0.10H_s$.

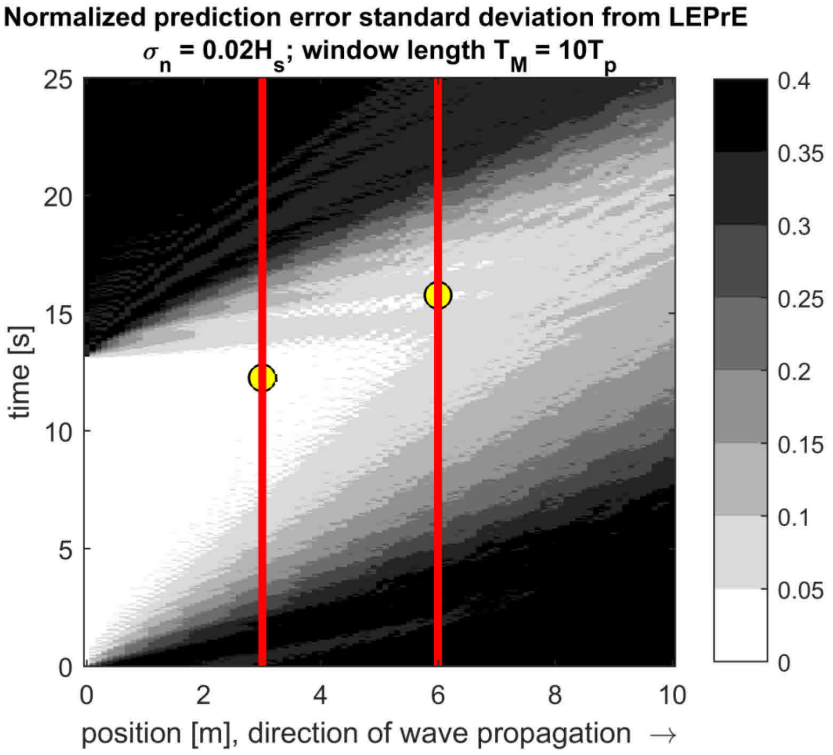

Figure 4.9: Map of normalized prediction error standard deviation $\sigma_{\varepsilon_\delta} / H_s$. Measurement noise level: $\sigma_n = 0.02 H_s$. The red lines report the position of the reconstruction points.

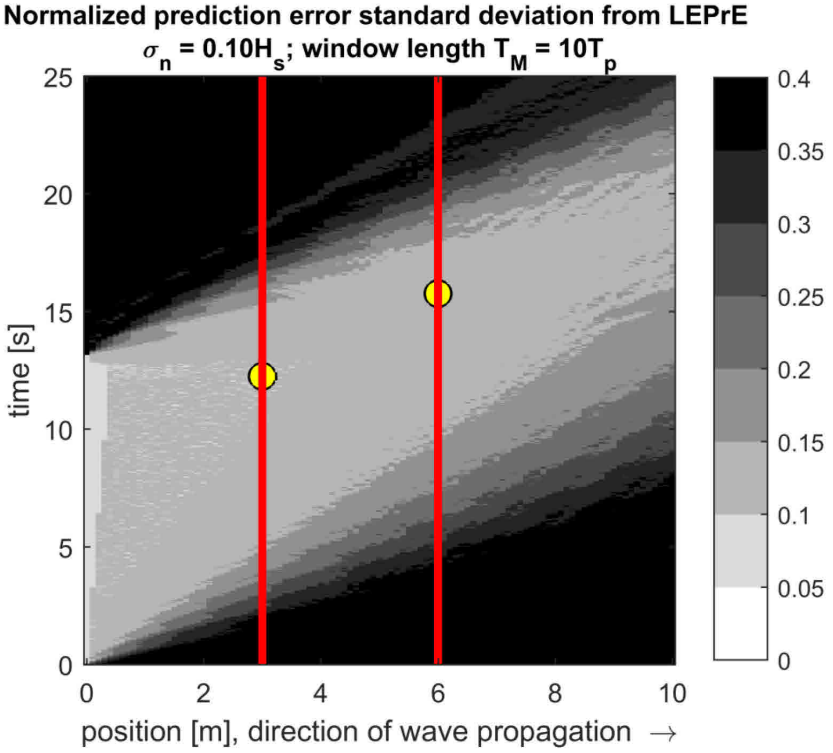

Figure 4.10: Map of normalized prediction error standard deviation $\sigma_{\varepsilon_\delta} / H_s$. Measurement noise level: $\sigma_n = 0.10 H_s$. The red lines show the position of the reconstruction points.

4.4.3 Effect of wave field nonlinearities for long crested seas

In this section, the LEPrE method, as measure of the standard deviation of the prediction error, has been compared with the error results for a set of 100 Monte Carlo linear DSWP application performed for different realization of long crested seas. Both linear and nonlinear wave fields have been considered as reference data for the fitting of the propagation model. The sea conditions account for two different Bretschneider spectra, both having peak period of $T_p = 11.97s$, but two different significant wave heights $H_s = 2.5, 6.5m$. The details about the generation of the nonlinear wave field are reported in section §2.5. In calculating the prediction error from the Monte Carlo simulation, the wave field is assumed to be perfectly retrieved by a wave radar like device allowing the fitting step of a linear DSWP to be performed on the true wave elevation. Then, a linear propagation step is performed, for both the case linear as well as nonlinear wave fields. Eventually, the resulting signal of the true wave elevation $\eta(x,t)$ and of the fitted and propagated wave elevation $\zeta(x,t)$ are compared, and the standard deviation of the prediction error from Monte Carlo simulations is calculated in the ensemble domain. The wave radar is assumed to image the sea surface at $t_0 = 0s$ and the measurement region is defined as the interval $x = [450, 2250]m$. The sea elevation is sampled on $N_x = 241$ points with space discretization of $dx = 7.5m$. The waves are assumed to propagate towards the wave radar antenna. A probing point has been defined at the position of the radar, $x_p = 0m$, corresponding to a relative distance with the closer edge of the fitting region of $d = 450m$. The DSWP propagation step is performed by a DFT application assuming the resulting wave numbers discretization $k_n = \frac{2\pi}{N_x dx} n$ with $n = 1,..,(N_x - 1)/2$. A deep water condition has been assumed, leading to wave frequencies being determined as $\omega_n = \sqrt{g k_n}$.

Figure 4.11 presents the comparison between LEPrE and Monte Carlo simulation results in case the underlying wave field is linear, for $H_s = 2.5$. In Figure 4.12 the same results are compared for the same sea condition but considering a nonlinear wave field. Despite the comparison is, overall, satisfactory, some differences can be found in the case of nonlinear waves.

Results for $H_s = 6.5m$, in case of linear waves, are reported in Figure 4.13. In terms of normalized standard deviation of the prediction error the expected results are indeed equivalent to the ones obtained for the lower significant wave height, presented in Figure 4.11, as a consequence of the linearity of the problem. Corresponding results are presented for the case of nonlinear waves, in Figure 4.14. Being the DSWP method linear, and the underlying wave field nonlinear, the prediction error assessed with the Monte Carlo simulation is no more consistent with the LEPrE results. This is a somewhat expected result which indicates the fact that the linearity assumption underlying the LEPrE approach is no longer suitable for this condition. In this respect, in Figure 4.15, the limits of a linear fitting and propagation model applied to a nonlinear wave elevation field are presented. The true and linearly predicted wave elevations of two realization of the same sea condition, $H_s = 6.5m$, are presented both in the case of linear and nonlinear underlying wave fields. The sea surface is reported for a generic time instant $t = 120s$. For the nonlinear case, the true wave elevation appears to be shifted towards the origin with respect to the corresponding linear prediction, and a systematic fitting problem in accounting for the smaller waves can be noted. The

observed behaviour could be related to the fact that the linear model cannot account for the correct nonlinear dispersion relation and for the correct propagation of the nonlinear bounds waves. It is however to be noted that the observed shifting is almost a rigid shifting. This seems to indicate that a significant portion of the large prediction error visible in Figure 4.14 from Monte Carlo simulations could be due to the rigid shift rather than a poor prediction of the wave elevation profile. This may indicate that an improvement of the dispersion relation used in the LEPrE approach could help in reducing the observed differences.

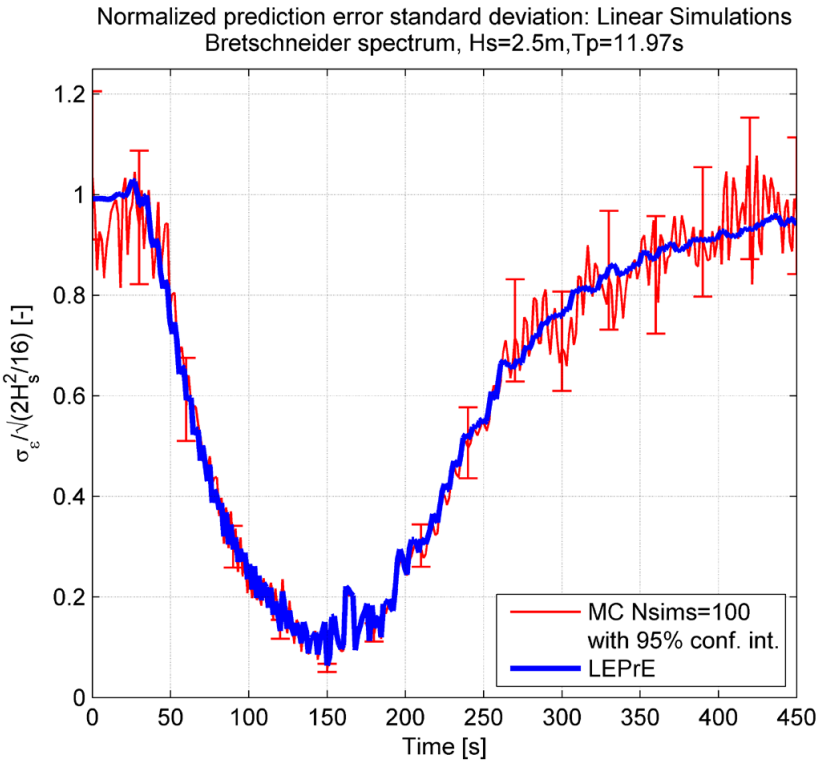

Figure 4.11: Normalized prediction error standard deviation at $x_p = 0m$: comparison between LEPrE and results from 100 Monte Carlo simulations. Linear waves generated for Bretschneider spectrum with $H_s = 2.5m$ and $T_p = 11.97s$.

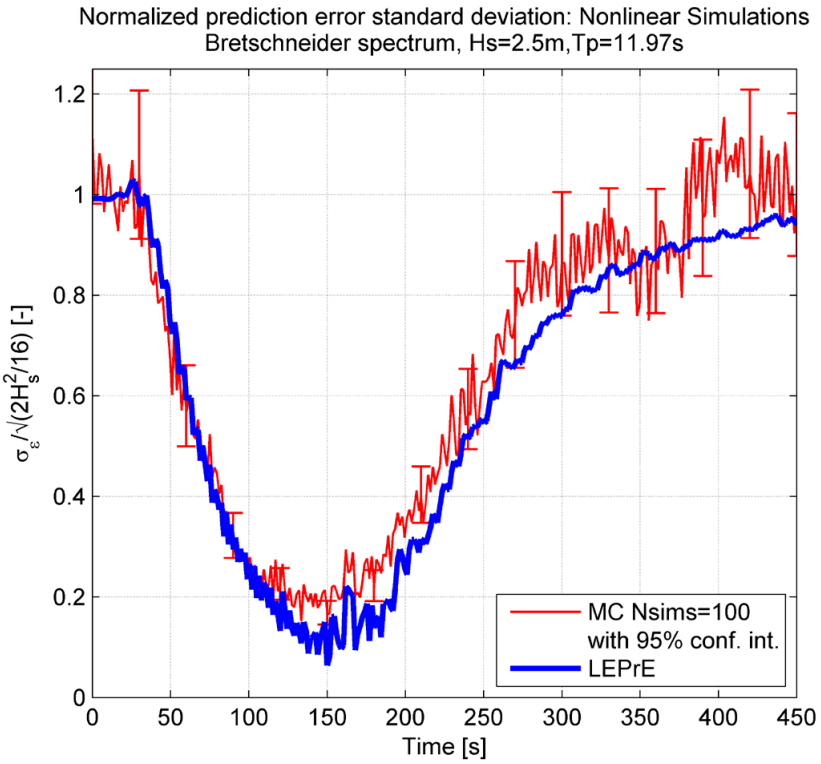

Figure 4.12: Normalized prediction error standard deviation at $x_p = 0m$: comparison between LEPrE and results from 100 Monte Carlo simulations. Nonlinear waves generated for Bretschneider spectrum with $H_s = 2.5m$ and $T_p = 11.97s$.

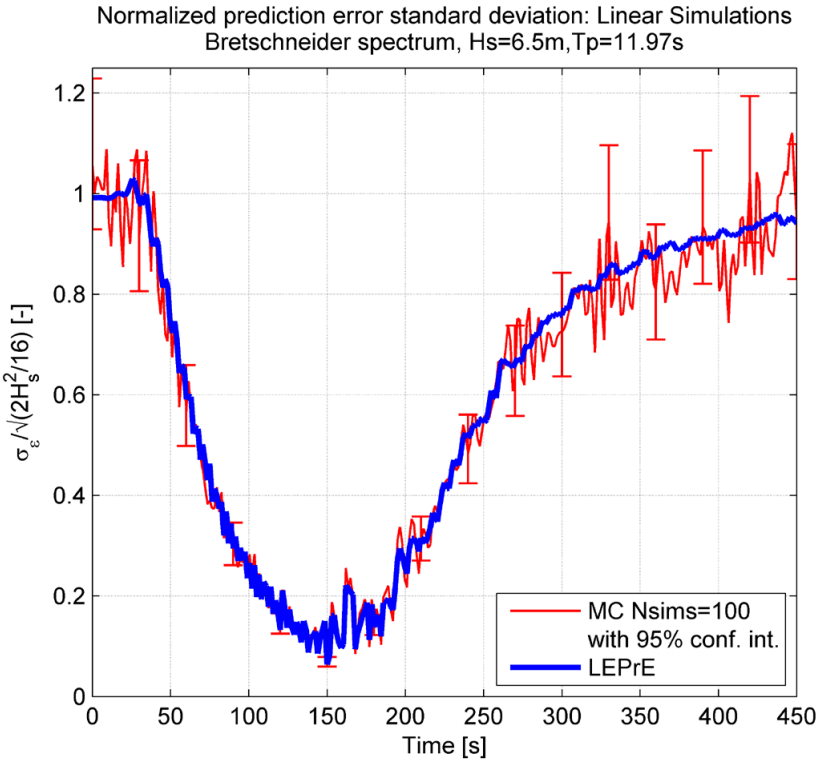

Figure 4.13: Normalized prediction error standard deviation at $x_p = 0m$: comparison between LEPrE and results from 100 Monte Carlo simulations. Linear waves generated for Bretschneider spectrum with $H_s = 6.5m$ and $T_p = 11.97s$.

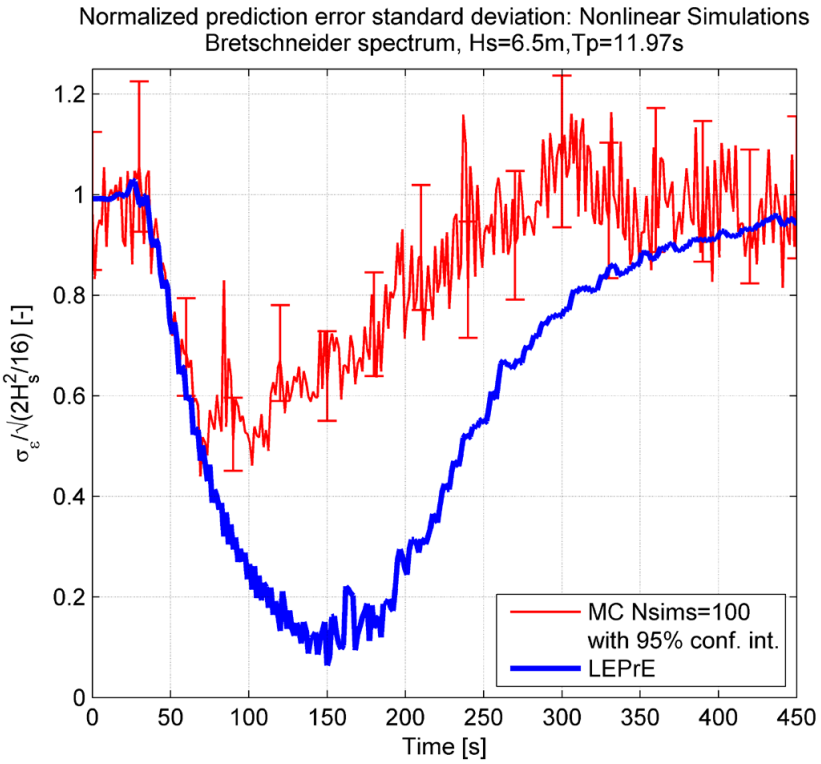

Figure 4.14: Normalized prediction error standard deviation at $x_p = 0m$: comparison between LEPrE and results from 100 Monte Carlo simulations. Nonlinear waves generated for Bretschneider spectrum with $H_s = 6.5m$ and $T_p = 11.97s$.

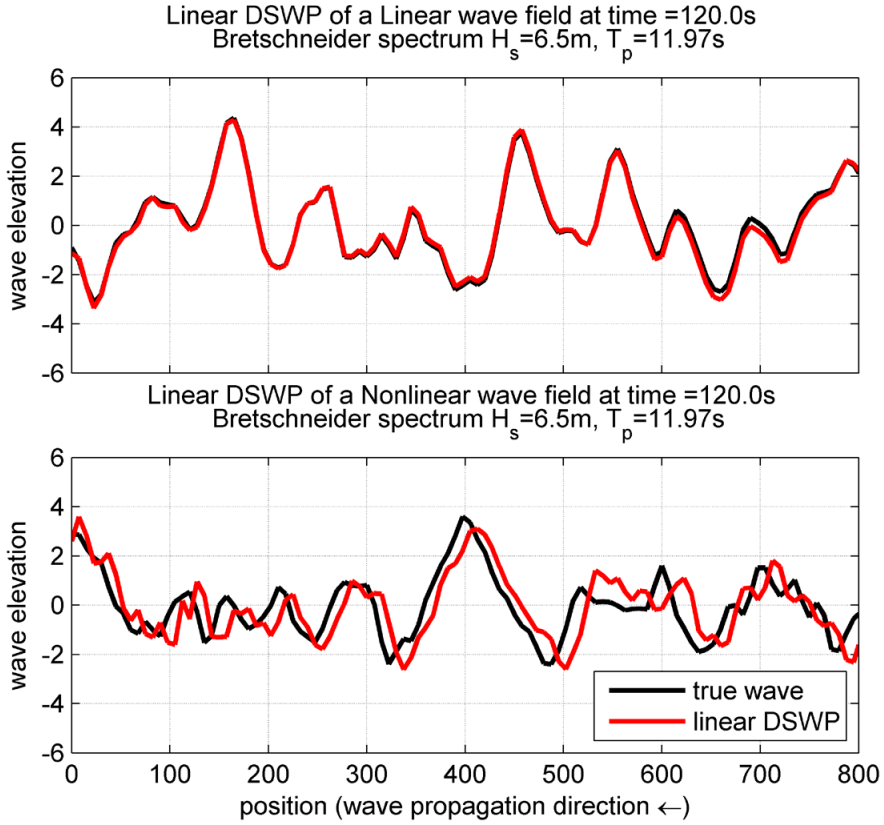

Figure 4.15: Two independent wave elevation realizations for: a linear wave field (top); and a nonlinear wave field (bottom). The true wave elevation is reported with the corresponding linear DSWP. The considered sea condition account for a Bretschneider spectrum with $H_s = 6.5m$ and $T_p = 11.97s$.

4.4.4 Effect of the wave radar inversion error for linear long crested seas

In this section, the LEPrE capability in dealing with the source of noise introduced by the radar inversion procedure is tested. The DSWP procedure has been based on the wave elevation data derived from the LSQR inversion procedure on wave radar images, see chapter §3. The idea is to provide the LEPrE method with an assessment of the noise introduced by the inversion procedure and then to compare the results of the LEPrE method with a set of 100 Monte Carlo simulations based on the actual LSQR reconstruction of wave elevation field. The radar images are assumed to be produced at time $t_0 = 0$, then a linear fitting and propagation is applied to the probe point $x_p = 0m$.

The DSWP model is based on the same discretization assumptions, about space and wave numbers, already presented in section §4.4.3. In particular, the assumed DSWP fitting region is defined by the space interval $x = [450, 2250]m$ that is actually a restriction of the space region where the actual radar images are derived (the reconstruction of the wave elevation is carried out by the LSQR approach within the interval $x = [150, 2542.5]m$, see §3.6.2). This assumption allows accounting for the reconstructed wave elevation in the central measurement region avoiding the spurious effect taking place at the edges of the reconstruction region, as reported in Figure 4.16 (see also section §3.6.2).

The inversion error is modelled by means of a simplified diagonal covariance matrix, C_{δ_M, δ_M}, in equation (4.25), associating at each point on the measurement region, $x_M \in [450, 2250]m$, the corresponding value of the inversion error variance. This assumption does not take into account the spatial correlation of the reconstruction error, but it allows a simpler implementation of the LEPrE method. The diagonal entries of the matrix have been defined on the basis of the inversion error assessment carried out in in section §3.6.2and then fitted to the assumed restricted fitting region, as reported in Figure 4.16.

The sea state conditions considered in this example are associated to a Bretschneider spectrum with $T_p = 11.97s$ and different significant wave heights $H_s = 2.5, 4.5, 6.5, 8.5m$. The underlying wave field is assumed to be linear.

Results of the LEPrE method, accounting for the additional noise introduced by the wave radar reconstruction error, are compared with Monte Carlo simulations results in Figure 4.17 to Figure 4.20, for increasing H_s. Despite the assumed simplified model for the reconstruction error, the LEPrE and Monte Carlo simulation presents an overall common behaviour. In particular, the value of the prediction error is consistently increased, in the time region around $t = 150s$, according to the increased value of the reconstruction error associated to different H_s. Moreover, the LEPrE prediction error can also account, quite satisfactorily, for the time dependence of the prediction error standard deviation, although some more notable differences can be found in the shape of the curve around its minimum values.

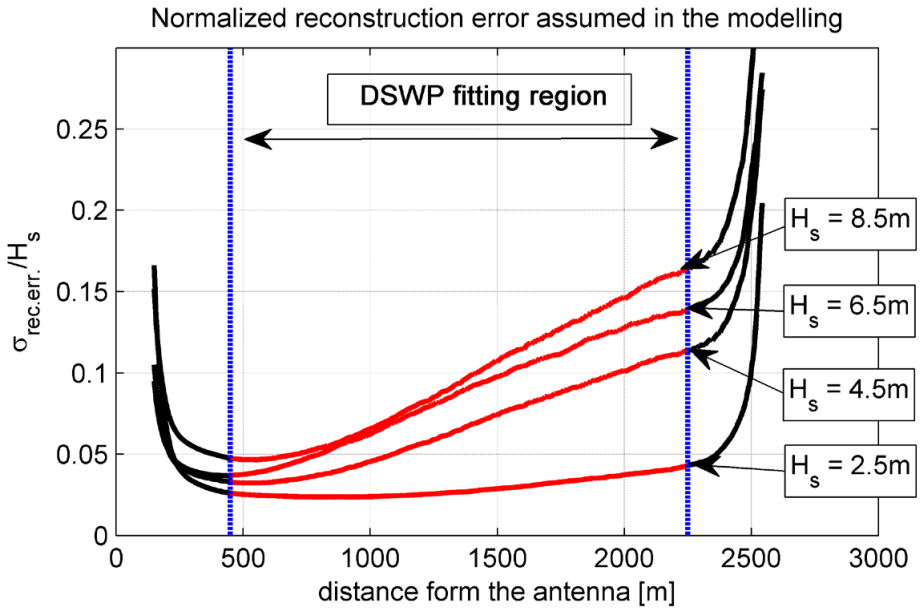

Figure 4.16: Definition of the error associated to the LSQR reconstruction procedure to be used in the LEPrE approach. A restricted region of space where the fitting of the DSWP is applied is highlighted.

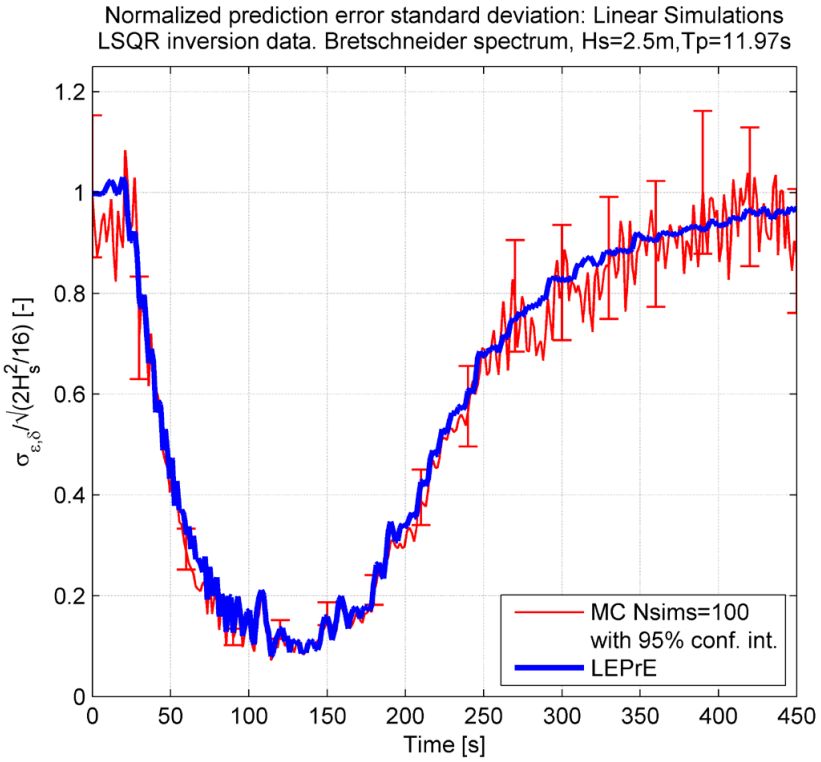

Figure 4.17: Normalized prediction error standard deviation at $x_p = 0m$: comparison between LEPrE and results from 100 Monte Carlo simulations. The noise source coming from the LSQR reconstruction procedure is accounted for by means of a simplified diagonal error covariance matrix. Linear waves generated for a Bretschneider spectrum with $H_s = 2.5m$ and $T_p = 11.97s$.

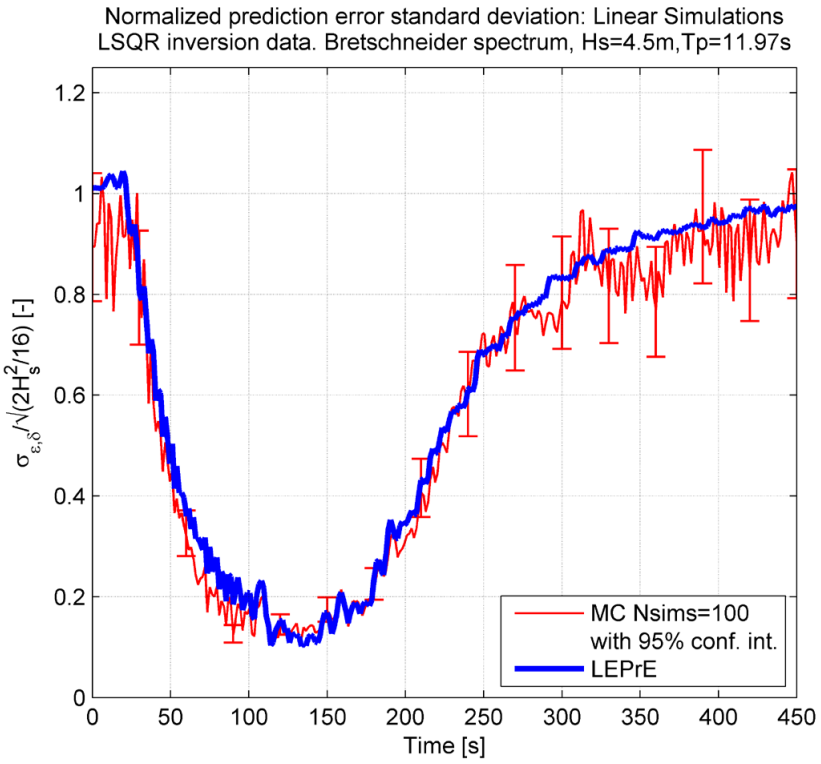

Figure 4.18: Normalized prediction error standard deviation at $x_p = 0m$: comparison between LEPrE and results from 100 Monte Carlo simulations. The noise source coming from the LSQR reconstruction procedure is accounted for by means of a simplified diagonal error covariance matrix. Linear waves generated for a Bretschneider spectrum with $H_s = 4.5m$ and $T_p = 11.97s$.

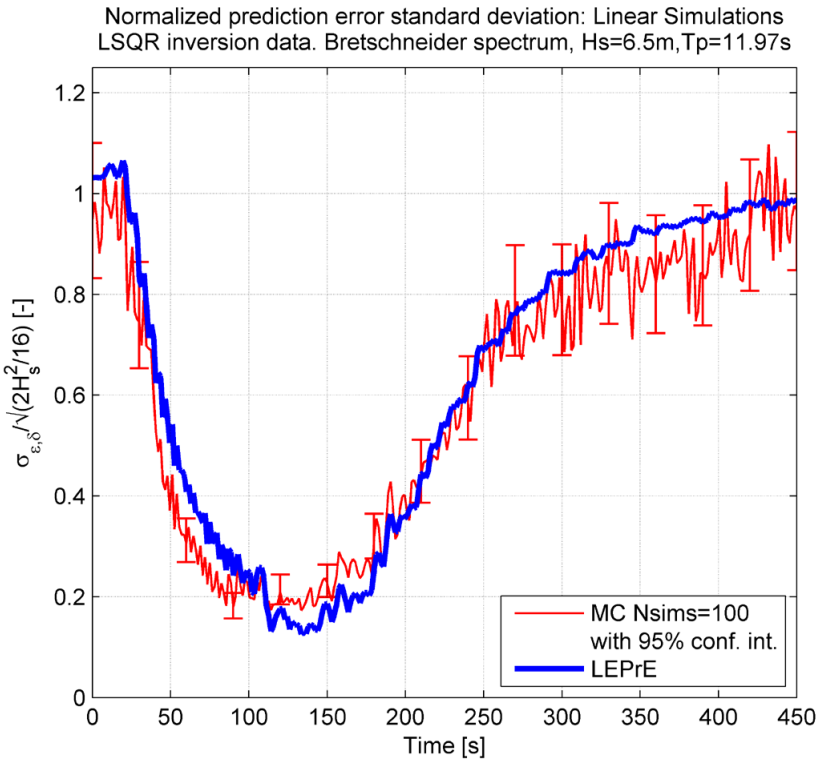

Figure 4.19: Normalized prediction error standard deviation at $x_p = 0m$: comparison between LEPrE and results from 100 Monte Carlo simulations. The noise source coming from the LSQR reconstruction procedure is accounted for by means of a simplified diagonal error covariance matrix. Linear waves generated for a Bretschneider spectrum with $H_s = 6.5m$ and $T_p = 11.97s$.

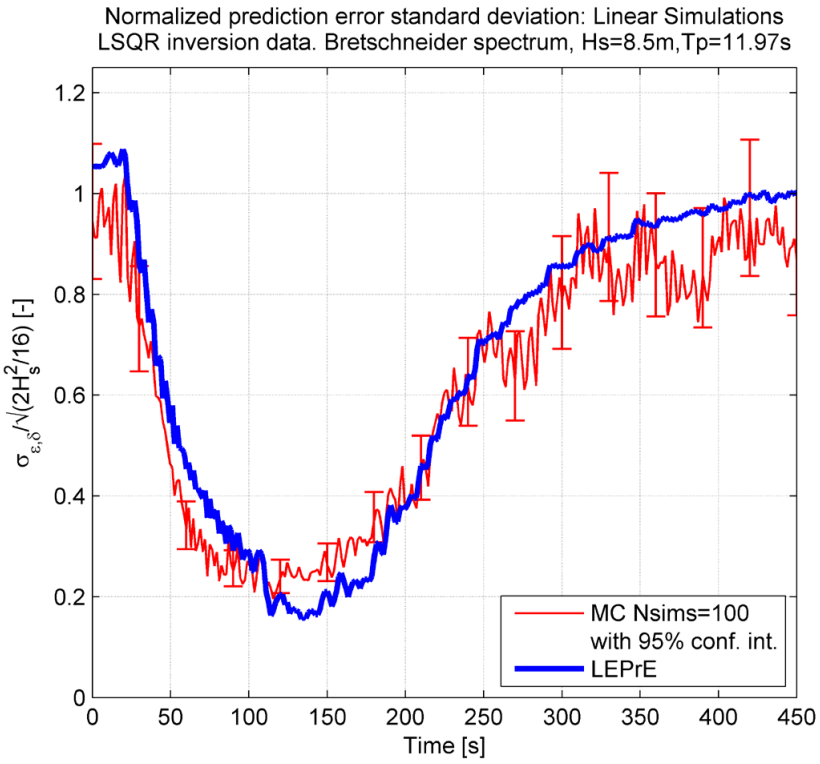

Figure 4.20: Normalized prediction error standard deviation at $x_p = 0m$: comparison between LEPrE and results from 100 Monte Carlo simulations. The noise source coming from the LSQR reconstruction procedure is accounted for by means of a simplified diagonal error covariance matrix. Linear waves generated for a Bretschneider spectrum with $H_s = 8.5m$ and $T_p = 11.97s$.

4.4.5 Short crested sea states

In this example case, the LEPrE methodology is applied to a realistic scenario where the wave elevation is predicted on the basis of the assumed availability of wave radar measurements. Figure 4.21 presents the overall scheme of the problem where a wave radar on an offshore structure scans the nearby sea surface. The wave elevation signal is considered to be measured in a annular domain defined by a maximum radar range $R = 3000m$ and limited by a proximity (blind) range $r = 250m$. The notional wave radar imaging bounds are considered to be representative of a usual wave radar measurement. For sake of simplicity, the wave radar is assumed to provide a reconstruction of the instantaneous wave field on the whole domain without errors. Accordingly the prediction error standard deviation is indicated as σ_ε and not as $\sigma_{\varepsilon_\delta}$. The fitting procedure is carried on a squared sub-domain of the sensing region with dimension $L_x = 1800m \times L_y = 1800m$, as reported in Figure 4.21, and the wave elevation signal is sampled on an evenly spaced grid with spacing $\Delta x = \Delta y = 10m$, which is a typical wave radar resolution. As observed by Blondel-Couprie and Naaijen [17] the propagation model based on the DFT fitting of an instantaneous wave radar image is particularly sensitive to misinterpretation of the correct propagation direction of the wave components, because of the leakage effects. This leads to an incorrect propagation of waves and is, in general, detrimental to a correct prediction of the wave field. In this work the problem has been dealt with by defining the wave numbers used in the fitting and propagation model to belong to the same quadrant of the main propagation direction of the waves so to have $\tilde{k}_x, \tilde{k}_y > 0$ (Blondel-Couprie and Naaijen [17]). This assumption basically corresponds to the implementation, in the fitting model, of specific

information regarding the directional wave spectrum, and the LEPrE methodology can directly handle this sort of situation.

A grid of $N_x N_y$ points, with $N_x = N_y = 181$, is used for the chosen domain. The time instant of the measurement is conventionally set to $t = 0s$ .The fitting/propagation model is defined on the basis of DFT analysis. The selected Fourier wave numbers for the fitting model are defined in vector form as $\underline{\tilde{k}}_{i,j} = \left(\tilde{k}_{x,i}, \tilde{k}_{y,i}\right)^T$ with $\tilde{k}_{x,i} = i2\pi / (N_x \Delta x)$ and $\tilde{k}_{y,j} = j2\pi / (N_y \Delta y)$ with $i = 0,...,\left(N_x - 1\right)/2$ and $j = 0,...,(N_y - 1)/2$. The zero wave number, $\underline{\tilde{k}} = (\tilde{k}_x = 0, \tilde{k}_y = 0)$ is excluded from the calculations. For the propagation model the infinite depth dispersion relation has been used, so that the wave frequency is calculated as $\tilde{\omega}_{i,j} = \sqrt{g \left\| \underline{\tilde{k}}_{i,j} \right\|}$ with $\left\| \underline{\tilde{k}}_{i,j} \right\| = \sqrt{\tilde{k}_{x,i}^2 + \tilde{k}_{y,j}^2}$.

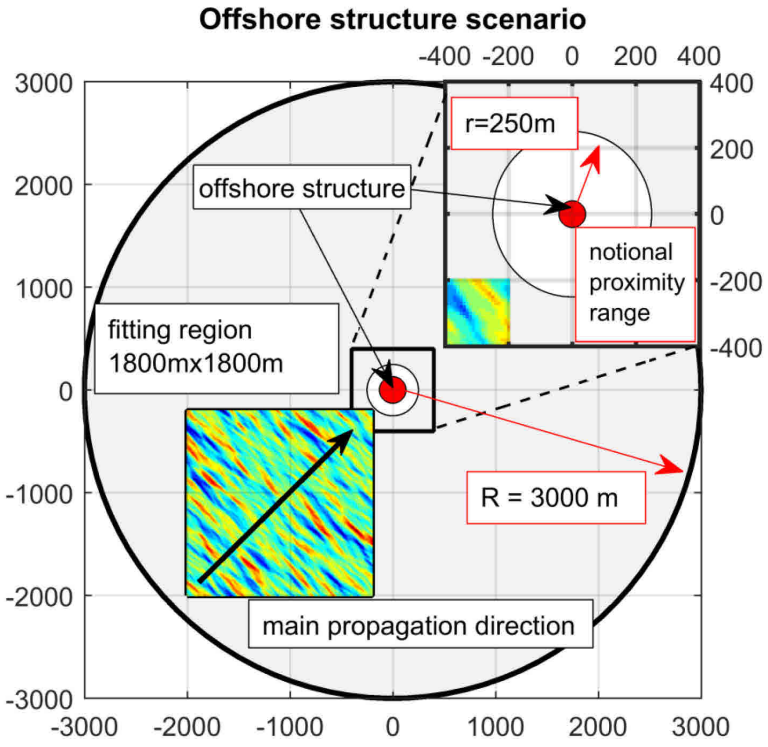

Figure 4.21: Schematic view of the offshore structure scenario. Radii R (maximum sensing range) and r (proximity range) limit the annular sensing region.

A JONSWAP wave elevation spectrum with significant wave height $H_s = 3m$, peak period $T_p = 12s$ and peak enhancement factor $\gamma = 3.3$, is considered in this case. The directional wave spectrum $S(k,\theta)$ is defined by using a multiplicative cosine squared spreading function $D(\theta)$ as follows:

$$\begin{cases} S(k,\theta) = S(k)D(\theta) \\ \mathrm{D}(\theta) = \dfrac{2}{\theta_{spread}} \cos\left(\pi \dfrac{\theta - \chi}{\theta_{spread}} \right)^2 \\ \theta \in \left[\chi - \dfrac{\theta_{spread}}{2}, \chi + \dfrac{\theta_{spread}}{2} \right] \end{cases} \tag{4.47}$$

where θ_{spread} is the spreading angle and χ is the main propagation direction. Different spreading angles are considered for the test, namely $\theta_{spread} = \{30, 60, 90\}$ deg, while the main propagation direction is kept constant, $\chi = 45$ deg. An example of directional spectrum is presented in Figure 4.22.

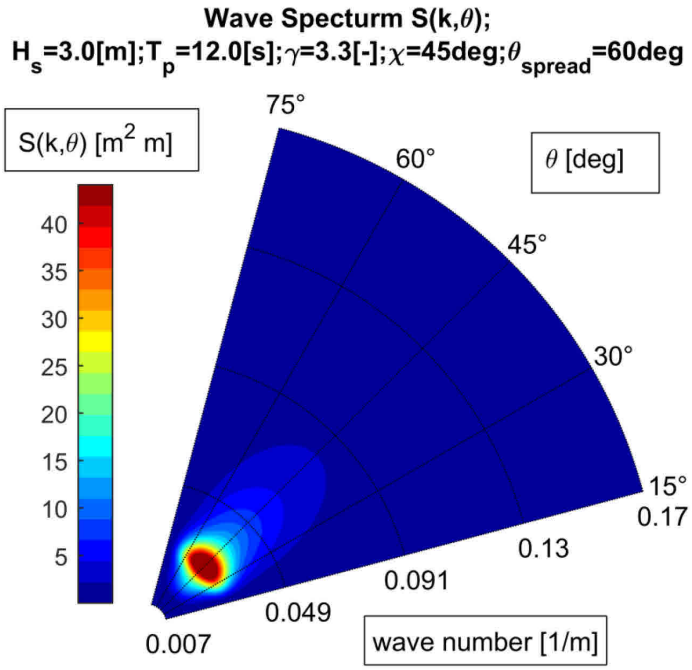

Figure 4.22: Example of directional wave spectrum used in the calculation. JONSWAP spectrum with cosine squared spreading function: main direction $\chi = 45$ deg; spreading angle $\theta_{spread} = 60$ deg (range $[15^\circ, 75^\circ]$).

The LEPrE approach is used here to determine the prediction error standard deviation associated with the assumed fitting and propagation scheme. The determination of the prediction error standard deviation allows also to define, on the one hand, an optimum time delay for the prediction (as shown before) and, on the other hand, a predictability region given a specified threshold value τ_ε (see (4.27)). In the following examples a conventional value $\tau_\varepsilon = 0.05 H_s$ is used. Reported results are also verified against a set of 100 Monte Carlo realizations, which have been analysed in ensemble domain providing estimated expected values and 95% confidence intervals for the prediction error standard deviation.

Figure 4.23 shows the comparison of normalized prediction error standard deviation between Monte Carlo simulation and LEPrE results at the offshore structure location. It is noted that the coordinates reported in Figure 4.23, and in the following ones, are referenced to the lower left corner of the sensing sub-domain shown in Figure 4.21, and therefore the structure is placed at coordinates $x = y = 2000m$. The very good matching between LEPrE results and Monte Carlo simulations, taking into account the sampling uncertainty reflected by confidence intervals, verifies the implementation of LEPrE also for directional sea state application. Similarly to the previously reported examples, the time history of the normalized error shows a minimum, which allows to identify the optimal time delay for a deterministic prediction to be carried out in the considered situation (fitting region, fitting model and sea spectrum). Furthermore, given the considered situation, the behaviour of the prediction error allows also to define the predictability region. The predictability region takes here the form of a predictability time window, as the time interval during which the prediction error standard deviation is below the defined threshold $\tau_\varepsilon = 0.05H_s$, i.e. the time window in the future within which the prediction error is considered to be acceptable, according to the threshold limit, from a probabilistic perspective.

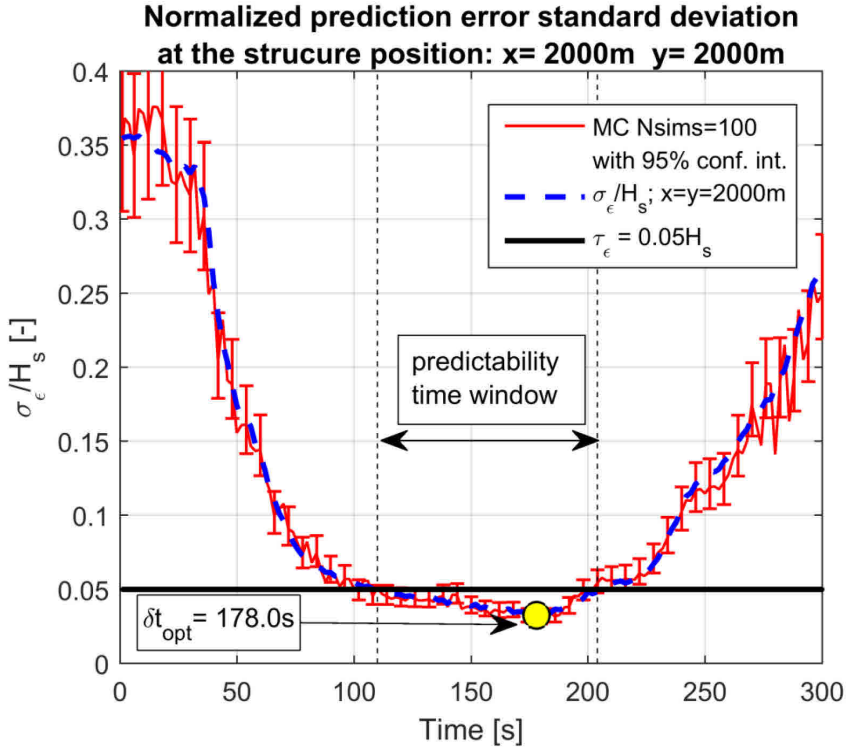

Figure 4.23: Normalized prediction error standard deviation at the structure location for $\theta_{spread} = 30\,\text{deg}$: comparison between LEPrE and results from 100 Monte Carlo simulations.

Figure 4.24 presents the LEPrE results, again at the offshore structure location, as obtained for different spreading angles $\theta_{spread} = \{30, 60, 90\}\,deg$. Results indicate that an increase of prediction error standard deviation is expected as the spreading angle increases. In the specific case of $\theta_{spread} = 90deg$ the prediction error standard deviation of the propagation model fails to drop below the specified (although notional) acceptable threshold limit. This indicates that in some cases a predictability region could not exist and this should be taken as an indication about the need of improving the fitting model and/or changing the measurement region.

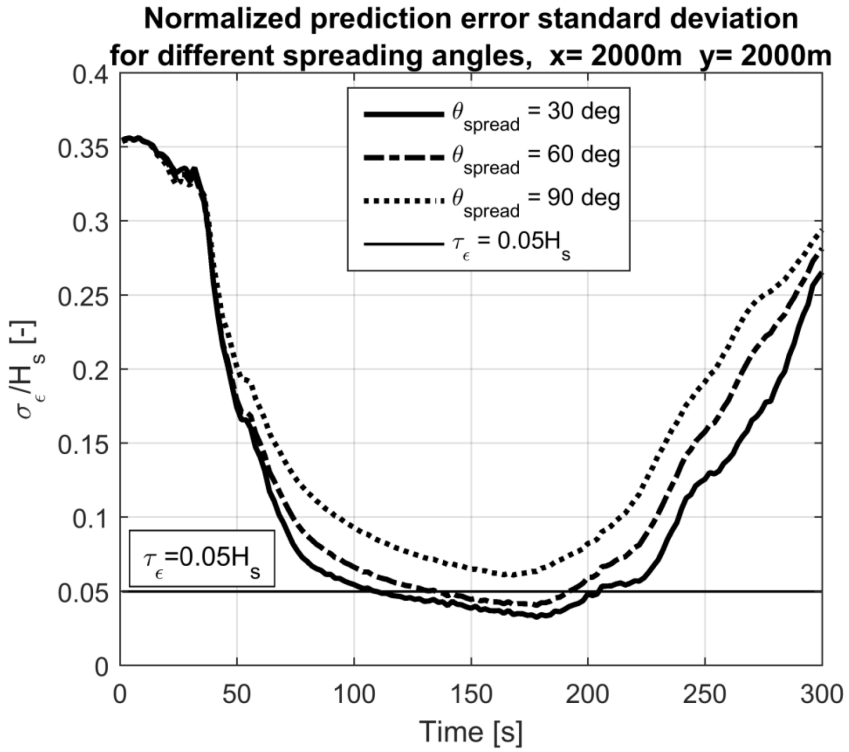

Figure 4.24: Normalized prediction error standard deviation at the structure location for $\theta_{spread} = \{30, 60, 90\}$ deg : LEPrE results.

Finally Figure 4.25 to Figure 4.29 provide maps of the normalized prediction error standard deviation in the space region surrounding the offshore structure, for different time instants, being $t = 0s$ the instant when the fitting of the propagation model takes place. Normalization in this case is carried out using the normalization factor $H_s / 2\sqrt{2}$. Results from Monte Carlo simulations are also reported as verification of the LEPrE predictions, showing that, considering the natural sampling uncertainty from Monte Carlo simulations, the LEPrE implementation can be considered to be verified. Looking at Figure 4.25 to Figure 4.29 as time evolution of the surface of normalized $\sigma_\varepsilon(\underline{x}, t)$, it can be noticed that the region of minimum of the surface, i.e. the region of better prediction from a probabilistic perspective, while modifying its shape in time, propagates along the main wave propagation direction. A smoothing of the "edges" (regions of large gradients) of the surface can be also noted as the time increases, particularly when comparing Figure 4.25 and Figure 4.26.

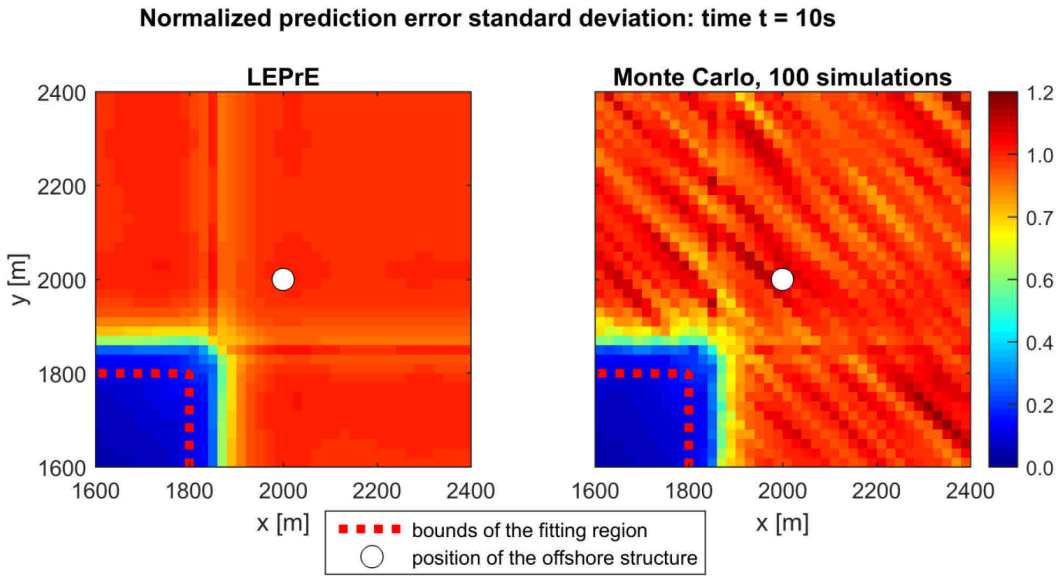

Figure 4.25: Map of normalized prediction error standard deviation at time $t = 10s$ for a spreading angle of $\theta_{spread} = 30\,\mathrm{deg}$. Normalization coefficient: $H_s / 2\sqrt{2}$.: Left: LEPrE results. Right: Monte Carlo simulation results.

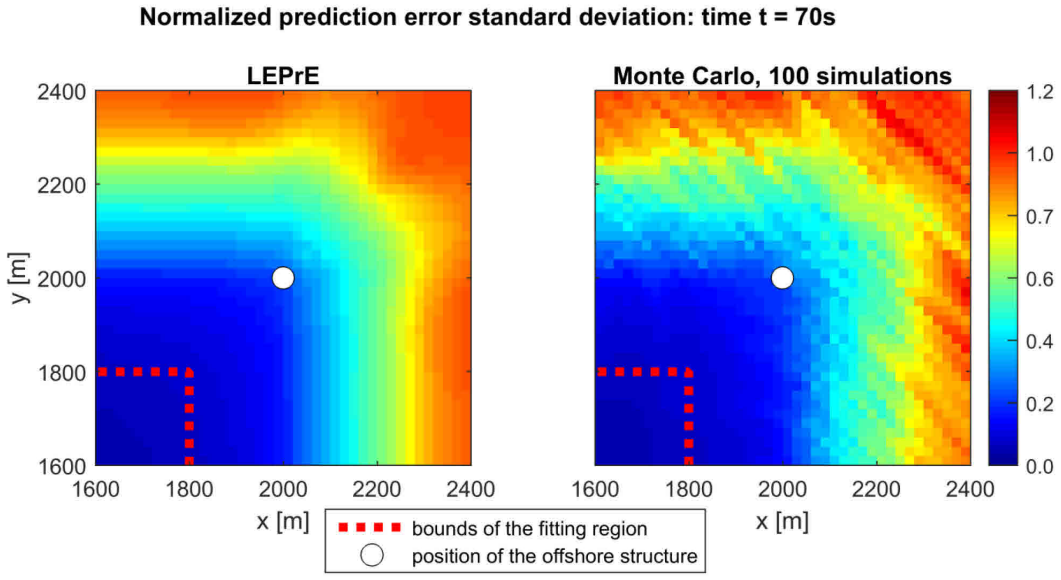

Figure 4.26: Map of normalized prediction error standard deviation at time $t = 70s$ for a spreading angle of $\theta_{spread} = 30\,\mathrm{deg}$. Normalization coefficient:_ $H_s / 2\sqrt{2}$. Left: LEPrE results. Right: Monte Carlo simulation results.

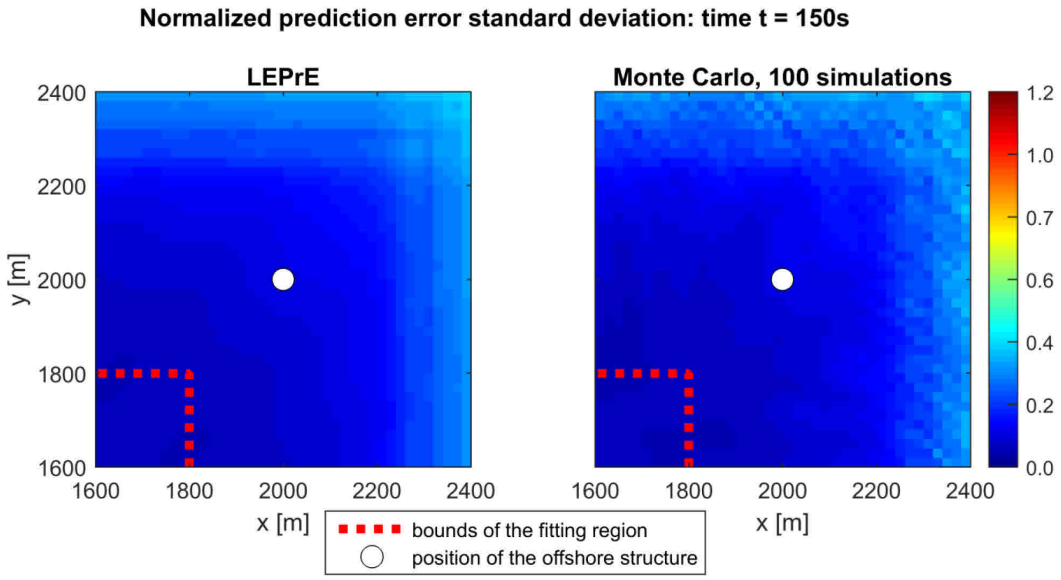

Figure 4.27: Map of normalized prediction error standard deviation at time $t = 150s$ for a spreading angle of $\theta_{spread} = 30\,\mathrm{deg}$. Normalization coefficient: $H_s / 2\sqrt{2}$. Left: LEPrE results. Right: Monte Carlo simulation results.

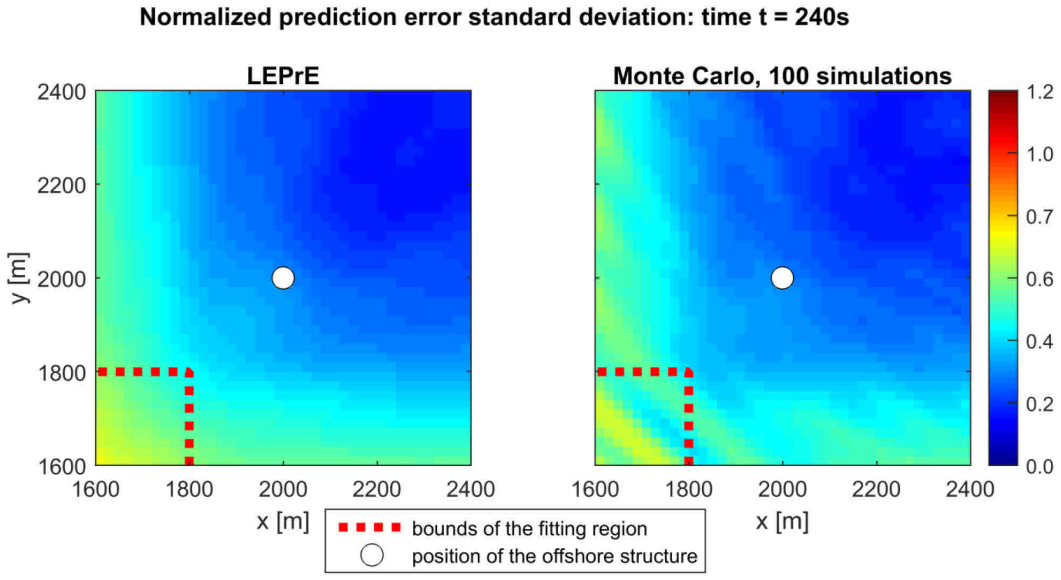

Figure 4.28: Map of normalized prediction error standard deviation at time $t = 240s$ for a spreading angle of $\theta_{spread} = 30\,\mathrm{deg}$. Normalization coefficient: $H_s / 2\sqrt{2}$. Left: LEPrE results. Right: Monte Carlo simulation results.

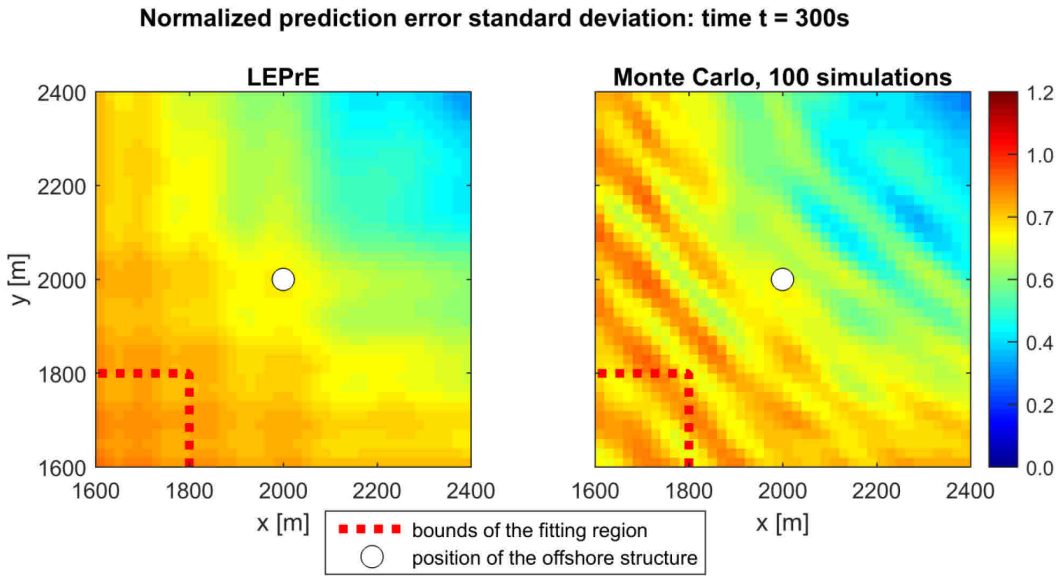

Figure 4.29: Map of normalized prediction error standard deviation at time $t = 300s$ for a spreading angle of $\theta_{spread} = 30\,\text{deg}$. Normalization coefficient: $H_s / 2\sqrt{2}$. Left: LEPrE results. Right: Monte Carlo simulation results.

4.5 Concluding remarks

In this chapter the determination of prediction error statistics for linear DSWP models has been addressed. The proposed approach is based on a redefinition of the problem in the framework of the stochastic processes. In fact, the basic assumptions are the modelling of the wave elevation as a Gaussian process and then assuming that the fitting and propagation model can be obtained by means of linear transformations. The final results is a semi-analytical methodology provided with the possibility to account for additional source of uncertainty, as for example, the ones coming from the error in the wave measurement. Eventually, the presented approach allows to obtain a Linear Estimator of Prediction Error (LEPrE) in space and time, where the prediction error is measured through its ensemble variance. This estimator embeds the characteristics of the fitting model, as well as the exact characteristics of the sea spectrum. The approach is applicable in both long crested and short crested sea states and allows to directly accounting for different types of fitting procedures for the coefficients of the fitting and propagation model.

The LEPrE approach allows to provide a stochastically consistent measure of prediction error and represents a conceptual step forward with respect to existing approaches (binary Predictability Region, and Prediction Error Indicator). Overall, the application of LEPrE methodology provides a full picture of the evolution of the standard deviation of prediction error in space and time. Furthermore, it allows a statistically consistent redefinition of the Predictability Region by specifying the acceptable level of prediction error standard deviation. A qualitative relation has been observed between the prediction error standard deviation from LEPrE and the Prediction Error Indicator. However, the presented methodology does not require the a-priori assumptions underlying the Prediction Error Indicator. In fact, all the properties of the LEPrE method stem directly from the assumption about the wave elevation as a stochastics process.

The LEPrE approach has been applied to a series of representative example cases, covering long crested and short crested seas, as well as unimodal and (archetypal) bimodal spectra. Corresponding Monte Carlo simulations have also been reported for verification purposes, showing the expected agreement with the LEPrE semi-analytical calculations. Some example cases have also accounted for the introduction of the measurement error, as an additional source of uncertainty in the prediction process. This topic has been faced for two long crested sea applications for which the measurement error is considered to be induced either by buoy-like or wave radar-like devices. The performances of the LEPrE have been tested also in the case of prediction of nonlinear wave elevation fields. Although the obtained results cannot be considered as comprehensive as those obtained in the linear case, they suggest some limits in applying the proposed method in the case of wave fields with significant nonlinear features. Eventually, a realistic short crested sea application has been presented with the purpose of stressing the capability of the LEPrE approach of determining the space time region of optimum prediction of the wave elevation. Also in this case there was an overall agreement with the reference Monte Carlo simulations proving this method to be potentially applicable for practical applications in complex sea states, at least in case of moderate steepnesses.

5 DETERMINISTIC SHIP MOTION FORECASTING AND PREDICTION ERROR ASSESSMENT

In this chapter the LEPrE approach is extended to the assessment of the prediction error for the case of linear responses and, in particular, to the case of linear ship motions. The background theory is presented and the prediction of the ship motions has been implemented as a linear transformation applied to a linear DSWP approach. Moreover, the effect of possible wave measurement error on the prediction of motions has been accounted for. A series of example application has been presented considering both a zero-speed floating unit and a ship advancing in the seaway. The extended LEPrE approach has been then verified against a set of Monte Carlo simulations and the main outcomes are discussed. Eventually, some technological and practical indication about the application of the LEPrE approach to ship motions has been reported.

5.1 Introduction

Phase-resolved wave elevation predictions can in principle be used, after a proper coupling with suitable ship motion models, for the deterministic prediction of the behaviour of offshore structures in a seaway. The feasibility of this kind of technology has been widely investigate (Connell et al. [33]; Clauss et al. [31]; Dannenberg et al. [36]; Naaijen and Huijsmans [99]; Naaijen et al. [103]; Naaijen and Blondel-Couprie [98]; Milewski et al. [93]; Reichert et al. [119]) and proposals of integrated system for computer aided decision support systems are becoming a reality (Alford et al. [3]; Clauss et al. [30]; Kusters et al. [75]). The wide majority of this combined models rely on the marine wave radar as the main source for the wave elevation measurement, though, Alford et al. [3] for example, also considered the possibility to integrate the radar measurements with other devices. Then, the propagation of the acquired wave information is carried out, most of the times, by means of linear wave propagation

models based on Fourier techniques resulting in a predicted wave elevation obtained as a linear superposition of wave harmonics. In this respect, the adoption of linear ship motion models appears to be a reasonable option (see for example Naaijen and Huijsmans [99], Kosleck [74]). In addition, the coupling of linear models for both waves and ship motion possibly allows to satisfy the computational time constraints required by an effective real-time prediction, thanks to the reduced computational time required by the application of linear models. In the work of Naaijen and Huijsmans [99] an interesting analysis of the performances of the wave prediction and motion prediction models has been carried out with the support of experimental observation. Interestingly, Naaijen and Huijsmans [99] has shown that, as long as linear ship motions are concerned, the relation between the wave prediction error and the ship motion prediction error is not immediate since a prominent role is played by the wave-structure interaction in terms of response of the dynamical system to the wave forcing. More precisely, it has been shown that the normalized prediction error of the motion depends on the combination of the shape of the sea spectrum and of the motion transfer function (i.e., eventually, of the motion spectrum). This leads, for example, to satisfactory motion prediction even in case of suboptimal wave elevation prediction. Clearly, the opposite can also be true and both the results can be explained by thinking at the structure dynamic response as a linear filter acting on the wave elevation, and so, weighting differently the sea elevation spectrum.

The question arises if, at least in the linear framework, the motion prediction can be directly provided with an error measure capable of consistently accounting for the wave-structure interaction. In fact, a widespread method for assessing in advance the possibility of a satisfactory motion prediction, is to associate this quantity to the time/space region where prediction of the wave elevation is considered as possible, oftentimes identified by means of methods like Predictability Indicator or Predictability Region, see §4. Although the latter can be considered as a reasonable assumption this implicitly assumes the wave elevation and the ship motion predictability horizon to be consistently overlapping (Kosleck [74]), a fact that has been at least questioned by the experiments of Naaijen and Huijsmans [99]. Indeed, since in this simplified approach the wave-structure interaction effects are neglected, the error of the wave elevation prediction is not sufficient for a satisfactory characterization of the motion prediction performance leaving, as open, the problem for a consistent measure of the motion prediction error. Moreover, another aspect, oftentimes overlooked, is the assessment of the influence of wave measurement uncertainties on the motion predictions methods. In this respect, Stredulinsky and Thornhill [136] have found the wave radar, especially when used as a shipborne device on moving platforms, as possibly prone to a considerable dispersion in the measure of the significant wave height that can be eventually corrected by instrument calibration. This brings into play the need of accounting for such measurement uncertainties in a consistent way and to embed the measurement error in the motion prediction methodology.

In this respect, the LEPrE method, developed in §4 as a measure of the ensemble variance of wave elevation prediction error, is herein extended to account for the wave-structure interaction. Indeed, in the framework of the linear seakeeping, the ship responses to the wave excitation can be computed as a linear transformation in frequency domain of the wave complex amplitudes. The resulting adaptation of the LEPrE methodology is straightforward, involving the addition of the linear transformation corresponding to the motion transfer functions. Besides, the additional linear transformations do not affect the stochastic assumption about the error process, and this allows the LEPrE methodology to be consistently extended to the assessment of

the ensemble variance of the motion prediction error. In the same framework, an additional term accounting for the wave measurement error can also be introduced.

The chapter is organized as follows. First the linear model of the ship motion is briefly introduced. Then the LEPrE methodology for the assessment of the ensemble variance of motion prediction error is discussed. Eventually, example applications are reported for two different ships. The first vessel is considered at zero-speed, whereas the second is assumed to be advancing in the seaway with forward speed. The results of the motion prediction error calculated by means of the LEPrE methodology are compared with Monte Carlo simulations results for verification purposes and some example deterministic motion prediction, relevant to the discussion, is also reported to show how the proposed approach can supplement the prediction with a confidence band. Furthermore, the main aspects about the introduction of the wave measurement error are discussed. Eventually some technological and practical indication about the assessment of the motion prediction error is reported.

5.2 Linear ship motion model

The theoretical framework reported herein is derived in the framework of linear seakeeping theory. The derivation is carried out in a right handed inertial reference frame which is steadily translating with the average forward ship speed $\underline{U}_{ship}$. This reference system is identified as $Oxyz$. An additional earth-fixed reference frame, $O'x'y'z'$, is defined as parallel to the translating reference frame $Oxyz$, and considered as coincident to $Oxyz$ at the arbitrary time instant $t = 0$. The location of the centre O of the reference system does not affect the derivation. However, it is convenient to consider the plane Πxy to correspond to the calm water plane.

It is assumed that, in the reference system $Oxyz$, the average ship speed $\underline{U}_{ship}$ becomes

$$\underline{U}_{ship} = \left[U_{ship}, 0, 0 \right]^T \tag{5.1}$$

In this framework, a linear monochromatic Airy wave takes the following form:

$$\begin{cases} \eta\left(\underline{x},t\right) = A\cos\left(\underline{k}\cdot\underline{x} - \omega_e t - \psi_\eta\right) = \\ = a\cos\left(\underline{k}\cdot\underline{x} - \omega_e t\right) + b\sin\left(\underline{k}\cdot\underline{x} - \omega_e t\right) = \underline{p}_\eta\left(\underline{x},t\right)\underline{\alpha} \\ with \\ \underline{p}_\eta\left(\underline{x},t\right) = \left[\cos\left(\underline{k}\cdot\underline{x} - \omega_e t\right), \sin\left(\underline{k}\cdot\underline{x} - \omega_e t\right)\right] \\ \underline{\alpha} = \left[a,b\right]^T \end{cases} \tag{5.2}$$

where $\underline{k} = \left[k_x, k_y \right]^T$ is the wave number vector for the i-th harmonic component, and ω_e is the encounter wave frequency, which can be determined starting from the wave frequency ω, the wave number vector $\underline{k}$ and the ship speed $\underline{U}_{ship}$, as follows:

$$\omega_e = \omega - \underline{k}\cdot\underline{U}_{ship} \tag{5.3}$$

The wave number vector and the wave frequency are linked by the linear dispersion relation as follows:

$$\omega = \sqrt{g\left\|\underline{k}\right\|\tanh\left(\left\|\underline{k}\right\|d\right)} \tag{5.4}$$

where g is the gravitational acceleration and d is the water depth.

It is now assumed that the ship, on average, is at a generic position $\underline{x}_{ship}$ in the reference system $Oxyz$. For sake of simplicity, the position $\underline{x}_{ship}$ will be considered coincident with the origin of $Oxyz$. Thanks to the assumption of linear ship motions, the harmonic response $h(t)$, at steady state, induced by the wave $\eta(\underline{x},t)$ can be determined by means of the transfer function having magnitude $H\left(\underline{k},U_{ship}\right)$ and phase $\gamma_h\left(\underline{k},U_{ship}\right)$ as follows:

$$\begin{cases} h(t) = H\left(\underline{k},U_{ship}\right)A\cos\left(\underline{k}\cdot\underline{x}_{ship} - \omega_e t - \psi_\eta - \gamma_h\left(\underline{k},U_{ship}\right)\right) = \\ = H\left(\underline{k},U_{ship}\right)\left[a\cos\left(\underline{k}\cdot\underline{x} - \omega_e t - \gamma_h\left(\underline{k},U_{ship}\right)\right) + b\sin\left(\underline{k}\cdot\underline{x} - \omega_e t - \gamma_h\left(\underline{k},U_{ship}\right)\right)\right] = \\ = \underline{p}_\eta\left(\underline{x}_{ship},t\right)\underline{\underline{H}}\left(\underline{k},U_{ship}\right)\underline{\alpha} \\ \\ \text{where} \\ \\ \underline{\underline{H}}\left(\underline{k},U_{ship}\right) = H\left(\underline{k},U_{ship}\right)\begin{bmatrix} \cos\left(\gamma_h\left(\underline{k},U_{ship}\right)\right) & -\sin\left(\gamma_h\left(\underline{k},U_{ship}\right)\right) \\ \sin\left(\gamma_h\left(\underline{k},U_{ship}\right)\right) & \cos\left(\gamma_h\left(\underline{k},U_{ship}\right)\right) \end{bmatrix} \end{cases} \tag{5.5}$$

It is underlined that the response transfer function, in terms of magnitude and phase, depends on the wave number vector $\underline{k}$ (i.e. on the wave length and wave propagation direction with respect to the vessel) and on the average forward ship speed. Equation (5.5) is associated to the case of a single monochromatic wave. However, the assumed linearity of the problem allows the use of superposition in case of presence of multiple wave components with different lengths and/or propagation directions, and this will be exploited in the next section. The derivation in the next section is obtained as a generalisation of the LEPrE methodology presented in Fucile et al. [52] [53].

5.3 LEPrE approach for ship motions

Similarly to the case of LEPrE methodology for the assessment of ensemble variance of wave elevation prediction error, presented in §4, (see also Fucile et al. [52] [53]), the true wave elevation is assumed to be given, in discretised form, as the sum of N_η harmonic components:

$$\begin{cases} \eta\left(\underline{x},t\right)=\sum_{i=1}^{N_\eta} a_i \cos\left(\underline{k}_i\cdot\underline{x}-\omega_{e,i}t\right)+b_i \sin\left(\underline{k}_i\cdot\underline{x}-\omega_{e,i}t\right)=\underline{p}_\eta\left(\underline{x},t\right)\underline{\alpha} \\ \underline{p}_\eta\left(\underline{x},t\right)=\left[\begin{array}{l}\cos\left(\underline{k}_1\cdot\underline{x}-\omega_{e,1}t\right),\sin\left(\underline{k}_1\cdot\underline{x}-\omega_{e,1}t\right), \\ ...,\cos\left(\underline{k}_{N_\eta}\cdot\underline{x}-\omega_{e,N_\eta}t\right),\sin\left(\underline{k}_{N_\eta}\cdot\underline{x}-\omega_{e,N_\eta}t\right)\end{array}\right] \\ \underline{\alpha}=\left[a_1,b_1,...,a_{N_\eta},b_{N_\eta}\right]^T \\ \underline{p}_\eta\left(\underline{x},t\right)\in\mathbb{R}^{1,2N_\eta};\underline{\alpha}\in\mathbb{R}^{2N_\eta,1}\end{cases} \tag{5.6}$$

It is also assumed that $\eta\left(\underline{x},t\right)$ can be measured at certain points in space ($\underline{x}\in\mathbb{R}^{2,1}$) and/or time ($t\in\mathbb{R}$), and that the measured wave elevation $\eta_M\left(\underline{x},t\right)$ is associated with a certain measurement error δ_η, i.e.:

$$\eta_M\left(\underline{x},t\right)=\eta\left(\underline{x},t\right)+\delta_\eta\left(\underline{x},t\right) \tag{5.7}$$

The case of measurements without error represents a special case of (5.7) where $\delta_\eta\left(\underline{x},t\right)=0$ for all positions and time instants.

It is now assumed that the true wave elevation is fitted through a phase-resolved wave model $\zeta\left(\underline{x},t\right)$ having the following expression, similar to that of $\eta\left(\underline{x},t\right)$:

$$\begin{cases} \zeta\left(\underline{x},t\right)=\sum_{m=1}^{N_\zeta}\tilde{a}_m\cos\left(\underline{\tilde{k}}_m\cdot\underline{x}-\tilde{\omega}_{e,m}t\right)+\tilde{b}_m\sin\left(\underline{\tilde{k}}_m\cdot\underline{x}-\tilde{\omega}_{e,m}t\right)=\underline{p}_\zeta\left(\underline{x},t\right)\underline{\beta} \\ \underline{p}_\zeta\left(\underline{x},t\right)=\left[\begin{array}{l}\cos\left(\underline{\tilde{k}}_1\cdot\underline{x}-\tilde{\omega}_{e,1}t\right),\sin\left(\underline{\tilde{k}}_1\cdot\underline{x}-\tilde{\omega}_{e,1}t\right), \\ ...,\cos\left(\underline{\tilde{k}}_{N_\zeta}\cdot\underline{x}-\tilde{\omega}_{e,N_\zeta}t\right),\sin\left(\underline{k}_{N_\zeta}\cdot\underline{x}-\omega_{e,N_\zeta}t\right)\end{array}\right] \\ \underline{\beta}=\left[\tilde{a}_1,\tilde{b}_1,...,\tilde{a}_{N_\zeta},\tilde{b}_{N_\zeta}\right]^T \\ \underline{p}_\zeta\left(\underline{x},t\right)\in\mathbb{R}^{1,2N_\zeta};\underline{\beta}\in\mathbb{R}^{2N_\zeta,1}\end{cases} \tag{5.8}$$

It is noted that the phase-resolved fitting wave model implicitly account for Doppler effect by using the encounter frequency in the propagation vector $\underline{p}_\zeta\left(\underline{x},t\right)$. Given a set of N_M measurements $\eta_M\left(\underline{x}_j,t_j\right)\ \ j=1,...,N_M$ at different points in space and/or time, the coefficients vector $\underline{\beta}$ is assumed to be determined by a linear transformation of the available measurements through an appropriate matrix $\underline{\underline{T}}_M$ (Fucile et al. [52] [53]), i.e.:

$$\begin{cases} \underline{\beta}=\underline{\underline{T}}_M\underline{\eta}_M \\ \underline{\underline{T}}_M\in\mathbb{R}^{2N_\zeta,N_M} \\ \underline{\eta}_M=\left[\eta_M\left(\underline{x}_1,t_1\right),...,\eta_M\left(\underline{x}_{N_M},t_{N_M}\right)\right]^T\in\mathbb{R}^{N_M,1}\end{cases} \tag{5.9}$$

In the framework of linear theory, exploiting linear superposition, the true response $h_\eta(t)$, i.e. the system response induced by the true wave elevation $\eta(\underline{x},t)$, is given by:

$$h_\eta(t) = \underline{p}_\eta\left(\underline{x}_{ship},t\right)\underline{\underline{H}}_\eta\,\underline{\alpha} \tag{5.10}$$

where the transfer function matrix $\underline{\underline{H}}_\eta$ is a block diagonal matrix as follows:

$$\underline{\underline{H}}_\eta = \begin{bmatrix} \underline{\underline{H}}\left(\underline{k}_1,U_{ship}\right) & \underline{\underline{0}} & \cdots & \underline{\underline{0}} \\ \underline{\underline{0}} & \underline{\underline{H}}\left(\underline{k}_2,U_{ship}\right) & \cdots & \vdots \\ \vdots & \vdots & \ddots & \underline{\underline{0}} \\ \underline{\underline{0}} & \cdots & \underline{\underline{0}} & \underline{\underline{H}}\left(\underline{k}_{N_\eta},U_{ship}\right) \end{bmatrix} \in \mathbb{R}^{2N_\eta,2N_\eta} \tag{5.11}$$

On the other hand, the response predicted by using the fitted model $\zeta(\underline{x},t)$ and the response transfer function is:

$$h_\zeta(t) = \underline{p}_\zeta\left(\underline{x}_{ship},t\right)\underline{\underline{H}}_\zeta\,\underline{\beta} \tag{5.12}$$

Where, also in this case, the transfer function matrix $\underline{\underline{H}}_\zeta$ is a block diagonal matrix as follows:

$$\underline{\underline{H}}_\zeta = \begin{bmatrix} \underline{\underline{H}}\left(\tilde{\underline{k}}_1,U_{ship}\right) & \underline{\underline{0}} & \cdots & \underline{\underline{0}} \\ \underline{\underline{0}} & \underline{\underline{H}}\left(\tilde{\underline{k}}_2,U_{ship}\right) & \cdots & \vdots \\ \vdots & \vdots & \ddots & \underline{\underline{0}} \\ \underline{\underline{0}} & \cdots & \underline{\underline{0}} & \underline{\underline{H}}\left(\underline{k}_{N_\zeta},U_{ship}\right) \end{bmatrix} \in \mathbb{R}^{2N_\zeta,2N_\zeta} \tag{5.13}$$

The prediction error for the considered response can then be written as:

$$\begin{aligned} &\varepsilon_{h,\delta}(t) = h_\zeta(t) - h_\eta(t) = \underline{p}_\zeta\left(\underline{x}_{ship},t\right)\underline{\underline{H}}_\zeta\,\underline{\beta} - \underline{p}_\eta\left(\underline{x}_{ship},t\right)\underline{\underline{H}}_\eta\,\underline{\alpha} = \\ &= \underline{p}_\zeta\left(\underline{x}_{ship},t\right)\underline{\underline{H}}_\zeta\,\underline{\underline{T}}_M\,\underline{\eta}_M - \underline{p}_\eta\left(\underline{x}_{ship},t\right)\underline{\underline{H}}_\eta\,\underline{\alpha} \end{aligned} \tag{5.14}$$

The subscript δ in $\varepsilon_{h,\delta}(t)$ highlights the fact that the prediction error takes into account also the presence of measurement noise which is embedded in $\underline{\eta}_M$ according to (5.7). Furthermore, using (5.6) and (5.7), the vector of measured wave elevation can be written as:

$$\begin{cases} \underline{\eta}_M = \underline{\eta} + \underline{\delta}_{\eta,M} = \underline{\underline{P}}_{\eta,M}\,\underline{\alpha} + \underline{\delta}_{\eta,M} \\ \underline{\underline{P}}_{\eta,M} = \begin{bmatrix} \underline{p}_\eta\left(\underline{x}_1, t_1\right) \\ \vdots \\ \underline{p}_\eta\left(\underline{x}_{N_M}, t_{N_M}\right) \end{bmatrix} \in \mathbb{R}^{N_M, 2N_\eta} \\ \underline{\delta}_{\eta,M} = \left[\delta_\eta\left(\underline{x}_1, t_1\right), \ldots, \delta_\eta\left(\underline{x}_{N_M}, t_{N_M}\right)\right]^T \in \mathbb{R}^{N_M, 1} \end{cases} \tag{5.15}$$

Substituting (5.15) in (5.14), it is possible to recast $\varepsilon_{h,\delta}\left(t\right)$ as follows:

$$\begin{cases} \varepsilon_{h,\delta}\left(t\right) = \underline{q}_h\left(t\right)\underline{\alpha} + \underline{n}_h\left(t\right)\underline{\delta}_{\eta,M} \\ \text{with} \\ \underline{q}_h\left(t\right) = \underline{p}_\zeta\left(\underline{x}_{ship}, t\right)\underline{\underline{H}}_\zeta\,\underline{\underline{T}}_M\,\underline{\underline{P}}_{\eta,M} - \underline{p}_\eta\left(\underline{x}_{ship}, t\right)\underline{\underline{H}}_\eta \\ \underline{n}_h\left(t\right) = \underline{p}_\zeta\left(\underline{x}_{ship}, t\right)\underline{\underline{H}}_\zeta\,\underline{\underline{T}}_M \\ \underline{q}_h\left(t\right) \in \mathbb{R}^{1,2N_\eta} \;;\; \underline{n}_h\left(t\right) \in \mathbb{R}^{1,N_M} \end{cases} \tag{5.16}$$

Similarly to the case of deterministic wave elevation prediction, the error $\varepsilon_{h,\delta}\left(t\right)$ has two sources. The first term, $\underline{q}_h\left(t\right)\underline{\alpha}$, represents the error due to the fact that the fitted model for the wave elevation, in general, differs from the actual wave elevation process. As a result, the true response and the predicted response, which are obtained through the transfer function of the system at the respective wave numbers, differ as well. The second term, $\underline{n}_h\left(t\right)\underline{\delta}_{\eta,M}$, represents the propagation of the measurement error through the fitted model. Both error sources also embed the effect of the fitting procedure.

In order to obtain error statistics, exactly as in Fucile et al. [52] [53], also in this case it is assumed that $\eta\left(\underline{x}, t\right)$ is a (discretised) linear Gaussian process. Hence, the amplitudes a_i and b_i of the harmonic components are considered as zero mean independent Gaussian variables, which are linked to the (single side) directional wave energy spectrum $S_\eta\left(\underline{k}_i\right)$ as follows:

$$\begin{cases} a_i \sim N\left(0, \sigma_i^2\right) \;;\; b_i \sim N\left(0, \sigma_i^2\right) \;;\; \sigma_i^2 = S_\eta\left(\underline{k}_i\right)\Delta k_{x,i}\Delta k_{y,i} \\ COV\left\{a_i, a_j\right\} = \begin{cases} 0 & i \neq j \\ \sigma_i^2 & i = j \end{cases} \;;\; COV\left\{b_i, b_j\right\} = \begin{cases} 0 & i \neq j \\ \sigma_i^2 & i = j \end{cases} \\ COV\left\{a_i, b_j\right\} = 0 \quad \forall i, j \end{cases} \tag{5.17}$$

It then follows that the mean value of the random vector $\underline{\alpha}$ and its covariance matrix are:

$$\begin{cases} \underline{\mu}_{\underline{\alpha}} = E\left\{\underline{\alpha}\right\} = \underline{0} \\ \underline{\underline{C}}_{\underline{\alpha},\underline{\alpha}} = E\left\{\left(\underline{\alpha} - \underline{\mu}_{\underline{\alpha}}\right)\left(\underline{\alpha} - \underline{\mu}_{\underline{\alpha}}\right)^T\right\} = \begin{bmatrix} \sigma_1^2 & 0 & \dots & 0 & 0 \\ 0 & \sigma_1^2 & \cdots & 0 & 0 \\ \vdots & \vdots & \ddots & \vdots & \vdots \\ 0 & 0 & \cdots & \sigma_{N_\eta}^2 & 0 \\ 0 & 0 & \cdots & 0 & \sigma_{N_\eta}^2 \end{bmatrix} = \\ = diag\left(\sigma_1^2, \sigma_1^2, ..., \sigma_{N_\eta}^2, \sigma_{N_\eta}^2\right) \end{cases} \tag{5.18}$$

It is also assumed at this stage that the wave measurement error vector at the measurement points $\underline{\delta}_{\eta,M}$ is a zero mean Gaussian vector with a given covariance matrix depending on the assumed measurement error characteristics, i.e.:

$$\begin{cases} \underline{\mu}_{\underline{\delta}_{\eta,M}} = E\left\{\underline{\delta}_{\eta,M}\right\} = \underline{0} \\ \underline{\underline{C}}_{\underline{\delta}_{\eta,M},\underline{\delta}_{\eta,M}} = E\left\{\left(\underline{\delta}_{\eta,M} - \underline{\mu}_{\underline{\delta}_{\eta,M}}\right)\left(\underline{\delta}_{\eta,M} - \underline{\mu}_{\underline{\delta}_{\eta,M}}\right)^T\right\} \end{cases} \tag{5.19}$$

By using (5.14), (5.18) and (5.19), the assumption that $\delta_\eta\left(\underline{x},t\right)$ is independent of η, and recalling that, from the considered assumptions, $\underline{q}_h\left(t\right)$ and $\underline{n}_h\left(t\right)$ are deterministic vector functions, it is now possible to provide a full probabilistic characterisation of the prediction error $\varepsilon_{h,\delta}\left(t\right)$. In fact, from (5.14), it follows that $\varepsilon_{h,\delta}\left(t\right)$ is a Gaussian process, since it is a linear combination of random Gaussian vectors. Furthermore, the mean and the variance of $\varepsilon_{h,\delta}\left(t\right)$ can be determined as follows:

$$\begin{cases} E\left\{\varepsilon_{h,\delta}\left(t\right)\right\} = 0 \\ Var\left\{\varepsilon_{h,\delta}\left(t\right)\right\} = \sigma_{\varepsilon_{h,\delta}}^2\left(t\right) = \underline{q}_h\left(t\right)\underline{\underline{C}}_{\underline{\alpha},\underline{\alpha}}\underline{q}_h^T\left(t\right) + \underline{n}_h\left(t\right)\underline{\underline{C}}_{\underline{\delta}_{\eta,M},\underline{\delta}_{\eta,M}}\underline{n}_h^T\left(t\right) \end{cases} \tag{5.20}$$

From the considered assumptions, it follows that the prediction error has zero mean. In addition, similarly to what was noticed when commenting (5.16), it can be noticed that also in (5.20) the variance of the prediction error is composed of two terms: the first term is associated with the inherent difference between the fitted model and the true process, while the second term represents the effect of the measurement error. In both terms the effect of the fitting procedure and of the transfer function of the system are automatically embedded.

Using now the fact that the covariance matrix $\underline{\underline{C}}_{\underline{\alpha},\underline{\alpha}}$ is diagonal (see (5.18)), it is possible to rewrite the ensemble variance of prediction error as:

$$\sigma^2_{\varepsilon_{h,\delta}}(t) = \underline{q}_h(\underline{x},t)\underline{\underline{C}}_{\alpha,\alpha}\underline{q}_h^T(t) + \underline{n}_h(t)\underline{\underline{C}}_{\underline{\delta}_{\eta,M},\underline{\delta}_{\eta,M}}\underline{n}_{h_j}^T(t) =$$

$$\underbrace{\underline{\underline{C}}_{\alpha,\alpha}}_{\text{diagonal}} \sum_{i=1}^{N_\eta}\left(q^2_{h,2i-1}(t) + q^2_{h,2i}(t)\right)\sigma_i^2 + \underline{n}_h(t)\underline{\underline{C}}_{\underline{\delta}_{\eta,M},\underline{\delta}_{\eta,M}}\underline{n}_h^T(t) = \tag{5.21}$$

$$= \sum_{i=1}^{N_\eta}\left(q^2_{h,2i-1}(t) + q^2_{h,2i}(t)\right)S_\eta(\underline{k}_i)\Delta k_{x,i}\Delta k_{y,i} + \underline{n}_h(t)\underline{\underline{C}}_{\underline{\delta}_{\eta,M},\underline{\delta}_{\eta,M}}\underline{n}_h^T(t)$$

In the limit the number of harmonics assumed in the model of $\eta(\underline{x},t)$ increases towards infinity ($N_\eta \to \infty$), the first term in (5.21) tends to an integral involving the spectrum of η, and the variance of the prediction error can be rewritten as:

$$\sigma^2_{\varepsilon_{h,\delta}}(t) = \iint\left(g_1^2(\underline{k},U_{ship},t) + g_2^2(\underline{k},U_{ship},t)\right)S_\eta(\underline{k})dk_x dk_y + \underline{n}_h(t)\underline{\underline{C}}_{\underline{\delta}_{\eta,M},\underline{\delta}_{\eta,M}}\underline{n}_h^T(t) \tag{5.22}$$

where $g_1^2(\underline{k},U_{ship},t)$ and $g_2^2(\underline{k},U_{ship},t)$ are functions depending on the fitting procedure and on the characteristics of the transfer function of the system for the response h.

In those special cases where the measurement errors δ_η at two different points in time and space are independent, the covariance matrix $\underline{\underline{C}}_{\underline{\delta}_{\eta,M},\underline{\delta}_{\eta,M}}$ becomes diagonal

$$\underline{\underline{C}}_{\underline{\delta}_{\eta,M},\underline{\delta}_{\eta,M}} = \begin{bmatrix} \sigma^2_{\delta_\eta}(\underline{x}_1,t_1) & 0 & \cdots & 0 \\ 0 & \sigma^2_{\delta_\eta}(\underline{x}_2,t_2) & \cdots & 0 \\ \vdots & \vdots & \ddots & \vdots \\ 0 & 0 & \cdots & \sigma^2_{\delta_\eta}(\underline{x}_{N_M},t_{N_M}) \end{bmatrix} \tag{5.23}$$

and the term $\underline{n}_h(t)\underline{\underline{C}}_{\underline{\delta}_{\eta,M},\underline{\delta}_{\eta,M}}\underline{n}_h^T(t)$, therefore, simplifies to

$$\underline{n}_h(t)\underline{\underline{C}}_{\underline{\delta}_{\eta,M},\underline{\delta}_{\eta,M}}\underline{n}_h^T(t) \quad \underbrace{=}_{\text{diagonal}} \quad \underline{\underline{C}}_{\underline{\delta}_{\eta,M},\underline{\delta}_{\eta,M}} \quad \sum_{j=1}^{N_M} n^2_{h,j}(t)\sigma^2_{\delta_\eta}(\underline{x}_j,t_j) \tag{5.24}$$

It is finally noted that the LEPrE methodology developed by Fucile et al. [52] [53] for the estimation of the ensemble variance of the wave elevation prediction error is a special case in the framework presented herein. In fact, it can be obtained by simply considering the transfer function matrix $\underline{\underline{H}}(\tilde{\underline{k}},U_{ship})$ as the 2x2 identity matrix.

5.4 Example applications

A series of example applications have been carried out only considering the case of long crested seas. Two different sea conditions, both characterised by a Bretschneider spectrum, and with significant wave height $H_s = [2.5, 6.5]m$ and peak period $T_p = [11.97, 17.60]s$, respectively, have been considered. The motion prediction procedure has been set up as depicted in Figure 5.1.

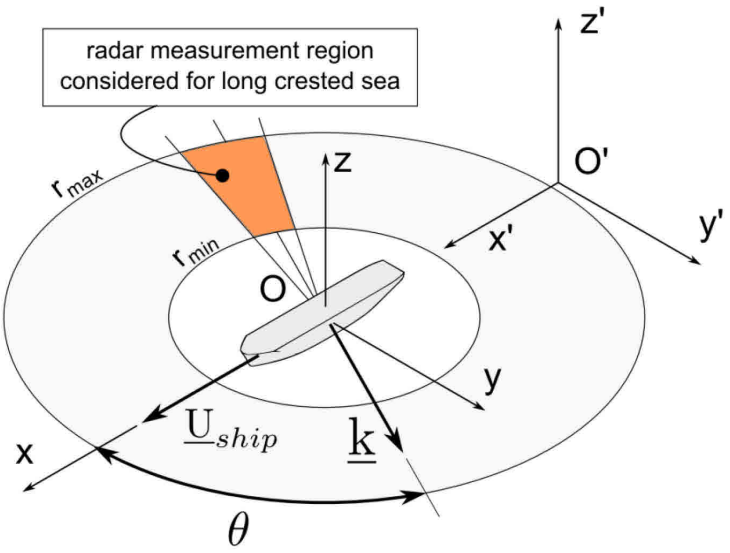

Figure 5.1: Scheme for the set-up of the motion prediction methodology for the case of long crested sea.

In the examples reported in this section it is assumed that wave radar is capable of retrieving the true wave elevation without measurement error. The effect of measurement error is separately discussed in §5.5. Since only long crested seas are considered, the measurement of the wave elevation is assumed to be carried out along the direction of the wave vector $\underline{k}$ and in the space region from which the waves are considered to come from. The wave elevation data are considered to be available every $\tau_a = 1.5s$ and on a grid of points with spatial discretization $dr = 7.5m$. The radar images are considered to be available in an annular region, as report Figure 5.1, with inner bound defined as r_{min}. The maximum extent of the sensing region is given by the radius r_{max}. Three different inner and outer bounds have been considered for the calculations, corresponding to different values of r_{min}, in particular $r_{min} = [150, 300, 600, 1200]m$, and different lengths $L_M = r_{max} - r_{min}$ of the spatial intervals over which the wave elevation is measured, namely $L_M = [1200, 2400, 4800]m$.

LEPrE predictions and Monte Carlo simulations have been carried out for a set of different ship-wave encounter angles $\theta = [0, 45, 90, 135, 180]\,\text{deg}$. The calculations of the motions are referred to the seakeeping reference point, placed over the mid perpendicular of the ship, on the centreplane, and at a height corresponding to the calm water, and $\underline{x}_{ship} \equiv O$.

The motion transfer function has been calculated by means of strip theory tool (Bulian and Francescutto [24]). For each of the encounter angle the corresponding Response Amplitude Operator of the motion (RAO) has been calculated. The RAO have been then re-interpolated on the basis of the wave number discretization coming from the fitting step of the wave elevation propagation. In the case of forward speed the correction of the encounter frequency has been taken into account by means of the relation (5.3).

5.4.1 FPSO at zero speed

5.4.1.1 Ship geometry and mechanical data

The ship used for the zero speed calculation is based on the geometry and the main mechanical data of a Floating Production Storage and Offloading unit (FPSO) ship as reported by Greco et al. [60] [61] and Lugni et al. [80]. Views of the three dimensional geometry are shown in Figure 5.2. The main geometrical data and mechanical data are reported in Table 5.1 and Table 5.2, respectively.

The FPSO is provided with bilge keels, see Table 5.3, and the additional quadratic damping term for the roll motion has been accounted for as a linear equivalent roll damping approach, in order to keep the linear framework. Greco et al., [60] [61] and Lugni et al. [80] reported the values of the equivalent linear roll damping calculated from the roll decay experiment. However, during the roll decay test, the model was fixed to a gimble restraining the sway and yaw motions. For this reason, herein, the equivalent roll damping has been recalculated taking as reference the work of de Oliveira and Fernandes [37] and interpolating the reported data for the bilge keels and the ship data considered herein. The equivalent linear damping reported in Table 5.3 has been calculated for two reference roll amplitudes $\phi_e = [5,10]\text{deg}$ and it is reported in Table 5.3 in dimensionless form, normalized with respected to critical roll damping.

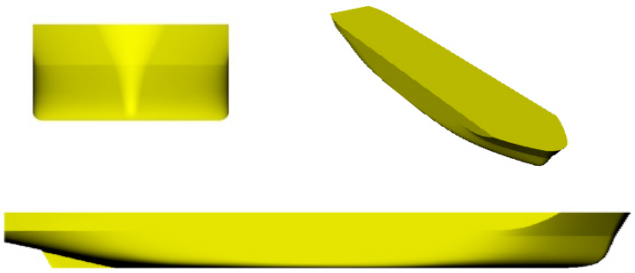

Figure 5.2: FPSO hull. Representative views.

Table 5.1: FPSO. Main geometrical data.

Ship length between perpendiculars L_{BP}	m	*168.80*
Ship Breath B	m	*32.26*
Draught T	m	*10.00*
Trim	m	*0.00*
Hull volume ∇	m^3	*42401*

Table 5.2: FPSO. Main mechanical data.

Vertical position of the centre of gravity (w.r.t. the keel point) KG	m	*12.922*
Transversal metacentric height GM_T	m	*1.44*
Dimensionless (w.r.t. B) dry roll radius (w.r.t CoG)	-	*0.37*
Dimensionless (w.r.t. L_{BP}) dry pitch and yaw radii (w.r.t. CoG)	-	*0.27*

Table 5.3: FPSO. Bilge keels data, equivalent roll damping and natural roll period.

Length of bilge keels	m	*67.52*
Span of bilge keels	m	*0.50*
Roll natural period	s	*22.15*
Equivalent dimensionless (w.r.t. critical) linear roll damping for 5deg at zero-speed	-	*0.029*
Equivalent Dimensionless (w.r.t. critical) linear roll damping for 10deg at zero-speed	-	*0.056*

5.4.1.2 Test conditions

Calculations have been performed for a Bretschneider spectrum with significant wave height $H_s = 6.5m$ and peak period $T_p = 17.60s$. The considered wave encounter angle is $\theta = 90\,\text{deg}$ (beam waves) and the assumed linear damping accounted for is the one calculated for the roll amplitude $\phi_e = 10\,\text{deg}$. Results from the application of the LEPrE methodology have been compared with a set of 100 Monte Carlo simulations. For the simulations of the deterministic predictions of motions it is assumed that the wave elevation data are available at a single the time instant $t = 0s$ and in a spatial interval of length $L_M = 2400m$. Then a linear wave prediction model propagates the wave from the measurement region, see Figure 5.1, to the ship reference position, O, which coincides with O' at zero speed. Then, accounting for the motion transfer functions, the predicted motions are calculated. The wave prediction model is based on a discretized set of wave numbers $N = 160$ defined as $\|k_n\| = \frac{2\pi}{L_M} n$ with $n = [1,...,160]$ and with corresponding wave frequency calculated for the deep water condition $\omega_n = \sqrt{g\|k_n\|}$.

5.4.1.3 Results

The main aim of this section is to show, by means of a simple example, how the LEPrE methodology can account for the relative shapes of the motion transfer functions and the input wave spectrum, producing a consisted assessment of the deterministic motion prediction error. To this end, the normalized sea spectrum and the normalized motion spectrum for heave, roll and pitch motions are reported with the normalized RAO, in Figure 5.3, Figure 5.4 and Figure 5.5. The comparison of the normalized standard deviation of motion prediction error between the LEPrE methodology and the Monte Carlo results is presented in Figure 5.7. The normalization constant is two times the variance of exact motion calculated by using the true wave elevation spectrum as $\sigma^2_{\eta,h_j} = \int RAO^2_{h_j} S_\eta(k)dk$. The LEPrE approach, within the sampling uncertainties associated to the reduced number of Monte Carlo simulation, can be considered as verified also in the case of the linear ship motion. Moreover, it is interesting to note how the prediction error of heave, roll and pitch motions exhibit completely different behaviours. For the heave motion, the time interval for which the prediction error attains its lower values is very much consistent with the corresponding time interval of the prediction error for the wave elevation as presented in Figure 5.6. On the contrary, the roll motion presents a much focused region where the minimum of the error is attained. Further, the pitch motion, though characterized by an expectable low response in beam sea, see Figure 5.8, shows the larger region of minimum of the prediction error. Indeed,

these results are visually confirmed by the time history of an example linear deterministic motion prediction, presented in Figure 5.8. A qualitative understanding of the observed behaviour could be gained by looking at Figure 5.3, Figure 5.4 and Figure 5.5 and noting the different shapes of the motion spectra. In the case of roll, the transfer function acts like as a band-pass pass filter at relatively low frequencies. For the pitch the transfer function also acts as a band-pass filter, but centred at higher frequency, such that the pitch motion spectrum retain only the high frequency components. Finally the heave, being characterised by an almost constant transfer function in the considered wave spectrum region, retains almost all the features of the wave elevation spectrum. This means that the transfer function can be thought as "filtering/modifying" the prediction error characteristics accounting, in the case of roll for the error associated with the propagation of the longer waves, for heave for the prediction error for the whole spectral bandwidth and for pitch only for the error associated with the propagation of the shorter and slower waves. This line of reasoning could also explain the fact that the prediction error associated with roll is larger than the other two. This is mainly related to the small dimension of the fitting region, $L_M = 2400m$ which, compared to the typical wave length of the spectrum $\lambda_p \equiv \frac{g}{2\pi} T_p^{\,2} = 484m$, suggests a lack of frequency resolution especially in catching the longer wave components (i.e. the lower wave frequency components). In order to support these last arguments, in section §5.6, the roll prediction error has also been calculated in the case of extended or reduced measurement regions.

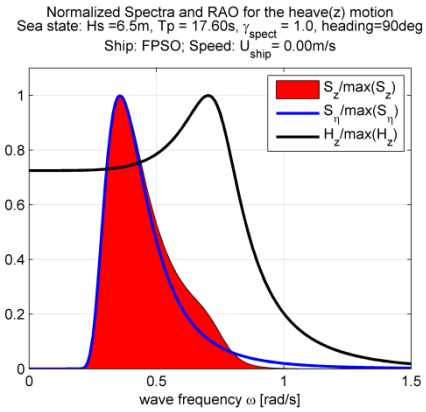

Figure 5.3: FPSO at zero speed with wave encounter angle 90deg (beam waves). Normalized spectrum of the wave elevation, normalized spectrum of the heave motion and normalized RAO of the heave motion.

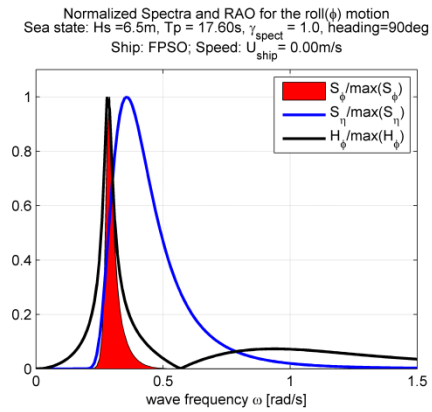

Figure 5.4: FPSO at zero speed with wave encounter angle 90deg (beam waves). Normalized spectrum of the wave elevation, normalized spectrum of the roll motion and normalized RAO of the roll motion..

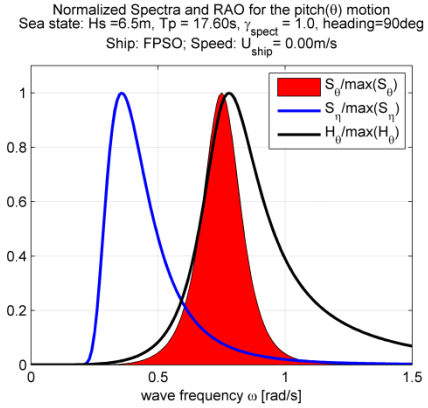

Figure 5.5: FPSO at zero speed with wave encounter angle 90deg (beam waves). Normalized spectrum of the wave elevation, normalized spectrum of the pitch motion and normalized RAO of the pitch motion.

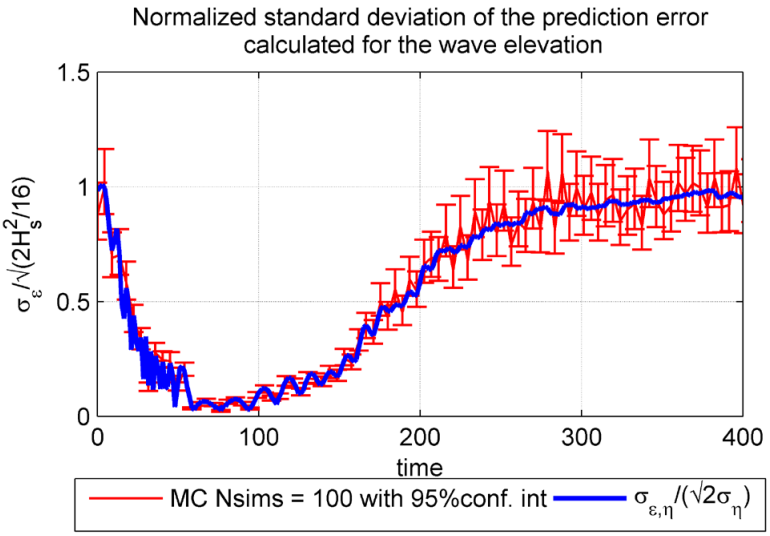

Figure 5.6: Normalized standard deviation of the prediction error for the wave elevation, in the case of a Bretschneider spectrum with significant wave height $H_s = 6.5m$ and peak period $T_p = 17.60s$.

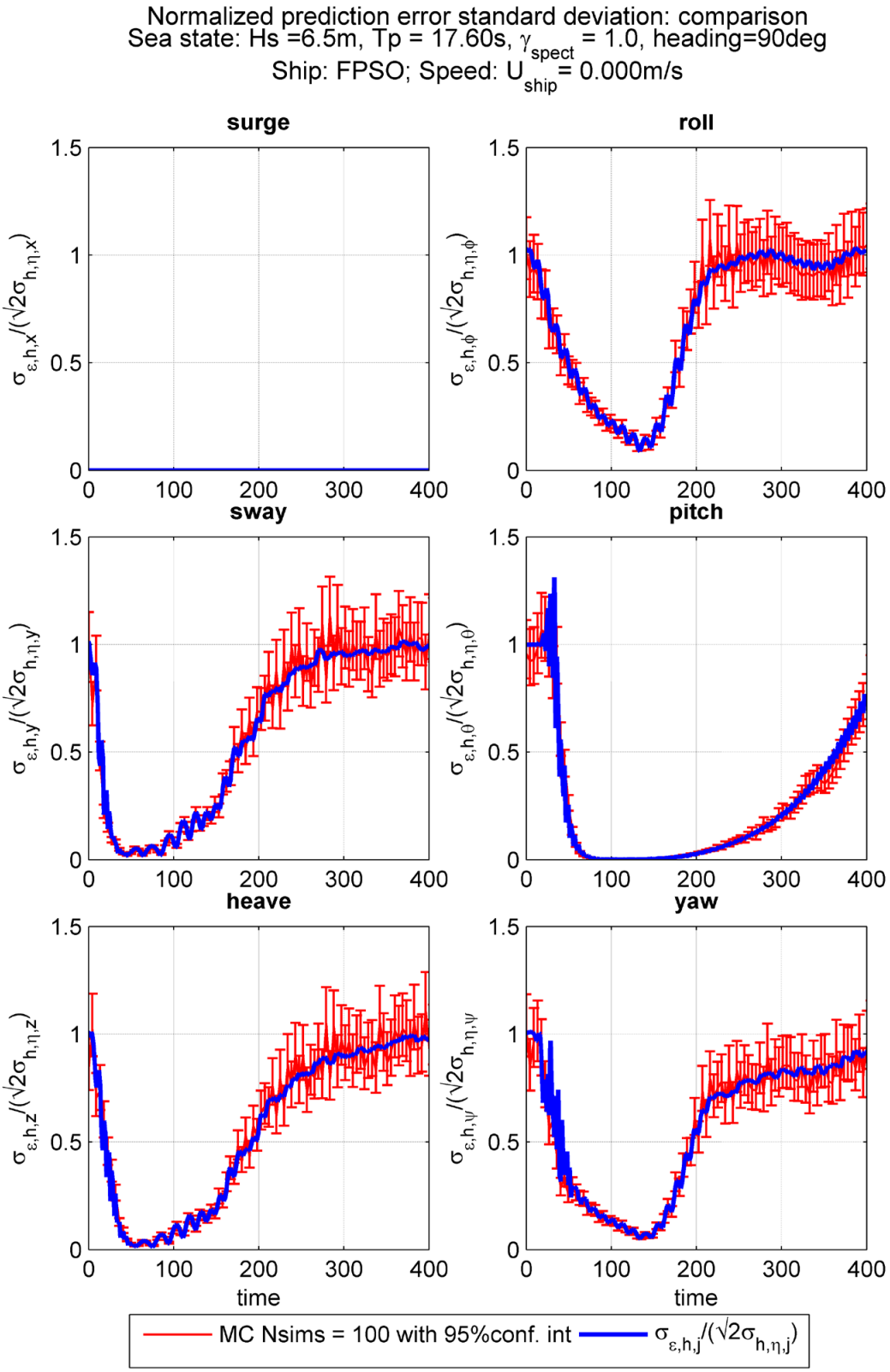

Figure 5.7: FPSO at zero speed with wave encounter angle 90deg (beam waves). Normalized standard deviation of the prediction error for the motions. Bretschneider spectrum with significant wave height $H_s = 6.5m$ and peak period $T_p = 17.60s$.

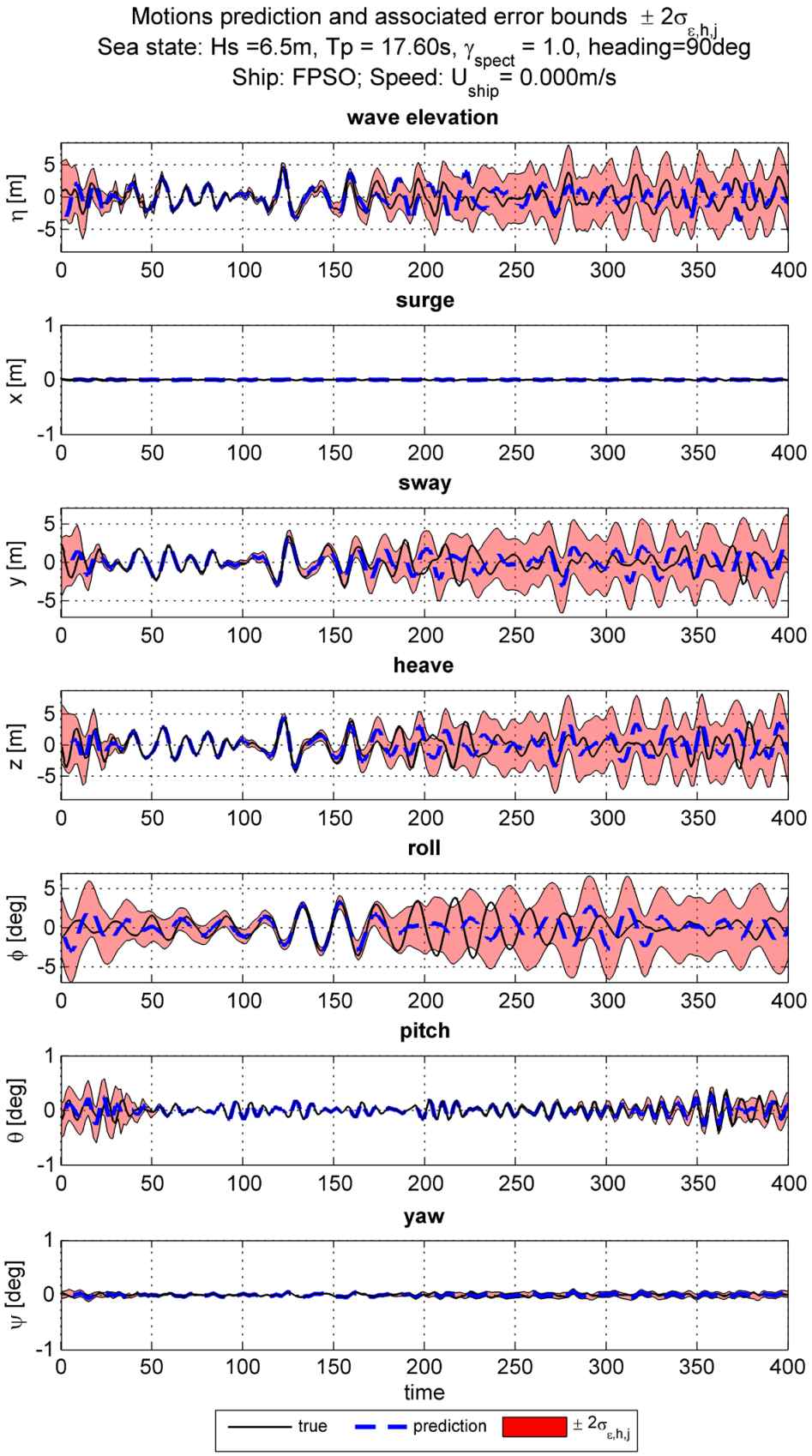

Figure 5.8: FPSO at zero speed and heading 90deg (beam waves). Example deterministic prediction of time histories wave elevation and motions. Bretschneider spectrum with significant wave height $H_s = 6.5m$ and peak period $T_p = 17.60s$.

5.4.2 Container ship in forward speed

5.4.2.1 Ship geometry and mechanical data

Example calculations with forward speed have been carried out for a Container ship which has been already studied by Bulian et al. [23] [25] and Moro et al. [95]. Figure 5.9 reports a set of representative views of the Container ship, while Table 5.4 and Table 5.5 present the main geometrical and mechanical data considered for the simulations. The ship is considered as moving with the forward speed of $U_{ship} = 5.144 m/s$ corresponding to a 10knots. The main data about bilge keels fitted on the ship are reported in Table 5.6. The equivalent linear damping reported in Table 5.6 has been calculated for two reference roll amplitudes $\phi_e = [5,10]\text{deg}$ at the corresponding forward speed of 10 knots, and it is reported in dimensionless form, normalized with respected to critical roll damping.

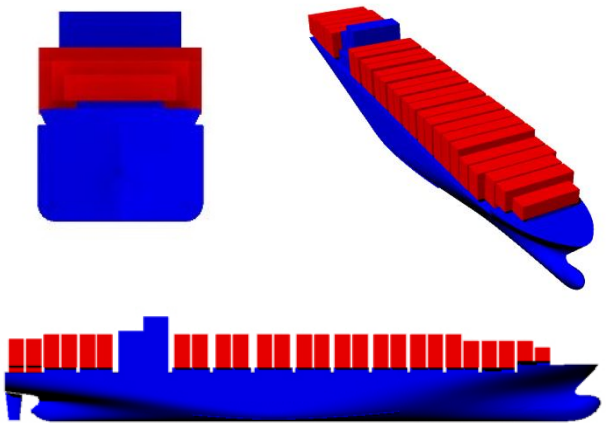

Figure 5.9: Container ship. Representative views.

Table 5.4: Container ship. Main geometrical data.

Ship length between perpendiculars L_{BP}	m	*217.00*
Ship Breath B	m	*32.25*
Draught T	m	*12.20*
Trim	m	*0.00*
Hull volume ∇	m^3	*55460*

Table 5.5: Container ship. Main mechanical data.

Vertical position of the centre of gravity (w.r.t. the keel point) KG	m	*12.922*
Transversal metacentric height GM_T	m	*2.0*
Dimensionless (w.r.t. B) dry roll radius (w.r.t CoG)	-	*0.40*
Dimensionless (w.r.t. L_{BP}) dry pitch and yaw radii (w.r.t. CoG)	-	*0.24*

Table 5.6: Container ship. Bilge keels data, equivalent roll damping and natural roll period.

Length of bilge keels	m	*80.0*
Span of bilge keels	m	*0.50*
Roll natural period	s	*19.60*
Equivalent dimensionless (w.r.t. critical) linear roll damping for 5deg for U_{ship} = 5.144m/s=10kn	-	*0.0343*
Equivalent dimensionless (w.r.t. critical) linear roll damping for 10deg for U_{ship} = 5.144m/s=10kn	-	*0.0505*

5.4.2.2 Test conditions

Calculations have been performed for a Bretschneider spectrum with significant wave height $H_s = 2.5m$ and peak period $T_p = 11.97s$. The considered wave encounter angles considered are $\theta = 135\,\text{deg}$ (bow quartering waves) and $\theta = 180\,\text{deg}$ (head sea). The assumed linear damping accounted for is the one calculated for the roll amplitude, $\phi_e = 5\,\text{deg}$. A set of 100 Monte Carlo simulations has been carried out assuming, for the deterministic prediction of the motions, that the true wave elevation data is available at a single the time instant $t = 0s$ and on a spatial interval of length $L_M = 2400m$. The linear wave prediction model propagates the wave from the measurement region, see Figure 5.1, to the ship reference position, O. This latter, for a generic time instant, is located at $x' = U_{ship}t$. The wave prediction model is based on a discretized set of wave numbers $N = 160$ defined as $\|k_n\| = \frac{2\pi}{L_M}n$ with n=[1,...,160] and with corresponding wave frequency calculated for the deep water condition $\omega_n = \sqrt{g\|k_n\|}$.

5.4.2.3 Results

The normalized standard deviations of the motion prediction error are presented, for the case of the Container ship in forward speed and for the two considered encounter angles $135-180\,\text{deg}$, in Figure 5.10 and Figure 5.11. Example deterministic prediction of wave elevation and motions are reported in Figure 5.12 and Figure 5.13. The obtained results show a satisfactory agreement with the Monte Carlo simulations, thus further verifying the implementation of the LEPrE approach. The Doppler effect, induced by the forward speed, results in a narrowing of the time interval where the motion predictions attain their minimum. This behaviour is quite well represented in the case of the surge, heave and pitch motions, and, comparing the results for the two encounter angles $135\,\text{deg}$ and $180\,\text{deg}$, a contraction of the region where good prediction performance can be noted. The obtained ensemble domain results are qualitatively confirmed by the example deterministic predictions of wave elevation and ship motions presented in Figure 5.12 and Figure 5.13.

The prediction error of roll motion presents an erratic behaviour characterized by high values of the standard deviation of the prediction error and strong oscillations. This effect can be associated to the motion spectrum presented in Figure 5.15. In fact, the roll motion spectrum is characterized by a bimodal shape with two separated peaks with

almost equal energy content, one in the low frequency region and one in the high frequency region. The high prediction error could be associated with the lack of frequency resolution, similarly to what was already discussed in the previous section for the FPSO, which is particularly affecting the resolution of the lower wave numbers. The oscillations are reasonably due to the presence of the higher part of the spectrum. The same kind of arguments can explain why the pitch motion presents a longer prediction time widow if compared, for example, with the heave motion (see Figure 5.10, Figure 5.12, Figure 5.14 and Figure 5.16). Also in this case the resolution of the longer waves, which are more relevant for heave, may play a significant role.

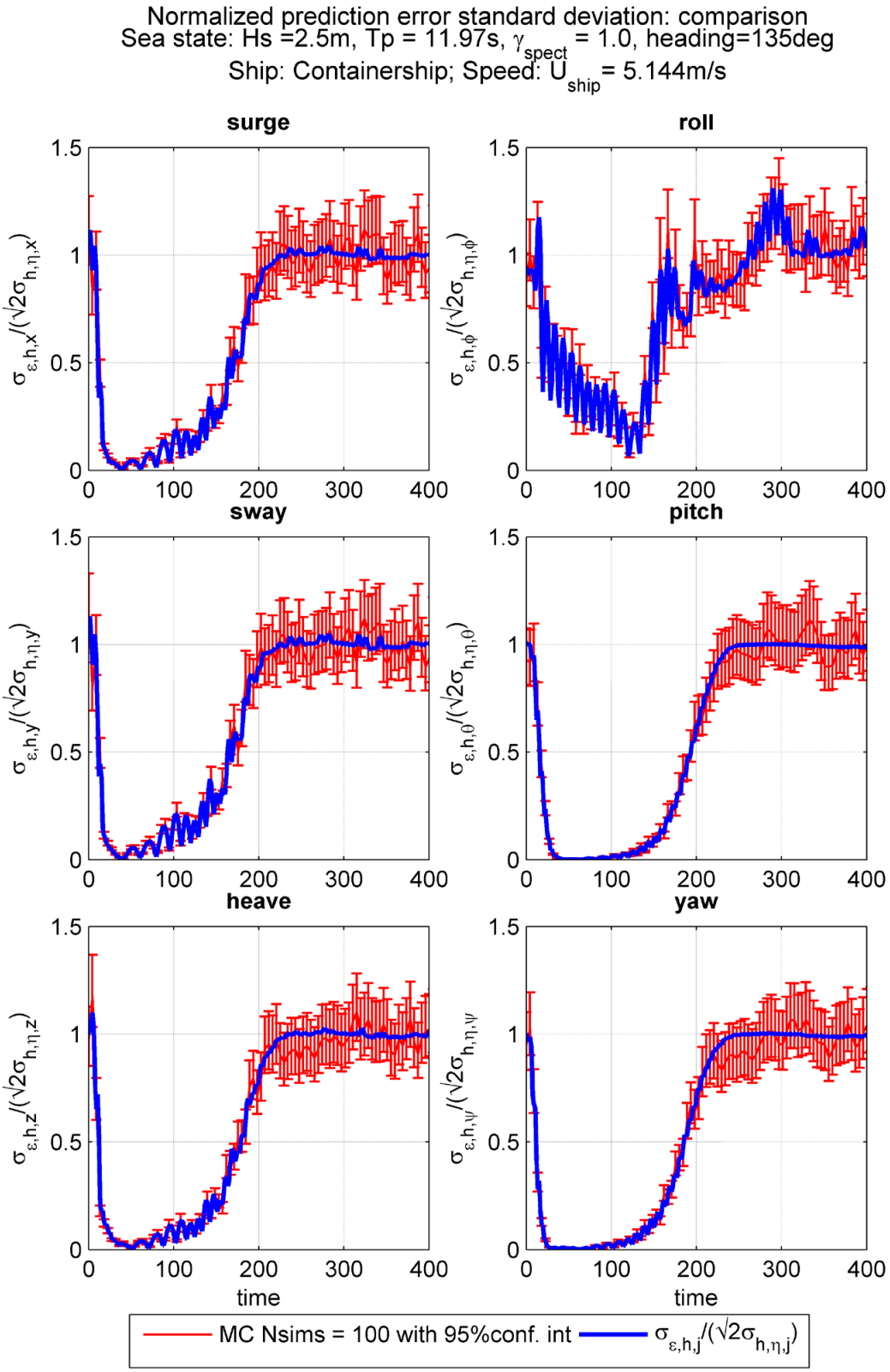

Figure 5.10: Container ship advancing at 10knots with wave encounter angle 135deg (bow quartering waves). Normalized standard deviation of the prediction error for the motions. Bretschneider spectrum with significant wave height $H_s = 2.5m$ and peak period $T_p = 11.97s$

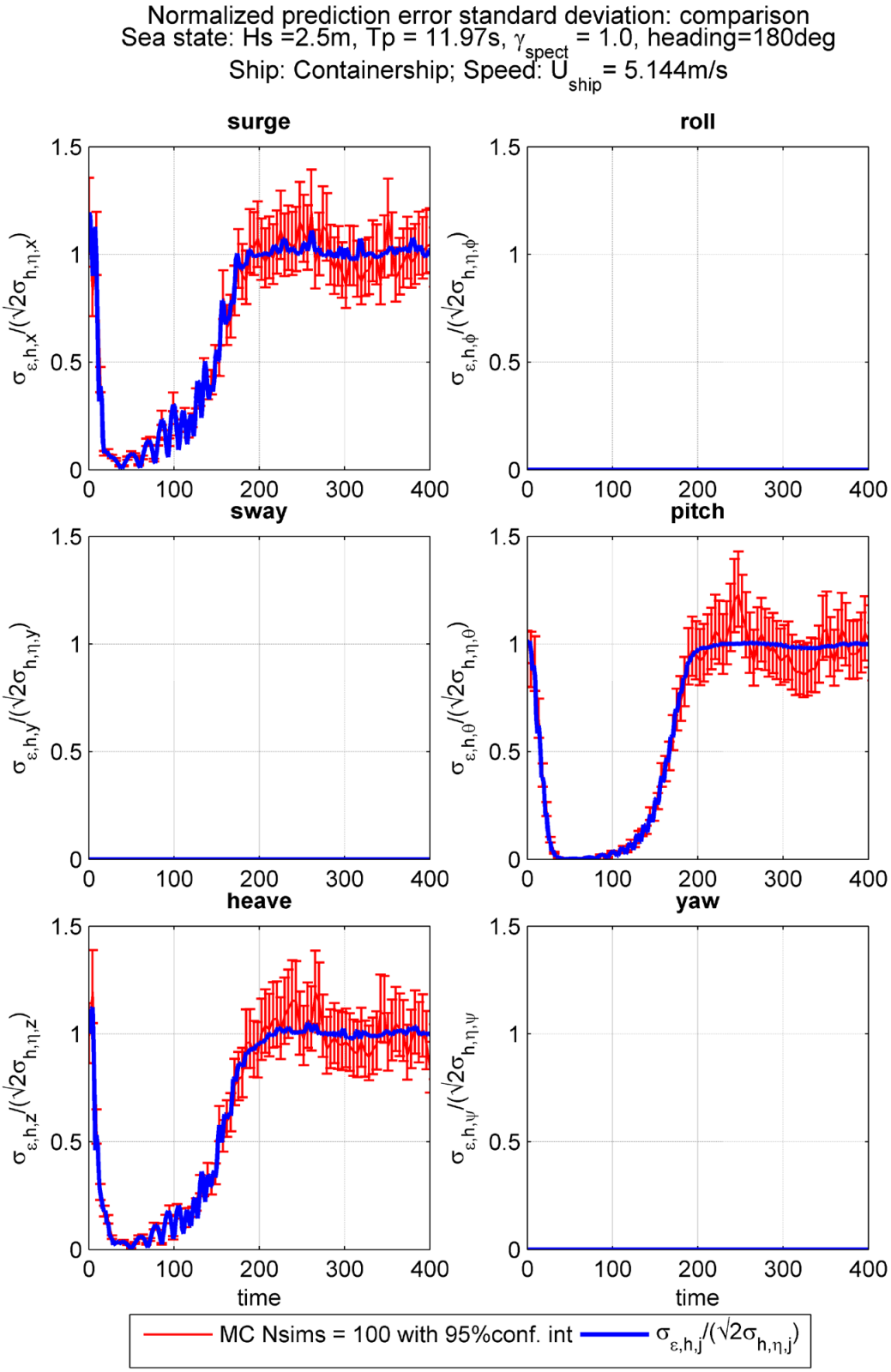

Figure 5.11: Container ship advancing at 10knots with wave encounter angle 180deg (head sea). Normalized standard deviation of the prediction error for the motions. Bretschneider spectrum with significant wave height $H_s = 2.5m$ and peak period $T_p = 11.97s$.

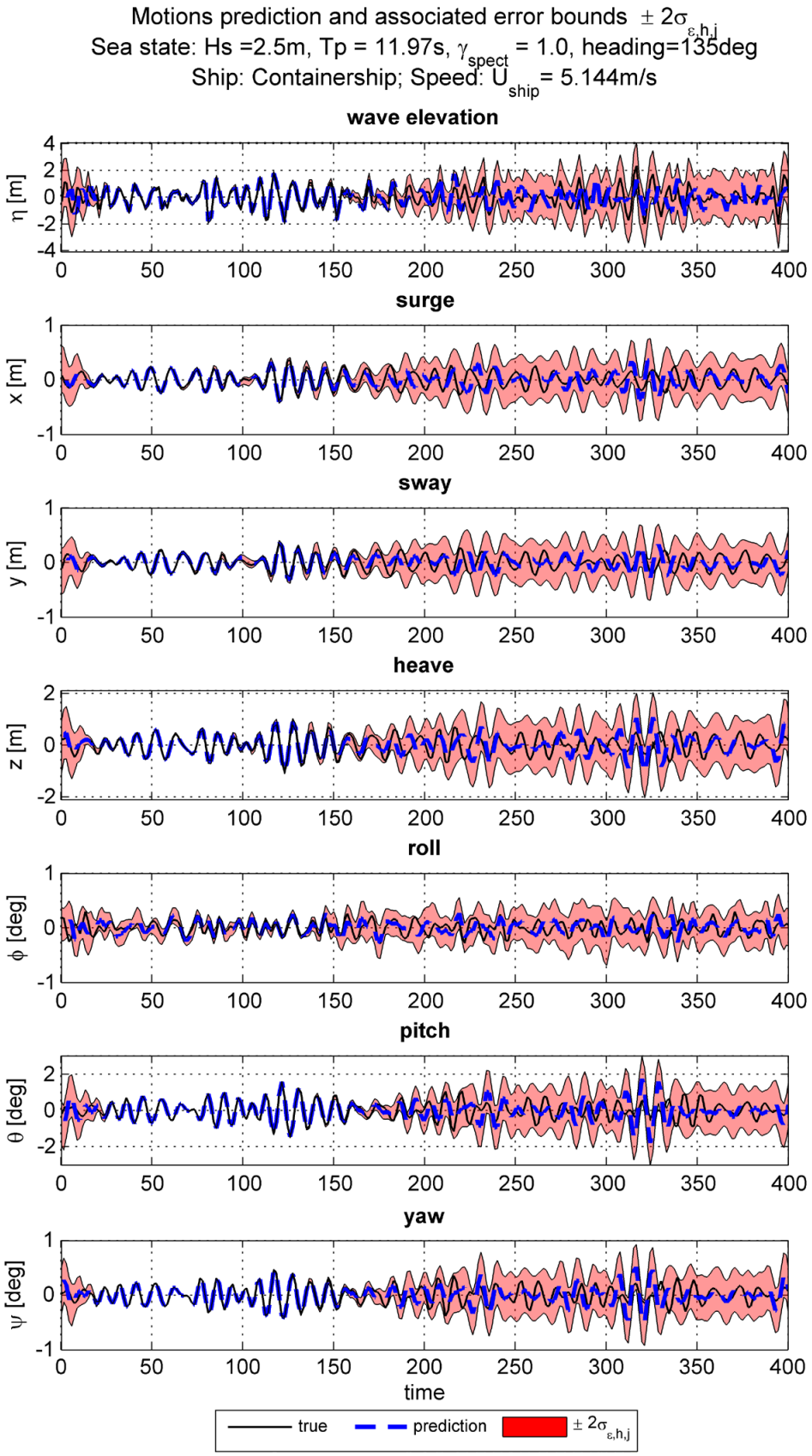

Figure 5.12: Container ship advancing at 10knots with wave encounter angle 135deg (bow quartering waves). Example deterministic prediction of time histories of wave elevation and motions. Bretschneider spectrum with significant wave height $H_s = 2.5m$ and peak period $T_p = 11.97s$.

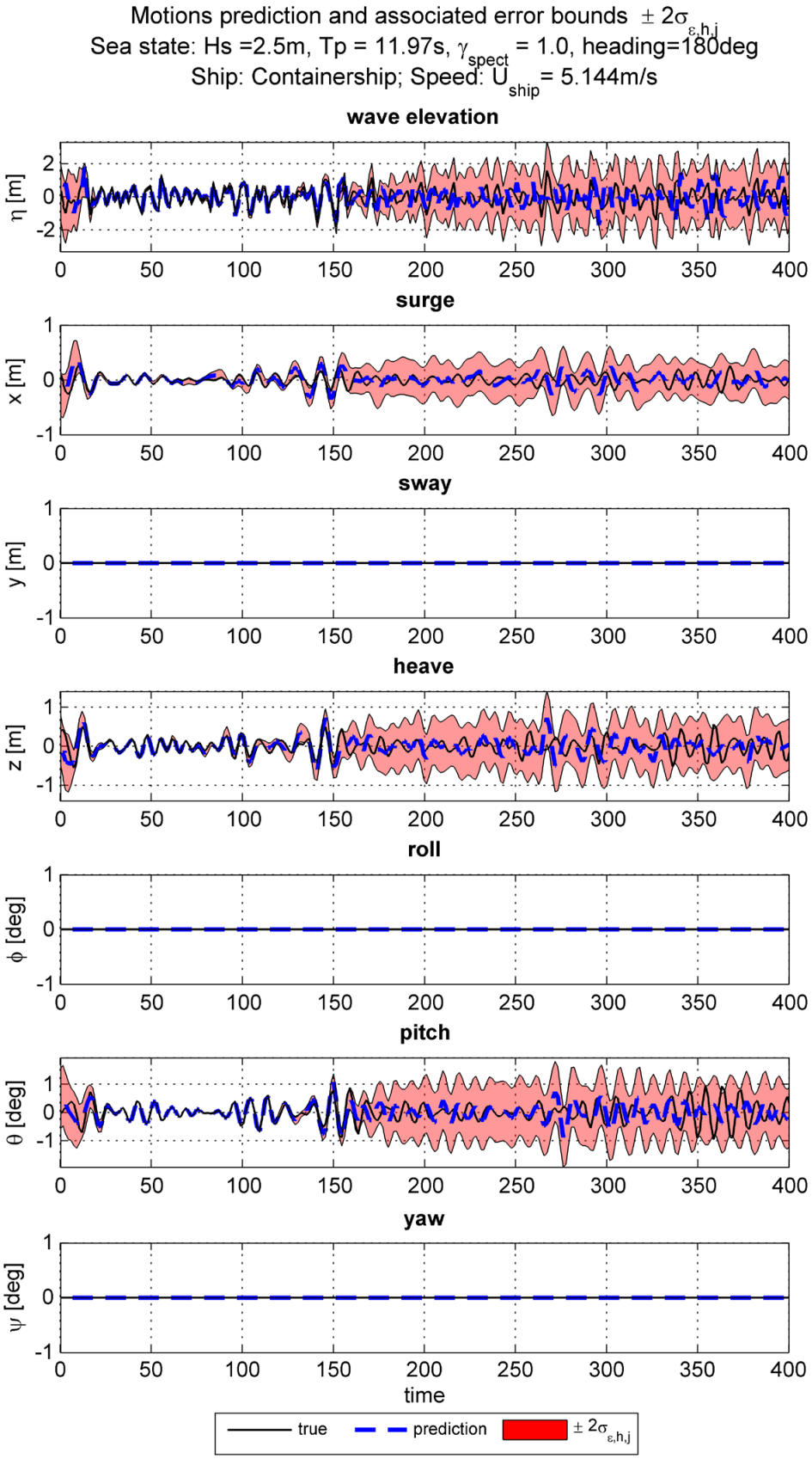

Figure 5.13: Container ship advancing at 10knots with wave encounter angle 180deg (head waves). Example deterministic prediction time histories of wave elevation and motions. Bretschneider spectrum with significant wave height $H_s = 2.5m$ and peak period $T_p = 11.97s$.

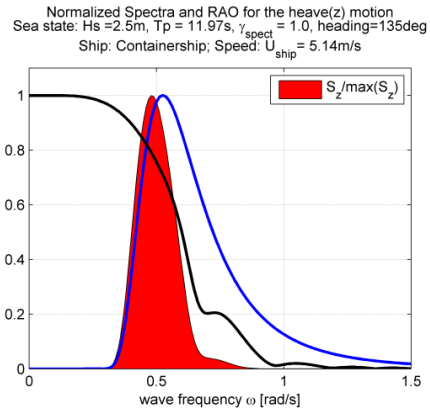

Figure 5.14: Container ship advancing at 10knots with wave encounter angle 135deg (bow quartering waves). Normalized spectrum of the wave elevation, normalized spectrum of the heave motion and normalized RAO of the heave motion.

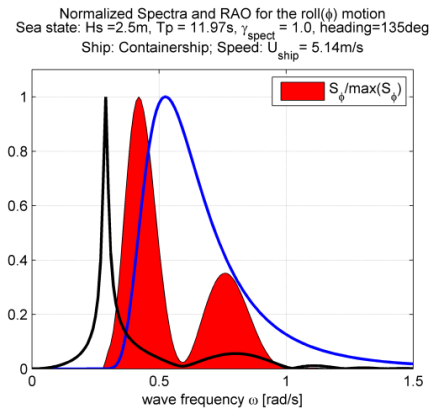

Figure 5.15: Container ship advancing at 10knots with wave encounter angle 135deg (bow quartering waves). Normalized spectrum of the wave elevation, normalized spectrum of the roll motion and normalized RAO of the roll motion.

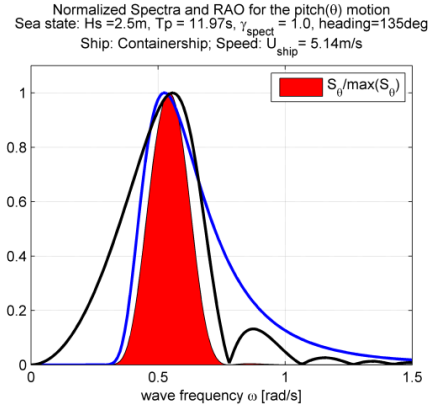

Figure 5.16: Container ship advancing at 10knots with wave encounter angle 135deg (bow quartering waves). Normalized spectrum of the wave elevation, normalized spectrum of the pitch motion and normalized RAO of the pitch motion.

5.5 Effect of measurement error

The assessment of the significant wave height by means of shipborne wave radar, in particular when installed on a ship advancing in the seaway, appears to be prone to measure dispersion issues (Stredulinsky and Thornhill [136]). For this reason, in this example application, the measurement error associated with an imprecise measure of the H_s is simulated by the introduction of an additional random noise to the of the true wave elevation data. The additional noise is modelled as a Gaussian random process with zero mean and standard deviation $\sigma_\delta = 0.25 H_s$. The chosen value has been selected mainly for presentation purposes. This simple formulation of the noise measurement corresponds, in the framework of the wave radar inversion error, see §3 and §4, in assuming a covariance matrix for the error simply defined as an identity matrix multiplied by the value of the noise variance. The results of application the LEPrE methodology applied to the ship motion accounting also for the measurement error are presented in Figure 5.17. The considered example case refers to the Container ship advancing at 10knots in bow quartering waves (135deg). The prediction error of the LEPrE, accounting for the measurement error, is reported as a black line, while the

LEPrE without measurement error is reported as a blue line. The reported Monte Carlo simulations provided with a 95% confidence interval refer only to the case with measurement noise, for verification purposes. It can be noticed that different degrees of freedom are indeed differently affected by the introduction of the measurement noise. For all the motions a degradation of the performance of the deterministic motion prediction is observed, and the most affected degrees of freedom is roll. On the other hand, the yaw and the pitch motion seem to maintain a reasonable region of predictability, although this is characterised by a higher prediction error. The same results can also be qualitatively observed in the example deterministic prediction time histories as reported in Figure 5.18.

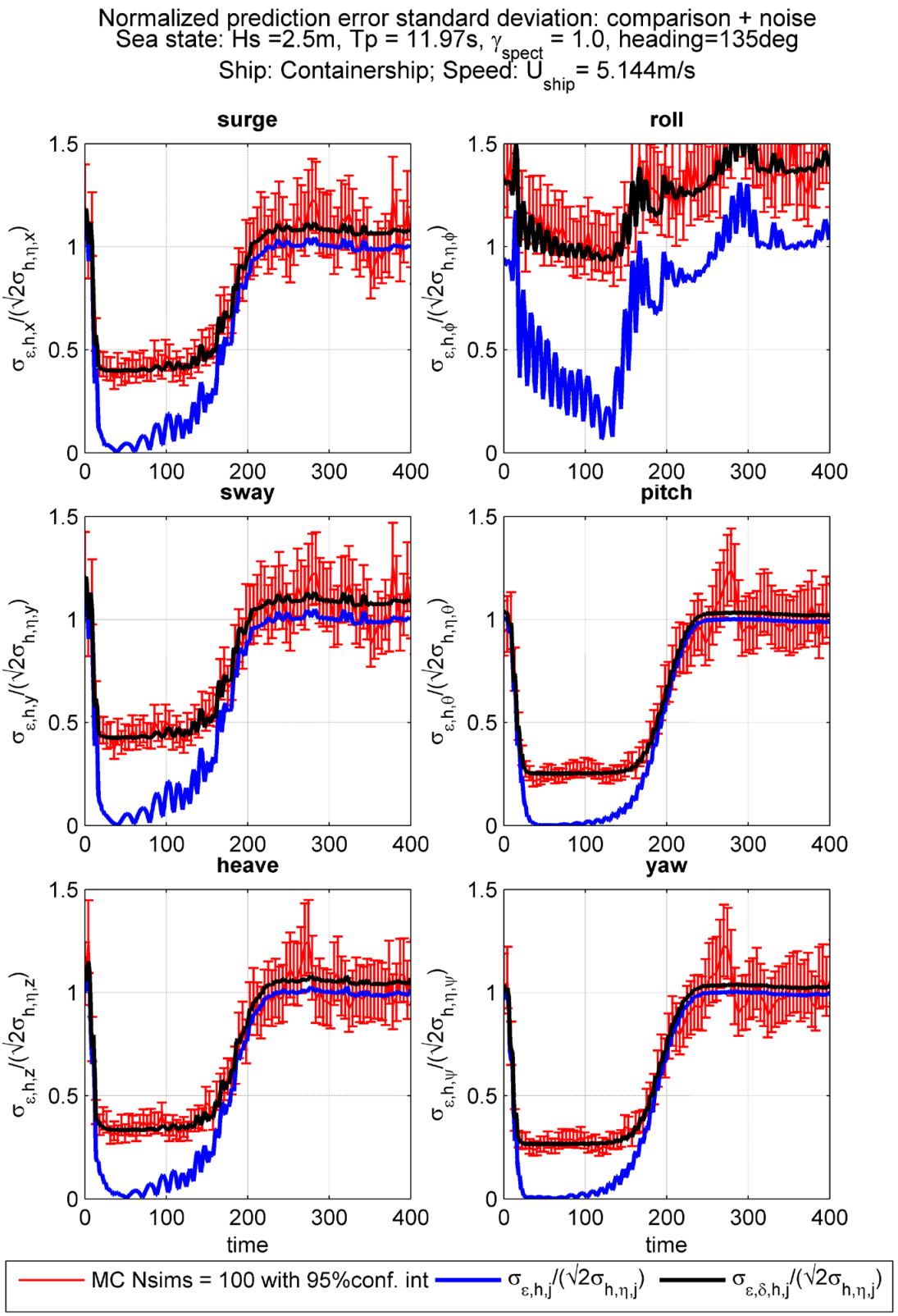

Figure 5.17: Container ship advancing at 10knots with wave encounter angle 135deg (bow quartering waves). Normalized standard deviation of the prediction error for the motions. Bretschneider spectrum with significant wave height $H_s = 2.5m$ and peak period $T_p = 11.97s$. An additional measurement error affecting the wave elevation data is modelled as Gaussian noise with standard deviation $\sigma_\delta = 0.25H_s$.

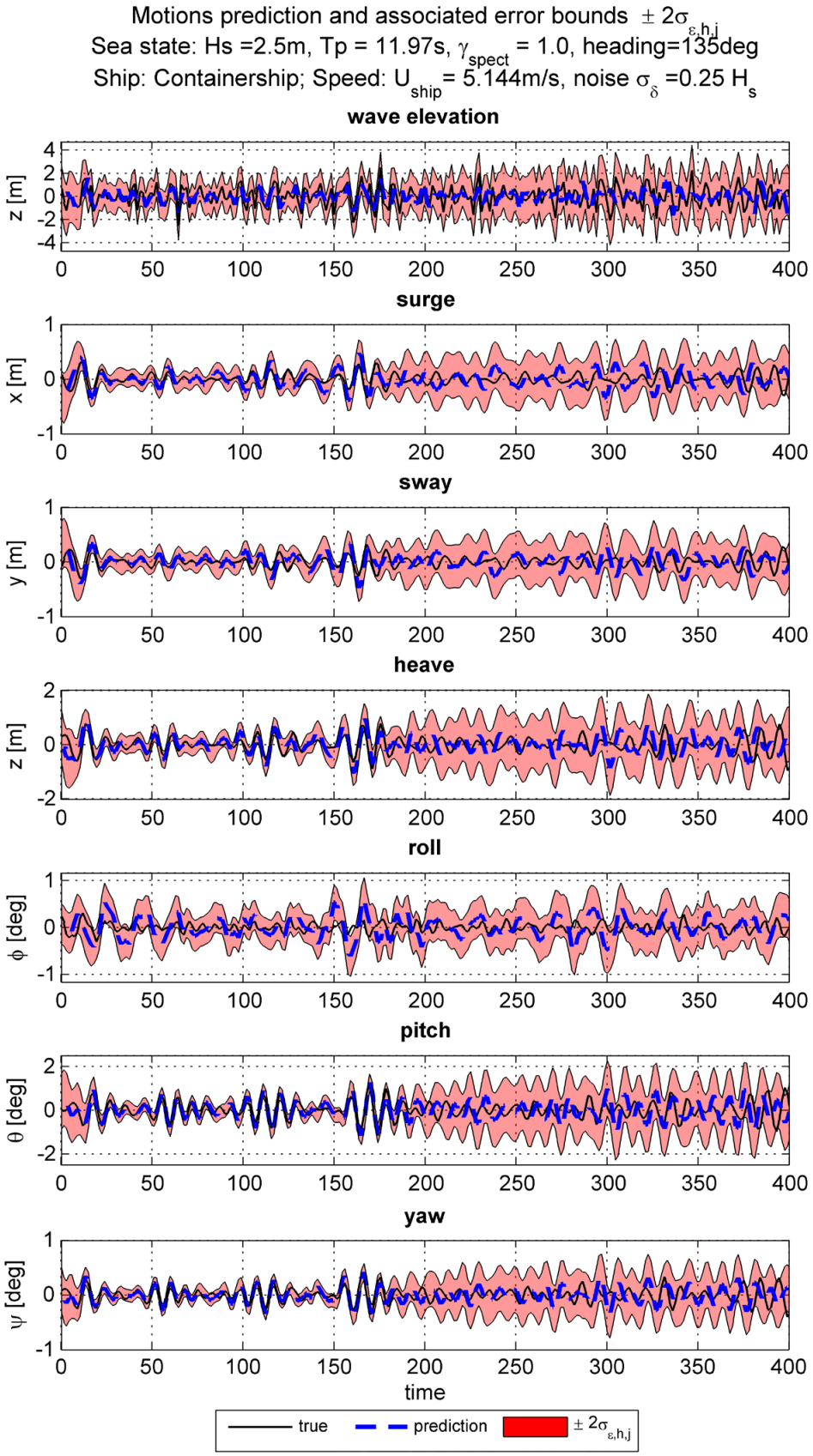

Figure 5.18: Container ship advancing at 10knots with wave encounter angle 135deg (bow quartering waves). Example deterministic prediction of time histories of wave elevation and motions. Bretschneider spectrum with significant wave height $H_s = 2.5m$ and peak period $T_p = 11.97s$. An additional measurement error affecting the wave elevation data is modelled as Gaussian noise with standard deviation $\sigma_\delta = 0.25H_s$.

5.6 Technological and procedural indications

At the early stages of the definition of the prediction process, the LEPrE methodology, as extended to the assessment of the motion prediction error, can be used as a tool for the choice of the main parameters for the implemented deterministic sea wave and ship motion prediction procedure. The effects of widening the measurements region, considering radar images taken at different distance from the structure or changing the prediction model are oftentimes investigated only considering the prediction error of the wave elevation. In this respect, the extended LEPrE approach can be used to ground these considerations on more solid basis considering for example the motion prediction error accounting for a specific degree of freedom or for any linear combination in the framework of the linear seakeeping theory. To stress this argument, hereinafter, two simple examples are carried out.

First, the effect of accounting for a larger region of space where to measure the wave elevation is presented in the case of the prediction error for the roll motion of the FPSO at zero speed in beam waves. In this case, the calculation has been carried out by measuring the wave elevation from the point $r_{min} = 150m$ up to the length $L_M = [1200, 2400, 4800]m$. The measurements have been taken for a single time instant or on a set of time instant in the past within an interval based on the peak period of the wave spectrum, i.e. $t = 0$, $t \in [-2T_p, 0]$ or $t \in [-4T_p, 0]$. The time discretization considered is $dt = 1.5s$. The wave prediction model is based on a discretized set of wave numbers $N = [80, 160, 320]$ on the basis of the considered measurement region defined as $\|k_n\| = \frac{2\pi}{L_M} n$ with n=[1,..,N] and with corresponding wave frequency calculated for the deep water condition $\omega_n = \sqrt{g\|k_n\|}$. The fitting has been then carried out using least square approach eventually considering more than one time instant, for the relevant cases.

Figure 5.19 presents the normalized standard deviation of the wave elevation prediction error, as well as that of roll motion. It can be noticed from the results in Figure 5.19 that, by widening the measurement region, the roll prediction error attains lower values confirming that the prediction of roll motion would benefit from a finer resolution in the wave frequency of the prediction model. Moreover, this suggests how the choice of main parameter of the prediction model, as well as of the underlying measurement technology, can be based on the specification of target prediction accuracies regarding motions.

In the second example, the Container ship advancing at 10knots in bow quartering waves is considered, and the minimum distance from the measurement region r_{min} (which can be considered to correspond, for instance, to the wave radar blind region) is varied considering $r_{min} = [150, 300, 600, 1200]m$. The length of the measurement interval is kept constant to $L_M = 2400m$. Such long range measurements are, herein, considered only because relevant to the discussion. However, although such figure is within typical wave radar maximum range, in the case of shipborne devices some detrimental effect in the inversion of the radar images can be expected. The analysis is carried out on the prediction error for wave elevation and, as an example, for ship motions, and results from the analysis are reported in Figure 5.20.

The observed increasing of the minimum of the prediction error as r_{min} increases, as well, as the change of the shape of the prediction error curve for the wave elevation, is a well-known result (Naaijen et al. [102]; Vettor [146]). It is however noted that the prediction error for the pitch motion seems to be less affected from the changing of the distance of the ship from the measurement region, apart from the increasing delay linked to the propagation of the wave elevation model.

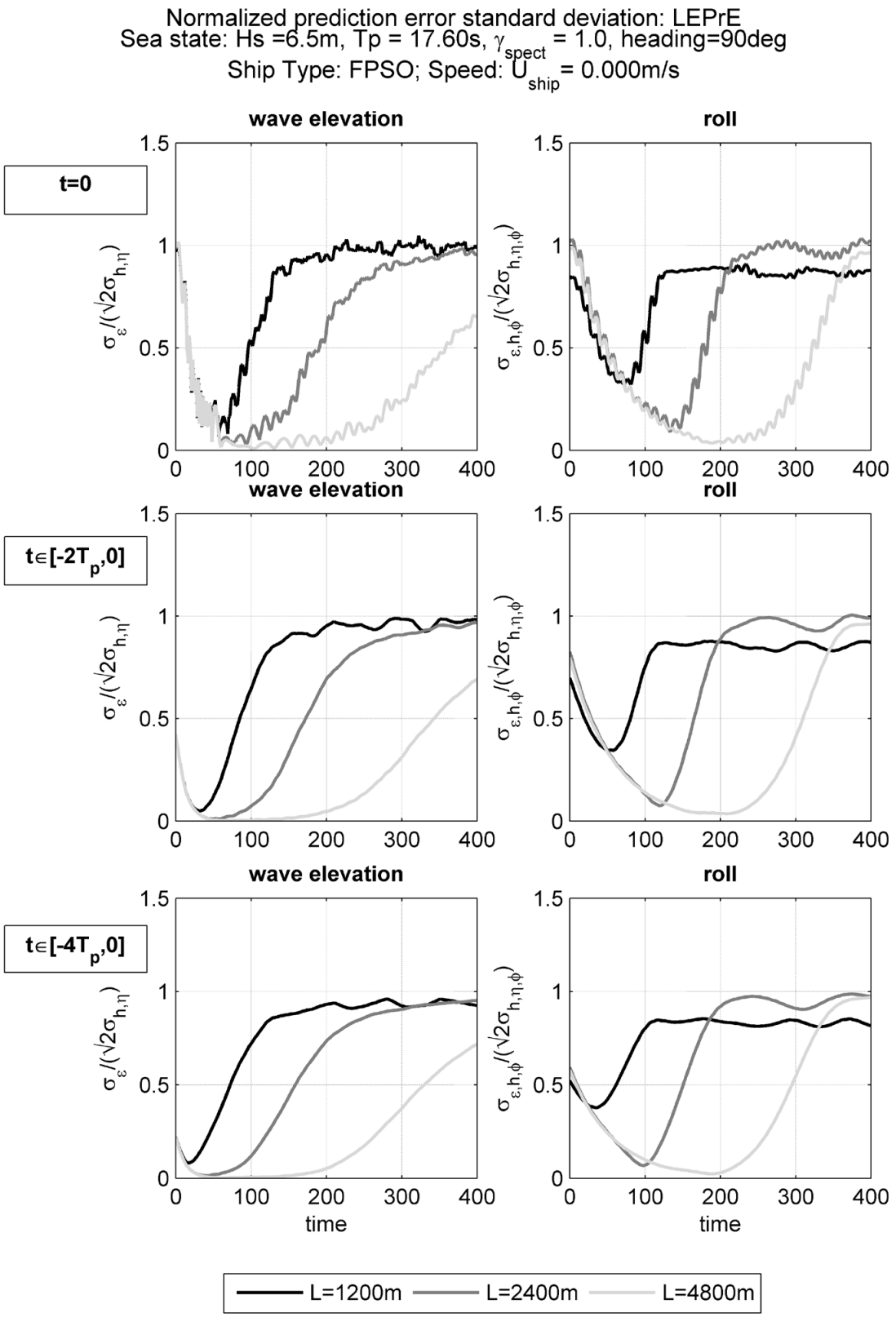

Figure 5.19: FPSO at zero speed with wave encounter angle 90deg (beam waves). Assessment of dimension of measurement region on prediction error. Normalized standard deviation of the prediction error of wave elevation (left column) and of roll motion (right column) . Bretschneider spectrum with significant wave height $H_s = 6.5m$ and peak period $T_p = 17.60s$.

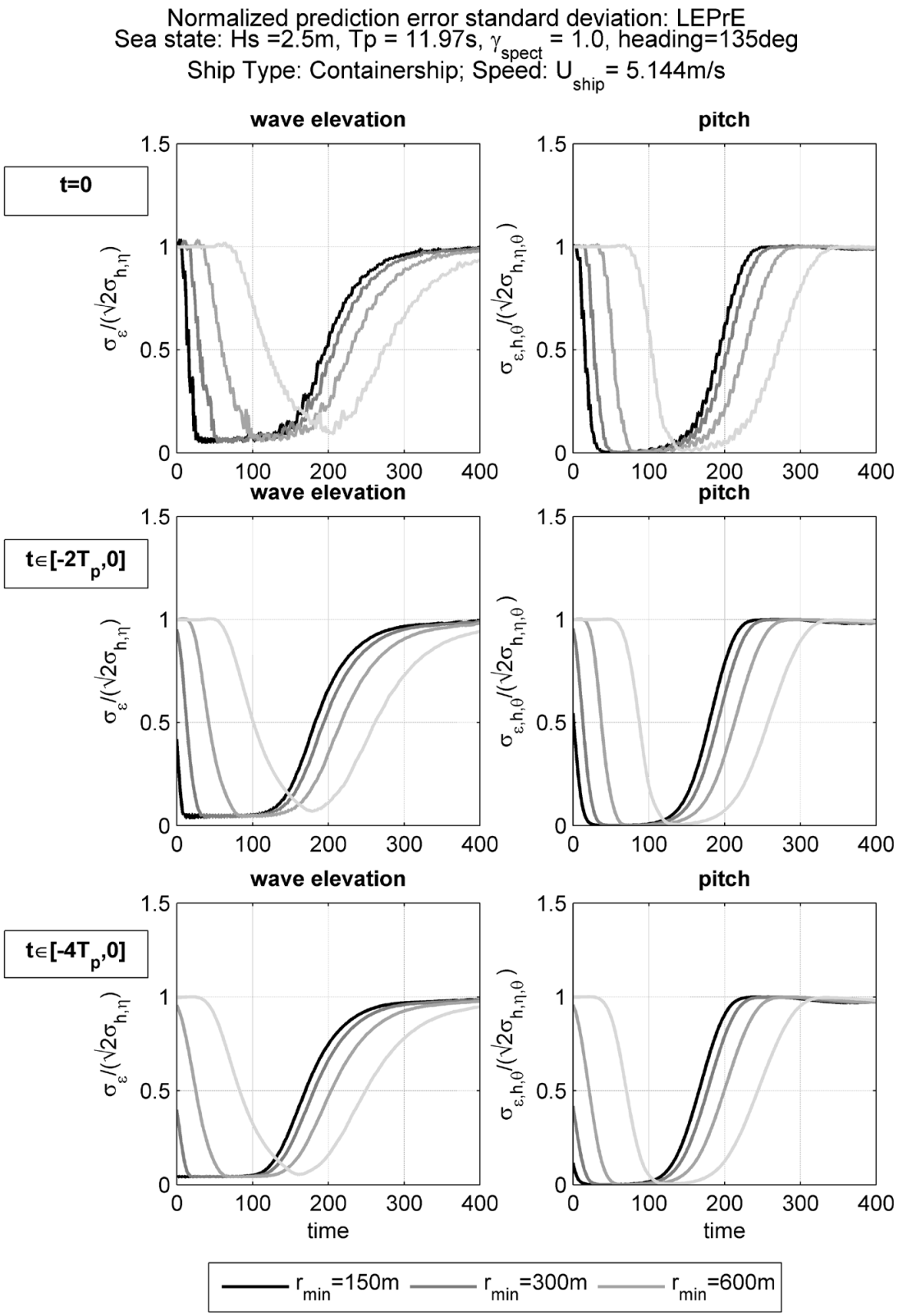

Figure 5.20: Container ship advancing at 10knots with wave encounter angle 135deg (bow quartering waves). Assessment of effect of taking radar images at different distance from the ship. Normalized standard deviation of the prediction error of wave elevation (left column) and of pitch motion (right column). Bretschneider spectrum with significant wave height $H_s = 2.5m$ and peak period.

5.7 Concluding remarks

In this chapter, the LEPrE approach, originally developed for the estimation of prediction error in case of wave elevation, has been extended to the case of linear ship motions. In fact, the linearity assumption of the LEPrE methodology naturally allows extending this technique to take into account any linear transformation on the prediction model coefficients. As a result, in the case of linear ship motion, it was sufficient to consistently take into account the transfer functions of the motions in order to arrive at a direct semi-analytical assessment of the motions prediction error. Moreover, in the framework of linear theory, this method can be extend to account for any linear response which might arise from the wave field, from a combination/transformation of ship motions, or by a combination of ship motions and wave field. In the framework of the linear seakeeping theory, the approach could account for quantities like the relative motion with respect to the sea surface, keel emergence, accelerations at given point, linear forces, etc.

The LEPrE approach has proven to be capable in dealing also with the possible presence of wave measurement error, accounting for it also in the assessment of the motion prediction error. Furthermore, the LEPrE approach could be proposed as tool for a "motion oriented" setup of a linear deterministic sea wave and ship motion prediction procedures. In fact, presently, the wave elevation prediction error is considered as the reference quantity to judge on the feasibility of a deterministic prediction procedure. In the reported examples, however, it has been highlighted that the motion prediction performance can depart form the wave prediction performance. As a result, considering only the latter aspect of the prediction problem can be limiting and/or could lead to erroneous choices. It is also worth mentioning that the proposed approach can also be used to assess the influence of the wave measurement capabilities, providing potential indications for the most effective direction towards which developing the measurement technology.

6 CONCLUSIONS

In this thesis the main aspects of the deterministic prediction of ship motions has been studied. Starting from the observation of existing limitations in, and gaps between, different steps of an envisioned deterministic sea wave and ship motion prediction chain, the focus of the research has been put on development and investigation of new approaches, with the intention of contributing to the improvement of the existing state-of-the-art. To this end, the whole forecasting chain, starting from the analysis of wave radar inversion techniques and ending with the assessment of ship motions prediction error, has been analysed, trying to include, in the developed methodology, a way to consistently account for the unavoidable uncertainties coming from the measurement devices and eventually propagated by the prediction models.

This work has mainly dealt with linear deterministic forecasting procedures, although, in chapter §2, some aspects of nonlinear wave modelling and propagation have been studied. Indeed, a High-Order Spectral (HOS) method has been implemented as a flexible tool for the generation of nonlinear wave fields, which can represent a more "realistic" representation of the actual sea compared to linear models, particularly for severe sea states. The main aspects of its implementation have been presented with particular attention to initialization and stability issues. The HOS method has been conceived in the present work as a benchmarking tool for the testing of the other, mainly linear, developed methodologies. In chapter §3 a novel approach for the inversion of the wave radar images, the Least SQuares with Regularization (LSQR) technique, has been presented. The method shares some commonalities with already existing techniques, but its definition has allowed in dealing, innovatively, with some often overlooked problems in wave radar imaging inversion, as the shadowing effect. The error introduced by the LSQR inversion of synthetically generated radar images has been investigated and some proposal for the characterization of the main statistical features of the measurement error has been suggested, with reference to a possible application to deterministic sea waves and ship motions predictions techniques. In chapter §4 a new technique for the semi-analytical estimation of prediction error statistical characteristics, the Linear Estimator of the Prediction Error (LEPrE), has been introduced. This technique stems from the combination of predictions based on linear fitting procedures and the framework of Gaussian stochastic processes for the representation of the underlying wave field. The LEPrE approaches the deterministic sea wave prediction problem by embedding, in a simple methodology, the main features

coming from the linear fitting and the subsequent propagation procedure. The theoretical background of the LEPrE procedure allows a consistent statistical assessment of the wave elevation prediction error, which has also been extensively verified by means of Monte Carlo simulations. Furthermore, the LEPrE approach also allows to consistently account for the wave measurement error, which is an aspect often overlooked in the analysis of deterministic sea wave prediction error. Eventually, in chapter §5 the LEPrE methodology has been extended to the prediction of linear ship motions. The main features of the proposed approach have been discussed by presenting also some example application.

In investigating existing wave radar inversion models, potential sources of inversion issues have become apparent. This was particularly the case when considering the procedural approach, accounting for different layers of filtering and manipulation of the radar signal, which is typical of the techniques based on the concept of Modulation Transfer Function (MTF). In particular, the investigation has focussed on the necessity of trying to consistently address the inherent difficulties associated with the presence of the shadowing effect, an effect which is particularly relevant in the case of shipborne wave radars operating at low grazing angles. To this end, the LSQR technique has been conceived to take into account, from the very beginning of the inversion problem, the temporal and spatial lack of backscatter signal due to the shadowing effect. The inversion procedure has therefore been developed around the idea of considering the presence of shadowing as a missing data problem, by providing a solution of the inversion problem by means of a least squares regularized approach. The results obtained for linear long crested and short crested wave field confirm the potential of the LSQR method in dealing with the inversion problem. Furthermore, some example test carried out also in the case of nonlinear long crested seas, generated by means of the developed HOS tool, has shown encouraging results. The step by step fitting of the sea surface, on which the LSQR methodology is based on, has, in principle, the sufficient flexibility to reconstruct also a nonlinear wave field. However, without specific further modifications, the information retrieved by a naïve application of the LSQR approach is likely to be missing most of the original nonlinear features. In this respect, some future improvement of the LSQR technique could possibly address also nonlinear wave fields. In fact, it is possible to envisage a convenient adaptation of the LSQR method, for example accounting for iterative techniques, in order to extract nonlinear features of the wave field, as for example the second order bound waves, by considering the required underlying relation among free and bound wave components. Moreover, improvements can be envisaged, also in this case based on iterative techniques, in order to take into account nonlinear effects on the wave dispersion relation. In this respect, the envisaged improvements would represent a substantial step forward for wave radar inversion techniques. Finally, it must be stressed that the LSQR method, as presently implemented, have such computation cost that renders its direct application to a real time inversion of the wave radar images practically unfeasible. The main issues come from the adopted regularisation technique. In fact, the SVD algorithm, at the basis of this technique, presents a cubic scaling with respect to the number of unknowns in the inversion problem. Existing techniques, which potentially allow a real-time implementation, are based on FFT approaches, which outperform the presented LSQR technique in terms of computational time. Nevertheless, present FFT-based techniques are not capable of accounting for shadowing as missing information. Due to the computational cost, particularly in case of short crested seas, the LSQR technique, for the time being, could be considered as a complementary inversion technique. However, there is still a large margin of improvement by adopting more efficient regularization techniques, which are better suited to deal with large data set. Moreover, tests carried

out in case of short crested waves, indicate that gain in computational time could be achieved, thanks to the flexibility of the LSQR approach, by addressing only limited portions of the space in the inversion procedure, depending on the directional spreading of the wave field. These aspects, therefore, are worth additional investigation.

The most commonly used deterministic sea wave and ship motion prediction methodologies are mainly based on the assumption that linear models are sufficiently accurate for a practical deterministic prediction of the wave elevation and the ship motions. However, even in the linear framework, the problem of the error associated with the measurement of the sea surface is seldom addressed. Often the presence of wave measurement error is neglected *a-priori*, which represents a too optimistic assumption. The LEPrE technique developed in this thesis has shown to be able to naturally account for this source of error, by consistently embedding it in a larger framework for the assessment of the wave elevation prediction error. Moreover, the way the LEPrE methodology has been conceived does not require the debated assumption about the use of the wave group velocity, on which techniques like the Predictability Region and Prediction Error Indicator are based on. In this respect, in developing the LEPrE approach it appeared as more consistent to focus on the fitting and propagation problem. This has allowed the inherent characteristic of the prediction error, in terms of time-space evolution, to directly and naturally arise from the developed methodology, without any assumption apart from that regarding the linearity and Gaussianity of the underlying wave elevation process. More importantly, results provided by the LEPrE methodology represent quantities that have a clear probabilistic interpretation, allowing a more consistent characterisation of the prediction performance and giving the possibility to provide sound confidence bounds to a deterministic prediction. This approach is innovative and all at once it gives the possibility to account for measurement error, to account consistently for the fitting and propagation model and it can be straightforwardly extended to account for any linear transformation of the wave elevation field. In this respect, the extension to motion prediction error has come at almost no cost from the original theoretical background developed for the LEPrE for the wave elevation prediction. In the framework of linear seakeeping theory, this tool can be conveniently adapted for the estimation of the prediction error of many other relevant quantities, such as, for instance, the prediction of keel emergence, the prediction of velocity and acceleration at certain points of the ship, the relative clearances between moving structures. In general, the approach can directly account for all those quantities which can be modelled through a linear transfer function with respect to the wave elevation. Eventually, the proposed LEPrE approach can also represent a useful tool for the early design and setup of linear deterministic sea wave and ship motion procedures. In fact, the proposed approach allows to base choices considering the predictability horizon of wave elevation, as it is common nowadays, but also on the predictability horizon of motions or other quantities of interest. However, being based on linearity assumptions, the LEPrE method is clearly not suitable for problems that have to account for prominent nonlinearities of the wave field or ship motions. Some minor modifications can be introduced to better account for limited or simplified nonlinear features. However, more investigation is needed in order to address whether and how this methodology could be adapted or extended also in case of situations governed by nonlinear effects.

7 REFERENCES

[1] Abusedra, L., Belmont, M.R., 2011. Prediction diagrams for deterministic sea wave prediction and the introduction of the data extension prediction method. International Shipbuilding Progress 58, pp. 59–81.

[2] Alam, M.-R., 2014. Predictability horizon of oceanic rogue waves. Geophys. Res. Lett. 41, pp. 8477–8485.

[3] Alford, L.K., Beck, R.F., Johnson, J.T., Lyzenga, D., Nwogu, O., Zundel, A., 2015. A Real-Time System for Forecasting Extreme Waves and Vessel Motions. Proceedings of the ASME 2015 34th International Conference on Ocean, Offshore and Arctic Engineering (OMAE 2015), May 31-June 5, 2015, St. John's, Newfoundland, Canada, 7p.

[4] Alpers, W.R., Ross, D.B., Rufenach, C.L., 1981. On the detectability of ocean surface waves by real and synthetic aperture radar. Journal of Geophysical Research 86, pp. 6481-6498.

[5] Aragh, S., Nwogu, O., 2008. Variation Assimilating of Synthetic Radar Data into a Pseudo-spectral Wave Model. Journal of Coastal Research,pp. 235–244.

[6] Barrick, D.E., 1995. Near-grazing illumination and shadowing of rough surfaces. Radio Science 30, pp. 563–580.

[7] Bateman, W.J., Swan, C., Taylor, P.H., 2001. On the efficient numerical simulation of directionally spread surface water waves. Journal of Computational Physics 174, pp. 277–305.

[8] Beck, R.F., 2012. Optimum Vessel Performance in Evolving Nonlinear Wave Fields. Technical Report, No. 0704-0188, Nov., 38p.

[9] Belmont, M.R., Christmas, J., Dannenberg, J., Hilmer, T., Duncan, J., Duncan, J.M., Ferrier, B., 2014. An examination of the feasibility of linear deterministic sea wave prediction in multidirectional seas using wave profiling radar: Theory, simulation, and sea trials. Journal of Atmospheric and Oceanic Technology 31, pp. 1601–1614.

[10] Belmont, M.R., Horwood, J.M.K., Thurley, R.W.F., Baker, J., 2006. Filters for linear sea-wave prediction. Ocean Engineering 33, pp. 2332–2351.

[11] Belmont, M.R., Horwood, J.M.K., Thurley, R.W.F., Baker, J., 2007. Shallow angle wave profiling Lidar. J. Atmos. Oceanic Technol. 24, pp. 1150–1156.

[12] Benjamin, T.B., Feir, J.E., 1967. The disintegration of wave trains on deep water Part 1. Theory. Journal of Fluid Mechanics 27, pp. 417–430.

[13] Benjamin, T.B., Olver, P.J., 1982. Hamiltonian structure, symmetries and conservation laws for water waves. Journal of Fluid Mechanics 125,pp. 137–185.

[14] Blondel-Couprie, E., 2009. Reconstruction et prévision déterministe de houle à partir de données mesurées. Ph.D. Thesis. Université de Nantes, Ecole Centrale de Nantes (ECN).

[15] Blondel-Couprie, E., Bonnefoy, F., Ferrant, P., 2010. Deterministic non-linear wave prediction using probe data. Ocean Engineering 37, pp. 913–926.

[16] Blondel-Couprie, E., Bonnefoy, F., Ferrant, P., 2013. Experimental Validation of Deterministic Non-linear Wave Prediction Schemes in 2D. Proceedings of the Twentieth International Offshore and Polar Engineering Conference (ISOPE 2010), Beijing, China, June 20-25, 2010, pp. 284–292.

[17] Blondel-Couprie, E., Naaijen, P., 2012. Reconstruction and prediction of short-crested seas based on the application of a 3D-FFT on synthetic waves: Part 2 - Prediction. Proceedings of ASME 31st International Conference on Ocean, Offshore and Arctic Engineering (OMAE 2012), 1-6 July , Rio de Janeiro, Brazil, pp. 55-70.

[18] Blondel-Couprie, E., Naaijen, P., 2012. Deterministic Prediction of ocean waves based on X-band radar measurements. Presented at the 13èmes Journées de L'Hydrodynamique, Chatou, France.

[19] Bonnefoy, F., 2005. Modélisation expérimentale et numérique des états de mer complexes. Ph.D. Thesis. Université de Nantes, Ecole Centrale de Nantes (ECN).

[20] Brueckner, K.A., West, B.J., 1988. Vindication of mode-coupled descriptions of multiple-scale water wave fields. Journal of Fluid Mechanics 196, pp. 585–592.

[21] Bryant, P.J., 1983. Cyclic gravity waves in deep water. The Journal of the Australian Mathematical Society. Series B. Applied Mathematics 25, pp. 2–15.

[22] Bryant, P.J., 1983. Waves and Wave Groups in Deep Water, in: Nonlinear Waves. CUP Archive.

[23] Bulian, G., Bresciani, F., Francescutto, A., Fucile, F., 2016. Effect of large initial ship stability on ship safety: An example study, Proc. 26th European Safety and Reliability Conference (ESREL2016), 25-29 September 2016, Glasgow, Scotland, UK, in "Risk, Reliability and Safety: Innovating Theory and Practice", Walls, Revie & Bedford (Eds), CRC Press/Balkema, Taylor & Francis Group, London, 2017, pp. 2302-2309.

[24] Bulian, G., Francescutto, A., 2009. Experimental results and numerical simulations on strongly non-linear rolling of multihulls in moderate beam seas. Proceedings of the IMechE 223, pp. 189–210.

[25] Bulian, G., Moro, L., Brocco, E., Bresciani, F., Biot, M., Francescutto, A., 2015. Using time domain nonlinear ship motion simulations to assess safety of people and cargo onboard a container vessel, in: Soares, C.G., Dejhalla, R., Pavletic, D. (Eds.), Towards Green Marine Technology and Transport. CRC Press, pp. 99-110.

[26] Canuto, C., Hussaini, M.Y., Quarteroni, A., Zang, T.A., 1988. Spectral Methods in Fluid Dynamics. Springer Series, in Computational Physics. Springer-Verlag, Berlin, Heidelberg, 1988.

[27] Chen, Z., Zhang, B., He, Y., Qiu, Z., Perrie, W., 2015. A new modulation transfer function for ocean wave spectra retrieval from X-band marine radar imagery. Chin. J. Ocean. Limnol. 33, pp. 1132–1141.

[28] Clamond, D., Francius, M., Grue, J., Kharif, C., 2006. Long time interaction of envelope solitons and freak wave formations. European Journal of Mechanics - B/Fluids, Rogue waves 25, pp. 536–553.

[29] Clauss, G.F., Klein, M., Dudek, M., Onorato, M., 2015. Deterministic Non-Linear Wave Forecast and Motion Prediction for Short-Term Offshore Operations. Proceedings of Twenty-fifth International Ocean and Polar Engineering Conference (ISOPE 2015), Kona, Big Island, Hawaii, USA, June 21-26, 2015, p. 1236-1244.

[30] Clauss, G.F., Kosleck, S., Testa, D., 2008. CASH - Decision Support System for Computer Aided Ship Handling. Proceedings of Annual General Meeting of the Schiffbautechnische Gesellschaft e.V. p. 30 p.

[31] Clauss, G.F., Kosleck, S., Testa, D., 2009. Critical Situations of Vessel Operations in Short Crested Seas: Forecast and Decision Support System. Proceedings of the ASME 2009 28th International Conference on Ocean, Offshore and Arctic Engineering (OMAE2009), May 31 - June 5, 2009, Honolulu, Hawaii, USA, 14 p.

[32] Colicchio, G., Landrini, M., 2003. On the use of boundary-integral equation methods for unsteady free-surface flows. Journal of engineering mathematics 46, pp. 127–146.

[33] Connell, B.S.H., Rudzinsky, J.P., Brundick, C.S., Milewski, W.M., Kusters, J.G., Farquharson, G., 2015. Development of an environmental and ship motion forecasting system. Proceedings of ASME 34th International Conference on Ocean, Offshore and Arctic Engineering (OMAE 2015), May 31-June 5, St. John's, Newfoundland, Canada, 11p.

[34] Dankert, H., Horstmann, J., Rosenthal, W., 2005. Wind- and wave-field measurements using marine X-band radar-image sequences. IEEE Journal of Oceanic Engineering 30, pp. 534–542.

[35] Dankert, H., Rosenthal, W., 2004. Ocean surface determination from X-band radar-image sequences. J. Geophys. Res. 109, C04016.

[36] Dannenberg, J., Hessner, K., Naaijen, P., Boom, H.V.D., Reichert, K., 2010. The On board Wave and Motion Estimator OWME. The Twentieth International Offshore and Polar Engineering Conference (ISOPE 2010), 20-25 June, 2010 Beijing, China, pp.424–431.

[37] de Oliveira, A.C., Fernandes, A.C., 2012. An Empirical Nonlinear Model to Estimate FPSO With Extended Bilge Keel Roll Linear Equivalent Damping in Extreme Seas. Proceedings of the AMSE 2012 31st International Conference on Ocean, Offshore and Arctic Engineering (OMAE 2012). 1-6, July, July 1-6, 2012, Rio de Janeiro, Brazil, pp. 413–428.

[38] Dean, R.G., Dalrymple, R.A., 1991. Water Wave Mechanics for Engineers and Scientists. World Scientific Publishing.

[39] Debnath, L., 1994. Nonlinear Water Waves. Academic Press Inc.

[40] Dommermuth, D., 2000. The initialization of nonlinear waves using an adjustment scheme. Wave Motion 32, pp. 307–317.

[41] Dommermuth, D.G., Yue, D.K.P., 1987. A high-order spectral method for the study of nonlinear gravity waves. Journal of Fluid Mechanics 184, pp. 267–288.

[42] Ducrozet, G., 2007. Modélisation des processus non-linéaires de génération et de propagation d'états de mer par une approche spectrale. Ph.D. Thesis. Université de Nantes, Ecole Centrale de Nantes (ECN).

[43] Ducrozet, G., Bingham, H.B., Engsig-Karup, A.P., Bonnefoy, F., Ferrant, P., 2012. A comparative study of two fast nonlinear free-surface water wave models. Int. J. Numer. Meth. Fluids 69, pp. 1818–1834.

[44] Ducrozet, G., Bonnefoy, F., Le Touzé, D., Ferrant, P., 2007. 3-D HOS simulations of extreme waves in open seas. Natural Hazards and Earth System Science 7, pp. 109–122.

[45] Edgar, D.R., Horwood, J.M.K., Thurley, R., Belmont, M.R., 2000. The effects of parameters on the maximum prediction time possible in short term forecasting of the sea surface shape. International Shipbuilding Progress 47, pp. 287–301.

[46] Fedele, F., Brennan, J., León, S.P. de, Dudley, J., Dias, F., 2016. Real world ocean rogue waves explained without the modulational instability. Scientific Reports 6, 11p.

[47] Fedele, F., Lugni, C., Fucile, F., Campana, E.F., 2016. On the prediction of rogue waves during Hurricane Joaquin. NTSB Tehnical report. https://dms.ntsb.gov/public/58000-58499/58116/598564.pdf

[48] Fenton, J.D., 1988. The numerical solution of steady water wave problems. Computers and Geosciences 14, pp. 357–368.

[49] Fenton, J.D., 1999. Numerical methods for nonlinear waves. Advances in coastal and ocean engineering 5, pp. 241–324.

[50] Fenton, J.D., 2014. Use of the programs FOURIER, CNOIDAL and STOKES for steady waves.

[51] Fornberg, B., 1998. A practical guide to pseudospectral methods. Cambridge university press.

[52] Fucile, F., Bulian G., Lugni, C., 2016. A probabilistic approach for the quantification of prediction error in deterministic phase-resolved wave forecasting. Under review.

[53] Fucile, F., Bulian, G., Lugni, C., 2016. Quantifying error in deterministic predictions based on phase-resolved linear wave models. Proc. 26th European Safety and Reliability Conference (ESREL2016), 25-29 September 2016, Glasgow, Scotland, UK, in "Risk, Reliability and Safety: Innovating Theory and Practice", Walls, Revie & Bedford (Eds), CRC Press/Balkema, Taylor & Francis Group, London, 2017, pp. 355-361, ISBN 978-1-138-02997-2.

[54] Fucile, F., Ludeno, G., Serafino, F., Bulian, G., Soldovieri, F., Lugni, C., 2016. Some Challenges in Recovering Wave Features From a Wave Radar System. Proceedings of the Twenty-sixth (2016) International Ocean and Polar Engineering Conference (ISOPE2016), Rhodes, Greece, June 26-July 1, Volume 3, ISBN 978-1-880653-88-3, ISSN 1098-6189, pp. 319-326.

[55] Furhman, D.R., Madsen, P.A., 2006. Short-crested waves in deep water: a numerical investigation of recent laboratory experiments. Journal of Fluid Mechanics 559, pp. 391–411.

[56] Furhman, D.R., Madsen, P.A., Bingham, H.B., 2006. Numerical simulation of lowest-order short-crested wave instabilities. Journal of Fluid Mechanics 563, pp. 415–441.

[57] Gallego, G., Benetazzo, A., Yezzi, A., Fedele, F., 2008. Wave Statistics and Spectra via a Variational Wave Acquisition Stereo System. Proceedings of 27th International Conference on Offshore Mechanics and Arctic Engineering (OMAE 2008), June 15-20, 2008, Estoril, Portugal pp. 801–808.

[58] Golub, G.H., Van Loan, C.F., 2013. Matrix computations (Fourth edition). The Johns Hopkins University Press, Baltimore.

[59] Golub, G.H., Von Matt, U., 1997. Tikhonov regularization for large scale problems. Proceeding of the Workshop on Scientific Computing (1997), March 10-12 1997, Hong Kong, pp. 3–26.

[60] Greco, M., Lugni, C., Faltinsen, O.M., 2014. Can the water on deck influence the parametric roll of a FPSO? A numerical and experimental investigation. European Journal of Mechanics-B/Fluids 47, pp. 188–201.

[61] Greco, M., Lugni, C., Faltinsen, O.M., 2015. Influence of motion coupling and nonlinear effects on parametric roll for a floating production storage and offloading platform. Philosophical Transactions of the Royal Society of London A: Mathematical, Physical and Engineering Sciences 373, 20140110.

[62] Guyenne, P., Nicholls, D.P., 2007. A high-order spectral method for nonlinear water waves over moving bottom topography. SIAM Journal on Scientific Computing 30, pp. 81–101.

[63] Halliday, J.R., Dorrell, D.G., Wood, A.R., 2011. An application of the Fast Fourier Transform to the short-term prediction of sea wave behaviour. Renewable Energy 36, pp. 1685–1692.

[64] Hansen, P.C., 1998. Rank-Deficient and Discrete Ill-Posed Problems: Numerical Aspects of Linear Inversion. Mathematical Modeling and Computation. Society for Industrial and Applied Mathematics.

[65] Hansen, P.C., 1999. The L-curve and its use in the numerical treatment of inverse problems. Department of Mathematical Modelling, Technical University of Denmark.

[66] Hansen, P.C., O'Leary, D.P., 1993. The use of the L-curve in the regularization of discrete ill-posed problems. SIAM Journal on Scientific Computing 14, pp. 1487–1503.

[67] Hassanaliaragh, S., 2009. Radar Data Assimilation and Forecasts of Evolving Nonlinear Wave Fields. Ph.D. Thesis. University of Michigan.

[68] Hilmer, T., Thornhill, E., 2014. Deterministic wave predictions from the WaMoS II. Proceedings of OCEANS 2014 – MTS-IEEE, Taipei, Taiwan, 7-10 April, 2014 8p.

[69] Hilmer, T., Thornhill, E., 2015. Observations of predictive skill for real-time Deterministic Sea Waves from the WaMoS II. OCEANS 2015 - MTS/IEEE Washington, Washington DC, 19-22 October 2015, 7p.

[70] Johnson, R.S., 1997. A Modern Introduction to the Mathematical Theory of Water Waves. Cambridge University Press.

[71] Kaiser, J.F., Reed, W.A., 1977. Data smoothing using low-pass digital filters. Review of Scientific Instruments 48, pp. 1447–1457.

[72] Kanevsky, M.B., 2009. Radar imaging of the ocean waves. First edition, Elsevier, Amsterdam.

[73] Kofiani, K.N., 2009. A new numerical method for the problem of nonlinear long-short wave interactions. Ph.D. Thesis. Massachusetts Institute of Technology.

[74] Kosleck, S., 2013. Prediction of Wave-Structure Interaction by Advanced Wave Field Forecast. Ph.D. Thesis, Naval Architecture and Ocean Engineering Department, Technical University Berlin, Germany.

[75] Kusters, J.G., Cockrell, K.L., Connell, B.S.H., Rudzinsky, J.P., Vinciullo, V.J., 2016. FutureWaves™: A real-time Ship Motion Forecasting system employing advanced wave-sensing radar. Proceeding of OCEANS 2016 MTS/IEEE, Monterey, 9p.

[76] Lake, B.M., Yuen, H.C., Rungaldier, H., Ferguson, W.E., 1977. Nonlinear deep-water waves: theory and experiment. Part 2. Evolution of a continuous wave train. Journal of Fluid Mechanics 83, pp. 49–74.

[77] Le Touze, D., 2003. Spectral methods for modelling nonlinear unsteady free-surface flows. Ph.D. Thesis. Université de Nantes, Ecole Centrale de Nantes (ECN).

[78] Lee, S.-B., Choi, Y.-M., Do, J., Kwon, S.-H., 2014. Prediction of propagated wave profiles based on point measurement. International Journal of Naval Architecture and Ocean Engineering 6, pp. 175–185.

[79] Ludeno, G., Brandini, C., Lugni, C., Arturi, D., Natale, A., Soldovieri, F., Gozzini, B., Serafino, F., 2014. Remocean System for the Detection of the Reflected Waves from the Costa Concordia Ship Wreck. IEEE Journal of Selected Topics in Applied Earth Observations and Remote Sensing 7, pp. 3011–3018.

[80] Lugni, C., Greco, M., Faltinsen, O.M., 2015. Influence of yaw-roll coupling on the behavior of a FPSO: An experimental and numerical investigation. Applied Ocean Research 51, pp. 25–37.

[81] Lund, B., Collins, C.O., Tamura, H., Graber, H.C., 2016. Multi-directional wave spectra from marine X-band radar. Ocean Dynamics, 66, pp. 973–988.

[82] Lund, B., Collins, C.O., Graber, H.C., Terrill, E., Herbers, T.H., 2014. Marine radar ocean wave retrieval's dependency on range and azimuth. Ocean Dynamics 64, pp. 999–1018.

[83] Lyzenga, D.R., Maffett, A.L., Shuchman, R.A., 1983. The Contribution of Wedge Scattering to the Radar Cross Section of the Ocean Surface. IEEE Transactions on Geoscience and Remote Sensing GE-21, pp. 502–505.

[84] Ma, Q., 2010. Advances in Numerical Simulation of Nonlinear Water Waves, Advances in Coastal and Ocean Engineering. World Scientific.

[85] Madsen, P.A., Fuhrman, D.R., 2012. Third-order theory for multi-directional irregular waves. Journal of Fluid Mechanics 698, pp. 304–334.

[86] Madsen, P.A., Furhman, D.R., 2006. Third-order theory for bichromatic bi-directional water waves. Journal of Fluid Mechanics 557, pp. 369–397.

[87] McLean, J.W., 1982. Instabilities of finite-amplitude gravity waves on water of finite depth. Journal of Fluid Mechanics 114, pp. 331–341.

[88] McLean, J.W., Ma, Y.C., Martin, D.U., Saffman, P.G., Yuen, H.C., 1981. Three-dimensional instability of finite-amplitude water waves. Physical Review Letters 46, 817 -821.

[89] McTaggart, K., de Kat, J.O., 2000. Capsize risk of intact frigates in irregular seas. SNAME Annual Meeting, Vancouver, BC, October, 2000.

[90] Mei, C.C., 1989. The applied dynamics of ocean surface waves. World scientific.

[91] Mei, C.C., Stiassnie, M., Yue, D.K.-P., 1989. Theory and Applications of Ocean Surface Waves: Part 1: Linear Aspects Part 2: Nonlinear Aspects. World Scientific.

[92] Milder, D.M., 1990. The effects of truncation on surface-wave Hamiltonians. Journal of Fluid Mechanics 217, pp. 249–262.

[93] Milewski, W.M., Connell, B.S., Vinciullo, V.J., Kirschner, I.N., 2015. Reduced order model for motion forecasts of one or more vessels. Proceedings of the ASME 2015 34th International Conference on Ocean, Offshore and Arctic Engineering (OMAE 2015), May 31-June 5, 2015, St. John's, Newfoundland, Canada. 11p.

[94] Mori, N., Yasuda, T., 2002. Effects of high-order nonlinear interactions on unidirectional wave trains. Ocean Engineering 29, pp. 1233–1245.

[95] Moro, L., Bulian, G., Brocco, E., Bresciani, F., Biot, M., Francescutto, A., 2015. Failure analysis of container stacks by non-linear FE simulations under non-linear inertial loads, in: Soares, C.G., Dejhalla, R., Pavletic, D. (Eds.), Towards Green Marine Technology and Transport. CRC Press, pp. 745–754.

[96] Morris, E. L., Zienkiewicz, H. K., Belmont, M. R., 1998. Short term forecasting of the sea surface shape. International Shipbuilding Progress 45 (444), pp. 383-400.

[97] Naaijen, P., Blondel-Couprie, E., 2012. Reconstruction and prediction of short-crested seas based on the application of a 3D-FFT on synthetic waves: Part 1 - Reconstruction. Proceedings of ASME 31st International Conference on Ocean, Offshore and Arctic Engineering (OMAE 2012), 1-6 July, Rio de Janeiro, Brazil, pp. 43-55.

[98] Naaijen, P., Blondel-Couprie, E., 2012. Wave induced motion prediction as operational decision support for offshore operations. Proceedings of the International Conference Marine Heavy Transport & Lift III, 24-25 October, 2012, London, UK, pp. 11-18.

[99] Naaijen, P., Huijsmans, R., 2008. Real Time Wave Forecasting for Real Time Ship Motion Predictions. Proceedings of ASME 27th International Conference on Ocean, Offshore and Arctic Engineering (OMAE 2008), 15-20 June, Estoril, Portugal, 8p.

[100] Naaijen, P., Huijsmans, R.H.M., 2010. Real Time Prediction of Second Order Wave Drift Forces for Wave Force Feed Forward in DP. Proceedings of ASME 29th International Conference on Ocean, Offshore and Arctic Engineering, American Society of Mechanical Engineers (OMAE 2010), June 6-11, 2010, Shanghai, China. pp. 357–364.

[101] Naaijen, P., Roozen, D.K., Huijsmans, R.H.M., 2016. Reducing Operational Risks by On-Board Phase Resolved Prediction of Wave Induced Ship Motions. Proceedings of the ASME 35th International Conference on Ocean, Offshore and Arctic Engineering (OMAE2016), June 19-24, 2016, Busan, South Korea, 11 p.

[102] Naaijen, P., Trulsen, K., Blondel-Couprie, E., 2014. Limits to the extent of the spatio-temporal domain for deterministic wave prediction. International Shipbuilding Progress 61, pp. 203–223.

[103] Naaijen, P., van Dijk, R.R.T., Huijsmans, R.H.M., El-Mouhandiz, A.A., 2009. Real time estimation of ship motions in short crested seas. Proceedings of ASME 28th International Conference on Ocean, Offshore and Arctic Engineering (OMAE 2009), May 31 - June 5, Honolulu, Hawaii, pp. 243-255.

[104] Naaijen, P., Wijaya, A. P. 2014. Phase resolved wave prediction from synthetic radar images. Proceeding of ASME 33rd International Conference on Ocean, Offshore and Arctic Engineering, (OMAE 2014), 8-13 June, San Francisco, California, 9p.

[105] Nieto Borge, J., Rodriguez, G.R., Hessner, K., González, P.I., 2004. Inversion of Marine Radar Images for Surface Wave Analysis. J. Atmos. Oceanic Technol. 21, pp. 1291–1300.

[106] Nieto Borge, J., Soares, C.G., 2000. Analysis of directional wave fields using X-band navigation radar. Coastal Engineering 40, pp. 375–391.

[107] Nieto Borge, J.C., 1997. Análisis de campos de oleaje mediante radar de navegación en banda X. Ph.D. Thesis. Universidad de Alcalá de Henares.

[108] Nieto-Borge, J., Hessner, K., Jarabo-Amores, P., De La Mata-moya, D., 2008. Signal-to-noise ratio analysis to estimate ocean wave heights from X-band marine radar image time series. Sonar Navigation, IET Radar, 2, pp. 35–41.

[109] Nouguier, F., Grilli, S. T., Guerin, C. A. 2014. Nonlinear ocean wave reconstruction algorithms based on simulated spatio-temporal data acquired by a flash LiDAR camera. Geoscience and Remote Sensing, IEEE Transactions on 52(3), pp. 1761–1771.

[110] Orszag, S.A., 1971. Numerical Simulation of Incompressible Flows within Simple Boundaries. I. Galerkin (Spectral) Representations. Studies in Applied Mathematics 50, pp. 293–327.

[111] Patterson Jr., G.S., Orszag, S.A., 1971. Spectral Calculations of Isotropic Turbulence: Efficient Removal of Aliasing Interactions. Physics of Fluids (1958-1988) 14, pp. 2538–2541.

[112] Paulsen, B., 2011. Inversion of Marine Radar Imagery to Surface Realizations and Dual-Polarization Analysis. Msc. Thesis. University of Massachusetts Amherst.

[113] Phillips, O.M., 1960. On the dynamics of unsteady gravity waves of finite amplitude Part 1. The elementary interactions. Journal of Fluid Mechanics 9, pp. 193–217.

[114] Plant, W.J., 1990. Bragg Scattering Of Electromagnetic Waves From The Air/Sea Interface, in: Geernaert, G.L., Plant, W.J. (Eds.), Surface Waves and Fluxes. Springer Netherlands, Dordrecht, pp. 41–108.

[115] Plant, W.J., 2003. Microwave sea return at moderate to high incidence angles. Waves in random media 13, pp. 339–354.

[116] Plant, W.J., Farquharson, G., 2012. Origins of features in wave number-frequency spectra of space-time images of the ocean. J. Geophys. Res. 117, C06015.

[117] Plant, W.J., Keller, W.C., 1990. Evidence of Bragg scattering in microwave Doppler spectra of sea return. Journal of Geophysical Research 95, 16299.

[118] Prabhu, K.M.M., 2013. Window functions and their applications in signal processing. CRC Press Taylor& Francis Group.

[119] Reichert, K., Dannenberg, J., van den Boom, H., 2010. X-Band radar derived sea surface elevation maps as input to ship motion forecasting. OCEANS 2010 IEEE-Sydney. IEEE, pp. 1–7.

[120] Rienecker, M.M., Fenton, J.D., 1981. A Fourier approximation method for steady water waves. Journal of Fluid Mechanics 104, pp. 119–137.

[121] Saket, A., Peirson, W.L., Banner, M.L., Barthelemy, X., Allis, M.J., 2015. Wave breaking of two-dimensional deep-water wave groups in the presence and absence of wind. arXiv:1508.07702 [physics].

[122] Schäffer, H.A., 2008. Comparison of Dirichlet–Neumann operator expansions for nonlinear surface gravity waves. Coastal Engineering 55, pp. 288–294.

[123] Schwartz, L.W., 1974. Computer extension and analytic continuation of Stokes' expansion for gravity waves. Journal of Fluid Mechanics 62, pp. 553–578.

[124] Schwartz, L.W., Fenton, J.D., 1982. Strongly nonlinear waves. Annual review of fluid mechanics 14, pp. 39–60.

[125] Seemann, J., Ziemer, F., 1995. Computer simulation of imaging ocean wave fields with a marine radar, in: OCEANS'95. MTS/IEEE. Challenges of Our Changing Global Environment. Conference Proceedings. IEEE, pp. 1128–1133.

[126] Seemann, J., Ziemer, F., Senet, C.M., 1997. A method for computing calibrated ocean wave spectra from measurements with a nautical X-band radar, in: OCEANS'97. MTS/IEEE Conference Proceedings. IEEE, pp. 1148–1154.

[127] Senet, C.M., Seemann, J., Ziemer, F., 2001. The near-surface current velocity determined from image sequences of the sea surface. IEEE Transactions on Geoscience and Remote Sensing 39, pp. 492–505.

[128] Serafino, F., Lugni, C., Nieto Borge, J. C., Soldovieri, F. 2011. A simple strategy to mitigate the aliasing effect in X-band marine radar data: numerical results for a 2D case. Sensors 11(12), pp. 1009–1027.

[129] Serafino, F., Lugni, C., Soldovieri, F., 2008. Sea surface topography reconstruction from X-band radar images. Advances in Geosciences 19, pp. 83–86.

[130] Serafino, F., Lugni, C., Soldovieri, F., 2010. A Novel Strategy for the Surface Current Determination From Marine X-Band Radar Data. IEEE Geoscience and Remote Sensing Letters 7, pp. 231–235.

[131] Shen, S.S., 2012. A Course on Nonlinear Waves. Springer Science & Business Media.

[132] Skandrani, C., Kharif, C., Poitevin, J., 1996. Nonlinear evolution of water surface waves: the frequency down-shift phenomenon, in: Dias, F., Ghidaglia, J.-M., Saut, J.-C. (Eds.), Mathematical Problems in the Theory of Water Waves: A Workshop on the Problems in the Theory of Nonlinear Hydrodynamic Waves, May 15-19, 1995, Luminy, France. Contemporary Mathematic, 200, pp. 157-171.

[133] Skjelbreia, L., Hendrickson, J., 1960. Fifth order gravity wave theory. Proceedings of 7th Coastal Engineering Conference, Hague, Netherlands, 1960, 1, pp. 184–196.

[134] Stiassnie, M., Shemer, L., 1984. On modifications of the Zakharov equation for surface gravity waves. Journal of Fluid Mechanics 143, pp. 47–67.

[135] Stoker, J.J., 1992. Water Waves: The Mathematical Theory with Applications. John Wiley & Sons.

[136] Stredulinsky, D.C., Thornhill, E.M., 2011. Ship motion and wave radar data fusion for shipboard wave measurement. Journal of ship research 55, pp. 73–85.

[137] Tanaka, M., 2001. A method of studying nonlinear random field of surface gravity waves by direct numerical simulation. Fluid Dynamics Research 28, pp. 41–60.

[138] Tanaka, M., 2001. Verification of Hasselmann's energy transfer among surface gravity waves by direct numerical simulations of primitive equations. Journal of Fluid Mechanics 444, pp. 199–221.

[139] Tannuri, E.A., Simos, A.N., Sparano, J.V., Matos, V.L.F., 2012. Motion-based wave estimation: small-scale tests with a crane-barge model. Marine Structures 28, 67–85.

[140] Toffoli, A., Benoit, M., Onorato, M., Bitner-Gregersen, E.M., 2009. The effect of third-order nonlinearity on statistical properties of random directional waves in finite depth. Nonlinear Processes in Geophysics 16, pp. 131–139.

[141] Toffoli, A., Gramstad, O., Trulsen, K., Monbaliu, J., Bitner-Gregersen, E., Onorato, M., 2010. Evolution of weakly nonlinear random directional waves: laboratory experiments and numerical simulations. Journal of Fluid Mechanics 664, pp. 313–336.

[142] Trefethen, L.N., Bau, D., 1997. Numerical Linear Algebra. Society for Industrial and Applied Mathematics.

[143] Tsai, W.-T., Yue, D.K., 1996. Computation of nonlinear free-surface flows. Annual review of fluid mechanics 28, pp. 249–278.

[144] Tucker, M. J., Challenor, P. I., Carter, D. J. T, 1984. Numerical simulation of a random sea: a common error and its effect upon wave group statistics. Applied Ocean Research 6(2), 118-122

[145] Valenzuela, G.R., 1978. Theories for the interaction of electromagnetic and oceanic waves - A review. Boundary-Layer Meteorology 13, pp. 61–85.

[146] Vettor, R., 2010. Sviluppo di una metodologia di nowcasting del moto ondoso finalizzata all'operatività di mezzi offshore (Development of wave elevation nowcasting methodology for the operability of offshore units). M.Sc. Thesis (In Italian). University of Trieste.

[147] Vogel, C.R., 2002. Computational methods for inverse problems. Society for Industrial and Applied Mathematics.

[148] Voronovich, A.G., 1996. On the theory of electromagnetic waves scattering from the sea surface at low grazing angles. Radio Sci. 31, pp. 1519–1530.

[149] Watson, K.M., West, B.J., 1975. A transport-equation description of nonlinear ocean surface wave interactions. Journal of Fluid Mechanics 70, pp. 815–826.

[150] Wei, Y., Zhang, J.-K., Lu, Z., 2016. A Novel Successive Cancellation Method to Retrieve Sea Wave Components from Spatio-Temporal Remote Sensing Image Sequences. Remote Sensing 8, 607, 19p.

[151] West, B.J., Brueckner, K.A., Janda, R.S., Milder, D.M., Milton, R.L., 1987. A new numerical method for surface hydrodynamics. J. Geophys. Res. 92, pp. 11803–11824.

[152] Wetzel, L.B., 1977. A model for sea backscatter intermittency at extreme grazing angles. Radio Science 12, pp. 749–756.

[153] Wetzel, L.B., 1990. Electromagnetic Scattering from the Sea at Low Grazing Angles, in: Geernaert, G.L., Plant, W.J. (Eds.), Surface Waves and Fluxes. Springer Netherlands, Dordrecht, pp. 109–171.

[154] Wetzel, L.B., 2008. Sea Clutter, in: Skolnik, M. (Ed.), Radar Handbook, Third Edition. McGraw-Hill Education.

[155] Whitham, G.B., 2011. Linear and Nonlinear Waves. John Wiley & Sons.

[156] Wijaya, A.P., Naaijen, P., Adonowati, van Groesen, E., 2015. Reconstruction and future prediction of the sea surface from radar observations. Ocean engineering 106, pp. 261–270.

[157] Wright, J., 1966. Backscattering from capillary waves with application to sea clutter. IEEE Transactions on Antennas and Propagation 14, pp. 749–754.

[158] Wright, J., 1968. A new model for sea clutter. IEEE Transactions on Antennas and Propagation 16, pp. 217–223.

[159] Wu, G., 2004. Direct simulation and deterministic prediction of large-scale nonlinear ocean wave-field . Ph.D. Thesis. Massachusetts Institute of Technology.

[160] Wu, G., Liu, Y., Yue, D.K.P., 2007. Ocean Wave Prediction Using Large-Scale Phase-Resolved Computations. Proceedings of High Performance Computing Modernization Program Users Group Conference, DoD, (HPCMP-UGC), 18 -21 June 2007, Pittsburgh, PA, pp. 449–454.

[161] Xiao, W., 2013. Study of directional ocean wavefield evolution and rogue wave occurrence using large-scale phase-resolved nonlinear simulations. Ph.D. Thesis. Massachusetts Institute of Technology.

[162] Xiao, W., Liu, Y., Wu, G., Yue, D.K.P., 2013. Rogue wave occurrence and dynamics by direct simulations of nonlinear wave-field evolution. Journal of Fluid Mechanics 720, pp. 357–392.

[163] Xiao, W., Liu, Y., Yue, D.K.P., 2009. Ocean Wave Prediction Using Large-Scale Phase-Resolved Computations. Proceedings of DoD High Performance Computing Modernization Program Users Group Conference, DoD, (HPCMP-UGC), 15 -18 June 2009, San Diego, CA, pp. 278–284.

[164] Xu, L., Guyenne, P., 2009. Numerical simulation of three-dimensional nonlinear water waves. Journal of Computational Physics 228, pp. 8446–8466.

[165] Xue, M., Xu, H., Liu, Y., Yue, D.K., 2001. Computations of fully nonlinear three-dimensional wave–wave and wave–body interactions. Part 1. Dynamics of steep three-dimensional waves. Journal of Fluid Mechanics 438, pp. 11–39.

[166] Yoon, S., Kim, J., Choi, W., 2016. An Explicit Data Assimilation Scheme for a Nonlinear Wave Prediction Model Based on a Pseudo-Spectral Method. IEEE Journal of Oceanic Engineering 41, pp. 112–122.

[167] Young, I.R., Rosenthal, W., Ziemer, F., 1985. A three-dimensional analysis of marine radar images for the determination of ocean wave directionality and surface currents. J. Geophys. Res. 90, pp. 1049–1059.

[168] Yue, D.K.P, 2008. Nonlinear Wave Environments for Ship Motion Analysis. 27th Symposium of Naval Hydrodynamics, Seul, Korea; 5-10 October, 2008, 19p.

[169] Zakharov, V.E., 1968. Stability of periodic waves of finite amplitude on the surface of a deep fluid. Journal of Applied Mechanics and Technical Physics 9, pp. 190–194.

[170] Zakharov, V.E., Dyachenko, A.I., Vasilyev, O.A., 2002. New method for numerical simulation of a nonstationary potential flow of incompressible fluid with a free surface. European Journal of Mechanics - B/Fluids 21, pp. 283–291.

[171] Zeimer, F., Rosenthal, W., 1987. On the transfer function of a shipborne radar for imaging ocean waves. GKSS-Forschungszentrum, Geesthacht.

[172] Zhang, J., Chen, L., 1999. General Third-Order Solutions for Irregular Waves in Deep Water. Journal of Engineering Mechanics 125, pp. 768–779.

[173] Zhang, J., Yang, J., Wen, J., Prislin, I., Hong, K., 1999. Deterministic wave model for short-crested ocean waves: Part I. Theory and numerical scheme. Applied Ocean Research 21, pp. 167–188.

[174] Zhao, H., Song, Z., Li, L., Kong, J., 2014. On the Fourier approximation method for steady water waves. Acta Oceanologica Sinica 33, pp. 37–47.